ROBUST TEXTURE FEATURES WITH APPLICATIONS IN MEDICAL IMAGING

by

Rouzbeh Maani

A thesis submitted in partial fulfillment of the requirements for the degree of

Doctor of Philosophy

Department of Computing Science

University of Alberta

Abstract

Image texture is defined as visual patterns appearing in images. The powerful perceptive capability of texture features has made texture analysis a major research topic in computer vision and image processing. Texture features are used to detect defective products in factories, to understand human actions in surveillance systems, to identify people from biometric data (e.g., fingerprint, iris scan, and face photo), and to find abnormality in medical images. Indeed, many advanced applications take a direct or indirect advantage of texture analysis in their processing.

An ideal texture feature should not only be discriminative but also be robust to imaging distortions. The developement of robust texture features is first motivated by applying texture analysis to Amyotrophic Lateral Sclerosis (ALS). ALS is a fatal neurodegenerative disease in which evidence of the disease is not perceptible in routine magnetic resonance images (MRI) of the brain even to a trained eye. Unlike brain tumors or multiple sclerosis, the lack of observable features possesses challenges to the detection and diagnosis of ALS. These challenges and the great need in the ALS research community to find a biomarker and to detect the patterns of degeneration in the brain have encouraged the author to study this disease using texture analysis. The results of this thesis suggest texture analysis is a potential biomarker for the disease and hence, open up new avenues towards understanding the disease.

This thesis presents a useful approach for texture analysis of the brain. In contrast to the current methods, the proposed approach does not need a region of interest. It performs a voxel based texture analysis and provides a statistical map showing the regions in the brain statistically different between the groups of patients and healthy subjects. A Computer Aided Diagnosis (CAD) tool is developed for this purpose. This toolbox is called the Statistical MAp fRom Texture (SMART) and helps doctors make diagnoses and monitor the progression of diseases using texture analysis.

Distortions and effects in real images (e.g., noise, illumination change, blurr effect) increase demand for developing robuts texture features. To address the robustness issues, a novel approach is presented called the Local Frequancy Descriptor (LFD). The LFD is the basis of several novel 2D and 3D texture features presented later in this thesis. It is also the basis of new image gradient operators for 2D and 3D images and a novel image matching method. All texture features, methods, and gradient operators defined based on the LFD show high accuracy and outperform the state-ofthe-art methods. In addition, they present remarkable robutness to imaging effects.

Preface

Research for this thesis was conducted under the supervision of Dr. Herbert Yang and Dr. Sanjay Kalra at the University of Alberta. Portions of this thesis were published as:

- Chapter 5: R. Maani, Y. H. Yang, and S. Kalra. Voxel-based Texture Analysis of the Brain, PLOS ONE, To Appear.

- Chapter 6: R. Maani, Y. H. Yang, and S. Kalra. Texture analysis of the brain in Amyotrophic Lateral Sclerosis. Poster presented at 19th Annual Meeting of the Organization for Human Brain Mapping (OHBM), June 16–20, Seattle, USA, 2013.

- Chapter 7: R. Maani, S. Kalra, and Y. H. Yang. Noise robust rotation invariant features for texture classification. Pattern Recognition, 46(8):2103–2116, 2013.

- Chapter 7: R. Maani, S. Kalra, and Y. H. Yang. Rotation invariant local frequency descriptors for texture classification. IEEE Transactions on Image Processing, 22(6):2409–2419, 2013.

- Chapters 7 and 8: R. Maani, S. Kalra, and Y. H. Yang. Robust edge aware descriptor for image matching. In Proceedings of 12th Asian Conference on Computer Vision (ACCV), Nov 1–5, Singapore, Singapore, 2014.

- Chapters 7 and 9: R. Maani, S. Kalra, and Y.H. Yang. Robust volumetric texture classification of magnetic resonance images of the brain using local frequency descriptor. IEEE Transactions on Image Processing, 23(10):4625–4636, 2014.

I, Rouzbeh Maani, was responsible for the concept, analysis, and manuscripts composition, while my supervisors provided guidance, feedback, and comments on the manuscripts.

To my lovely wife, Fatemeh Kazemeyni
For her inspiration, encouragement, and unwavering love.

Acknowledgements

Table of Contents

List of Tables

List of Figures

xi

Acronyms

1D:	One Dimensional
2D:	Two Dimensional
3D:	Three Dimensional
AD:	Alzheimer's Disease
ALS:	Amyotrophic Lateral Sclerosis
ALSFRS:	ALS Functional Rating Scale
ANN:	Artificial Neural Network
AR:	AutoRegressive
CLBP:	Completed model of Local Binary Patterns
BGLAM:	Basic Gray Level Aura Matrix
BOLD:	Blood Oxygen Level Dependent
CM:	Cerebral Microangiopathy
CNS	Central Nervous System
CT:	Computed Tomography
CSF:	Cerebrospinal Fluid
CST:	Corticospinal Tract
DFT:	Discrete Fourier Transform
DTI:	Diffusion Tensor Imaging
DWT:	Discrete Wavelet Transform
EDSS:	Expanded Disability Status Scale
EM:	Expectation Maximization
FFT:	Fast Fourier Transform
FLAIR:	FLuid Attenuated Inversion Recovery
fMRI:	Functional MRI
FTD	Frontotemporal Dementia
FTLD:	FrontoTemporal Lobar Degeneration
GLAM:	Gray Level Aura Matrix
GLCM:	Gray Level Cooccurrence Matrix
GLM:	General Linear Model
GM:	Gray Matter
GRF:	Gibbs Random Fields
INU:	Intensity Non Uniformity
LBP:	Local Binary Patterns
LBPV:	Local Binary Patterns Variance
LDA:	Linear Discriminant Analysis
LFD:	Local Frequency Descriptors
LMN:	Lower Motor Neurons
MCI:	Mild Cognitive Impairment
MFS:	Multi-Fractal Spectrum
MR:	Magnetic Resonance
MRC:	Mixed Raster Content
MRF:	Markov Random Field
MRI:	Magnetic Resonance Imaging
MRS:	Magnetic Resonance Spectroscopy

MS:	Multiple Sclerosis
MTL:	Medial Temporal Lobe
NAWM:	Normal Appearing White Matter
NWM:	Normal White Matter
NGF:	Normalized Gabor Filter
OCR:	Optical Character Recognition
PET:	Positron emission tomography
PNS	Peripheral Nervous System
nLDA:	Null-space based Linear Discriminant Analysis
NN:	Nearest Neighbor
RF:	Random Field
RLM:	Run Length Matrices
ROI:	Region Of Interest
SAR:	Simultaneous Auto Regressive
SAR:	Synthetic Aperture Radar
SBM:	Surface Based Morphometry
SPM:	Statistical Parametric Map
SE:	Structuring Element
SIFT:	Scale Invariant Feature Transform
STFT:	Short Term Fourier Transform
SVM:	Support Vector Machine
TBM:	Tensor Based Morphometry
UMN:	Upper Motor Neurons
VLBP:	Volume Local Binary Patterns
VBM:	Voxel Based Morphometry
WM:	White Matter

Brain Anatomy Terms

Prefixes	Description
Superior (Dorsal):	The upper side
Inferior (Ventral):	The lower side
Anterior (Rostral):	The front
Posterior (Caudal):	The rear
Lateral:	The sides (left and right)
Medial:	The middle part

Anatomical Region	Description
Auditory cortex:	A region of the brain that processes sound; located in the temporal lobe
Basal ganglia:	A group of nuclei located deep within the cerebrum; involved with several functions including motor control
Caudate nucleus:	A nucleus located within the basal ganglia
Central sulcus:	The fissure in the cerebral cortex separating the parietal lobe from the frontal lobe
Centrum semiovale:	The white matter found underneath the gray matter on the surface of the cerebrum
Cerebral cortex:	The sheet of neural tissue that is outermost to the cerebrum of the brain; contains the cell bodies of neurons
Cingulate cortex:	A part of the brain located in the medial aspect of the cortex
Corona radiata:	A white matter sheet that continues ventrally as the internal capsule and dorsally as the centrum semiovale
Corticospinal tract:	The neurons that conduct impulses from the brain (mainly from the motor cortex) to the spinal cord
Frontal lobe:	One of the four lobes in each hemisphere located at the front of the cerebrum
Globus pallidus:	Part of the basal ganglia
Hippocampus:	Located in the medial temporal lobe; important for memory storage
Inferior frontal gyrus:	The fold located in inferior region of the frontal lobe and anterior to the precentral gyrus
Insula:	A portion of the cerebral cortex folded deep within the lateral sulcus
Internal capsule:	A dense bundle of white matter in the brain that separates the caudate nucleus and the thalamus from the putamen and the globus pallidus
Lateral sulcus:	The fissure separating the temporal lobe from the parietal and frontal lobes.
Medulla (oblongata):	The lower half of the brainstem
Midbrain:	A portion of the central nervous system located in the brainstem
Motor cortex:	A region of the cerebral cortex located in the frontal lobe and in front of the central sulcus
Occipital lobe:	One of the four lobes in each hemisphere located in the rearmost portion of the brain; involved in visual processing

Anatomical Region	Description
Orbitofrontal cortex:	A part of prefrontal cortex region in the frontal lobes
Parahippocampal gyrus:	A gray matter cortical region of the brain that surrounds the hippocampus
Parietal lobe:	One of the four lobes in each hemisphere located superior to the occipital lobe and posterior to the frontal lobe; involved in sensory processing
Pons:	A structure located on the brain stem
Postcentral gyrus:	The fold located in front of the parietal lobe just posterior to the central sulcus; the location of the primary sensory cortex
Posterior parietal cortex:	A portion of the parietal lobe located posterior to the primary somatosensory cortex
Precentral gyrus:	The fold located in posterior region of the frontal lobe just anterior to the central sulcus; the location of the primary motor cortex
Prefrontal cortex	The anterior part of the frontal lobe
Premotor cortex	The area of motor cortex lying within the frontal lobe of the brain just anterior to the primary motor cortex
Primary motor cortex:	A brain region located in the posterior portion of the frontal lobe
Primary somatosensory cortex:	A part of parietal lobe located in the postcentral gyrus
Putamen:	Part of the basal ganglia
Sensorimotor cortex	Refer to the primary somatosensory cortex
Superior frontal gyrus:	A part of the frontal lobe located on top of the brain, running down towards the front
Supplementary motor area:	A part of the cerebral cortex located on the midline surface of the hemisphere just in front of the primary motor cortex
Temporal lobe:	One of the four lobes in each hemisphere located beneath the frontal and parietal lobes, and anterior to the occipital lobe; involved with hearing, emotions, memory, and language
Thalamus:	A midline symmetrical structure within the brain located between the cerebral cortex and midbrain. A relay station for sensory information entering the brain

Chapter 1

Introduction

1.1 Motivation

Texture refers to the intensity variations or visual patterns in images. Indeed, what helps us to perceive images is not limited to color. In gray scale images the human eye is able to distinguish different objects and scenes by means of visual patterns. Intensity variations and visual patterns not only help us identify objects but also can reveal the material of the objects. For instance, rugged objects are perceived as uneven surfaces to the eye. Sharp objects appear with thin edges. Polished surfaces look shiny. Hence, texture features play an important role in our perception. This important role motivated several researchers including Bela Julesz to perform different experiments to understand the visual perception of textures in human [168; 169].

The findings of Julesz and other researchers have established a foundation for todays texture analysis methods and have made texture analysis an important research topic in computer vision and image processing. Texture methods have been successfully used in many applications including but not limited to automatic inspection, document processing, remote sensing, fingerprint identification, object recognition, image matching, and medical imaging. Thanks to texture analysis methods, we detect oil spills, ice surfaces, urban areas, mountains and woods from Synthetic Aperture Radar (SAR) images. Biometric information (e.g., fingerprints, iris scans, face photos) is extensively used by security agencies for accurate and fast personal identification. Three dimensional models of cities and objects are constructed by matching texture features in ordinary two dimensional images. Robots use texture features to understand their surroundings in space explorations and in other environments. Doctors are aided by CAD tools to detect, analyze, and monitor different disease by means of texture features. Movie and game industries use textures for special visual effects. Factories take advantage of texture methods to identify defective products. Nowadays, many applications employ methods that make a direct or indirect use of texture features.

One of the main applications of texture analysis is medical imaging. In this area, a motivation of this thesis is to explore the capability of texture analysis to detect cerebral changes in MR images of patients with ALS. ALS is a fatal neurodegenerative disease, the cause of which is unknown.

To the best knowledge of the author, there is no known biomarker for ALS to date. A biomarker, is generally referred to a measurable indicator of a biological state or condition and therefore, is used to specify the state of a disease (i.e., ALS). Finding biomarkers is one of the most intense areas of research in the general medical community, and particularly in neurology. A biomarker helps doctors make the right diagnosis and make it sooner. It helps track disease progression and see how that progression changes with treatment. Finally and more importantly, a biomarker leads to the discovery of drugs faster as it is a more accurate measure of response than the crude non-quantitative clinical measures.

Imaging is a popular method to identify biomarker for several diseases. It is a repeatable non-invasive approach which provides spatial information of the region of interest. The spatial information is used to find the changes occurring due to the pathology of a disease. Nevertheless, the current medical imaging techniques to study ALS have several drawbacks and MR images are usually used to rule out diseases that mimic ALS. From a technical point of view, analysis of the MR images in ALS is challenging because the images do not show any changes visible to the human eye. For the first time, this study shows that texture analysis can detect small variations in the brain images of patients with ALS although they are not perceptible to the human eye. In addition to the technical importance, this study suggests that texture analysis is a potential quantitative biomarker in ALS. Such a biomarker is highly required because it facilitates research of the disease and helps evaluate new drugs for ALS. Nonetheless, texture features are extracted from MR images, and hence, the features should be robust to imaging effects inherited in MR images. The robustness lays out the objectives of this thesis.

Indeed, development of robust texture features is important in many applications. In realistic situations imaging effects are inevitable. For instance, MR images suffer from noise and non uniform intensity changes. Scattered images look blurry. Illumination conditions change when images are captured at different times or from different view points. Hence, developing robust and accurate texture features has a marked impact in number of different applications particularly in medical image analysis.

1.2 Objectives

This thesis explores the application of texture analysis in medical image analysis. The current texture analysis methods are defined for a given region of interest. This imposes a huge burden for medical image analysis. For instance, the texture analysis methods require an accurate segmentation of the region of interest which is usually done manually. Moreover, region of interest based methods require a priori hypothesis of where the disease is located spatially, however this may not always be evident. To address these issues, this thesis presents an automatic method which obviates the need for segmentation and finds the defective regions automatically.

The next goal of this thesis is to apply texture analysis methods to some select neurological

diseases, including ALS. Since texture analysis has been very successful in many areas, using it in ALS to develop such a biomarker is certainly promising. The success of the developed methods in ALS will further motivate its usage in other neurodegenerative and non-neurodegenerative diseases. In addition to ALS, the goal is to apply the proposed texture analysis methods to Alzheimer's Disease (AD). The pattern of degeneration in AD is more consistent across patients, hence, it assists in the validation of the proposed methods.

Since the proposed texture methods can help detecting, analyzing, and monitoring different brain related diseases, a CAD tool is developed which can be easily used by doctors to conduct research.

Ideal texture features are not only discriminative but are also robust to imaging distortions and are invariant to different geometric transformations such as rotation, change of scale and viewpoint. Indeed, texture features of an object in a given image should remain the same in spite of the view under which the image is taken. Moreover, the features should not be affected by imaging distortions and illumination conditions. Imaging distortions include different types of noise and blur effects. In realistic imaging these distortions are sometimes unavoidable. For instance, magnetic resonance images usually have noise, underwater images are blurred, and images with long exposure or fast movements suffer from motion blur. Illumination conditions make the situation more difficult. While the intensity of images can change rapidly under different illumination conditions, texture features should be invariant to such changes. Because of the mentioned challenges, there are still many research groups trying to define robust and invariant features, making texture analysis an active research topic in computer vision and image processing.

The next objective of this thesis is to develop texture features that have three properties:

1. highly discriminative,

2. invariant to some geometrical transformations, and

3. robust to common imaging effects.

This thesis introduces a new method called the Local Frequency Descriptor (LFD) which is the basis of accurate, robust, and invariant features. LFD is inspired from one of the most successful and popular texture methods called the Local Binary Patterns (LBP). Like the LBP, the LFD method in 2D considers a neighboring function at each pixel on gray scale images. This discrete function consists of N sample points located on a circle of radius R. The value of each point is computed by bilinear interpolation if the point is not located on a center of a pixel. Then the function undergoes a 1D Fourier transform. The frequency components of this function are called the LFD and form the basis of several new methods for texture analysis and image processing presented in this thesis.

Since 2D texture analysis methods are popular and widely used in different applications, the first objective is to develop better 2D methods. Because there is a growing demand on 3D texture analysis methods particularly in medical image analysis, the next goal of this research is to develop

3D texture features with the aforementioned properties. In this regard, the LFD method is extended to 3D and used to classify 3D volumetric data.

In addition to 2D and 3D texture methods, this research extends the application of the proposed LFD methods to other areas of computer vision and image processing. In this regard, the next objective of this thesis is to develop new image gradient operators. Image gradient information is used in numerous applications in computer vision and image processing. Operators with robustness to imaging effects will help these applications in challenging imaging conditions. To further show the ability of the LFD method, this thesis also aims to extend the proposed method to the image matching problem which is one of the widely used application in computer vision.

1.3   Thesis Organization

In Chapter 2 a general overview of texture analysis is presented. The chapter gives an introduction to texture analysis, defines the general domains of research in texture analysis, explains the main approaches taken by varying methods to define texture features, and discusses some applications of texture analysis.

Chapter 3 focuses on the medical applications of texture analysis and, in particular, four well-known brain related diseases: the brain tumour, epilepsy, multiple sclerosis (MS), and Alzheimer's disease (AD). This thesis entails texture analysis of the structural brain images acquired by MRI. Thus, the main issues and challenges of MRI are also introduced in this chapter.

Chapter 4 provides an overview of ALS and the neuropathology of the disease. The current medical imaging approaches to study the disease are also explained. The approaches include structural MRI, diffusion tensor imaging, functional MRI and magnetic resonance spectroscopy. The utility and shortcomings of each approach are discussed.

Chapter 5 presents a novel voxel based texture analysis approach useful for hypothesis-free analysis of the brain images. This method obviates the need for defining the region of interest and automatically detects regions with significant statistical difference between the group of healthy subjects and patients.

In Chapter 6 texture analysis is performed to study ALS. First, a 2D analysis is performed in a region of interest. Then, the proposed voxel based analysis approach is used to detect regions in the brain that are statistically different between patients with ALS and healthy subjects.

In Chapter 7 the LFD is defined for 2D analysis. Two novel 2D texture classification methods are presented as well. These methods use the magnitude and the phase of the LFD. The features are rotation invariant and show robustness to noise. These methods have been published in [225] and [226]. A novel image gradient computation operator is also suggested for 2D images. This operator is based on the second component of LFD and has been published in [227] and [228].

Chapter 8 explains how the proposed 2D method can be extended to a fundamental computer vision applications namely image matching. The proposed method not only outperforms the state-

of-the-art methods but also presents high degree of robustness to imaging effects and illumination changes. This method has been published in [227]

In Chapter 9 the texture classification method and the gradient operator are extended to 3D. This method has been published in [228]. The method is applied to synthetic and realistic MR images successfully and provides the highest accuracy compared to the state-of-the-art 3D methods.

Finally, in Chapter 10, the summary of this thesis is given and future works are discussed. This thesis includes four appendices.

In Appendix A the Computer Aided Diagnosis (CAD) tool developed for brain analysis using texture features is explained. This tool is called the Statistical MAp fRom Texture (SMART) and is developed as a toolbox for the Statistical Parametric Map (SPM), a famous brain analysis software. Appendix B includes examples of computing image gradient using the method proposed in Chapter 7. In Appendix C, additional results of the proposed voxel based method (Chapter 5) are presented. Finally, in Appendix D, the detailed proof of the theorem used in Chapter 8 is given.

Chapter 2

Texture Analysis

2.1 Introduction

In many computer vision applications image regions are characterized by means of a small set of features. One characteristic of a region is its color. The intensity of color in many real objects is not uniform and its variations provides another important characteristic called texture. The textural features give very distinctive information of a region or object. In many cases, the human eye can detect different regions of a gray scale image using only texture features. Figure 2.1 shows some texture examples.
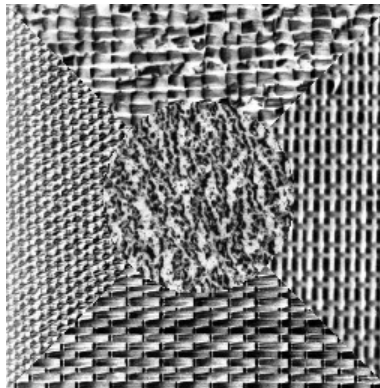
Figure 2.1: Five texture samples from the Brodatz [38] album. Top: raffia, left: cotton canvas, bottom: straw matting, right: oriental straw cloth, and center: pressed calf leather.

Texture analysis includes four general research domains:

1. Classification: Texture classification is one of the most popular research topics in texture analysis. Here, the textural features are used to determine to which class or category the observed texture belongs. One application of texture classification is to determine if an image belongs to a healthy subject or to a patient. This has been applied successfully to the classification and detection of different diseases, including brain tumour [139; 107], breast [141] cancer, epilepsy [307], multiple sclerosis [342; 401], and alzheimer's disease [73; 373].

2. Segmentation : The goal of the methods in this domain is to partition a given image into homogeneous regions using textural features. For instance, a brain image can be segmented into gray matter, white matter and cerebrospinal fluid regions using texture features [29] or in an aerial photograph of natural habitats, the goal may be to segment an animal from the surrounding environment by means of its texture features [183].

3. Texture synthesis: The third group of methods, particularly in computer graphics applications, uses textural features to cover a given object to make it look different. For instance, in a computer game the floor of a given environment can be covered by sand, grass, or any given texture. Some known examples of texture synthesis include the Markov Random Fields [269], the Aura matrices [284], texture exemplars [190; 128], and the grouplet transform [272].

4. Shape from texture: The methods in this domain use texture features of an object in a 3D scene to estimate the surface orientation of the object. Some recent works include estimating shape based on deformation of texture elements [221], or based on Fourier analysis [97; 98].

The performance of a texture descriptor is usually assessed using texture classification [266; 234]. Since the applications in this thesis including medical imaging applications are mainly categorized in the classification group, this thesis focuses on the texture classification domain. The texture classification procedure usually consists of four steps:

1. Pre-processing: This step includes operations performed before extracting texture features. For instance in medical image analysis the Region of Interest (ROI) should be chosen. The images are also normalized in this step. The purpose of normalization is standardizing the intensity range, such that the extracted properties from the images are comparable. Removing artifacts (e.g., noise) are also performed in this step.

2. Feature extraction: Textural features of images are extracted in this step. Different methods are used to find textural features.

3. Feature selection: In this step, useful features are selected. Sometimes the number of features is huge. As well, some features may not be informative. The goal of this step is to reduce the number of extracted features by selecting those giving discriminative textural information.

4. Classification: In this step, each image is assigned to one of the known texture classes. Different classification methods can be used in this step. Some popular methods used in classification include the Support Vector Machines (SVMs), and the Nearest Neighbor (NN) classifiers.

As mentioned before in the introduction chapter of the thesis, an ideal texture feature should be invariant to geometric transformations (e.g., rotation) and be robust to different imaging effects such as blurriness, noise, distortions, and illumination changes. In the next section, different approaches for extracting invariant features are explained.
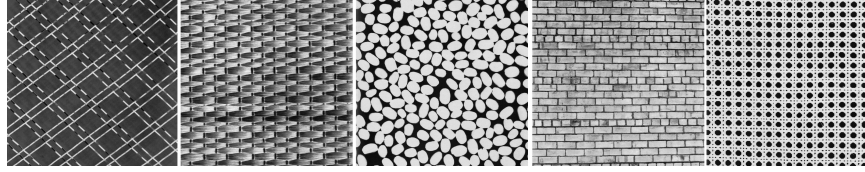
Figure 2.2: Human eye can perceive the structural information of some textures. The texture samples are from the Brodatz [38] album.

2.2 Invariant Texture Methods

There are many different methods for texture classification, which can be categorized into four general groups:

1. Structure-based methods: These methods decompose textures into textural elements known as primitives or texels and use the invariant properties of the textural elements as features.

2. Model-based methods: This class of texture methods defines textures as probabilistic models. The invariant texture features are extracted on the assumed model.

3. Filter-based methods: This group of methods applies filters to images in the spatial or the frequency domains. The responses of the filters are used as texture features.

4. Statistical-based methods: The methods in this group use statistical features of textures. The statistical information are gathered in a way that makes the features invariant to rotation and/or other geometrical transformations.

Nonetheless, one may note that these categories are not completely independent of each other and may overlap among themselves. Moreover, some methods may use a combined approach (e.g., statistical information and filter responses). In the next subsections, each category is briefly explained and some well-known representative methods in each group are described. In particular, this thesis focuses on filter-based and statistical-based methods due to their popularity and their success compared to the first two groups.

2.2.1 Structure-Based Methods

The structure-based methods assume that textures are composed of some elements called primitives or texels. The texels and their spatial arrangements are used to characterize textures. The main motivation of using structural information is that the human eye can perceive the structural information of some textures easily (Figure 2.2).

There are different approaches to finding texels and their invariant features. Some methods define a texel as a maximally connected set of pixels with the same attributes [114; 115]. The attribute is represented by the pixel's characteristics (e.g., intensity or gradient). Then, different

invariant properties of the texels such as the average element intensity [114], and the compactness of texels are computed.

To extract texels, Zhang and Tan [399] segment a texture image into regions with uniform intensity using adaptive thresholding and use morphological operations to remove small holes in texel regions. They define the area ratio matrix where each entry $r(i,j)$ is the ratio of area of the ith and j^{th} texels. Assuming that there are n texels, the probability that a texel pair has a value of $r(i,j)$ is $f_r = k_r/N$, where k_r is the number of texel pairs (i,j) and $N = n(n+1)/2$ is the total number of possible texel pairs. The area-ratio histogram is defined as $h(r) = f_r$, which is invariant to affine transformation.

A popular structure-based approach is to apply morphological operations to extract texture features. Mathematical morphology is a set-theoretic approach to analyzing geometrical structures in images. A structuring element (i.e., geometrical pattern) is used to study how this shape fits in an image. One of the basic morphological operations is "opening." Opening of a binary image A with a binary structuring element (SE) B is defined as the union of all the translations of B by vector z that are subsets of A (i.e., fits in A) [112]:

$$A \circ B = \bigcup \{(B)_z : (B)_z \subseteq A\}, \tag{2.1}$$

where $(B)_z$ is the translations of B by vector z. Morphological operations have been successfully applied to granulometry in extracting texture features [19; 26; 30]. An opening granulometry is defined based on a sequence of morphological openings using scaled SEs (B_t). The first element, B_1, has the same scale as B $(B_1 = B)$. The scaled SEs are defined as $B_t = B_1 \circ B_{t-1} (t = 2, ..., n)$. Opening A with B_t, where $(t = 1, ..., n)$, results in the following sequence:

$$A \circ B_1 \supset A \circ B_2 \supset ... \supset A \circ B_n. \tag{2.2}$$

The ratio of an image area removed after t successive openings of A by B to the original image area defines the pattern spectrum:

$$\Phi(t) = \frac{P[A] - P[A \circ B_t]}{P[A]}, \tag{2.3}$$

where operator $P[.]$ gives the area of the region. Different properties of the pattern spectrum such as the mean, and standard deviation of granulometric moments are used as invariant features [180]. Some methods also compute the pattern spectrum without a need to define the SEs based on merging the flat zones in the image [305; 306; 352].

Another approach in structure-based methods is fractal analysis [174; 370; 374; 379]. A fractal is a structure which keeps its shape at all scales. In other words, a fractal can be decomposed into N similar copies of itself, each scaled down by a factor s. Mathematically, a fractal follows the power law between the N and s, $N(s) \propto s^{-D}$, where D is known as the fractal dimension which is used as a texture feature. One simple way to compute the fractal dimension is known as box-counting [309; 212]. Consider an object E in an image. The general idea in box counting is to cover

the image by squares (boxes) with side of length ϵ and count the number of squares that are occupied by E. The dimension is then computed as:

$$\lim_{\epsilon \to 0} \frac{log N(\epsilon, E)}{-log \epsilon}. \tag{2.4}$$

Some recent examples of using fractal for analyzing textures include the Multi-Fractal Spectrum (MFS) method [380], multifractal analysis on wavelet domain [160; 382], multifractal analysis with Gabor filter [377], and the dynamic fractal analysis [381].

Topographic map [44] is another approach in structure-based methods. A topographic map consists of level lines defined as the boundaries of level sets. Consider an image, which is a mapping function from pixels to real intensity values, $I : \Omega \mapsto \Re$. An upper level set $X_\lambda(I)$ includes all pixels that have a value equal to or greater than λ:

$$X_\lambda(I) = x \in \Omega, I(x) \geq \lambda. \tag{2.5}$$

A lower level set can be similarly defined. The boundaries of the (upper or lower) level sets are the level lines. The level sets are nested. As a result the level lines can be represented in a tree structure [254] which presents the topographic map. The topographic map has been used by several groups for texture analysis [126; 372].

A key problem of the structure-based methods is how to define texels that represent different texture structures paticularly when the texture has no structure. In general, the structure-based methods are better suited for textures with large structures (macrostructure) and do not work well with non-structure textures and microtextures [400].

2.2.2 Model-Based Methods

The model-based methods assume that textures can be represented by probabilistic models. The most well-known models include the Random Field (RF) models such as the Markov Random Fields (MRF) [59; 392], and Gibbs Random Fields (GRF) [76; 83; 105]. The random field methods model a texture as a stochastic process (random field) and characterizes the texture as distributions (joint or conditional) of some random variables.

The MRF [66] of a random variable X is defined as a joint probability density with the following three properties:

1. Positivity: $p(X) > 0$ for all X,

2. Markovianity: $p(X(x, y)|$ all points in the image except $(x, y)) = p(X(x, y)|$ neighbors of $(x, y))$,

3. Homogeneity: $p(X(x, y)|$ neighbors of $(x, y))$ depends only on the configuration of the neighbors of (x, y). The homogeneity property also indicates that $p(X(x, y)|$ neighbors of $(x, y))$ is translation invariant as long as the translation keeps the same neighborhood configuration.
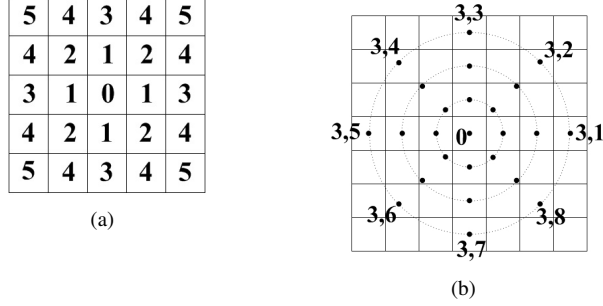
Figure 2.3: Neighborhood configuration in the MRF. (a) The rectangular neighborhood configuration. The numbers show the order of the neighbors. The rectangular neighborhood configuration has been used by the conventional MRF-based texture methods [66]. (b) The circular neighborhood configuration. There are three orders (eight neighbors at each order) in this figure. Rotation invariant MRF-based methods [75; 239] use the circular neighborhood configuration.

Figure 2.3 shows two popular neighborhood configurations used by the MRF models.

One well-known texture analysis example using the MRF model is the Anisotropic Circular Gaussian Markov Random Field (ACGMRF) model presented by Deng and Clausi [75]. In their method, N concentric circular neighbors of a pixel are considered. The pixel's value is estimated as:

$$I(x,y) = \sum_{(x+\Delta x, y+\Delta y) \in N} \beta(\Delta x, \Delta y) I(x + \Delta x, y + \Delta y) + \nu(x, y), \tag{2.6}$$

where N is the neighborhood system, $(\Delta x, \Delta y)$ the relative position with respect to the center pixel, $\beta(\Delta x, \Delta y)$ the weight for the neighbors, and $\nu(x, y)$ a Gaussian noise with zero mean and known autocorrelation. Then the 1D Fourier transform is applied to the MRF parameters and the magnitude of the frequency component is computed as the texture feature.

Another example of using the MRF model in texture analysis is the Simultaneous Auto Regressive (SAR) model [165; 239]. In the SAR model, the mean gray value of the image is considered [239]:

$$I(x,y) = \mu + \sum_{(x+\Delta x, y+\Delta y) \in N} \theta(\Delta x, \Delta y) I(x + \Delta x, y + \Delta y) + \nu(x, y), \tag{2.7}$$

where μ is the mean gray value of the image, and θ the parameter characterizing the dependence of a pixel to its neighbors. To make the model rotation invariant, the neighbors on concentric circles around a pixel are considered. The parameters θ and μ are computed by least squares estimate and considered as the texture features.

The next popular model is the GRF, but before explaining the GRF method, the definition of cliques is described. Given a neighborhood system N, a clique C is defined as some single locations or a subset of multiple locations in which each pair of distinct locations are neighbors. Figure 2.4 illustrates the concept of cliques. A Gibbs distribution has the following form [76]:

$$p(x,y) = \frac{1}{Z} e^{(-E(x,y))}, \tag{2.8}$$

11

(a)   (b)
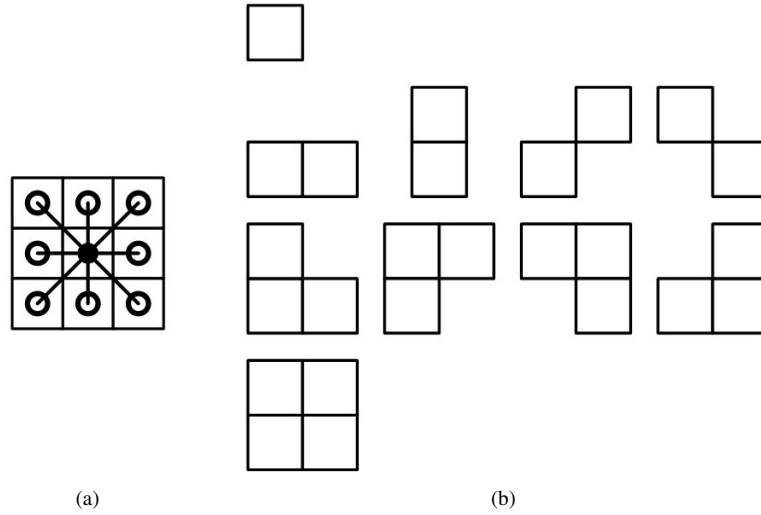
Figure 2.4: a) A clique is a single location or a subset of multiple locations in which each pair of distinct locations are neighbors. b) Considering an 8-neighbor system. The figure shows the first, second, third and fourth order cliques.

where Z is the normalizing constant also known as the partition function, and E the Gibbs energy:

$$Z = \sum_{all(x,y)} e^{-E(x,y)}, \tag{2.9}$$

$$E(x,y) = \sum_{c \in C} V_c(x,y), \tag{2.10}$$

where V_c is a function of the pixel values in clique c, called the clique potential.

The key issue in the model-based methods is how to choose the correct model for a given texture and how to effectively map a texture into the selected probability model [400]. In addition, these models require many parameters to be determined which is not trivial when the neighborhood size is large. Consequently, model-based methods are not as popular as other texture analysis methods.

2.2.3 Filter-Based Methods

This group of methods apply filters to images in the spatial or frequency domain. A basic frequency domain analysis is usually performed by applying the Fourier transform. Fourier analysis has some advantages that make it very popular for image processing. For instance, it is commonly known that Fourier analysis is robust to perturbations in images (e.g. additive noise). In addition, the Fast Fourier Transform (FFT) algorithm makes computing the frequency components efficient.

Since digital images are in the discrete domain, the Discrete Fourier Transform (DFT) is used for image processing. The discrete Fourier transform of a 1D signal is defined as:

$$F(u) = \sum_{x=0}^{X-1} f(x)e^{-2\pi ixu/X}, \tag{2.11}$$

where $f(x)$ denotes the 1D signal, X, the number of the components, $i = \sqrt{-1}$, and $F(u)$ the frequency components. Applying the DFT to a discrete function with N points generates N complex numbers. If the N samples are real numbers, $N/2 - 1$ components of $F(u)$ are complex conjugates of the other $N/2 - 1$ components. The 2D DFT is similarly defined:

$$F(u,v) = \sum_{x=0}^{X-1} \sum_{y=0}^{Y-1} f(x,y)e^{-2\pi i(\frac{xu}{X} + \frac{yv}{Y})}, \tag{2.12}$$

where X and Y are the number of columns and rows, respectively, assuming that the coordinate system ranges from $[0,0]$ to $[X-1, Y-1]$. Fourier analysis can be performed in the log-polar coordinate system to provide scale and rotation invariant features [13].

Since the Fourier transform is applied to the whole domain of an image, it cannot capture local texture features. As a result, localized spatial filters are suggested [36]. These filters are based on the windowed signal processing approach by which the frequency information is computed in a window rather than for the whole image. As a result, joint spatial/frequency information related to the local spatial data is obtained. Windowed Fourier filters (also known as short term Fourier transform, STFT) [27; 268; 287] and the multichannel Gabor filters [36; 125; 286] are among the popular texture methods using joint spatial/frequency information. The short term Fourier transform is defined as:

$$F(u,x) = \sum_{y \in N_x} f(x-y)e^{-2\pi i u^T y}, \tag{2.13}$$

where x is the location of the pixel, u the frequency, and y the location of all neighbors located in the neighboring window around x. Note that in this definition, u, x, and y are all vectors (the size of the vector depends on the dimension of the space, e.g., in a 2D image space the vector size is 2×1). A special case of STFT where the window function is Gaussian is called the Stockwell transform (also known as the S transform) proposed by Stockwell [327] about two decades ago.

The Gabor function for a given pixel (x,y) with center frequency (U, V) is defined as:

$$h(x,y) = g(x', y')e^{2\pi i(Ux + Vy)}, \tag{2.14}$$

where $(x', y') = (x\cos(\phi) + y\sin(\phi), -x\sin(\phi) + y\cos(\phi))$ are rotated coordinates, and g is a Gaussian function with aspect ratio λ and scale parameter σ:

$$g(x,y) = \frac{1}{2\pi\lambda\sigma^2}e^{-\frac{(x/\lambda)^2 + y^2}{2\sigma^2}}. \tag{2.15}$$

The spatial frequency response of the Gabor function (2.14) is:

$$H(u,v) = e^{-2\pi^2\sigma^2[(u'-U')^2\lambda^2 + (v'-V')^2]}, \tag{2.16}$$

where (u', v') and (U', V') are the rotations of (u, v) and (U, V), respectively. To have rotation and scale invariance the responses obtained at different orientations (ϕ) and different scales (σ) are used

13
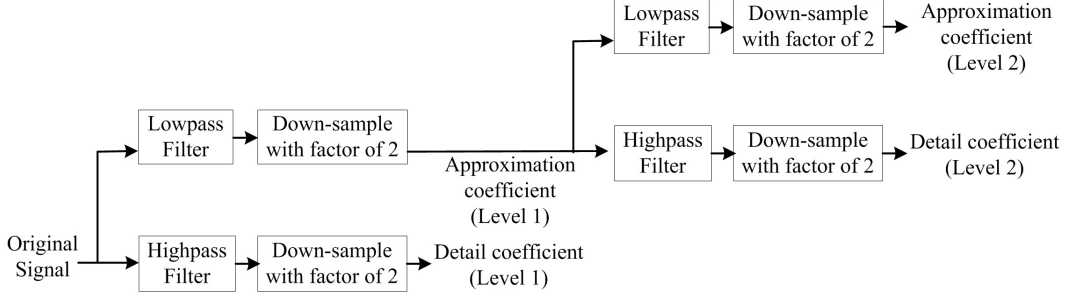
Figure 2.5: Computing the DWT coefficients using the pyramid scheme [235] with two levels. At each level two coefficients are computed: the detail and the approximation coefficients. The approximation coefficient is used as input to the next level.
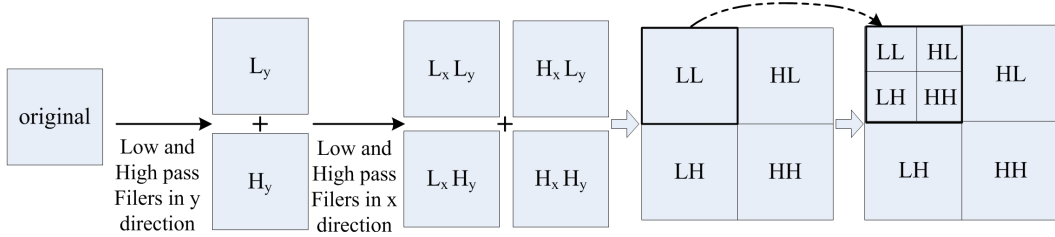
Figure 2.6: The 1D DWT is applied to the image in the vertical and horizontal directions resulting in four sub-bands: LL(low-low), HL(high-low), LH(low,high), and HH(high-high). The LL sub-band is further decomposed into four sub-bands.

as features. In a recent work, Chu and Chan [56] use tunable Gabor filter banks to define rotation and scale invariant features.

The wavelet transform [235] is also a very popular method for texture analysis. The one dimensional Discrete Wavelet Transform (DWT) decomposes a 1D function in terms of a family of basis functions (known as wavelets):

$$f(x) = \sum_{m=0}^{\infty} \sum_{n=0}^{\infty} C_n^m \psi_{m,n}(x) \tag{2.17}$$

where $\psi_{m,n}(x) = 2^{-m/2}\psi(2^{-m}x - n)$ is produced by dilations and translations of the basis function $\psi(x)$ known as the mother wavelet. The C_n^m coefficient can be efficiently computed using a pyramid scheme implemented with a pair of lowpass($g[n]$) and highpass($h[n]$) filters [235] as shown in Figure 2.5.

In the first step, the signal is filtered by a lowpass and a highpass filter and then the output from each filter is down sampled by a factor of 2. The output obtained from the highpass filter after downsampling is kept as the detaile coefficient and the output of the lowpass filter after downsampling is input to the next step. The decomposition can iteratively continue. For texture analysis the 2D DWT is applied. This can be done by performing the 1D DWT in the vertical and in the horizontal directions. Figure 2.6 shows the steps to construct a two-level DWT decomposition of an image.

Instead of the pyramidal structure in which the low band is decomposed, Chang and Kuo [49] propose using a tree-structured wavelet transform to further analyze the components located in the

14
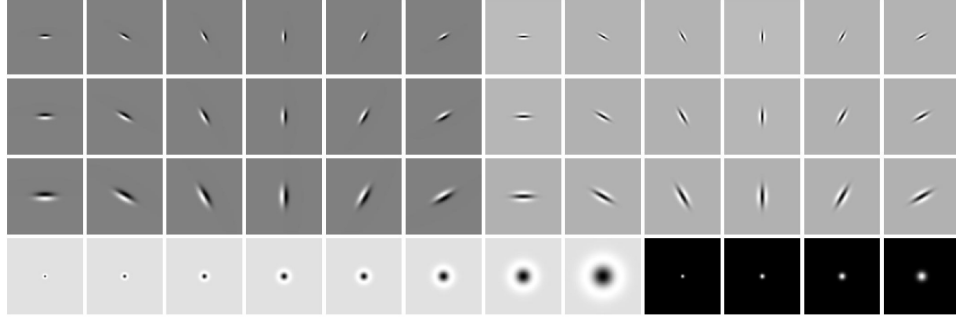
Figure 2.7: Leung and Malik [208] use 48 filters: two Gaussian derivative filters at six orientations and three scales, eight Laplacian of Gaussian filters, and four Gaussian filters as their filter bank.

middle frequency channels. Jafari-Khouzani and Soltanian-Zadeh [154] extract rotation invariant features using the Radon transform along with the wavelet transform. The wavelet transform is used with a linear regression model for texture analysis by Wang and Yong [415]. In their model the correlation between frequency regions are considered.

In addition to the methods that perform analysis in the frequency domain, some research studies define texture features in the spatial domain. The most well-known invariant methods in this group are the methods of Leung and Malik [208], Cula and Dana [67], and Varma and Zisserman [356; 357]. The main contribution of these methods is a framework to *learn* illumination and geometrical changes occurring in textures from a given training set. The training set includes images of textures acquired with different illumination conditions and from different viewpoints. A bank of filters is applied to each image in the spatial domain. The filter banks consist of orientation and spatial-frequency selective linear filters to capture textural features at different orientations and scales. For instance, Leung and Malik [208] use 48 filters: two Gaussian derivative filters at six orientations and in three scales, eight Laplacian of Gaussian filters, and four Gaussian filters (Figure 2.7).

By gathering the responses of the filters, at each pixel a vector of N_{filt} responses is constructed, where N_{filt} is the number of filters. Then, the responses of all the images of the same texture in the training set are concatenated together to form a set of data vectors. The data vectors are then clustered using the K-means algorithm. Assuming that there are N_{img} images of the same texture class in the training set, the output of the K-means algorithm is a matrix of $N_{filt} \times K$ centers. Each row of the output (with size($1 \times K$)) is called a texton. By learning textons from different texture classes, a texton dictionary is created. Finally, each texture image is represented as a histogram of textons.

In a subsequent work, Varma and Zisserman [356] show that keeping all responses is not needed. In their method known as Maximum Response (MR), they use two Gaussian derivative filters at six orientations and three scales (the first 36 filters shown in Figure 2.7); however, they keep only the maximum response of each scale (i.e., six responses). They also use 2 rotationally symmetric filters, a Gaussian and a Laplacian of Gaussian filters, resulting in eight responses in total. With this

approach they not only improve the performance but also reduce the memory requirement of the method. However, in their recent method, Varma and Zisserman [357] argue that the filters remove some informative texture information and demonstrate that the local patches of the original image can provide a better performance.

Finally, some filter-based methods use local frequencies of samples around pixels to capture the local changes. A popular approach is by applying the 1D Fourier transform to samples on a circle (or multiple circles) around a pixel [17; 75; 216]. Any rotation induces a circular shift to the circular samples, keeping the magnitude of the frequency components unchanged. The method of Arof and Deravi [17] uses two concentric circles around a pixel. The magnitudes of the 1D Fourier transform of the samples and of the difference of the samples with the center pixel are used as features. A similar approach is used by Deng and Clausi [75] to construct the anisotropic circular Gaussian MRF (ACGMRF) model (explained in Section 2.2.2). In a recent work, Liao and Chung [216] propose the Composite Fourier Domain (CFD) method. Considering samples located on three concentric circles around a pixel, the method computes the magnitude of the 1D Fourier transform on each circle. Then a global multidimensional Fourier transform is applied to form the composite Fourier domain. The null-space based linear discriminant analysis (nLDA) is used to construct the final features.

2.2.4 Statistical-Based Methods

The statistical-based methods are the most popular and successful approaches for texture analysis. The main motivation of these methods is based on the findings of Julesz [168; 169], suggesting that the human visual system uses statistical features to distinguish textures. The gray level co-occurrence matrix (GLCM) proposed by Haralik et al. [131] is one of the first well-known methods using this approach.

Suppose that a 2D image I with a length of N_x and a width of N_y has N_g gray level values (i.e., intensities of the image range 1 to G). The image I is represented as a function mapping the spatial domain to the gray values:

$$I : L_y \times L_x \rightarrow G, \tag{2.18}$$

where $L_y = \{1, ..., N_y\}$ denotes the spatial domain along the y axis, $L_x = \{1, ..., N_x\}$ the spatial domain along the x axis, and $G = \{1, ..., N_g\}$ the gray values. Here, the Haralik et al. notation [131] is followed which assigns the y axis to the first dimension.

A co-occurrence matrix represents the relationship between intensity levels for a given direction and distance (i.e., offset) in an image. An offset with distance d and direction angle θ is represented by $O = [a, b] = [d sin(\theta), d cos(\theta)]$ connecting pixel $I(k, l)$ to pixel $I(m, n)$ such that $m = k + a$ and $n = l + b$. For instance, an offset with distance of 1 and angle of $90°$ increases m by 1 and n by 0 (or offsets them from the original position with $[1, 0]$). $GLCM_O$ is defined for the specific offset
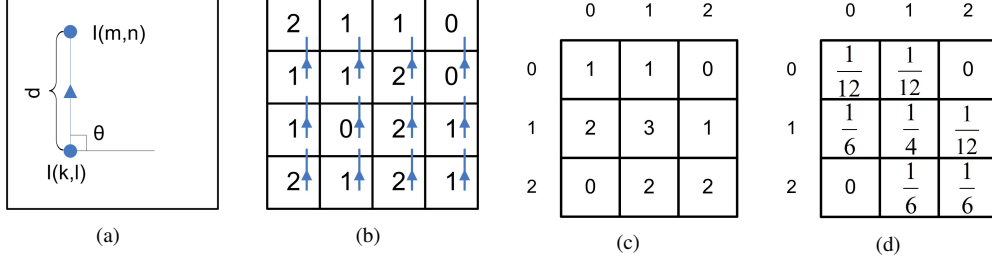
Figure 2.8: Computing the GLCM. (a) A sample offset offset $O = [1, 0]$ ($d = 1, \theta = 90°$). (b) A sample image and the offset. (c) The computed GLCM. (d) The normalized GLCM.

$O = [a, b]$ as follows:

$$GLCM_O(i, j) = \#\Big\{ ((k, l), (m, n)) \in (L_y \times L_x) \times (L_y \times L_x)|$$
$$m = k + a, n = l + b, I(k, l) = i, I(m, n) = j \Big\}. \tag{2.19}$$

In other words, the GLCM for a specific offset is an $N_g \times N_g$ matrix where the entry (i, j) shows the number of times that $I(k, l) = i$ and $I(m, n) = j$. In the GLCM, usually eight directions are used (i.e. $0°, \pm 45°, \pm 90°, \pm 135°, 180°$). A common approach is to combine diagonally opposite pairs (i.e., θ and $\theta + 180°$), making the GLCM symmetric and reducing the number of directions from eight to four. The GLCM is also normalized (i.e., divided by the sum) to represent the probability of the co-occurrence between gray levels.

Figure 2.8 illustrates the procedure of computing the GLCM of a sample image with gray level values of $0, 1, 2$ for offset $O = [1, 0]$. Different textural features are computed using the normalized GLCM. Some well-known properties of GLCM are listed in Table 2.1.

The gray level Aura matrix (GLAM) [274; 275] is the generalization of the GLCM, developed based on set theory. Consider an image I as a finite rectangular lattice with a neighborhood system $N = \{N_s, s \in I\}$. The neighborhood N_s is built by translating the basic neighborhood (structuring element) E to location s. Given two subsets: $A, B \subseteq I$, the Aura of A with respect to B for the neighborhood system N, is defined as [275]:

$$\vartheta_B(A, N) = \bigcup_{s \in A} (N_s \cap B). \tag{2.20}$$

Similarly, the Aura measure of A with respect to B is defined as

$$m(A, B, N) = \sum_{s \in A} |N_s \cap B|. \tag{2.21}$$

Intuitively, the Aura of A with respect to B characterizes how the subset B is present in the neighborhood of A and the Aura measure represents the number of B's sites presented in the neighborhood of A. Note that $m(A, B, N)$ does not show the number of elements in the Aura set $\vartheta_B(A, N)$, and in general $m(A, B, N) \neq |\vartheta_B(A, N)|$. The Aura measures between different gray level values are used to define the GLAM. Assume that there are G gray levels in the image,

17

Table 2.1: Some popular texture features defined based on the co-occurrence matrix. P is the normalized GLCM, G the number of gray levels. $\mu_x, \mu_y, \sigma_x,$, and σ_y denote the means and standard deviations of the row and column sums of P [†].

Texture Feature	Formula
Autocorrelation	$f_1 = \sum\limits_{i=1}^{G} \sum\limits_{j=1}^{G} (ij)P(i,j)$
Homogeneity	$f_2 = \dfrac{1}{1+|i-j|} \sum\limits_{i=1}^{G} \sum\limits_{j=1}^{G} P(i,j)$
Energy	$f_3 = \sum\limits_{i=1}^{G} \sum\limits_{j=1}^{G} P(i,j)^2$
Correlation	$f_4 = \dfrac{\sum\limits_{i=1}^{G} \sum\limits_{j=1}^{G} (i-\mu_y)(j-\mu_x)P(i,j)}{\sigma_x \sigma_y}$
Dissimilarity	$f_5 = \sum\limits_{i=1}^{G} \sum\limits_{j=1}^{G} |i-j|P(i,j)$
Sum of Squares: Variance	$f_6 = \sum\limits_{i=1}^{G} \sum\limits_{j=1}^{G} (i-\mu)^2 P(i,j)$
Sum average	$f_7 = \sum\limits_{i=2}^{2G} i P_{x+y}(i)$ [††]
Sum entropy	$f_8 = -\sum\limits_{i=2}^{2G} P_{x+y}(i)log(P_{x+y}(i))$ [††]
Contrast	$f_9 = \sum\limits_{i=1}^{G} \sum\limits_{j=1}^{G} |i-j|^2 P(i,j)$
Inverse difference moment normalized	$f_{10} = \sum\limits_{i=1}^{G} \sum\limits_{j=1}^{G} \dfrac{1}{1+(i-j)^2/G^2} P(i,j)$
Sum variance	$f_{11} = \sum\limits_{i=2}^{2G} (1-f_8)^2 P_{x+y}(i)$ [††]
Entropy	$f_{12} = -\sum\limits_{i=1}^{G} \sum\limits_{j=1}^{G} P(i,j)log(P(i,j))$
Difference variance	$f_{13} =$ variance of P_{x-y} [†††]
Difference entropy	$f_{14} = -\sum\limits_{i=0}^{G-1} P_{x-y}(i)log(P_{x-y}(i))$ [†††]

[†] $\mu_x = \sum\limits_{i=1}^{G} \sum\limits_{j=1}^{G} j.P(i,j)$

$\mu_y = \sum\limits_{i=1}^{G} \sum\limits_{j=1}^{G} i.P(i,j)$

$\sigma_x = \sqrt{\sum\limits_{i=1}^{G} \sum\limits_{j=1}^{G} (j-\mu_x)^2.P(i,j)}$

$\sigma_y = \sqrt{\sum\limits_{i=1}^{G} \sum\limits_{j=1}^{G} (i-\mu_y)^2.P(i,j)}$

[††] $P_{x+y}(k) = \sum_{i=1}^{G} \sum_{\substack{j=1 \\ i+j=k}}^{G} P(i,j)$

[†††] $P_{x-y}(k) = \sum_{i=1}^{G} \sum_{\substack{j=1 \\ |i-j|=k}}^{G} P(i,j)$

I. The pixels that belong to each gray level are considered as a set $I_i (0 \leq i \leq G-1)$, such that
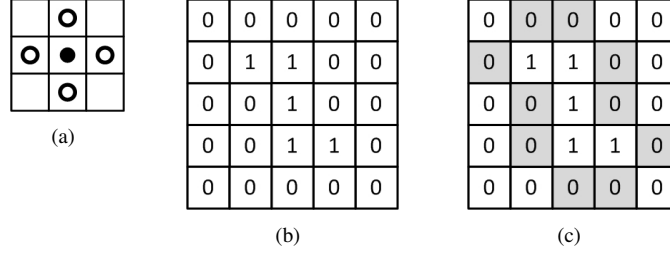
Figure 2.9: Computing the GLAM. (a) The basic neighborhood (structuring element). ● denotes the reference pixel and ○ the neighboring pixel. (b) A sample binary image. (c) Assuming that subset A is the set of all 1s and subset B the set of all 0s, the Aura set of A with respect to B, $\vartheta_B(A, N)$, for the given basic neighborhood is shown in light gray.

$\bigcup\limits_{i=0}^{G-1} I_i = I$, and $I_i \cap I_j = \emptyset$ for $i \neq j$. The GLAM is a matrix with Aura measures as the entries, in particular,

$$GLAM = m(I_i, I_j, N). \tag{2.22}$$

Figure 2.9 shows an example of the Aura set of a sample binary image. The GLAM of this sample image with the given basic neighborhood is

$$GLAM = \begin{bmatrix} m(0,0,N) & m(0,1,N) \\ m(1,0,N) & m(1,1,N) \end{bmatrix} = \begin{bmatrix} 48 & 12 \\ 12 & 8 \end{bmatrix}$$

Similar to the GLCM, the GLAM is normalized and the texture features are computed using the normalized GLAM (Table 2.1).

More recently, the GLAM have been extended to basic gray level Aura matrices (BGLAM) by Qin and Yang [282; 283]. The BGLAM is an extension of the GLAM in which the neighborhood system consists of only one element. Qin and Yang show that texture images can be retrieved with a high precision using the BGLAM [282]. They also demonstrate that textures can be faithfully synthesized from the BGLAM features [283; 284].

To have invariant features, the GLCM (and similarly the GLAM and the BGLAM) are computed for several directions and distances. Since computing the features at different directions and distances makes the feature vector large, a feature selection step (e.g., Principal Component Analysis (PCA) [164]) is usually applied.

The Run Length Matrices (RLM) [99; 335] method defines a gray level run as consecutive pixels of the same gray level in a given direction, and the length of the run is used as a texture feature.

Recently, the Local Binary Patterns (LBP) proposed by Ojala et al. [267] has been recognized as one of the most successful statistical methods. Its popularity is due to its simple computation and high accuracy. It has been extended by many research groups [123; 124; 137; 143; 202; 217; 410]. The method represents the relationship of each pixel and its neighbors (located on a circle around the pixel) by a binary pattern and uses the histogram of these patterns for texture classification.
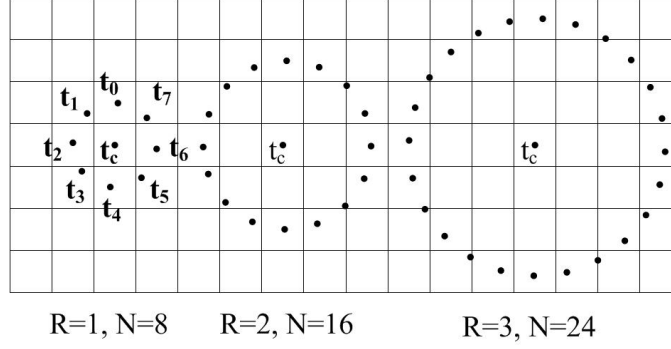
Figure 2.10: Three common neighborhood settings in the LBP.

Consider N points on a circle with radius R at center pixel, t_c. These N points $(t_0, t_1, ..., t_{N-1})$ are considered as the neighbors of the center pixel and their gray level values are determined by interpolation if they are not located at the pixel locations. Figure 2.10 shows three popular configurations with radius of one, two, and three and their corresponding neighborhood size of 8, 16 and 24. The eight neighbors in the first neighborhood setting are labeled.

The signs of the differences of the gray value of the center pixel with the neighboring pixels are computed. The sign is one if the difference is greater than or equal to zero, and zero otherwise. By assigning a binomial factor 2^n to each of the signs of differences and summing them together, a binary number (pattern) is created,

$$LBP_{N,R} = \sum_{n=0}^{N-1} s(t_n - t_c).2^n, s(x) = \left\{ \begin{array}{ll} 1 & x \geq 0 \\ 0 & x < 0 \end{array} \right. , \tag{2.23}$$

where s is the sign function and N the number of neighbors. To have rotation invariance, the binary pattern is circularly shifted and the minimum value is kept as the final binary pattern. In other words, the rotation invariant LBP is defined as

$$LBP_{N,R}^{ri} = min\{ROR(LBP_{N,R}, i)|i = 0, 1, ..., N-1\}, \tag{2.24}$$

where $ROR(x, i)$ performs i times bitwise circular right shift on the binary number x.

The major problem of the LBP is the exponential growth of the number of patterns with respect to the neighborhood size. To address this problem, several methods have been proposed. Ojala et al. [267] show that some binary patterns are more common than others in some textures. These patterns known as uniform patterns have a common property: the number of spatial transition between zero and one in the binary pattern (i.e., uniformity) is at most two. The uniformity measure is defined as

$$U(LBP_{N,R}) = |s(t_{N-1} - t_c) - s(t_0 - t_c)| +$$
$$\sum_{n=1}^{N-1} |s(t_n - t_c) - s(t_{n-1} - t_c)|. \tag{2.25}$$

20

Rotation invariant uniform patterns have the uniformity of two or less and are defined as

$$LBP_{N,R}^{riu2} = \begin{cases} \sum_{n=0}^{N-1} s(t_n - t_c).2^n & \text{if } U(LBP_{N,R}) \leq 2 \\ N+1 & \text{otherwise.} \end{cases} \qquad (2.26)$$

To further improve the results, $VAR_{N,R}$ operation is defined as follows and the joint histogram of $LBP_{N,R}^{riu2}/VAR_{N,R}$ is used for classification [267]:

$$VAR_{N,R} = \frac{1}{N} \sum_{n=0}^{N-1} (t_n - \mu)^2, \ \mu = \frac{1}{N} \sum_{n=0}^{N-1} t_n. \qquad (2.27)$$

Later, Guo et al. [124] argue that the VAR operation produces continuous values and the correct quantization of these values is challenging. They propose the LBP Variance (LBPV) in which the histogram of $LBP_{N,R}$ is weighted by the $VAR_{N,R}$ instead of using the joint histogram of $LBP_{N,R}^{riu2}/VAR_{N,R}$. The histogram of $LBPV_{N,R}$ is computed as

$$LBPV_{N,R}(k) = \sum_{i=1}^{N} \sum_{j=1}^{M} w(LBP_{N,R}(i,j),k), \ k \in [0, K], \qquad (2.28)$$

where N and M are, respectively, the number of rows and columns of the LBP, and the weight is computed as

$$w = \begin{cases} VAR_{N,R}(i,j) & \text{if } LBP_{N,R}(i,j) = k \\ 0 & \text{otherwise.} \end{cases} \qquad (2.29)$$

Before computing $LBPV_{N,R}$, they use the LBP to find the principal orientation of the texture and align the binary patterns to that orientation (i.e. global matching).

The next approach to reducing the number of binary patterns is the work of Liao et al. [217]. They show that the uniform patterns are not necessarily the dominant patterns in all datasets and suggest choosing the dominant patterns instead of the uniform ones. Unlike the uniform patterns, the number of patterns for classification is not constant and is determined by choosing the k dominant patterns such that they consist of 80% of the whole patterns; in particular,

$$k = \underset{k}{\operatorname{argmin}} \left(\frac{\sum_{n=0}^{k-1} H[n]}{\sum_{n=0}^{2^N-1} H[n]} \geq 80\% \right), \qquad (2.30)$$

where N is the neighborhood size in $LBP_{N,R}$, and H the histogram of patterns sorted in a descending order. The final histogram for classification is $H[0...k]$. They also use the Normalized Gabor Filter (NGF) responses of the frequency spectrum to improve the classification rate.

Guo et al. [122] use the Fisher separation criterion to choose patterns. In their approach, the dominant patterns in each image are found. The representative patterns of each texture class are computed as the intersection of patterns that are dominant in all images of the same texture class. Finally, the union of all class representative patterns is used to select the final patterns. The proposed approach tries to maximize the inter-class distance and to minimize the intra-class similarity (i.e., the Fisher separation criterion).

In a recent work, Guo et al. [123] present the completed model of LBP (CLBP) in which they use not only the sign of the difference between the center pixel and its neighbors but also the magnitude

of this difference and the magnitude of the center pixel. They define three operators: $CLBP\_S$, $CLBP\_M$, and $CLBP\_C$. The first operator is the same as the ordinary $LBP_{N,R}$ and makes a binary pattern based on the sign of the difference of the center pixel and its neighbors. To make a binary pattern from the magnitude of difference, $CLBP\_M$ is defined as

$$CLBP\_M_{N,R} = \sum_{n=0}^{N-1} s(t_n - c).2^n, \tag{2.31}$$

where s is the sign function defined in equation (2.23) and c an adaptive threshold set to the mean value of t_n. Finally, to take the center pixel's value into account, $CLBP\_C$ is defined as

$$CLBP\_C_{N,R} = s(t_c - c_I), \tag{2.32}$$

where s is the sign function and c_I a threshold set to the average gray value of all pixels. They use the joint and concatenated frequency histogram of patterns produced by $CLBP\_S$, $CLBP\_M$, and $CLBP\_C$.

There are other statistical methods such as using high order statistics [256; 345] and invariant moments of an image [362; 320]; however, they are not robust in the presence of noise and other distortions.

2.3   3D Texture Features

In some applications the images are in a 3D form. In particular, in medical imaging the acquired slices of images form a volume. As a result, there is a great need in this area to efficiently capture 3D texture features. In spite of this demand, there are only a few methods that have been developed to analyze 3D data mainly due to the computational cost in 3D image analysis.

The developed methods are usually the extension of the current popular 2D methods. For instance, Kurani et al. [196] present a simple extension of the GLCM by considering the vectors in 3D. That is, a vector $v = (\Delta x, \Delta y, \Delta z)$ connects voxel $I(x_1, y_1, z_1)$ to voxel $I(x_2, y_2, z_2)$ such that $x_2 = x_1 + \Delta x$, $y_2 = y_1 + \Delta y$, and $z_2 = z_1 + \Delta z$.

By considering the 3D connections and assuming 26 neighbors for each voxel, Xu et al. [376] propose a simple 3D extension of the RLM.

Kovalev et al. [191] extend the GLCM method to extract 3D features from MRI using local gradient information in addition to the gray values. Considering an arbitrary voxel pair (i, j) with the Euclidean distance $d(i, j)$, they define a 6D co-occurrence matrix:

$$W = ||w(I(i), I(j), G(i), G(j), a(i, j), d(i, j))||, \tag{2.33}$$

where w is the quantization function, $G = \sqrt{G_x^2 + G_y^2 + G_z^2}$ the local gradient magnitude, and $a = cos^{-1}(G(i).G(j))$ the angle between local gradient vectors.

Qin and Yang [284] apply the 2D BGLAM to the three viewing directions (x,y,z) to synthesize volumetric textures. However, they do not have a method to analyze 3D textures.
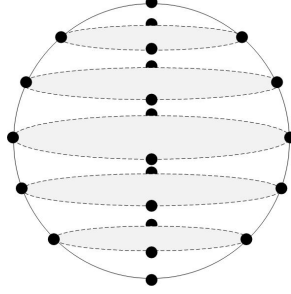
Figure 2.11: The neighboring points considered by Paulhac et al. [270] to define the 3D LBP.

Jafari-Khouzani et al. [156] define 3D texture features as the energy of the 3D wavelet transform of a volume. Three dimensional filtering has also been used by Reyes-Aldasoro and Bhalerao [15; 289] to extract 3D texture features. Madabhushi et al. [231] use statistical, gradient and Gabor filter features at multiple scales and orientations to define 3D texture features.

There are also some recent model-based methods for 3D images. Ranguelova and Quinn [288] present a 3D MRF model to capture 3D textures features. In recent works by Upadhyay et al. [351] and Jain et al. [158], the Gaussian random field is used to model 3D textures features.

The LBP method has also been extended to 3D by Paulhac et al. [270], considering the neighbors g_p on the surface of a sphere around a center voxel, g_c. Assume that S parallel planes cross the sphere creating parallel circles on the surface of the sphere. For each circle, P vertices are regarded as the neighbors (Figure 2.11). The relative coordinates of the neighbors with respect to the center of the sphere are $(Rcos(\pi p'/(S-1))cos(2\pi p/P), Rcos(\pi p'/(S-1))sin(2\pi p/P), Rsin(p'\pi)/(S-1))$ where R is the sphere radius, S the number of circles used to represent the sphere, P the number of vertices in each circle, and p' the index of the circles. The 3D LBP is defined as

$$LBP_{P',R}^{riu2} = \begin{cases} \sum_{p=0}^{P'-1} s(g_c - g_p) & \text{if } LBP_{N,R}(i,j) = k \\ P'+1 & \text{otherwise,} \end{cases} \quad (2.34)$$

where $P' = (S-2)P + 2$ is the total number of neighbors.

There is another class of 3D texture methods that model textures that are not naturally 3D but temporal such as the flame of a fire or the running water in a waterfall. This type of textures is known as dynamic textures. Here, the 3D data includes a sequence of 2D images, each of which is acquired at a different time. Some recent examples of these methods include but are not limited to extensions of the LBP (e.g., the volume local binary patterns (VLBP) [404], the LBP on three orthogonal planes (LBP-TOP) [408]), applying 3D steerable filters [398], using free form deformations [187], wavelet decomposition [81], and distributions of space time orientation structure [77].

2.4   Applications

Texture features have been used in many applications including but not limited to automatic inspection, document processing, remote sensing, fingerprint identification, object recognition, image

matching, and medical imaging.

Automatic inspection includes applications that employ texture features to detect defects in different products such as printed circuit boards [142; 149], wood [300], pearl [411], tunnel walls [395], solar wafer surfaces [214; 344], steel surfaces [388], and food products [200; 322]. Some recent reviews of the application of texture analysis to defect detection can be found in [195; 261; 375].

Document processing is the next popular application of texture analysis methods. After the appearance of Optical Character Recognition (OCR) technology to convert scanned images of text into machine readable, texture analysis methods have been widely used to detect and localize the text. These methods use different texture features extracted from the wavelet transform [389; 409], the Gabor filter responses [391], the Fourier transform [319], and the GLCM [130]. Another interesting document processing application is in text segmentation using texture features [117; 220; 302]. The segmentation results can be used in mixed raster content (MRC)[1] compression [129].

Texture features are also used to classify remotely sensed images, in particular, the Synthetic Aperture Radar (SAR) images. The SAR images are insensitive of meteorological conditions and illumination conditions, and therefore are popular for automatic and semiautomatic land cover classification [46]. Some applications include detecting oil spills [378], sea ice [104], urban areas [74], and forests [397]. Recent land cover classification methods can be found in [46; 84; 233].

Fingerprint identification is another application of texture analysis. The application of texture features to analyze fingerprints dates back to the 80's [48]. Some methods employ frequency-based features such as the responses of different filters (e.g., the Gabor filter [383], the short time Fourier transform (STFT) [53], and the wavelet transform [255]). Non-frequency based features have also been proposed [31; 54; 259].

Texture features can be used in object recognition and image matching. In particular, the rotation invariant features can be easily extended for this purpose. Object recognition and image matching are based on invariant local descriptors. These descriptors are created in two steps. In the first step some salient points are detected in the image (region detection step). In the second step the area around these salient points are used to extract features that are invariant under a class of transformations and image distortions (region description step). The most well-known method which is used for both detection and description is the Scale Invariant Feature Transform (SIFT) [224]. Many region detection methods (e.g., Laplacian, Hessian, and Harris region detectors) define an elliptical region around salient points. These elliptical regions are then normalized to a circle reducing the affine transformation to a rotation transformation [248]. As a result, by using rotation invariant features, one can define local descriptors that are invariant to affine transformations. This approach makes rotation invariant texture features suitable for object recognition and image matching. One recent example is the extension of LBP as an invariant local descriptor [137].

---

[1]The mixed raster content (MRC) is a framework for layer-based document compression that enables the preservation of text detail while reducing the bit rate of encoded raster documents. The idea is to separate the text from the image which are then compressed separately by efficient corresponding algorithms.

Medical imaging is one of the most popular areas for the application of texture analysis. Texture methods have been used in a variety of medical applications including but not limited to medical image enhancement [18; 206], automatic [387] and semi-automatic [291] segmentation, and detection and monitoring of different diseases [175; 198]. Since the target application of this thesis is in medical imaging and, in particular, neurodegenerative diseases, the applications of texture analysis to brain related diseases are discussed further in Chapter 3.

Nonetheless, the applications of texture features are not limited to what are presented in this document. Texture features can be extended to facial expression recognition [11], human action recognition [390], background subtraction [136], and image retrieval [333] as well as to many other computer vision and graphics applications. A complete review of all of these applications is certainly beyond the scope of this document.

2.5 Summary

Texture analysis includes methods that use intensity variations of images to capture their features. In general there are four research domains defined in texture analysis; namely, classification, segmentation, texture synthesis, and shape from texture. Nonetheless, the performance of a texture descriptor is usually assessed using texture classification. The texture methods can be broadly divided into four general approaches:

1. Structure-based methods: these methods decompose textures into textural elements and use the invariant properties of the textural elements. These methods are usually useful for macro-textures.

2. Model-based methods: this class of texture methods defines textures as probability models and based on the assumed model extract invariant features. The main issue in this group of methods is choosing a correct model and also providing a faithful map from the image to the model.

3. Filter-based methods: this group of methods applies filters on texture images in spatial domain or analyzes images in frequency domain. The responses of the filters are used as features. The features extracted by these methods are robust, but they are not as discriminative as the ones extracted by the statistical-based methods.

4. Statistical-based methods: this group of methods use statistical features of textures. The methods usually demonstrate higher performances compared to the other groups.

Table 2.2 summarizes the methods explained in this chapter. One may note that the actual number of texture methods is much higher than the methods explained in this chapter. However, it was attempted to include the well-known and popular methods. The readers may also note that the borders between categories are sometimes vague. For instance, some studies may categorize the

Table 2.2: The well-known texture analysis methods. They are classified into four categories: structure-based, model-based, filter-based, and statistical-based.

Category	Methods	References
Structure-based	Shape as maximally connected set of pixels	[114; 115]
	Shape as regions with uniform intensity	[399]
	Granulometry	[19; 26; 30; 180; 305; 306; 352]
	Fractal analysis	[160; 174; 370; 374; 377; 379; 380; 381; 382]
	Topographic map	[126; 372]
Model-based	Markov Random Field	[59; 66; 75; 165; 239; 392]
	Gibbs Random Field	[76; 83; 105]
Filter-based	Fourier and STFT	[13; 27; 268; 287]
	Wavelets	[49; 154; 160; 382; 415]
	Gabor Filters	[36; 56; 125; 286; 377]
	Spacial Filters	[67; 208; 356; 357]
	Fourier transform of circular samples	[17; 216]
Statistical-based	Cooccurrence-based methods	[131; 274; 275; 282; 283; 284]
	Run Length Matrices	[99; 335]
	LBP	[123; 124; 137; 143; 202; 217; 267; 410]
	High order statistics	[256; 345]
	Invariant moments	[320; 362]

fractal analysis methods under the model-based approaches; however, this thesis defines the model based approaches as the ones using probabilistic models for textures. Moreover, some methods may use combinations of different approaches like using fractal analysis on the wavelet transform [382; 160]. Hence, in Table 2.2 such methods are put under both categories in the references column. In the next chapter the applications of texture methods in medical imaging is discussed.

Chapter 3

Texture Analysis in Medical Imaging

3.1 Introduction

Texture analysis methods have found success in different medical applications. In general, the applications use textural features to identify abnormalities. The majority of methods are developed for 2D images. The imaging modality used is different depending on the disease. Some well-known modalities include ultrasound, Computed Tomography (CT), and Magnetic Resonance Imaging (MRI). In neuroimaging and in applying texture analysis methods to brain related diseases, MRI is preferred. One on the advantages of MRI for brain imaging is that it provides high resolution information. In contrast to CT which provides good details on bony structures, MRI captures details of soft tissues effectively. Ultrasound images have the disadvantages of having low resolution and being noisy. It is not possible to image the adult brain with ultrasound. Therefore, MRI is more desirable for brain imaging. Additionally, and in contrast to CT, patients are not exposed to harmful radiation with MRI which makes it a safer choice.

Routine structural MRI is used to observe the physical structure of the brain and as mentioned above is preferred for texture analysis in neurological diseases. Hence, this chapter focuses on this method of imaging. Depending on the protocols used to acquire MRI, different structural information is captured from the brain. Some common protocols are T1-weighted, T2-weighted, and Fluid Attenuated Inversion Recovery (FLAIR) MRI. The important distinctions between T1-weighted, T2-weighted, and FLAIR with regards to the brain is the differences in the appearance of the gray matter (GM), white matter (WM), and cerebrospinal fluid (CSF). In T1-weighted images, GM is darker than WM and CSF is black, whereas in T2-weighted images, WM is darker than GM and CSF is essentially white. FLAIR is a T2-weighted image with the CSF signal suppressed so it appears black. A contrast agent, usually Gadolinium, may also be administered intravenously to the subject to increase the contrast of abnormalities in T1-weighted images. Figure 3.1 shows images from these three types of MRI sequences. In the next section the applications of texture analysis in different diseases are discussed.

<div align="center">(a)   (b)   (c)</div>
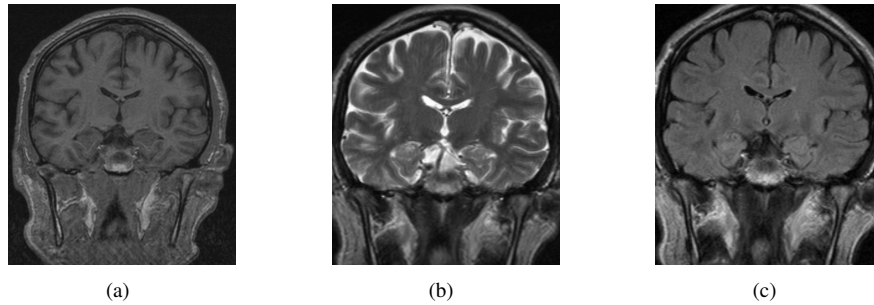
Figure 3.1: The most common imaging types for texture analysis of the brain are T1-weighted, T2-weighted, and FLAIR MRI. a) T1-weighted MR image, b) T2-weighted MR image, and 3) FLAIR MR image of the same region of the brain.

3.2 Brain Tumors

The characterization of brain tumors is one of the applications of texture analysis. Schad et al. [313] and Lerski et al. [207] are among the first groups which have used texture features to characterize brain tumors. Lerski et al. [207] use GLCM features along with the histogram and gradient information of the images to differentiate WM, GM, CSF, solid tumour, and edema. The features are extracted from both T1-weighted and T2-weighted images. Schad et al. [313] use the RLM, the GLCM, the gray level histogram, and the gradient distribution of images. Similar texture features are employed by Herlidou-Meme et al. [139] to differentiate tumour from normal brain tissue. They also examine the robustness of texture methods using three different scanners and report highly reproducible results in the texture features.

Textural features extracted by fractal analysis have been used for tumour detection in several research studies [144; 146; 147; 414]. It is shown in [414] that the tumour region has a statistically significant lower fractal dimension compared to that of a normal region. The combination of wavelet and fractal analysis is used by Iftekharuddin et al. [145] for tumour detection. Kharrat et al. [179] develop a three stage tumour detection method. In the first step they enhance the image by morphological operations. Then, the image is segmented using wavelet features. Finally, the k-means algorithm is employed to detect the tumour. Zacharaki et al. [396] use the Gabor filter and rotationally invariant filters in the Fourier domain to extract texture features from T1-weighted, T2-weighted and FLAIR.

Some methods use the Stockwell transform to study brain tumors [40; 79]. Brown et al. [40] apply the Stockwell transform to T2-weighted MR images to detect oligodendroglioma among tumour genotypes and achieve a sensitivity and specificity of 93% and 96%, respectively. Drabycz et al. [79] apply the Stockwell transform to T2-weighted images to find the patients with high-grade gliomas. They report that the texture features are significantly different between methylated and unmethylated cases (p-value< 0.05).

The application of texture analysis to brain tumour segmentation is also noted by several research

groups. Xuan and Liao [384] use the Gabor filter to compute textural features. These textural features along with features extracted from the intensity and symmetry of the brain are used for brain tumour segmentation. They achieve an average accuracy of 96.82% on tumour segmentation for 10 patients. By extracting fractal features from (gadolinium-enhanced) T1-weighted, T2-weighted, and FLAIR MR images, Iftekharuddin et al. [147] achieve 100% accuracy on the tumour segmentation of nine patients.

In addition to brain tumours, texture analysis has been used in other types of cancers such as breast [10; 87; 211; 140], prostate [57; 324], lung [100; 102], colorectal [101; 250], and cervical [161; 257].

3.3   Epilepsy

Epilepsy is a neurological disorder characterized by seizures. Texture analysis has been used in epilepsy to detect the lesions (focal pathology) that are responsible for seizures, such as cortical dysplasia and hippocampal sclerosis [175]. The statistical-based texture methods are widely used for epilepsy study [16; 307; 393]. There are also some methods that use the wavelet transform [152; 153; 156].

To detect focal cortical dysplasia, Bernasconi et al. [33] extract gradients of intensities from T1-weighted MR images as texture features. They achieve 87.5% sensitivity and 95% specificity with a dataset of 16 patients and 20 healthy controls. Antel et al. [16] use the GLCM features along with the gray level intensities of T1-weighted MR images. In their method, first, a Bayesian classifier is trained to classify voxels as GM, WM, CSF, transitional, or lesional. Then the voxels classified as lesional are reclassified based on the GLCM texture features. In images acquired from 18 patients and 14 healthy controls, they achieve 100% specificity and 83% sensitivity.

Yu et al. [393] apply texture analysis to proton density-weighted and T2-weighted images of 23 patients with unilateral temporal lobe epilepsy and 9 healthy controls to identify hippocampal sclerosis. The texture features used in this work include the intensity histogram, the gradient statistical information (e.g., mean, variance, etc.), the RLM, and the GLCM. Sankar et al. [307] use gradient and intensity information along with the GLCM features extracted from T1-weighted and T2-weighted images to study temporal lobe epilepsy on 23 patients and 20 healthy controls. Their method identifies hippocampal atrophy with 65% sensitivity and 100% specificity.

Bonilha et al. [35] extract textural features from T1-weighted MR images of 19 patients with temporal lobe epilepsy and 39 healthy control subjects. They compute similar texture features as in the work of Yu et al. [393]; however, the features are extracted from T1-weighted, T2-weighted, and FLAIR MR images. Using the multivariate analysis of variance, they find eight texture features that are able to discriminate between sclerotic and healthy hippocampi ($p < 0.01$).

Jafari-Khouzani et al. [153] extract texture features from T1-weighted images to study epilepsy in the hippocampus. To do so, they first segment the hippocampus and then apply multiwavelet,

wavelet, and wavelet packet transforms. The energy and entropy features in each sub-band are used for texture analysis. In another study [156], they find the texture features of hippocampus using 2D and 3D wavelet transforms. By combining hippocampus volume and texture features [155], they identify the laterality of the epileptogenic area with more than 92% accuracy on a dataset of 55 patients. In their recent work [152], they apply texture analysis to T1-weighted and FLAIR images of 25 healthy subjects and 36 patients for lateralizing mesial temporal lobe epilepsy. Texture analysis using the wavelet transform lateralizes the epileptogenic area correctly in 94% of cases.

Hippocampal segmentation has an important application in the study of temporal lobe epilepsy. As a result some studies use texture features for this purpose. For instance, Kim et al. [181; 182] have recently employed texture features for hippocampal segmentation. They use the Gabor filter responses along with gradient and intensity information to find the regional texture model which is used for segmentation. In another work, Kim et al. [184] use intensity, spatial location, and neighborhood features as well as GLCM properties. In this work, textural features and multiple atlases are used for hippocampal segmentation.

3.4 Multiple Sclerosis

MS is an inflammatory disease of the central nervous system. In this disease, the insulating myelin sheath around the axons of the brain and spinal cord are damaged (demyelination). This demyelination impairs the transmission of signals along axons resulting in functional impairment.

In the early stages of MS (known as the relapsing-remitting stage), the inflammation can be readily identified using gadolinium-enhanced T1-weighted MR imaging. However, in the advanced stage (i.e., secondary-progressive), the conventional MR imaging markers are not very helpful for monitoring the disease [297]. Texture analysis has been used in several studies for identifying active MS lesions and monitoring disease progression.

Yu et al. [394] are among the first who apply texture analysis to MS. In their approach, texture features are extracted from T2-weighted images using the GLCM, the RLM, and the gradient matrix. Linear Discriminant Analysis (LDA) is used to classify lesions into active and nonactive classes. Applying this method to the images acquired from eight MS patients (four with active lesions), they report that the GLCM features are not discriminative; however, the features extracted from the RLM can classify the active lesions and the non-active lesions correctly with 88% sensitivity and 96% specificity, respectively.

Zhang et al. [402] use the GLCM features to investigate the discriminative power of texture analysis in classifying MS lesions, normal appearing white matter (NAWM) and normal white matter (NWM) in early stages of MS. In the feature selection step, the features that provide the largest difference between different tissue types are selected (i.e., MS lesions versus NWM, MS lesions versus NAWM, and NWM versus NAWM). Applying their method to T2-weighted MR images acquired from 16 relapsing remitting MS patients and 16 healthy subjects, they report over 90%

classification accuracy between MS lesions and NAWM or NWM, 88.89% among the three tissue groups, and 66.67% between NAWM and NWM. In a subsequent work, Zhang et al. [401] extract more textural features. Here, features are computed from the gradient matrix, the run-length matrix, the GLCM, the autoregressive (AR) model, and wavelet analysis. Using the same approach for feature selection and classification, they report classification accuracy of 100% between MS lesions and NAWM (or NWM), 88.89% among the three tissue groups, and 58.33% between NAWM and NWM suggesting that GLCM-based features are more discriminative between NAWM and NWM, but the combined features are more effective for classification between MS lesions and NAWM (or NWM).

Theocharakis et al. [338], employ texture analysis to differentiate lesions of MS from that of cerebral microangiopathy (CM). They use histogram information along with the GLCM and run length properties of FLAIR images of 11 patients diagnosed with MS and 18 patients diagnosed with CM. They report statistically significant differences between texture features of MS and CM lesions.

Zhang et al. [407] apply the polar Stockwell transform to T2-weighted images on 12 acute lesions before, during, and after the development of gadolinium-enhancement. The sum of low frequency energy is used as the texture feature. They demonstrate that the texture feature increases in acute lesions during enhancement ($p < 0.05$). The texture feature does not change in NAWM, while it increases in chronic T2-weighted lesions. The study suggests that texture analysis is more informative than the conventional MRI analysis. It also reports that the texture method is able to find abnormalities in pre-lesional normal appearing WM, quantify tissue injury in acute lesions, and detect mild tissue injury in chronic lesions. In their recent work, Zhang et al. [406] use a similar approach to differentiate between new T1-weighted hypointense lesions that persist and those that resolve over time.

There are some works that demonstrate the correlation of texture features to the changes associated with patient's disability. Mathias et al. [241] use the mean and variance of the intensity and the gradient along with the GLCM features extracted from T2-weighted images of the spinal cord to quantify pathological changes in MS. They report that the mean gradient and the mean intensity values are significantly correlated with disability as assessed by the expanded disability status scale (EDSS) in MS subjects. In a recent study, Tozer et al. [342] also demonstrate that texture features are correlated with neurological disability in MS.

In addition to the works that use texture analysis as a tool to study MS, there are some studies to evaluate the robustness of the texture features. One recent example is the study by Harrison et al. [132], evaluating the robustness of texture features with respect to image acquisition and processing protocols. Three types of imaging sequences (T1-weighted with and without contrast agent, and T2-weighted), two anatomical levels of interest (corona radiata and centrum semiovale), and two methods of drawing the region of interest (standard-size boxes of 10×10 pixels versus freehand)

are considered in this study. To find the significance of image slice selection, three sequential image slices are used for analysis. A total of 280 texture features are evaluated including features extracted from the histogram, the gradient, the run-length matrix, the GLCM, the AR model, and the wavelet transform. The study reports an excellent distinction between the image regions corresponding to MS plaques and WM or NAWM (with 96% to 100% accuracy) with no significant difference in the results of classification between imaging sequences or between anatomical levels. According to this report, using T2-weighted or T1-weighted MR images with and without contrast agent sequences results in similar classifications with a slightly better results for T1-weighted images with contrast agent. The report concludes that texture analysis is a robust quantitative tool for evaluating MS lesions.

Finally, similar to tumour and epilepsy studies, texture features can be used for segmentation of the abnormal regions as proposed by Ghazel et al. [108; 109].

3.5 Alzheimer's Disease

AD is a progressive neurodegenerative disease and the most common cause of dementia. The definitive diagnosis of the AD is obtained from an autopsy or brain biopsy which is not usually done. Currently, there are no tests available to diagnose AD in vivo. As a result, texture analysis has been used evaluated a non-invasive tool to diagnose and monitor AD.

Freeborough and Fox [94] are among the first who have used texture features to study AD. They compute the GLCM for several directions and distances of T1-weighted images acquired from 40 normal controls and 24 AD patients. Using discriminant analysis they show that there is a statistical difference between the texture features for the control and AD groups ($p < 10^{-4}$).

Kaeriyama et al. [170] extract the properties of gray level intensity along with the RLM. They achieve 69.0% sensitivity, 86.2% specificity, and 77.6% classification accuracy on a dataset of 29 AD patients and 29 healthy contorols.

Kodama and Kawase [186] use the GLCM and the RLM to differentiate between AD and dementia with Lewy bodies (LBD, the second most frequent cause of dementia after AD). With a dataset of T1-weighted images of 10 patients with Lewy bodies, 36 patients with AD, and 25 healthy controls, they achieve a classification accuracy of 87.3%.

The capability of texture analysis to differentiate between amnestic mild cognitive impairment (MCI) [1] and AD is studied by de Oliveira et al. [73]. In this study, the GLCM features are extracted from T1-weighted and T2-weighted images from two regions: corpus callosum and thalamus. The datasets that they use include 17 patients with amnestic MCI, 16 patients with mild AD, and 16 healthy subjects. In the corpus callosum region, the pairwise comparison shows a significant difference between AD versus controls and AD versus amnestic MCI. The texture features extracted

---

[1]MCI refers to the cognitive impairments beyond those caused by the aging effect, that are mild and do not interfere with the patient's daily activities. However, those with MCI are at increased risk of eventually developing AD.

from thalamus reveal laterality. They report that the texture features on the right side of the brain are more discriminative than the ones extracted on the left side. The features extracted from thalamus present statistical difference in all pairwise comparisons: AD and control, AD and amnestic MCI, and amnestic MCI and control subjects. Wang et al. [364] also show that the textural features (the GLCM and the RLM) in the corpus callosum region are statistically different between the AD patients and and the healthy control group.

In a recent work, Xia et al. [373] show that the GLCM features can detect the underlying pathological changes in AD. In a dataset of T1-weighted images of 29 AD patients, 19 age-matched controls and 18 young healthy controls, the volumes of bilateral hippocampus and medial temporal lobe are computed. They report significant differences in the volumes ($p< 0.001$) and the texture features ($p< 0.01$) between the AD and the control groups. They also find a strong correlation between the texture features and the volume of bilateral hippocampus ($p< 0.01$) as well as the volume of medial temporal lobe ($p< 0.05$) and conclude that texture analysis can be used as a quantitative tool to measure pathological changes in AD.

In addition to the 2D texture methods, some research groups have used 3D texture analysis for AD. For instance, Li et al. [215] extract 3D features of the GLCM and the RLM from T1-weighted images to differentiate patients with AD, patients with MCI. In a dataset of 12 early AD patients, 12 MCI patients and 12 healthy controls, they demonstrate that the computed texture features are significantly different among the AD, the MCI and the healthy subject groups. In another recent work, Zhang et al. [403] compute 3D texture features of T1-weighted MR images of 17 AD patients and 17 healthy controls. Circular 3D ROIs are considered in the hippocampus and entorhinal cortex area. The features include statistical information extracted from the histogram of intensities, and the absolute gradient values in the images along with the GLCM, and the RLM features. They achieve a classification accuracy of 98.5% using an artificial neural network (ANN) classifier. Chincarini et al. [55] use local 3D filter responses as textural features to study medial temporal lobe (MTL) atrophy in AD. Using the SVM as a classifier, their method is able to discriminate controls from AD with sensitivity of 89% and specificity of 94% on T1-weighted images of 144 AD patients and 189 age-matched controls.

Texture analysis of AD has also been done using other modalities such as PET [312], and SPECT [80]; however, they are not as popular as structural MR images.

3.6 Challenges of MRI

MR images inherit some issues due to the limitations of the image acquisition process. As a result, the texture analysis methods that use MRI should consider these challenges. The main issues are:

- Noise

- Partial volume averaging

- Intensity non-uniformity

- Inter-slice intensity variations

- Intensity non-standardization

Noise is one of the inherent problems of MR images. A common approach to suppress noise is to filter the image in either the spatial or the frequency domain. Some conventional methods include using a median filter or a Gaussian filter. However, a good noise removal strategy should not make the image blur (which is not addressed in the conventional denoising methods). As a result edge preserving methods are preferred for noise removal [386]. Since noise in MR images follows the Rician distribution [262], several recent methods have been developed to remove the Rican noise from MR images including non-local means filter based methods [65; 237; 64], the wavelet sub-band coefficient mixing method [63], the RNRAD and ORNRAD filters [193], and the ODCT3D and the PRI-NLM3D filters [236].

The next issue of MR images is partial volume averaging. This issue is more evident in images with low resolutions. When the acquisition resolution is low (e.g., slice thickness is high), the intensity captured at each voxel will be affected by several types of tissue, appearing as the average intensity of the enclosed tissues. This effect imposes blurring effect to the MR images. Acquiring MR images with high resolution will alleviate this problem.

Intensity non-uniformity (INU also known as intensity inhomogeneity) is another issue in MR images, which refers to the smooth intensity variation across a slice or region. This artifact can be induced by different factors including the choice of the radio-frequency coil, the acquisition pulse sequence, or even the nature and geometry of the sample itself. Several methods have been proposed to address this problem and to correct this artifact. Some well-known approaches include modeling the intensity non-uniformity by a smooth surface [201; 244; 328], applying spatial filtering [37; 360; 412], performing frequency domain filtering [60; 127; 219], and modeling the intensity as a probability distribution of random variables [218; 323]. Some recent studies in intensity non-uniformity correction include using patches from an atlas of inhomogeneity-free images [298], modeling the intensity non-uniformity as a polynomial surface [321] and as multiple Gaussian surfaces [163], employing Markov random fields [316], and using the max filter [28].

The next issue in MR imaging is inter-slice intensity variations caused by gradient eddy currents and crosstalk [2] between slices. A simple approach for correcting this artifact is to define the intensity as a function of the slice intensity and its neighboring slice intensity [413]. Van Leemput et al. [205] model the MR images as a realization of a random process and apply an iterative expectation-maximization (EM) strategy to correct inter-slice intensity variations. Chen et al. [50] segment each slice to find the tissues. They consider the average intensity of each tissue type as

---

[2]If the slice distances are very small, the excitation pulses that should cover only one slice partially overlap. The tissues located in the overlapped regions receive double excitation and contribute little to the detected signal. This effect is known as crosstalk.

the normalized intensity value. Dauguet et al. [72] use histogram scale-space analysis to address inter-slice intensity variations. In this method, for each slice, a scale-space analysis of the histogram is computed by smoothing the slice with a Gaussian kernel with increasing width. The scale-space analysis provides a set of plausible tissue classification schemes. In an iterative procedure the best classification scheme for each slice is found by maximizing the spatial consistency of the classifications across all slices. A recent work for inter-slice intensity correction is presented by Lee et al. [204] which is a 3D wavelet-based method. In this method, two separate wavelet transformations are applied: one filter bank to correct for the inhomogeneity within 2D images, and the other filter bank along the slice direction to correct the inter-slice intensity variation.

Finally, the intensity of the MR images are not standardized. In other words, images of the same tissue acquired from different subjects using the same scanner and protocol present large intensity variations. Consequently, the *absolute* intensity values do not represent a specific tissue and cannot be compared between subjects. Therefore, standardization is needed for correcting inter-subject intensity variations. This issue was first demonstrated by Nyul and Udupa [263]. They present a framework with two steps: a training step and a transformation step. In the training step, some landmarks on a standard histogram are computed using the images in the training set. In the transformation step, the actual intensity transformation is found by mapping the landmarks on the histogram of a given image and the standard histogram obtained in the training step. This framework has been adopted in several other studies [103; 232; 264]. One of the popular approaches in recent methods of standardization is in using joint histograms [157; 280; 292]. For instance, Jager and Hornegger [157] perform a nonrigid image registration between the joint histogram of the reference image and that of the acquired images. The nonparametric transformation obtained from this registration is used as a mapping function between the corresponding intensity spaces. In another example, Robitaille et al. [292] use the joint histograms of the MR images to compute intensity correspondence for each tissue type between the input image and the standard images.

The above mentioned problem can also be addressed if the features are robust. For instance, texture methods that are robust to noise can be directly extracted from MR images without having to worry about the noise problem. Illumination invariant texture features can address the problems arising from intensity non-uniformity, inter-slice variability, and intensity non-standardization. Therefore, texture analysis is not only able to analyze images but also offers robustness against many challenges with MRI. Indeed, some recent studies corroborate this hypothesis by demonstrating that texture features are relatively robust to several imaging variables [242; 311].

3.7 Summary

In this chapter an overview of the applications of texture analysis in medical imaging is given. In particular, this chapter reviews the texture analysis methods used in four well-known diseases that affect the brain: brain tumors, epilepsy, MS, and AD. The general trend is to use statistical based

methods such as the GLCM and the RLM. The second popular approach is frequency-based methods such as the Stockwell and wavelet transforms. The challenges in MR images are discussed and some approaches to address them are described. The robust and invariant texture features can address the above mentioned issues and can be directly used without a preprocessing step. Some recent research studies have demonstrated the feasibility of such an approach [242; 311].

Nevertheless, the application of texture analysis is still missing in the study of ALS. The need is exacerbated because in contrast to the diseases reviewed in this chapter, the MR images of ALS patients do not demonstrate any visible pathological change that can be detected by the human eye. In the next chapter an overview of ALS and the current medical imaging approaches to study it are given.

Chapter 4

Medical Imaging Applications in Amyotrophic Lateral Sclerosis

4.1 Introduction

ALS is a fatal neurodegenerative disease. The progression of the disease is dramatically rapid and 80% of patients die within two to five years of diagnosis. The disease affects both the central nervous system (CNS) and the peripheral nervous system (PNS). The CNS consists of the brain and spinal cord. The PNS is responsible for transmitting messages between the CNS and the muscles and sensory receptors. The neurons of the CNS and PNS involved in movement are called the upper motor neurons (UMN) and the lower motor neurons (LMN), respectively. Both types of neurons are damaged in ALS.

The main physical examination features related to degeneration of UMNs include loss of dexterity, loss of muscle strength, spasticity, and hyperreflexia. Spasticity can appear as stiffness, slowness, and dexterity can produce awkwardness of skillful movements. Hyperreflexia is the overactive reflexes of muscles. The LMN degeneration signs in ALS include loss of muscle strength, muscle atrophy (reduced bulk), hyporeflexia, muscle hypotonia, fasciculations (involuntary muscle twitching), and muscle cramps.

As ALS progresses, the patients gradually loose their functional abilities. Progressing weakness of the limbs is severely disabling. Patients become increasingly dependent. They eventually are unable to move their limbs and are confined to bed. Many will lose their ability to speak. Many patients will have problem swallowing. Most patients eventually need to be fed by a feeding tube.

Respiratory impairment is the most critical consequence of ALS progression. Depending on the situation, invasive or non-invasive ventilation is eventually required. Most patients with ALS die from respiratory failure, usually within three to five years from the onset of symptoms (with median of 39 months) and only 4% survive longer than 10 years [349].

In addition to the symptoms mentioned above, mild cognitive and behavioral impairment is also observed in up to 50% of patients [371] with frontotemporal dementia in 15% [290].

ALS may begin at any age but it is most often observed in the later decades. The average age of onset is about 66 years [355]. In some cases the ALS is observed within families. As a result, some research studies have been conducted to find genetic disorders in ALS [166; 230; 296]. Nonetheless, familial ALS consists only about 10% of all ALS cases [166].

Unfortunately, no cure has been found for ALS. Riluzole is the only approved disease-modifying medicine for ALS. It can prolong survival by about 3 months [32; 199; 251]. Care of the patient with ALS is complex and requires a multidisciplinary approach with a focus on maintenance of quality of life.

At the moment, the diagnosis of ALS is based on the clinical assessment of UMN and LMN degeneration as mentioned above. The progression of the disease is assessed using the Amyotrophic Lateral Sclerosis Functional Rating Scale-Revised (ALSFRS-R). The ALSFRS-R is a score in the range $[0\ 48]$ representing the general disability of a patient. It is computed by means of a question-naire of 12 questions on daily activities (e.g. speech) and also on specific symptoms (e.g., shortness of breath). Nonetheless, ALSFRS-R does not directly measure the involvement of the UMNs and the LMNs in the disease.

While LMN dysfunction is more evident on examination and can be evaluated objectively by means of electrodiagnostic techniques, the degeneration of UMN cannot be characterized precisely. Another reason is that the manifestation of UMN clinical signs can be affected by severe simulta-neous LMN signs. As a result, there is a need for an objective method to precisely quantify UMN degeneration and cerebral degeneration in general. In this chapter the medical imaging methods used to study ALS are overviewed, in particular, those that study UMN degeneration in ALS.

4.2   Neuropathology of ALS

The nervous system consists of neurons. Neurons are electrically excitable cells transmitting and processing information in the nervous system. A neuron consists of three parts: the soma or cell body, dendrites, and the axon (Figure 4.1). Dendrites are the branched projections of the neuron receiving signals from other neurons. The signal is processed in the soma where the nucleus of the cell is located. Finally, when a signal is fired from the soma, it is transmitted along the axon and to the axon terminal. The signal is sent to a synapse, the junction that is passing the signal to the other neurons by way of chemical neurotransmitters. Axons are protected by a myelin sheath.

Different microscopic pathological impairments are observed in ALS. The most important pro-cess is loss of neurons in the cortex and their projecting axons. There is also injury to glial cells. Glial cells refer to the non-neuronal cells that maintain homeostasis, form myelin, and provide sup-port and protection for the neurons. Proliferation of glial cells in damaged areas of the CNS (known as gliosis) is one of the pathological features in ALS. Axonal swelling or spheroids is also a micro-scopic pathological feature of ALS.

The spatial distribution of CNS degeneration include different parts in the brain and spinal cord.
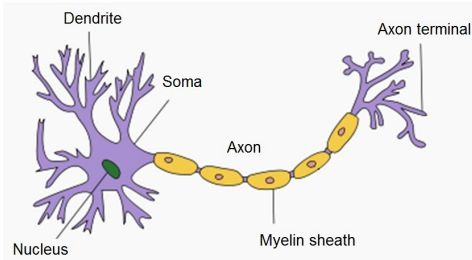
Figure 4.1: A neuron consists of three parts: the soma or cell body where the nucleus of the cell is located, dendrites, and the axon. Signals are received by dendrites, processed in the soma, and sent by the axon. This figure is an edited version of the image from [1].
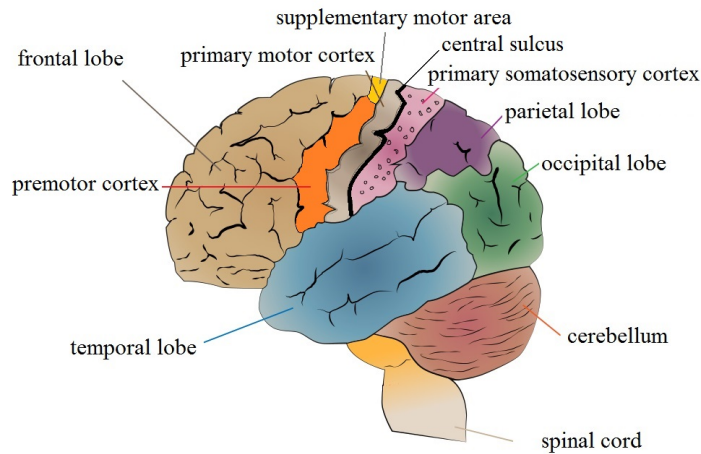
Figure 4.2: Brain consists of four lobes: frontal, temporal, parietal, and occipital. Motor cortex area is located along the central sulcus and consists of primary motor cortex, premotor cortex, supplementary motor area, and primary somatosensory cortex. This figure is an edited version of the image from [3].

There are three important regions considered in UMN degeneration: the motor cortex area, the corticospinal tract (CST), and the spinal cord.

The motor cortex area consists of UMNs and is responsible for planning, control, and execution of voluntary movements. It consists of several parts with overlapping areas (primary motor cortex, premotor cortex, supplementary motor area, and primary somatosensory cortex) located along a fold called the central sulcus. Figure 4.2 illustrates the main four lobes of the brain and the location of the motor cortex area.

In ALS, the number of large motor neurons (known as pyramidal cells) in the cerebral cortex is decreased. The neuronal loss also occurs in the adjacent cortex regions including premotor cortex, somatosensory cortex, and temporal cortex area. Studies show that in ALS the cortical neurons are sparse and damaged, and their dendrites are shortened, disjointed, and disorganized [273]. Accumulation of neurofilaments are also observed in the pyramidal cells. Nonetheless, the accumulations are more frequent in the motor neurons of spinal cord. There are some other pathological features
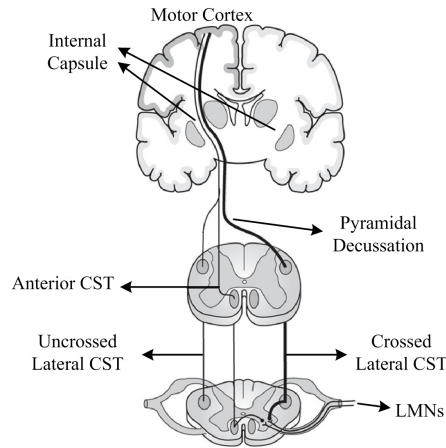
Figure 4.3: The CST pathway. CST connects the motor cortex area to the spinal cord. About 90% of CST fibers cross over to the contralateral side (at pyramidal decussation), going to the lateral CST. CST fibers are very dense in an area in the brain called the internal capsule. This figure is an edited version of the image from [2].
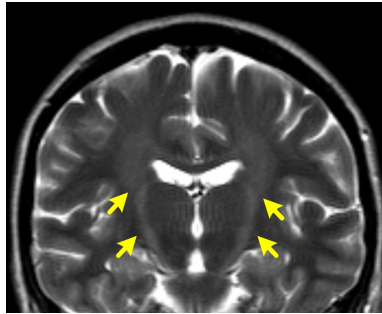
Figure 4.4: The CST fibers are very dense in the internal capsule region. This density can even be vaguely observed in T2-weighted images (yellow arrows).

like glial cell clusters which are not specific in ALS and can be observed in other conditions such as aging or other neurodegenerative diseases.

The next region of interest to study UMN degeneration in ALS is the CST. The CST consists of UMNs, extending from the motor cortex area to the LMNs in the spinal cord. The CST is divided into two separate tracts in the spinal cord: the lateral CST and the anterior CST. Most of the corticospinal fibers (about 90%) cross over to the contralateral side at the pyramidal decussation. These fibers travel in the lateral CST. The rest of the fibers descend uncrossed. Figure 4.3 illustrates the pathway of the CST. This pathway is a potential region to study UMN degeneration. Along this path, there is an interesting region called the internal capsule where the CST fibers converge and thus are very dense. The density can even be vaguely observed in T2-weighted images (Figure 4.4). The CST is damaged in ALS with axonal degeneration and accompanying demyelination. The other pathological changes in CST include spheroids (axonal swelling) in which the neurons contain packed neurofilaments and other cellular debris.

The spinal cord is also a region of interest in ALS and there are pathological changes in this

region [116; 162; 258] which is beyond the scope of this document.

In addition to motor cortex degeneration, other parts of the brain are also relevant for investigation. One very important current research trends is the study of degeneration of the frontal and temporal lobes in the brain known as frontotemporal lobar degeneration (FTLD) [223; 354]. FTLD is associated with cognitive and behavioral impairment. Some examples are behavioral variant, progressive non-fluent aphasia, and semantic dementia. FTLD is observed in about 15% of the patients with ALS [290].

According to many research studies, the CST is not the only region affected by ALS [58; 88; 346]. Therefore, the whole brain is usually analyzed. The next section reviews some of the common imaging methods to study ALS.

4.3 Medical Imaging Methods

A common modality to study brain diseases is MRI. The techniques include conventional structural MRI, diffusion tensor imaging (DTI), functional MRI (fMRI), and magnetic resonance spectroscopy (MRS). The next subsections explain the applications of these methods in ALS.

4.3.1 Structural MRI

Conventional MR images of the brain (T1-weighted, T1-weighted and FLAIR) are used in two ways: qualitative visual assessment, and quantification of brain changes by means of morphometry methods.

By using visual assessment, some studies report intensity changes of MR images in patients with ALS. One of the changes reported by some studies [52; 113; 135] is the increased intensity (hyperintensity) in the CST region in T2-weighted and FLAIR images. Nevertheless, CST hyperintensity does not correlate with clinical symptoms [134]. Moreover, the increased intensity in the CST region have also been observed in healthy subjects and in other diseases [176; 252; 310; 337]. The other change observed by some studies [52; 135; 366] is the decrement in the intensity (hypointensity) of the posterior rim of the precentral gyrus on T2-weighted images. Nonetheless, these changes in intensity are neither sensitive nor specific to the pathology of ALS and the purpose of routine MRI assessment in the neurology clinic is to rule out diseases that mimic ALS [5].

The next important usage of structural MRI is to measure regional atrophy by means of brain morphometry methods. The morphometry methods include voxel based morphometry (VBM), tensor based morphometry (TBM), and surface based morphometry (SBM). The most well known morphometry method used in ALS is VBM [151]. This method performs a voxel-wise comparison between two groups of subjects in the whole brain (WM and GM). The procedure consists of five steps:

1. Spatial normalization,

2. Segmentation,

3. Modulation,

4. Smoothing, and

5. Statistical analysis.

The first step is spatial normalization. The main objective of spatial normalization is to localize regions in a stereotactic space so the corresponding regions can be compared. Different registration methods might be used for this purpose. This step is crucial in VBM, because accurate spatial normalization and segmentation (i.e., the next step) are required such that the differences in the volumes can be attributed to local effects, rather than to artifacts produced due to mis-registration. Nonetheless, there are always some errors in this step. Errors usually happen because the corresponding points are not well defined between the images at a fine spatial scale. For example, many sulci are shared between brains, but this is not the case for all sulci. Therefore, some sulci can be used as corresponding points while others cannot.

In the second step, the images are segmented into the regions of interest, usually, gray matter, white matter, and cerebrospinal fluid. Performing an accurate segmentation is very important and has a significant impact to the final VBM results. If the segmentation is done after spatial normalization, the prior spatial information can be used as a probability map for the regions' location. This idea is used by Ashburner and Friston [151] to develop an iterative algorithm for segmentation based on the prior spatial information.

The spatial normalization step changes the volumes of brain regions because some regions grow and some shrink. To preserve the actual amounts of each region within each voxel the modulation step is performed. In this step, the partitioned images are multiplied (modulated) by the relative voxel volumes before and after spatial normalization. The relative volumes are computed using the Jacobian determinant of the images. If a point in a 3D space, $p_1(x_1, y_1, z_1)$ is mapped to $p_2(x_2, y_2, z_2)$, the Jacobian is defined as the derivative of the elements of p_1 with respect to the elements of p_2:

$$J = \begin{bmatrix} \frac{\partial x_1}{\partial x_2} & \frac{\partial x_1}{\partial y_2} & \frac{\partial x_1}{\partial z_2} \\ \frac{\partial y_1}{\partial x_2} & \frac{\partial y_1}{\partial y_2} & \frac{\partial y_1}{\partial z_2} \\ \frac{\partial z_1}{\partial x_2} & \frac{\partial z_1}{\partial y_2} & \frac{\partial z_1}{\partial z_2} \end{bmatrix}. \tag{4.1}$$

In the next step a smoothing filter is applied to the 3D image. As a result, the voxel intensity values smoothly change between neighboring voxels. The objective is to remove noise and the fine-scale structures that are not present among subjects. Indeed, by smoothing, one increases the sensitivity of VBM to differences that are expressed in a larger spatial scale.

In the final step, a statistical analysis is performed. The general linear model (GLM) is used to find the regions that are significantly different among the groups of subjects. The result of this step is called the statistical parametric map (SPM) showing significant regional effects.

VBM is one of the popular approaches to study ALS. Chang et al. [47] use VBM on T1-weighted MR images to show that patients with ALS and ALS/FTLD (ALS associated with frontotemporal lobar degeneration) have widespread gray matter atrophy in frontotemporal regions. They claim that the main regions affected are the motor and premotor cortices, and the anterior portion of the superior frontal gyrus. With a similar approach, Grosskreutz et al. [119] found in the precentral and postcentral gyri bilaterally. In recent years, VBM has been widely used by different research groups to study ALS including the works of Agosta et al. [8], Grosskreutz et al. [120], Chen and Ma [51], Senda et al. [315], and Tsujimoto et al. [347].

Nonetheless, VBM have some limitations. For instance, the accuracy of registration and segmentation can highly affect the VBM results. Consequently, any small error in registration or segmentation changes the final result. Moreover, the parametric statistical tests assumes that the data is normally distributed. Therefore, if the behavior of the data is not known, this assumption will be violated.

The next morphometry method used to study ALS is TBM [24]. The TBM method is based on the Jacobian matrix defined in Eq. 4.1. TBM is different from VBM in that it compares the rate of volume change. This rate of volume change is more reliable than absolute deformation value used by VBM. The reason is that the absolute deformation represents positions of brain structures, rather than local shape. Consequently, the absolute deformation should be quantified relative to some arbitrary reference position which needs registration. However, the rate of change captured by the Jacobian matrix provides information about the local changes (e.g., stretching, contractions) involved in the deformation and does not need registration. In a simple form of TBM, the relative rate of volume changes of different brain structures are compared using univariate statistics (t- or F-test) [23]. While the univariate statistics shows whether growth or volume loss has occurred, multi-variate statistics can provide more useful information such as any difference among lengths, areas and the amount of change. As a result, multi-variate statistics is used when the nature of changes is unknown.

TBM is used in the work of Agosta et al. [6] on T1-weighted MRI. The study shows gray matter atrophy in the left premotor cortex and the right basal ganglia in ALS patients compared to controls. It also reports atrophy in the motor cortical area, the left caudate, and the right putamen in patients with rapidly progressive ALS in comparison with patients with non-rapidly progressive ALS and controls. TBM per se is not as popular as VBM and has not been widely used to study ALS. Indeed, TBM is employed in the third step of VBM (modulation) to make VBM more accurate.

The main disadvantage of the above mentioned methods is that they disregard gyral and sulcal anatomical boundaries. As a result, these methods are not sensitive to detect subtle cortical differences. To address this problem SBM [89] is proposed. In SBM, the cortical surface is first segmented from the images. By using surface convexity and curvature features extracted from the cortical surface the gyral anatomy is registered to a standard spherical template [69; 89; 90]. This

procedure transfers the cortical surface into a stereotactic space in which the statistical comparisons between brains is possible. The studies that use SBM report cortical thinning in the precentral gyrus in patients with ALS. Some recent examples of SBM studies include the works of Roccatagliata et al. [293], and Verstraete et al. [359]. In their recent study, Agosta et al. [9] demonstrate widespread areas of cortical thinning including the primary motor, the prefrontal and ventral frontal cortices, the cingulate gyrus, insula, the superior and inferior temporal and parietal regions, and the medial and lateral occipital areas. Nonetheless, SBM is designed for estimation of cortical thickness.

4.3.2 Diffusion Tensor Imaging

A well-known MRI technique, DTI, is based on molecular diffusion of water. Molecular diffusion refers to the random motion of molecules (also known as Brownian motion). This random motion is caused by the thermal energy carried by these molecules and can give us important information about the microscopic structures of tissues. DTI captures the Brownian motion of water molecules due to its large concentration in brain tissue. During a typical diffusion time of about 50 milliseconds, water molecules move about 10 micrometers. Using statistical analysis the movement distribution of the water molecules can be found. This movement distribution provides valuable information about the structure and geometric organization of the tissues at a microscopic scale. Specifically, it gives us information about myelinated axonal fibers running in parallel because diffusion in the direction of the fibers is faster than in the perpendicular direction. This characteristic is used to map the orientation of the white matter fibers in the brain. When an abnormality occurs, it changes the normal direction of diffusion which can be detected in DTI.

The diffusion process in an isotropic medium is expressed by the diffusion coefficient D [82],

$$D = \frac{1}{6\tau} < RR^T >, \tag{4.2}$$

where R is the displacement vector, τ is the diffusion time, T is the transposition operator, and $< >$ denotes the averaging operator. The effect of diffusion on the MRI appears as attenuation, A, in the MRI signal [34]:

$$A = exp(-bD), \tag{4.3}$$

where b is a parameter characterized by the timing, amplitude, and shape of the gradient pulses in the MRI sequence.

To use DTI for image analysis, an anisotropic version of the diffusion process is needed. The diffusion coefficient, D, is defined as a tensor describing a molecule's motion along each direction (x, y, z) and the correlation between the directions [34]:

$$D = \begin{bmatrix} D_{xx} & D_{xy} & D_{xz} \\ D_{yx} & D_{yy} & D_{yz} \\ D_{zx} & D_{zy} & D_{zz} \end{bmatrix}. \tag{4.4}$$

Here, the attenuation effect appears as:

$$A = exp(- \sum_{i=x,y,z} \sum_{j=x,y,z} b_{ij} D_{ij}). \tag{4.5}$$

where the elements of matrix b are characterized by the same properties of the gradient pulses in the MRI sequence mentioned before. This equation is used to estimate D. To perform the estimation, at least six independent measurements associated with six directions are required. In addition one image is acquired without diffusion weighting ($b = 0$). In practice, images can be acquired in more directions to improve the estimation. The classical method of DTI uses the least squares technique to approximate D from the set of acquired images. This approximation gives a 3D image with 6 parameters describing the local tensor D at each voxel. A diffusion tensor D can be decomposed to its eigenvalues ($\lambda_1, \lambda_2, \lambda_3$) where $\lambda_1 \geq \lambda_2 \geq \lambda_3$ and eigenvectors (e_1, e_2, e_3). The eigenvectors represent the direction of diffusion and the eigenvalues reflect the amount of diffusion in each direction. The popular measurements on DTI are Mean Diffusivity (MD), Fractional Anisotropy (FA), and Relative Anisotropy (RA).

MD representing a directionless average measure of the diffusion rate is defined as:

$$MD = \frac{\lambda_1 + \lambda_2 + \lambda_3}{3}. \tag{4.6}$$

FA is the measurement of the directionality of diffusion and is defined as

$$FA = \sqrt{\frac{3}{2}} \sqrt{\frac{(\lambda_1 - MD)^2 + (\lambda_2 - MD)^2 + (\lambda_3 - MD)^2}{\lambda_1^{\,2} + \lambda_2^{\,2} + \lambda_3^{\,2}}}. \tag{4.7}$$

RA shows the ratio of the anisotropic part of the tensor to its isotropic part and is computed as

$$RA = \sqrt{\frac{(\lambda_1 - MD)^2 + (\lambda_2 - MD)^2 + (\lambda_3 - MD)^2}{3MD}}. \tag{4.8}$$

By following the tensors that reveal a large value in a specific direction, fiber tracts can be revealed and constructed. This approach called tractography is used to visually represent neural tracts.

DTI has been widely used, particularly in recent years, to study white matter degeneration in ALS. Sage et al. [304] show that changes in diffusion parameters occur throughout the brain, including the frontal, the temporal and the parietal lobes. Using fiber tracking analysis, they also observed that the CST is impaired in ALS patients. The CST degeneration was also observed by Wong et al. [159] reporting decreased FA and increased MD in the CST. The decreased value of FA in the CST has also been reported by Iwata et al. [150]. Zhang et al. [405] show that the FA decrement is related to disease progression by doing a longitudinal analysis of DTI data. Some other recent DTI studies related to ALS include but are not limited to the works of Nair et al. [258], Prudlo et al. [279], Sage et al. [303], Agosta et al. [7], and Canu et al. [43].

Nevertheless, DTI suffers from some limitations. The main issues of DTI are the partial volume effect (i.e., diffusion characteristics measured by DTI is influenced by the volume of brain structures) [361] and the problem of DTI to model non-Gaussian diffusions [25].

45

4.3.3 Functional MRI

Functional MRI (fMRI) is an MRI technique that measures regional cortical activation of the brain. Activation is detected by assessing changes in blood flow (e.g., using the blood oxygen level dependent (BOLD) contrast). In this approach, the subject is asked to do a task and the activity of the brain in response to that specific task is measured.

Konarl et al. [188] demonstrate that the activation pattern in ALS patients is different to that in healthy controls by using fMRI and asking subjects to perform a finger flexion task. In the study conducted by Schoenfeld et al. [314], the subjects press buttons with two simple and difficult sequences. They observe activity in ipsilateral motor areas, and difficulty-related activity in the left cerebellum of the ALS patients. They conclude that ALS patients use additional brain regions compared to healthy controls to perform a motor task as brain activation was observed outside the motor area. Increased activation of the contralateral sensorimotor cortex and the supplementary motor area in ALS patients have been reported by Konradet et al. [189], and Stanton et al. [326]. In regards to functional changes related to cognitive impairment, Abrahams et al. [4] show that there is impaired activation in the middle and inferior frontal gyri, the anterior cingulate gyrus, and regions of the parietal and temporal lobes during verbal fluency task in ALS patients.

Since controlling task performance is difficult for patients with cortical motor impairments, the concept of *functional connectivity* is noticed in recent studies. The idea is that different brain regions that are functionally connected can be considered as a network. These regions can be found during a rest state (while the subject is instructed not to perform any physical or mental task) by their spontaneous coherent fluctuations of the BOLD signal (i.e., resting state imaging technique) [253]. With this method, ALS can be investigated as a system failure of interconnected networks as suggested by Turner et al. [348]. This method is recently used by Mohammadi et al. [253] to study the changes of resting state brain networks in ALS. With a dataset of 20 healthy controls and 20 ALS patients, they find significant differences between the two groups in two networks: the default-mode and the sensorimotor networks. The default-mode network includes the ventral anterior cingulate cortex, the medial prefrontal cortex, the orbitofrontal cortex, the posterior cingulate cortex, the inferior parietal cortex, and the parahippocampal gyrus. The sensorimotor network consists of the primary motor cortex, the anterior part of the cingulate cortex, the somatosensory region, and the auditory cortex.

Another recent trend is to use fMRI along with structural MRI to study motor network degeneration. Some examples include the works of Verstraete et al. [358], Douaud et al. [78], and Cosottini et al. [62].

Nonetheless, fMRI is limited to finding alterations of cortical regions by detecting functional impairment and does not reveal the pathology related to the structural changes occurring in the whole brain.

4.3.4 Magnetic Resonance Spectroscopy

MRS is a specialized MRI technique used to measure tissue metabolites. Similar to MRI it uses signals from hydrogen protons; however in contrast to standard MRI that uses the signal information to create images from water-containing protons, MRS uses the signal information to quantify metabolites other than water. The main metabolites measured in MRS in neuropsychiatry are N-acetylaspartate (NAA), creatine (Cr), myo-inositol (Ins), and choline (Cho). Both the concentration of the metabolites and the ratio between them (e.g., NAA/Cr) are reported.

Pioro et al. [276] were among the first who used MRS to study ALS. Based on this study, ALS patients have a significant decrease of the NAA/Cr ratio in the motor cortex ($p < 0.001$), and in the primary sensory region ($p < 0.01$), as well as in the posterior premotor and the parietal regions ($p < 0.05$). In another study [277], they investigate metabolite changes in the brainstem, reporting decreased levels of NAx (N-acetylaspartate and N-acetylaspartylglutamate) and increased Glx (glutamate and glutamine) in the medulla. Cwik et al. [68] also report a reduction of the NA/Cr ratio in the pons and upper medulla. A large number of studies have been conducted in the primary motor cortex area. Gredal et al. [118] report a significantly decreased concentration of NAA in the primary motor cortex of ALS patients. The work of Wang et al. [363], corroborate the decrement of NAA/Cr and NAA/Cho in this area in ALS patients. This study also reports a correlation between the NAA/Cr ratio and the ALSFRS scores ($p < 0.05$). The study of Sarchielli et al. [308] demonstrates significantly lower concentration of NAA in the precentral gyrus of ALS patients; however, it does not find a correlation between this decrement and the ALSFRS scores. Kalra et al. [172] report a decrease in NAA/Ins ($p < 0.001$), NAA/Cr ($p < 0.04$), and NAA/Cho ($p < 0.05$), and an increase in Ins/Cr ($p < 0.04$) in the cerebral cortex of patients with ALS.

There are some longitudinal MRS studies to investigate if the change of metabolites occurs longitudinally in the disease. For instance, Pohl et al. [278] find a significant drop in the NAA/Cho ratio ($p < 0.01$) and a significant increase ($p < 0.01$) in the Cho/Cr ratio in the primary motor cortex in ALS patients during a period of 12.1 ± 8.7 months. In a longitudinal study by Suhy et al. [330], ALS patients are scanned after 1 month and 3 months following the initial acquisition. The study reports a decline in NAA, Cr, and Cho concentrations in the motor cortex region; however, no statistical change is observed in non motor regions in ALS patients.

MRS has also been used to investigate the effect of the potential drugs to retard the progression of ALS. Kalra et al. [171] find that the NAA/Cr ratio is decreased in the precentral and the postcentral gyri of patients with ALS. Whereas, in another study [173] using this approach, they report an improvement in the cortical metabolic function in the motor cortex area early after riluzole treatment evidenced by an increase in NAA/Cr.

Some recent studies of MRS in ALS include the works of Pyra et al. [281], Sudharshan et al. [329], and Usman et al. [353]. Pyra et al. [281] demonstrate that the ratio of NAA/Cho and of NAA/Cr are reduced in corona radiata and precentral gyrus. This finding indicates the degeneration

of the CST in ALS patients. Sudharshan et al. [329] report the degeneration of the mid cingulate cortex. Finally, Usman et al. [353] find that the medial prefrontal cortex is damaged in patients with ALS by the finding of reduced NAA/Ins ratio.

Nonetheless, MRS has some restrictions and disadvantages. The main disadvantage of MRS is the intrinsic insensitivity of the method. The signals recorded by MRS are small due to the low concentrations of the target metabolites. This tends to results in relatively high variability in the measures, and low resolution. Moreover, MRS is a complicated acquisition technique which limits its usage.

4.4 Summary

In this chapter different imaging methods used to study ALS have been reviewed. These methods can be categorized into four classes based on the imaging modality that they use: structural MRI, DTI, fMRI, and MRS. Structural MRI are used for two purposes, to rule out the diseases that mimic ALS, and to study the structural changes of the brain using different morphometry methods such as VBM, TBM, and SBM. VBM and TBM methods are not robust and SBM can be used only for cortical thickness measurements. DTI is used to find those parts of the brain that reveal abnormal diffusivity to probe white matter integrity. The main parameters used to characterize diffusivity are FA and MD. The limitations of DTI are the partial volume effect and modeling of non-Gaussian diffusions. The fMRI methods are used to find functional abnormalities in ALS and do not show the structural changes. Finally, MRS methods quantify tissue metabolites. The complicated acquisition procedure and the insensitivity of the method are the limitations of MRS. While the current methods provide promise in exploring the ALS pathology and each have their roles in evaluating cerebral degeneration, there is still a great need for more sensitive techniques that can objectively quantify UMN degeneration and cerebral degeneration in ALS.

Nonetheless, the ability of texture analysis has not been explored to study ALS. Texture analysis methods have been successfully used in different research fields and shown promise in medical image analysis. Several studies have shown that texture features are very discriminative and helpful to detect and monitor different diseases including but not limited to brain tumors, epilepsy, MS, and AD. In addition, as mentioned before in Section 3.6, texture features, in particular, the invariant ones, show robustness to the acquisition parameters of MRI and can address the main issues in MR imaging. Hence, developing texture analysis methods to study cerebral degeneration in ALS may fill the current gap in this field. The ability to accurately quantify cerebral disease will assist with making an accurate diagnosis quicker and with the evaluation of novel treatments. It could also improve our understanding of the disease and its pathology. Robust texture methods could also be used in other neurodegenerative diseases as well as in other non-medical applications. In the next chapter, the proposed work is presented with the current status of the research.

Chapter 5

Voxel-based Texture Analysis of the Brain

5.1 Introduction

As mentioned before in Chapter 3, texture analysis methods have been successfully used to study several brain neurological diseases including brain tumour, epilepsy, Alzheimer's disease, and multiple sclerosis. Robustness to MRI acquisition parameters makes texture analysis a reliable and attractive tool for investigation of neuropsychiatric conditions. Nonetheless, the current texture analysis methods are defined for a region of interest (ROI). This is a limiting factor particularly in brain image analysis, because it requires *a priori* hypotheses directing the analysis to specific regions.

An alternative approach to ROI analysis is the hypothesis free method in which regions with significant statistical differences are automatically detected between groups. One of the most popular examples of this type of analysis is the voxel based morphometry (VBM) [21] in brain imaging. VBM performs a voxel-by-voxel statistical analysis on gray matter (GM) or white matter (WM) density.

Inspired by VBM, a novel method to perform voxel-based texture analysis in brain images is presented in this chapter. The output of the proposed method is a statistical map, similar to that of the VBM, indicating regions with statistically significant differences. However, a texture feature, instead of the amount of GM or WM, is compared at each voxel. In Section 5.2 the proposed methods are presented. The evaluation is explained in Section 5.3. Finally, the summary of this chapter is given.

5.2 Voxel-based Texture Analysis Methods

In this section the voxel-based texture analysis methods are presented. The processing pipeline of the proposed method includes three main parts: pre-processing, texture feature computation, and voxel-based statistical analysis (Figure 5.1). The first and the last parts have been provided by several brain image analysis tools. The second part is the core of the proposed method and has been developed
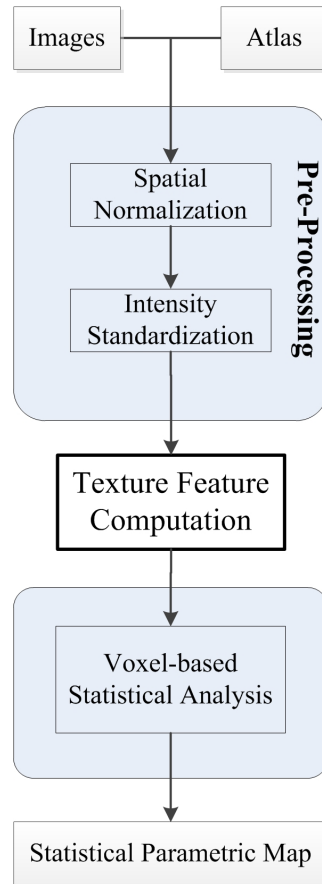
Figure 5.1: The processing pipeline of the voxel-based texture analysis method.

as a toolbox which can be easily integrated with other brain analysis tools easily (Appendix A). The next subsections explain each part in details.

5.2.1 Pre-Processing

The pre-processing part of the pipeline includes two main steps. The first step is to normalize (register) images with a template atlas. The second step of preprocessing is correcting non-uniformity variations and intensity standardization which makes the intensity of the images between subjects comparable. The preprocessing step is performed using the VBM8 toolbox (http://dbm.neuro.uni-jena.de/vbm/) with default parameters. The VBM8 toolbox is an extension of the unified segmentation model [22] using the high-dimensional DARTEL procedure [20] to normalize images to the MNI152 atlas.

The proposed methods in this section are the extensions of the 2D gray level co-occurrence matrix (GLCM) method [131] such that the texture features are computed in a voxel-by-voxel basis in 3D images.

5.2.2 VGLCM-3D

Suppose that a 2D image I with a length of N_x and a width of N_y has N_g gray level values (i.e., intensities of the image range 1 to G). The image I is represented as a function mapping the spatial domain to the gray values:

$$I : L_y \times L_x \to G, \tag{5.1}$$

where $L_y = \{1, ..., N_y\}$ denotes the spatial domain along the y axis, $L_x = \{1, ..., N_x\}$ the spatial domain along the x axis, and $G = \{1, ..., N_g\}$ the gray values. Here, the Haralik et al. notation [131] is followed which assigns the y axis to the first dimension.

On a 2D plane, an offset with distance d and direction angle θ is represented by $O = [a, b] = [d\sin(\theta), d\cos(\theta)]$ connecting pixel $I(k, l)$ to pixel $I(m, n)$ such that $m = k + a$ and $n = l + b$. For instance, an offset with distance of 1 and angle of $90°$ increases m by 1 and n by 0 (or offsets them from the original position with $[1, 0]$). $GLCM_O$ is defined for the specific offset $O = [a, b]$ as follows:

$$GLCM_O(i, j) = \#\Big\{ ((k, l), (m, n)) \in (L_y \times L_x) \times (L_y \times L_x)|$$
$$m = k + a, n = l + b, I(k, l) = i, I(m, n) = j \Big\}. \tag{5.2}$$

In other words, the GLCM for a specific offset is an $N_g \times N_g$ matrix where the entry (i, j) shows the number of times that $I(k, l) = i$ and $I(m, n) = j$. GLCM is easily expandable to 3D by considering offsets in a 3D space [196]. Formally, a 3D image with G gray levels is defined as:

$$I : L_y \times L_x \times L_z \to G, \tag{5.3}$$

where $L_z = \{1, ..., N_y\}$ denotes the spatial domain along the z axis. In the traditional GLCM, the texture features are computed for a region of interest while the goal of the proposed method is to find texture features at each voxel. To do this, a spherical volume of radius R is considered around each voxel. Formally, the voxel-based GLCM in 3D ("VGLCM-3D") is defined for a specific neighborhood of radius R, and offset $O = [a, b, c]$ for the voxel V located at (V_y, V_x, V_z):

$$VGLCM\text{-}3D_{R,O}(i, j) = \#\Big\{ ((k, l, u), (m, n, v)) \in$$
$$S^R(V_y, V_x, V_z) \times S^R(V_y, V_x, V_z)|$$
$$m = k + a, n = l + b, v = u + c,$$
$$I(k, l, u) = i, I(m, n, v) = j \Big\}, \tag{5.4}$$

where $S^R(V_y, V_x, V_z)$ denotes the neighborhood region with a radius of R around the voxel:

$$S^R(V_y, V_x, V_z) = \Big\{ (y, x, z)|y = \{1, ..., N_y\}, x = \{1, ..., N_x\}, z = \{1, ..., N_z\}$$
$$\sqrt{(y - V_y)^2 + (x - V_x)^2 + (z - V_z)^2} \leq R \Big\}. \tag{5.5}$$

After computing the co-occurrence matrices for all offsets, the GLCMs are summed over all offsets and normalized (i.e., divided by the sum):

$$VGLCM\text{-}3D_R^{sum}(i,j) = \sum_{\forall O} VGLCM\text{-}3D_{R,O}(i,j) \qquad (5.6)$$

$$VGLCM\text{-}3D_R^{norm}(i,j) = \frac{VGLCM\text{-}3D_R^{sum}(i,j)}{\sum_1^G \sum_1^G VGLCM\text{-}3D_R^{sum}(i,j)} \qquad (5.7)$$

In this thesis, eight texture features are computed for analysis (f_1 to f_8 from Table 2.1). Additional texture features can also be computed. Nonetheless, these eight features are enough to show their capability in texture analysis.

5.2.3 VGLCM-TOP-3D

It is notable that the computational expense of 3D analysis increases rapidly as distance d increases. For a distance of d, there are $(2d+1)2-1$ offsets in 2D and $(2d+1)3-1$ offsets in 3D. For example, for a distance of 1 there are 8 possible offsets in 2D (i.e., [-1,-1],[-1,0],...,[1,1]) but 26 offsets in 3D (i.e., [-1,-1,-1],[-1,-1,0],...,[1,1,1]). For a distance of 2, there are 24 offsets in 2D but 124 offsets in 3D. To alleviate the computational expense, in addition to the voxel-based GLCM on 3D space ("VGLCM-3D"), a less computationally-expensive approach called voxel-based GLCM on three orthogonal planes in 3D space ("VGLCM-TOP-3D") is proposed. Herein GLCM is computed individually in the axial, coronal, and sagittal planes at each voxel and the final feature value is the average of these 3 texture values in the three planes. Using this approach there are $3 \times ((2d+1)2-1)$ offsets for computation. For instance, this approach uses 24 offsets for a distance of 1 and 72 offsets for a distance of 2 (compared to 26 and 124 for VGLCM-3D), reducing the number of offsets particularly for large distances. Denote the z axis as the up-down direction, x axis the left-right direction, and y axis the anterior-posterior direction in an MRI image. The axial, sagittal, and coronal planes are defined as:

$$I_{axi}(k,l,u) = \big\{ I(y,x,z) | y = \{1,...,N_y\}, x = \{1,...,N_x\}, z = u \big\}, \qquad (5.8)$$

$$I_{sag}(k,l,u) = \big\{ I(y,x,z) | y = \{1,...,N_y\}, z = \{1,...,N_z\}, x = l \big\}, \qquad (5.9)$$

$$I_{cor}(k,l,u) = \big\{ I(y,x,z) | x = \{1,...,N_x\}, z = \{1,...,N_z\}, y = k \big\}, \qquad (5.10)$$

where $u = 1,...,N_z$, $l = 1,...,N_x$, and $k = 1,...,N_y$ denote the location of the slice in the axial, sagittal, and coronal views, respectively. The voxel-based GLCM on three orthogonal planes in 3D ("VGLCM-TOP-3D") is defined for a specific plane P with a neighborhood radius of R and offset

$O = [a, b, c]$ for voxel V located at (V_y, V_x, V_z):

$$VGLCM\text{-}TOP\text{-}3D_{P,R,O}(i,j) = \#\Big\{ ((k,l,u),(m,n,v)) \in$$
$$S_P^R(V_y, V_x, V_z) \times S_P^R(V_y, V_x, V_z)|$$
$$m = k + a, n = l + b, v = u + c,$$
$$I_P(k,l,u) = i, I_P(m,n,v) = j\Big\}, \qquad (5.11)$$

where I_P is defined by Eqs. 5.8, 5.9, and 5.10, and S_P^R is defined for the axial, sagittal, and coronal planes, respectively:

$$S_{axi}^R(V_y, V_x, V_z) = \Big\{ (y,x,z)|y = \{1,...,N_y\}, x = \{1,...,N_x\}, z = u$$
$$\sqrt{(y - V_y)^2 + (x - V_x)^2} \leq R\Big\}, \qquad (5.12)$$

$$S_{sag}^R(V_y, V_x, V_z) = \Big\{ (y,x,z)|y = \{1,...,N_y\}, z = \{1,...,N_z\}, x = l$$
$$\sqrt{(y - V_y)^2 + (z - V_z)^2} \leq R\Big\}, \qquad (5.13)$$

$$S_{cor}^R(V_y, V_x, V_z) = \Big\{ (y,x,z)|x = \{1,...,N_x\}, z = \{1,...,N_z\}, y = k$$
$$\sqrt{(x - V_x)^2 + (z - V_z)^2} \leq R\Big\}, \qquad (5.14)$$

Similar to VGLCM-3D, the VGLCM-TOP-3D obtained for each plane is summed over all offsets and normalized. Now, at each voxel three GLCMs have been computed corresponding to the axial, sagittal, and coronal planes (i.e., $VGLCM\text{-}TOP\text{-}3D_{axi,R,O}$, $VGLCM\text{-}TOP\text{-}3D_{sag,R,O}$, and $VGLCM\text{-}TOP\text{-}3D_{cor,R,O}$). In this step the actual texture feature is separately computed for each plane. Finally, each texture feature is obtained as the average of that feature computed in the axial, sagittal, and coronal GLCMs. This process is illustrated in Figure 5.2.

The results of texture feature computation can be visualized as texture maps. Samples of these texture maps are shown in Figure 5.3. The texture maps are subsequently used in a voxel-based statistical analysis explained in the next section.

5.2.4 The Space for Computing Features

There are two spaces to compute the features: the original space and the stereotaxic space (i.e., atlas). Indeed, registration imposes some errors in the processing procedures. Even if the registration is ideal the interpolation used to compute the values in the stereotaxic space produces some errors. These errors are inevitable, however, they can occur before or after computing texture features.

In the first approach, texture features are computed in the original space. As a result, the textures are computed with no registration error. However, when the textures are mapped into the stereotaxic space the registration errors are added to the final texture values.

In the second approach, the image is first mapped into the stereotaxic space. As a result, the registration errors are included in the image intensities. Then the textures are computed from these inaccurate values. Figure 5.4 illustrates the two approaches. In Section 5.3, these two approaches are compared.
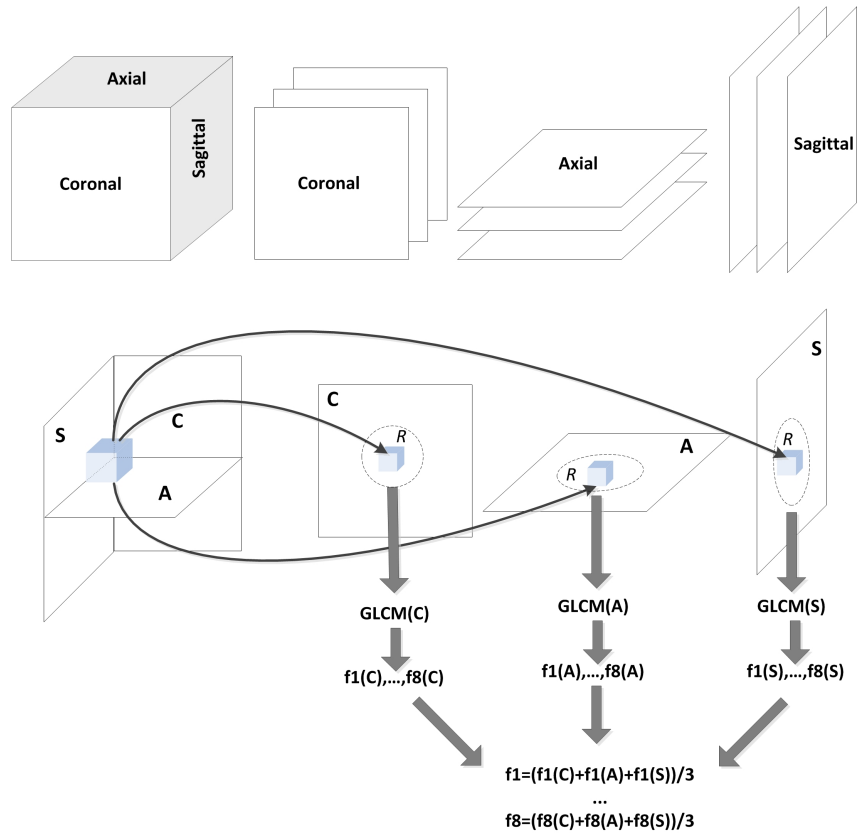
Figure 5.2: Derivation of VGLCM-TOP-3D texture features. Analysis for a voxel is performed in 3 orthogonal planes: Coronal (C), Axial (A), and Sagittal (S). Texture features (f_1,...,f_8) are computed within a circle with radius R in each plane (GLCM(C), GLCM(A), GLCM(S)). The final texture is the average of the 3 local textures in each plane.

5.2.5   Statistical Analysis

In this step, each voxel undergoes statistical analysis. Statistical analysis is possible because in the preprocessing step all 3D images are registered to the same steroetaxic space. As a result, a voxel located at (x,y,z) corresponds to the same location in the brain for all subjects. SPM8 software is used to perform the voxel-by-voxel statistical analysis using the texture features computed in the previous section. The F-test is used to produce statistical parametric maps. The F-test is chosen instead of the t-test because texture features of the patient group could have higher or lower values compared to that of the healthy subjects.

Since statistical analysis is applied to millions of voxels, correction for multiple comparisons is required to reduce the occurrence of false positives. There are several methods to perform such a correction. The most commons are the family-wise error (FWE) correction [95] and the false discovery rate (FDR) correction [106]. The FWE correction controls the chance of any false positives (as in Bonferroni methods) across the entire volume, while the FDR correction controls the expected proportion of incorrectly rejected null hypotheses (a.k.a., false positives or type I errors) in
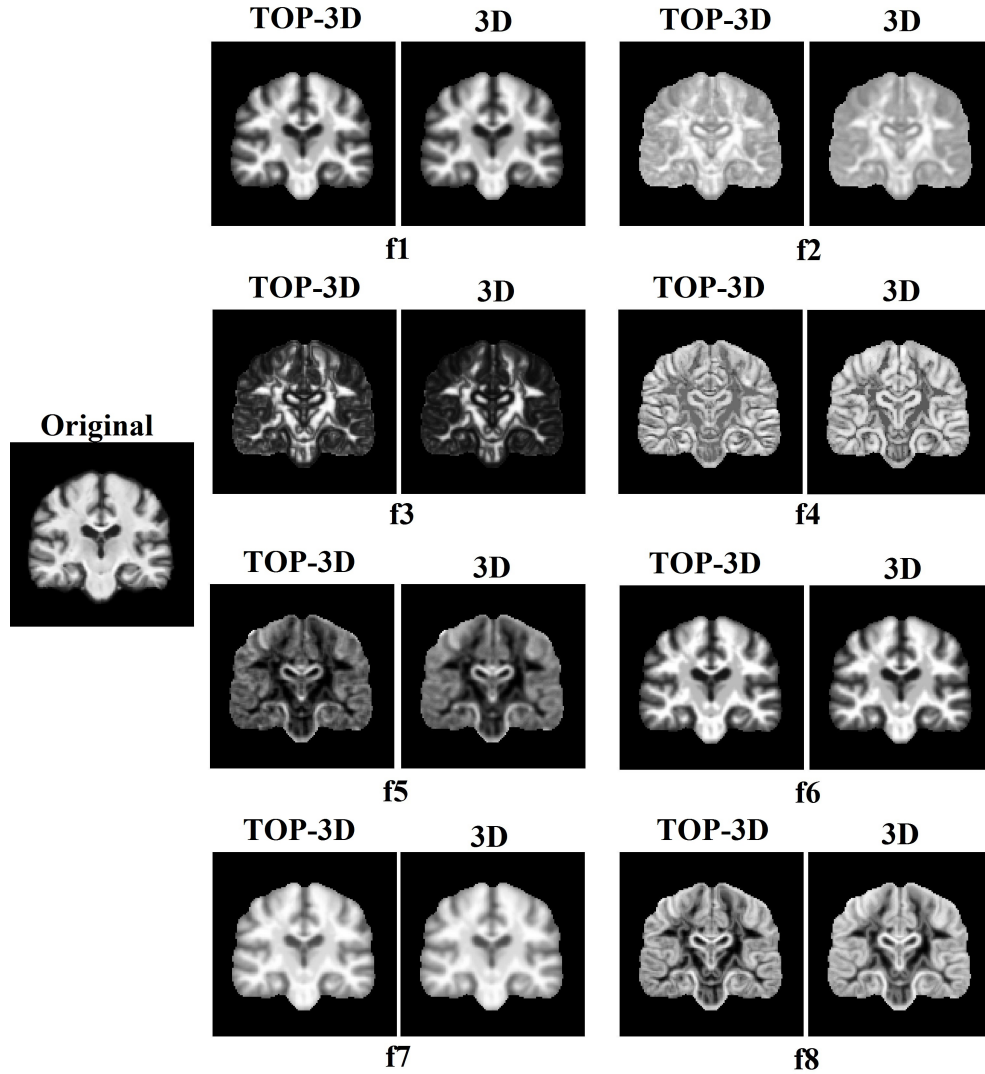
Figure 5.3: Example of texture features computed by VGLCM-TOP-3D and VGLCM-3D shown on a sample coronal image: autocorrelation (f1), homogeneity (f2), energy (f3), correlation (f4), dissimilarity (f5), sum of squares: variance (f6), sum average (f7), and sum entropy (f8).

a list of rejected hypotheses. In other words, FWE tries to reduce the probability of even one false discovery, as opposed to the expected proportion of false discoveries. Thus, FDR procedures have greater power at the cost of increased rates of false positive errors. For this analysis, the more lenient correction, FDR with $p < 0.05$ is used.

5.3 Evaluation

In this section the evaluation of the proposed voxel-based texture analysis method is explained. First, the descriptions of datasets are described. Then, the metrics used for the evaluation are described. Finally, the results are shown and discussed in the subsequent sections.
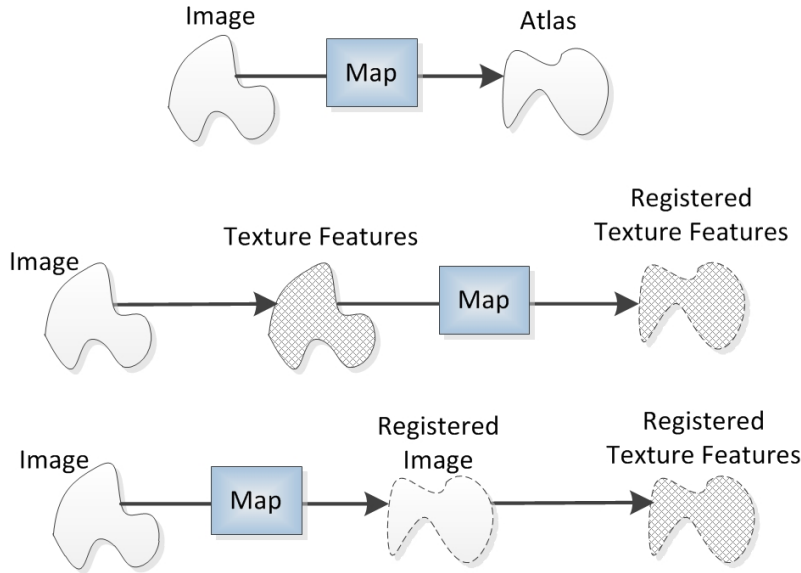
Figure 5.4: There are two spaces to compute the features: the original space and the stereotaxic space. In the first approach, the registration map is applied to the textures computed in the original space. In the second approach, the image is first mapped to the stereotaxic space and then the texture features are computed. The registration errors are represented by dashed line. The textures are shown by cross-hatching.

5.3.1 Datasets

To examine the validity of the proposed methods, two different approaches are used. First, an MRI dataset with artificial effects is generated. Second, a dataset of healthy subjects and patients with Alzheimer's disease (AD) is used. AD is chosen because the spatial distribution of pathological changes in the brain is well known in this disease. Both datasets are derived from the OASIS database [240] (http://www.oasis-brains.org) which includes a collection of 416 right handed healthy controls and patients with early-stage AD and accompanying 3D T1-weighted magnetization prepared rapid gradient echo (MPRAGE) images acquired at 1.5 Tesla (repetition time=9.7 ms, echo time=4.0 ms, inversion time=20 ms, flip angle=$10°$, orientation=sagittal, and resolution = 1.0×1.0 mm^2, slice thickness=1.25 mm). Subjects from this database with a diagnosis of mild (Clinical Dementia Rating, CDR=1) or moderate (CDR=2) AD are selected (total number of 30) for our analysis. Twenty of these subjects are female, 10 are male, and the average age is 78 years. A group of healthy control subjects from the OASIS database are selected that are matched for age and gender of the subjects with AD. A database of artificial effects is created as the ground truth to validate the proposed method. MRIs from the selected healthy control subjects are used for this purpose. Eight types of artifacts are added which include hyper-intense and hypo-intense Gaussian signals with varying size and properties. The specification of each type is given in Table 5.1.

For each type of artifact, 60 locations in the brain are chosen (30 in each hemisphere). Figure 5.5 illustrates the location of the signals. The locations include regions with pure GM, pure WM and

Table 5.1: Specifications of the artificial effects.

Type	Hypo/Hyper-Intense	Size	Mean of Gaussian	STD of Gaussian
I	Hypo-intense	$3 \times 3 \times 3$	200	50
II	Hyper-intense	$3 \times 3 \times 3$	200	50
III	Hypo-intense	$3 \times 3 \times 3$	400	50
IV	Hyper-intense	$3 \times 3 \times 3$	400	50
V	Hypo-intense	$4 \times 4 \times 4$	200	50
VI	Hyper-intense	$4 \times 4 \times 4$	200	50
VII	Hypo-intense	$4 \times 4 \times 4$	400	50
VIII	Hyper-intense	$4 \times 4 \times 4$	400	50
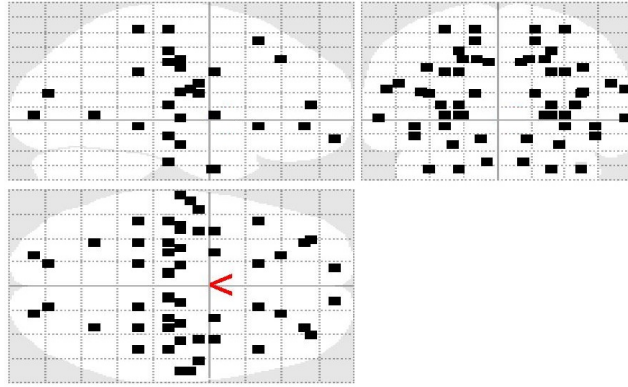
Figure 5.5: The location of artificial lesions.
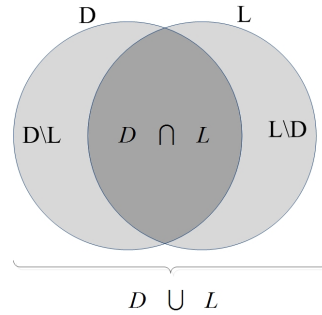
Figure 5.6: Schematic Venn diagram illustrating different possible regions considered for a detected region and an artificial lesion.

mixed GM/WM (border of GM/WM).

5.3.2 Evaluation Metrics

The first and the most important metric used in the evaluation of the proposed method is detection rate. The detection rate shows the percentages of the artificial lesions that are correctly identified. In addition to detection rate, three extra measurements are determined: the Jaccard coefficient, the false negative error, and the false positive error. The schematic Venn diagram in Figure 5.6 illustrates the derivation of these measures.

Assume that texture features detect region D as the lesion while the exact lesion region is L.

The voxels that are in D but not in L are denoted by $D\backslash L$ and the voxels that are in L but not in D are denoted by $L\backslash D$. A lesion detection occurs when $L\cap D$ is not empty.

The first quality measurement used in our experiments is the Union Overlap (UO) [185] or the Jaccard coefficient , the intersection over the union:

$$UO = \frac{\sum\limits_{r}|L_r\cap D_r|}{\sum\limits_{r}|L_r\cup D_r|}, \tag{5.15}$$

where r denotes the artificial lesions (r={1,...,60}), and $|.|$, the number of voxels. This measurement indicates how well the detected regions represent the location and extension of the lesions. The next measurement is the false negative (FN) error [185]:

$$FN = \frac{\sum\limits_{r}|L_r\backslash D_r|}{\sum\limits_{r}|L_r|}. \tag{5.16}$$

This measurement represents how much of the lesions are incorrectly found as non-lesion. Finally, the false positive (FP) error is defined [185]:

$$FP = \frac{\sum\limits_{r}|D_r\backslash L_r|}{\sum\limits_{r}|D_r|}. \tag{5.17}$$

FP shows how much of the detected regions are incorrectly labeled as lesion. These measurements are computed for all 8 artificial effect types (each type includes 60 artificial lesions). To better compare the effect of quantization level and the method of texture computation (VGLCM-TOP-3D vs VGLCM-3D) the measurements undergo statistical analysis using two-tailed t-test ($p < 0.05$) to show if a method or a specific quantization level is significantly better.

5.3.3 Results for Artificial Effects

In the first experiment, the performance of the methods is assessed when there is no registration error. For this purpose images are first registered into the atlas and then artificial lesions are added. The goal is to assess if texture analysis can detect lesions in the registered images (i.e., no registration is applied after lesions are added).

Eight texture features (autocorrelation (f_1), homogeneity (f_2), energy (f_3), correlation (f_4), dissimilarity (f_5), sum of squares: variance (f_6), sum average (f_7), and sum entropy (f_8)) have been computed using the voxel-based VGLCM-TOP-3D and VGLCM-3D method for two quantization levels of 8 and 16. Among these features f_6 (Sum of squares: variance) has the best performance. Table 5.2 shows the performance (i.e. detection rate, union overlap, false negative and false positive errors) of this feature.

This feature (f_6) achieves a 100% correct detection rate in all types of artificial lesions. The last row for each method shows the average over all artificial lesion types. The highest UO and the lowest FN and FP errors are 0.67, 0.07, and 0.23, respectively. The performances of the other

Table 5.2: The performance of the best texture feature, f_6 (Sum of squares: variance) computed for the 8 artificial effect types. For each artificial effect type 60 artificial lesions are generated. The statistical significance of quantization level is denoted by †. That is, if a quantization level significantly improves a measurement (its result is significantly better), it is denoted by †. The statistical significance of method (VGLCM-TOP-3D vs VGLCM-3D) is denoted by *. That is, if a method has a significantly better performance in a specific measurement, that measurement is denoted by * for the better method. The significance is set to ($p < 0.05$).

	Type	Q=8				Q=16			
		Detect	UO	FN Error	FP Error	Detect	UO	FN Error	FP Error
VGLCM-TOP-3D	I	100%	0.72±0.25	0.18±0.27	0.10±0.15	100%	0.71±0.25	0.16±0.26	0.13±0.19
	II	100%	0.66±0.26	0.30±0.28	0.05±0.11	100%	0.72±0.26	0.18±0.27	0.11±0.17
	III	100%	0.60±0.19	0.01±0.04	0.39±0.21	100%	0.56±0.20	0.02±0.05	0.43±0.22
	IV	100%	0.61±0.19	0.00±0.02	0.39±0.20	100%	0.65±0.22	0.00±0.01	0.35±0.22
	V	100%	0.76±0.19	0.13±0.21	0.12±0.13	100%	0.71±0.19	0.12±0.21	0.18±0.17
	VI	100%	0.80±0.18	0.13±0.19	0.08±0.10	100%	0.78±0.19	0.09±0.18	0.13±0.16
	VII	100%	0.61±0.16	0.01±0.02	0.39±0.17	100%	0.57±0.17	0.01±0.03	0.42±0.18
	VIII	100%	0.68±0.17	0.00±0.01	0.32±0.17	100%	0.70±0.20	0.00±0.01	0.30±0.20
	All	100%	0.67±0.21*	0.10±0.20	0.23±0.22*	100%	0.67±0.22*	0.07±0.18	0.25±0.23*
VGLCM-3D	I	100%	0.64±0.23	0.23±0.27	0.14±0.15	100%	0.61±0.22	0.20±0.27	0.21±0.20
	II	100%	0.57±0.24	0.37±0.28	0.08±0.11	100%	0.63±0.25	0.21±0.28	0.18±0.20
	III	100%	0.52±0.15	0.03±0.07	0.45±0.21	100%	0.48±0.15	0.04±0.09	0.49±0.20
	IV	100%	0.51±0.16	0.01±0.03	0.49±0.20	100%	0.56±0.19	0.01±0.02	0.44±0.20
	V	100%	0.68±0.16	0.14±0.20	0.20±0.13	100%	0.62±0.17	0.14±0.21	0.26±0.18
	VI	100%	0.72±0.16	0.17±0.19	0.12±0.10	100%	0.69±0.17	0.12±0.19	0.21±0.17
	VII	100%	0.54±0.15	0.01±0.04	0.45±0.17	100%	0.53±0.15	0.02±0.04	0.46±0.17
	VIII	100%	0.58±0.15	0.01±0.02	0.42±0.17	100%	0.61±0.17	0.01±0.02	0.38±0.17
	All	100%	0.59±0.19	0.12±0.21	0.29±0.23†	100%	0.59±0.19	0.09±0.19†	0.33±0.22

features are shown in Appendix C. The statistical significance of quantization level is denoted by †. That is, if a quantization level statistically improves a measurement (its result is significantly better), it is denoted by †. The statistical significance of the method (VGLCM-TOP-3D vs VGLCM-3D) is denoted by * ($p < 0.05$). In other words, if a method has a significantly better performance in a specific measurement, that measurement is denoted by * for the better method. For instance, UO in VGLCM-TOP-3D with Q=8 is significantly better (i.e., higher) than VGLCM-3D with Q=8 (shown by *), while the FN error is significantly better (i.e., lower) in VGLCM-3D with Q=16 compared to that of VGLCM-3D with Q=8 (denoted by †).

Statistical comparison of the rates reveals the VGLCM-TOP-3D has a higher UO and a lower FP error. It can also be observed that the VGLCM-3D does not outperform VGLCM-TOP-3D in any performance measurement.

With VGLCM-3D, a quantization level of 8 provides a lower FP error while a quantization level of 16 gives a lower FN error. The detection rate does not change significantly by changing the quantization level in either of the methods. To further compare the VGLCM-TOP-3D and the VGLCM-3D methods the average performances of all 8 texture features are shown in Tables 5.3.

Similar to f_6, the texture features computed by VGLCM-TOP-3D provide significantly higher UOs and lower FP errors compared to that of the features obtained by VGLCM-3D. On the other hand the FN error is significantly lower in the features computed by VGLCM-3D at Q=16. The overall FN error of features is lower at Q=16 while their FP error is less that at Q=8 for VGLCM-

Table 5.3: The average performance of the all features computed for the 8 artificial effect types. For each artificial effect type 60 artificial lesions are generated. The statistical significance of quantization level is denoted by †. That is, if a quantization level significantly improves a measurement (its result is significantly better), it is denoted by †. The statistical significance of method (VGLCM-TOP-3D vs VGLCM-3D) is denoted by *. That is, if a method has a significantly better performance in a specific measurement, that measurement is denoted by * for the better method. The significance is set to ($p < 0.05$).

| | | Q=8 | | | | Q=16 | | | |
	Type	Detect	UO	FN Error	FP Error	Detect	UO	FN Error	FP Error
VGLCM-TOP-3D	I	99%	0.48±0.27	0.35±0.31	0.31±0.25	99%	0.48±0.23	0.28±0.30	0.34±0.25
	II	89%	0.42±0.29	0.50±0.34	0.18±0.23	94%	0.46±0.28	0.36±0.37	0.27±0.25
	III	100%	0.41±0.18	0.13±0.22	0.56±0.20	100%	0.41±0.18	0.12±0.21	0.56±0.20
	IV	100%	0.42±0.19	0.14±0.24	0.54±0.20	99%	0.45±0.22	0.19±0.28	0.47±0.22
	V	100%	0.47±0.25	0.37±0.29	0.33±0.22	100%	0.48±0.22	0.29±0.29	0.36±0.21
	VI	99%	0.50±0.27	0.34±0.32	0.29±0.22	100%	0.49±0.25	0.31±0.31	0.34±0.22
	VII	100%	0.42±0.17	0.14±0.22	0.54±0.16	100%	0.42±0.16	0.13±0.22	0.54±0.17
	VIII	98%	0.45±0.23	0.27±0.31	0.40±0.25	99%	0.46±0.23	0.24±0.30	0.41±0.24
	All	99%	0.48±0.27*	0.35±0.31	0.31±0.25*	99%	0.48±0.23*	0.28±0.30†	0.34±0.25*
VGLCM-3D	I	98%	0.43±0.23	0.36±0.30	0.36±0.25	98%	0.42±0.21	0.29±0.30	0.42±0.26
	II	89%	0.35±0.25	0.53±0.34	0.25±0.27	94%	0.39±0.24	0.37±0.36	0.36±0.28
	III	100%	0.34±0.15	0.11±0.18	0.64±0.17	100%	0.33±0.15	0.09±0.17	0.64±0.17
	IV	100%	0.36±0.17	0.13±0.23	0.60±0.19	99%	0.39±0.20	0.16±0.25	0.56±0.22
	V	100%	0.42±0.21	0.36±0.28	0.43±0.21	100%	0.42±0.17	0.28±0.27	0.47±0.19
	VI	99%	0.45±0.23	0.33±0.31	0.37±0.24	99%	0.44±0.21	0.28±0.29	0.43±0.22
	VII	100%	0.37±0.14	0.11±0.18	0.62±0.14	100%	0.36±0.14	0.09±0.16	0.62±0.14
	VIII	100%	0.39±0.17	0.12±0.21	0.58±0.17	100%	0.41±0.19	0.18±0.23	0.55±0.19
	ALL	98%	0.39±0.20	0.26±0.30	0.48±0.25†	99%	0.39±0.20	0.22±0.28*†	0.50±0.24

TOP-3D. In addition, FN error is lower at Q=16 compared to that at Q=8 for VGLCM-TOP-3D. Finally, the detection rate does not significantly change by changing the quantization level for either method.

In general, the texture features have a higher performance on hypo-intense (Types I, III, V, VII) compared to hyper-intense (Types II, IV, VI, VIII) artificial lesions for T1-weighted images (Tables 5.2 and 5.3). This is favorable, because neurological diseases usually appear as hypo-intense signals in T1-weighted images.

The statistical maps of f_6 for the 8 different artificial effects computed by VGLCM-TOP-3D at quantization level of 8 is shown in Figure 5.7. It can be observed that the artificial lesions are correctly detected using the proposed method.

In the second experiment, the performance of textures is assessed in the presence of registration errors. Two approaches are compared: applying registration to the texture features computed in the original space and applying registration to the image and then computing textures in the registered image (Figure 5.4). For this purpose, VGLCM-TOP-3D with quantization level of 8 is used. Figure 5.8 compares the performance of the two approaches for the eight texture features. In this feature, detection rates have no error bars because they only represent one number (the proportion of the lesions detected by the feature). On the other hand, UOs, FN errors, and FP errors have error bars showing the standard deviations of the measurements (computed for each lesion separately).

The UOs, FN errors, and FP errors are not statistically different between the two approaches
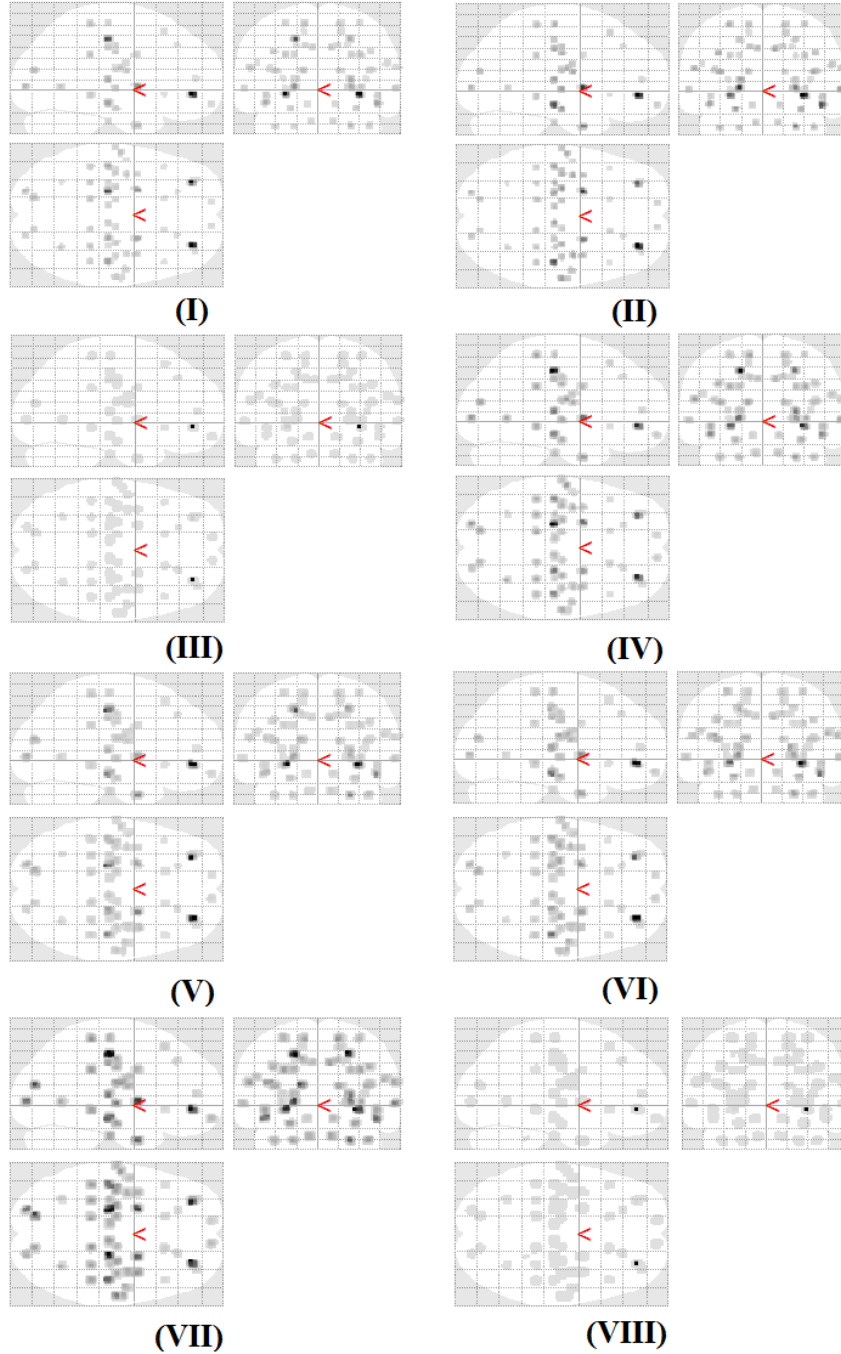
Figure 5.7: The statistical maps of sum of squares: variance (f_6). The regions with statistically significant difference (corrected by FRD at $p < 0.05$) are shown (i.e., detection regions). The ground truth locations of lesions are shown in Figure 5.5. The type of artificial lesion are shown by roman number (i.e., I, II,...,VIII). The maps are computed by VGLCM-TOP-3D at quantization level of 8. The intensities represent the significance of the detected region. A darker region shows a higher statistical difference. The detection capability of the texture feature varies depending on the location and the type of the lesions (some regions are darker than others).
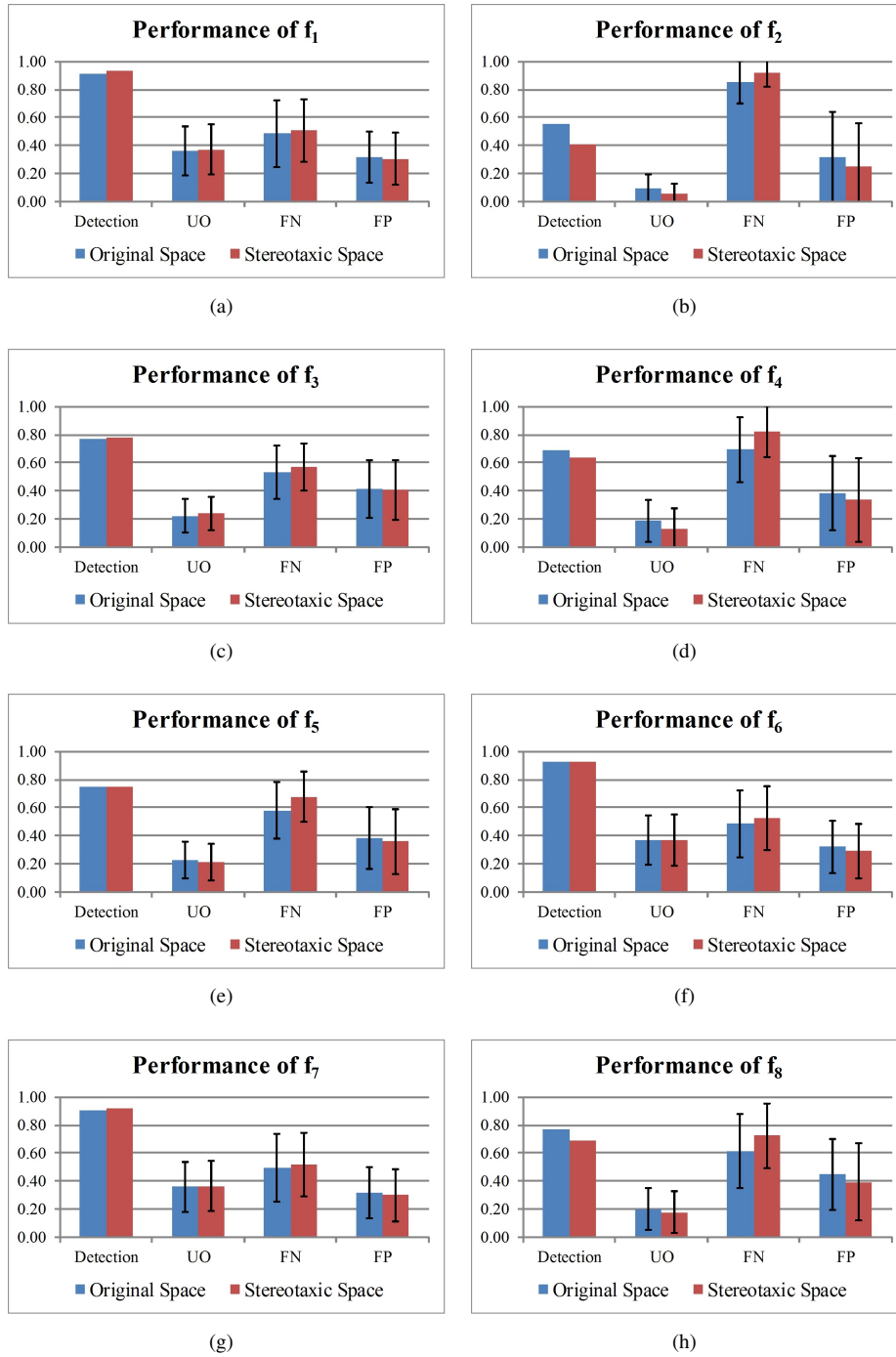
Figure 5.8: Comparing the performance of textures computed in the original versus stereotaxic spaces.

for any of the texture features. Also, the detection rates of f_1, f_3, f_5, f_6, and f_7 do not change noticeably between the two approaches. The detection rates of f_2, f_4, and f_8 are better when the texture is computed in the original space (first approach).

Table 5.4: Regions detected by texture features and comparing that with regions reported by other studies.

Brain Region	Laterality	Texture Features	Other studies
Anterior Cingulate	R	1,6,7,8	[317], [110], [41], [318]
Corpus Callosum	L	1,6,7	[340], [45]
Corpus Callosum	R	1,6,7	[340], [45]
Hippocampus	R	1,5,6,7,8	[317], [110]
Hippocampus	L	1,5,6,7,8	[317], [110]
Inferior Frontal Gyrus	R	1,6,7	[295], [41], [285]
Inferior Frontal Gyrus	L	1,7	[41], [318], [285]
Inferior Parietal Lobule	R	5	[41], [111]
Insula	L	1,6,7	[317], [110], [41], [111]
Insula	R	1,6,7	[317], [110]
Medial Frontal Gyrus	R	1,6,7,8	[110], [260]
Medial Frontal Gyrus	L	1,6,7	[110], [295], [41], [318]
Middle Frontal Gyrus	R	1,6,7	[295], [41],[318]
Middle Frontal Gyrus	L	1,6,7	[295], [41], [318], [285]
Midbrain	L	1,5,6,7,8	[368], [367], [111]
Parahippocampal Gyrus	R	1,5,6,7,8	[317], [295]
Parahippocampal Gyrus	L	1,5,6,7,8	[317], [295]
Precentral Gyrus	R	1,6,7	[285], [70], [148]
Superior Frontal Gyrus	L	7	[285]
Temporal Lobe	L	1,5,6,7,8	[317], [295], [318], [111], [285]
Temporal Lobe	R	1,5,6,7,8	[317], [295], [318], [111], [285]
Thalamus	L	1,5,6,7,8	[317], [295], [111]
Thalamus	R	1,5,6,7,8	[317], [295], [111]

5.3.4 Results for Dataset of AD

VGLCM-TOP-3D provided a better performance with detection of artificial lesions, and hence, VGLCM-TOP-3D at Q=8 is used to study cerebral changes in AD. Also, as shown in the previous section, the performance metrics do not change notably when texture features are computed in the original versus stereotaxic space specially in features with high performances (f_1, f_6, and f_7). Since computing features in stereotaxic space is faster in our experiments, they are used for the AD dataset.

To decrease the false positive error FDR is set at $p < 0.01$ instead of $p < 0.05$, and only clusters with at least 10 voxel extensions are considered in the generation of statistical maps. Figure 5.9 shows the statistical map produced by the eight texture features.

As can be seen in Figure 5.9, differences in AD in all textures except f_2, f_3, and f_4 are found. The bulk of the findings are concentrated in the medial temporal lobes. The results of f_5 and f_8 and the results of f_1, f_6, and f_7 are similar. Features f_1, f_6, and f_7 show larger regions compared to f_5 and f_8. The regions detected by the texture features are found in other studies. Table 5.4 summarizes the detected regions using the proposed method and from other studies in AD.
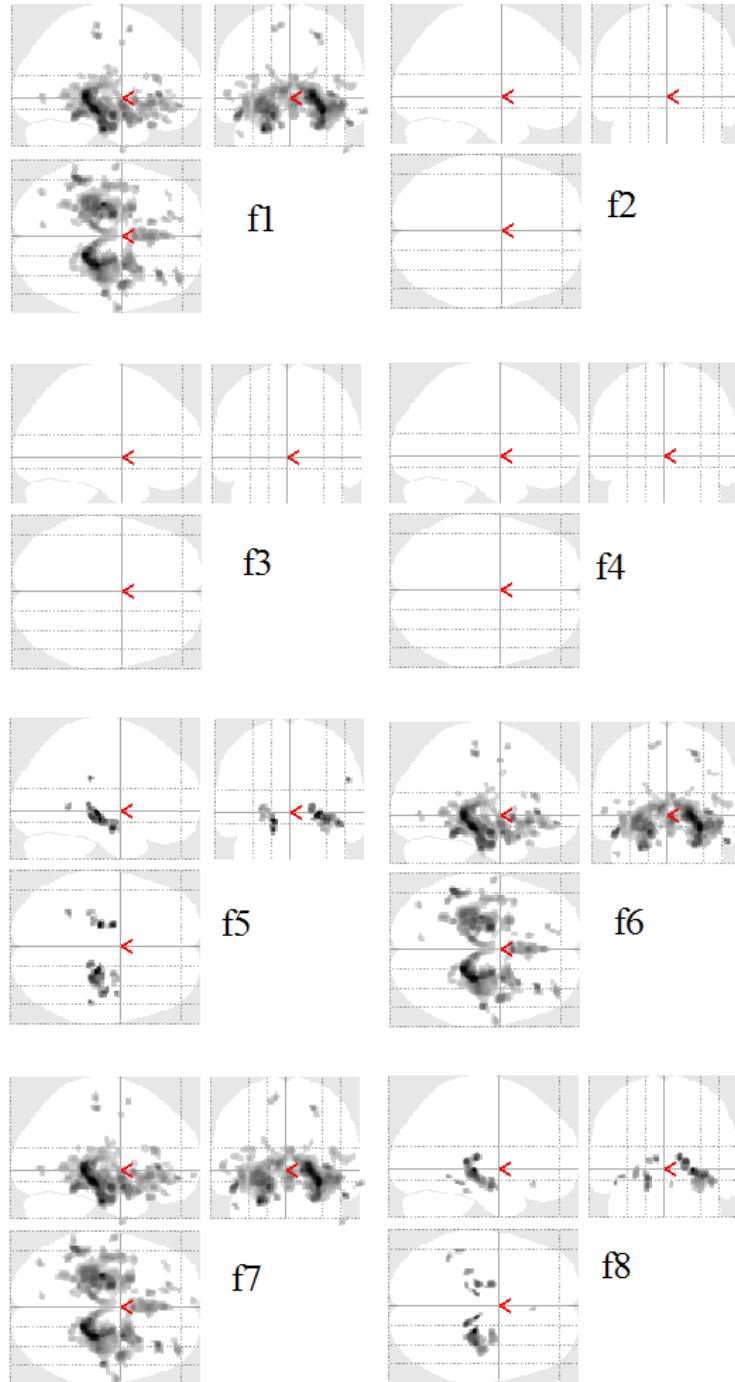
Figure 5.9: Statistical map of the local textures corrected by FDR at $p < 0.01$. VGLCM-TOP-3D at Q=8 is used to compute the features.

5.3.5 Discussion

While the current approach of ROI-based texture analysis has been successfully used in several applications such as brain tumors, epilepsy, multiple sclerosis, and AD, it is limited to the analysis of a specified anatomical region. To the best of our knowledge, there is no spatially non-specific
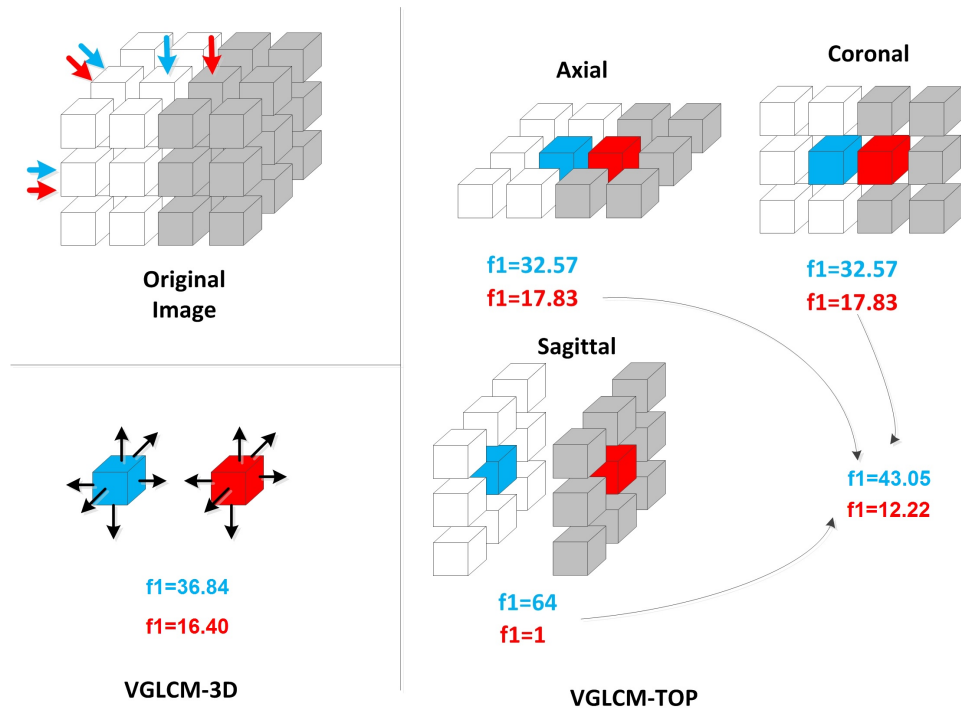
Figure 5.10: Computing f_1 by VGLCM-TOP-3D and VGLCM-3D methods for a voxel located on a sagittal edge (i.e., between dark and bright regions). Top left, the original image, bottom left VGLCM-3D, and right VGLCM-TOP-3D.

texture analysis method that provides a 3D statistical map. The most similar approach to our method was performed by Bernasconi et al. [33]. Their work is primarily based on the first-order texture analysis (i.e., GM thickness, gradient, relative intensity), which computes the ratio map (i.e., ratio map =(GM thickness × relative intensity)/gray level intensity gradient). In the approach presented in this thesis, however, a second order texture statistic (co-occurrence matrix) is used which is more precise and accurate than the first order statistic. Moreover, the output of our method is a statistical map similar to that provided by VBM.

In general, it can be observed that the proposed VGLCM-TOP-3D has a higher performance compared to that of VGLCM-3D. It is because the approach that VGLCM-TOP-3D uses to extract 3D information is more sensitive to subtle changes occurring at edges. This is illustrated in Figure 5.10.

In the example shown in Figure 5.10, the value of autocorrelation (f_1) using distance D=1 and neighborhood radius R=1 is computed. It is explained how the two methods (VGLCM-3D, and right VGLCM-TOP-3D) distinguish an edge that appears in the sagittal view (without loss of generality the edge can be considered in the other directions). Consider two neighboring voxels (blue and red) located on an edge. Assume that the blue and white voxels are located on the bright side of the edge with a gray value of 8 and the red and gray voxels are located on the dark side of the edge with a gray value of 1. As can be seen when the three orthogonal planes are considered at the red/blue

voxels, the edge appears in the axial and coronal planes while from the sagittal view the blue and red voxels are located in the pure bright and dark regions, respectively. As a result, the difference of the texture values (e.g. f_1) is remarkably different in the sagittal plane. This difference appears in the final texture value which is the average of the texture values at the three planes. On the other hand, VGLCM-3D considers all directions. As one can see, considering all directions results in a higher difference of the texture feature (f_1) compared to that of the coronal and axial views (Figure 5.10). However, the final feature difference of VGLCM-TOP-3D is higher because of the high difference of f1 in the sagittal view. In other words, since three different directions are considered in VGLCM-TOP-3D an edge shows a significant difference in at least one of the planes which results in a higher difference in the final feature values of the voxels located around the edge. This sensitivity to edges makes VGLCM-TOP-3D more discriminative than VGLCM-3D. It can be observed in Figure 5.3 that the VGLCM-3D features are more blur than VGLCM-TOP-3D (it is more evident in f_2, f_3, f_5, and f_8).

The comparison between two approaches for computing texture features in the original space versus the stereotaxic space shows slight improvement of detection rate only for three texture features (f_2, f_4, and f_8) when the computation is performed in original space. Detection rate and other quality measurements do not demonstrate the superiority of any of the approaches for other texture features.

The results on the AD database show statistically different regions particularly in the temporal lobe which is in concordance with the other findings of AD (Table 5.4) further confirming the validity of the proposed voxel-based texture analysis.

There are several choices of parameters when one performs local texture analysis, which include the number of gray levels, the neighborhood size, and the offset distance. Since texture features are computed in a small spherical region around voxels, a small value of gray levels (G) is enough to get good results (e.g., 8 or 16). Also, a change of G has negligible impact on the performance of the methods particularly for VGLCM-TOP-3D. For VGLCM-3D, increasing the number of gray levels reduces the FN error while it raises the FP error. The neighborhood radius (R) and the offset distance (d) should be large enough to be able to distinguish texture patterns, while small enough to detect local changes around each voxel. A value of 1 to 3 is a good choice for R and d.

The proposed methods do not require a pre-defined region of interest for analysis as they provide a hypothesis-free analysis tool to detect regions affected by a disease; as such the method is more easily applicable to clinical practice.

ROI-based texture analysis methods require segmentation. Accurate segmentation may best be achieved when performed manually and this could become the bottleneck of the processing pipeline, as was the case, for instance, in the work of [73] where relatively simple and easily segmented structures (corpus callosum and thalamus) were studied in AD. The proposed method in this thesis obviates the need for segmentation as it performs analysis on a voxel-by-voxel basis of the whole

brain. The presented tool can be incorporated into current popular brain imaging analysis software packages such as SPM and FSL and is a complementary method to VBM. In contrast to VBM which compares the density of GM or WM in voxels, the proposed texture analysis method compares the intensity value of the voxel with its neighboring voxels and captures structural information such as curves, shape, etc.

While texture analysis provides useful information it requires additional computations to process data. The average running time to compute texture features in stereotaxic space for a subject using a typical PC with an Intel quad core i7 2.60 GHz CPU with 16GB RAM running Windows 7 Professional is about 15 minutes for VGLCM-3D with Q=8, 33 minutes for VGLCM-3D with Q=16, 14 minutes for VGLCM-TOP-3D with Q=8, and 20 minutes for VGLCM-TOP-3D with Q=16. The runtime to compute texture features in original space increases by a factor of roughly 2.

It should be noted that the pattern, strength, and extension of hypo/hyper intense are different from disease to disease and therefore for each neurological disease a different set of texture features might be useful. For instance, in the AD database f_2, f_3, and f_4 did not reveal statistical difference after FDR at $p < 0.01$, and f_5, and f_8 show a smaller region compared to f_1, f_6, and f_7. As a result, our recommendation is to first do an exploratory analysis by computing all textures features. A combination of textures using methods such as discriminant analysis may be more robust.

5.4 Summary

In this chapter, a novel method for voxel-based 3D texture analysis is proposed as a powerful image analysis tool. The output is a statistical map comparable to that of VBM; however, a different type of information is used. The proposed analysis has been tested successfully to evaluate artificial lesions and probe cerebral changes in an MRI database of AD. The method could detect the artificial lesions accurately and the regions detected in the AD database are consistent with the known spatial pathological distribution of this disease. The proposed method has been implemented as a toolbox for SPM and can be used to study different diseases affecting the brain (please see Appendix A).

Chapter 6

Application in ALS

6.1 Introduction

In this chapter our texture analysis experiments to study ALS are presented. As mentioned before, the challenge is that MR images of the brain in patients with ALS do not show changes visible to human eyes and the goal is to evaluate texture analysis as a potential biomarker to detect these subtle changes.

The experiments include 2D and 3D texture analysis methods. For 2D methods, two slices are selected: one that maximally include the corticospinal tracts (this region has been reported by many research groups to be affected in ALS), and one through the occipital lobe (this region has minimal pathological changes due to ALS). Two well-known methods, GLCM and GLAM are used for texture extraction. A part of this study has been presented in [229]. The analysis is explained in Section 6.2.

For 3D analysis the proposed voxel-based texture analysis explained in Chapter 5 is used to detect regions affected by ALS. VBM analysis is also performed and its results are compared to our results. The 3D analysis approach is presented in Section 6.3. Finally a summary is given in Section 6.4.

6.2 2D Texture Analysis

Two well-known methods, GLCM and GLAM, are employed to extract texture features from routine T1-weighted and T2-weighted MR images. Texture features are analyzed by statistical inference, and receiver operator characteristic curve (ROC) analysis. Also the features are classified by support vector machine to determine the ability of texture features to differentiate between patients with ALS and healthy subjects.

6.2.1 Preprocessing Procedure

The imaging analysis pipeline for 2D analysis include pre-processing, texture feature extraction, and feature selection. The features then undergo statistical analysis, as well as classification.

<div align="center">(a)   (b)   (c)</div>
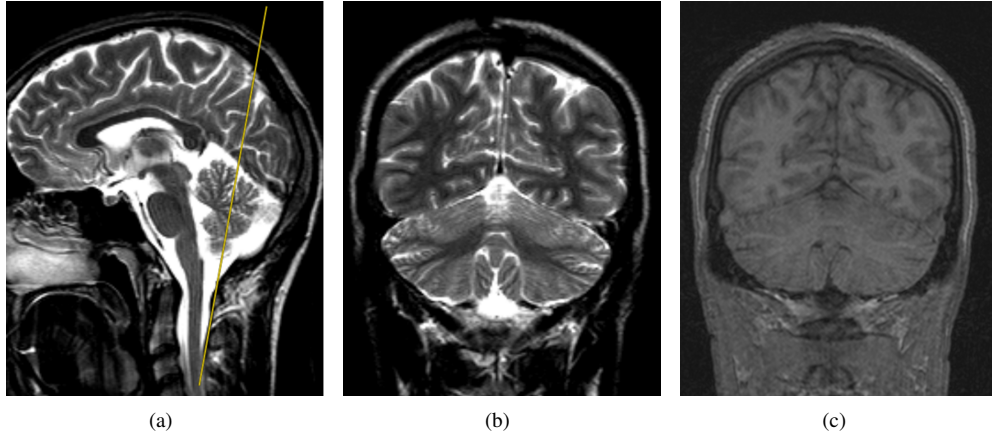
Figure 6.1: Midline sagittal T2-weighted image (a) demonstrating slice selection for corresponding coronal T2-weighted (b) and T1-weighted (c) images of the occipital lobe. These are used as an internal control for texture analysis to compare with coronal images containing the CST.

Pre-processing

The pre-processing step includes slice and ROI selection, and intensity normalization. Two slices are chosen for texture analysis on each of the coronal T1-weighted and T2-weighted images. The slice that maximally includes the CST is selected, because, this is where the most significant pathological changes of ALS are expected [150; 159; 304; 281]. As an internal control, a slice through the occipital lobe is selected where there are minimal if any pathological changes due to ALS (Figure 6.1). An intracranial ROI is manually defined for the CST slice to include the region above the inferior horn of the lateral ventricles, and for the occipital lobe slice the region excluding the cerebellum (Figure 6.2).

Image ROIs are normalized by converting each pixel's gray value to $z = (v - \mu)/\sigma \times \Sigma + M$, where v is the original gray value at the pixel, μ the average gray value of the ROI, σ the standard deviation of the ROI, M the new average, and Σ the new standard deviation of the ROI. $M = 0.5$ and $\Sigma = 0.1$ are used for our experiments. Using $M = 0.5$ and $\Sigma = 0.1$ result in the majority of pixels to be set in the range of [0 1], however, there might be some outliers having a value out of this range. Before further analysis pixel values below 0 are set to 0 and those above 1 are set to 1.

Finally, the gray values are quantized into N gray levels for texture analysis by $Z = round(z \times (N - 1) + 1)$ which maps the real number z in the range [0 1] to an integer number Z in the range [1 N]. In our experiments, 32 gray levels are used ($N = 32$). This number of gray levels provides accurate results without adding too much computational costs.

Texture Features Extraction

For GLCM usually eight directions are considered in 2D (i.e. $0°, \pm45°, \pm90°, \pm135°, 180°$). A common approach is to consider diagonally opposite pairs together (i.e., θ and $\theta + 180°$), making

<div align="center">(a)   (b)</div>
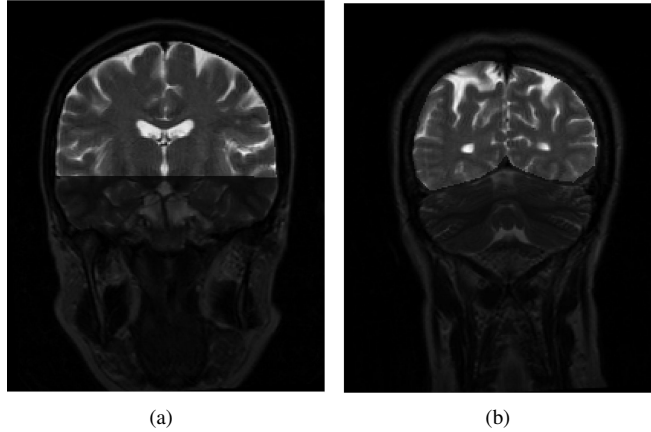
Figure 6.2: Defined regions of interest on sample coronal T2-weighted images enclosing the (a) CST and (b) occipital lobe.

the GLCM symmetric and reducing the number of directions from eight to four. In our experiments a distance of $d = 1$ with a symmetric GLCM with four directions (considering diagonally opposite pairs together) is used. Fourteen texture features of GLCM (listed in 2.1) are extracted and used as textural features.

For GLAM all possible neighborhood system with size of 3×3 are considered. Similar to GLCM, the GLAM matrix is normalized and 14 features of the normalized GLAM are computed as texture features.

Texture Selection

Among the 14 features extracted for texture analysis, three features providing the highest performance for both T1-weighted and T2-weighted MR images are chosen: correlation, contrast, and inverse difference moment normalized (f_4, f_9, and f_{10} in 2.1). It has been observed that combining the features does not improve the classification rate (by our SVM classifier). In addition, a single feature can be easily shown in a figure. Therefore, each texture feature is analyzed separately and the feature vector consists of only one feature for classification and statistical analysis.

Classification

Classification is the task of separating samples and assigning them to different classes which are patients and controls in this study. Classification is usually performed in two stages. In the first stage the classifier is trained by known samples of both patient and control classes. Then, in the next stage, it determines to which class the given sample belongs. The Support Vector Machine (SVM) [61] is used for classification. SVM [61] is a well-known classifier used in many medical imaging applications [121; 222; 385; 325].

The SVM finds the optimal hyperplane which partitions the feature space of the training samples

(of both control and patient groups) into two halves. Each training sample consists of a feature vector and a label showing its class (patient or control). Suppose that the kth training sample is labeled by $l_k = p, c$ (p as patient or c as control) and $\vec{x}_k$ is its feature vector. A function, y, is used to map each label to either 1 or -1:

$$y(l) = \left\{ \begin{array}{ll} +1 & \text{if l=p} \\ -1 & \text{if l=c} \end{array} \right. . \tag{6.1}$$

The inverse of y, Y, is defined such that it provides the label of a given value (i.e. $Y(y(l)) = l$). The SVM assigns the class of the given test sample $\vec{x}_t$ as follows:

$$class(\vec{x}_t) = Y(Sgn(\sum_{\forall k, l_k \in \{p,c\}} y(l_k)\alpha_k K(\vec{x}_t, \vec{x}_k) + b)), \tag{6.2}$$

where Sgn is the sign function, b the bias parameter of the optimal hyperplane of the SVM, α_k the Lagrangian multiplier for the training sample k, and K the kernel function. The parameters b and α_k are estimated by maximizing the margin of the decision boundary of the training samples belonging to the patient and control groups [61]. The kernel function usually maps data into higher dimensional spaces hoping that the data could be more easily separated. A linear kernel is used in our experiments which is simply the dot product between two vectors. It is experimentally found that the linear kernel provides the best results in our experiments.

To train the SVM, half of the subjects are chosen randomly for training and half for test. The experiment is repeated 1000 times to reduce the effect of randomness. The average accuracy (classifications rate) is assessed for analysis.

Statistical Analysis

The Kruskal-Wallis [194] test is used for statistical analysis. This test is a non-parametric method for testing whether samples originate from the same distribution and, therefore, can show if the features extracted from patients with ALS and those extracted from healthy subjects are statistically different. Statistical significance was set at 2-tailed $p < 0.05$. Receiver operating characteristic (ROC) curve analysis is performed as a supplementary method. The ROC curve shows the true positive rate versus false positive rate. The area under the ROC curve (AUC) is used as a standard method to assess and compare the performance of the features. Finally, the optimal sensitivity and specificity (minimal false negatives and false positives) are determined with ROC curve analysis.

6.2.2   Evaluation of 2D Methods

In this section, the specifications of the dataset used for evaluation is described. Also, the method of aqcuisition is explained. It is always useful to compare the results of a new method (here, textrure analysis) with a commonly used method in an analysis. Hence, a commonly used method of brain atrophy analysis, the brain parenchymal fraction (BPF) method, is explained. The BPF is used as a
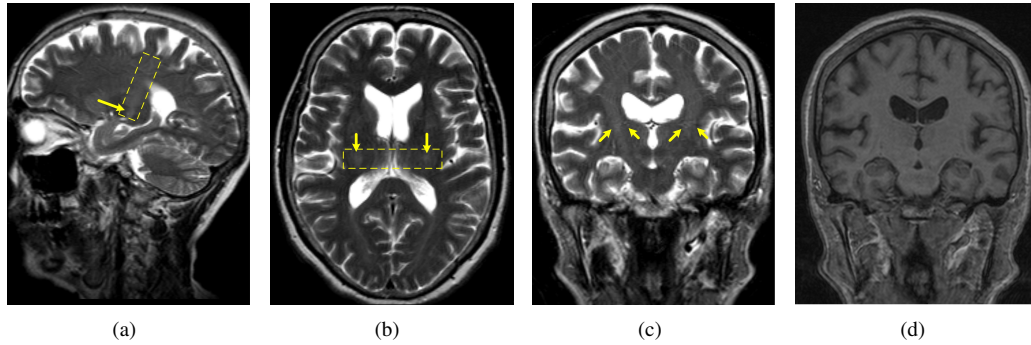
Figure 6.3: Sagittal T2-weighted (a) and axial T2-weighted (b) images were used to assist in planning the coronal T2-weighted (c) and coronal T1-weighted MPRAGE (d) imaging which were used for texture analysis. The CST appears hyperintense on the T2-weighted images.

baseline for evaluation of the 2D texture analysis. Finally, the results of texture analysis and BPF analysis are presented.

DataSets

Nineteen patients (ten males, nine females) with clinically probable or definite sporadic ALS according to the revised El Escorial criteria [39] have been recruited. All patients have clinical evidence of UMN and LMN involvement. Patients have an average age of 56.7 ± 13.7 years (range 27–72 years) with a symptom duration of 25.5 ± 16.3 months (range 9–72 months).

Twenty healthy control subjects (nine males, eleven females) without neurological or psychiatric disease are included. Their average age is 56.8 ± 12.4 years (range 24–81 years).

MR images have been acquired on a 1.5 Tesla system (Magnetom Sonata, Siemens Medical Systems). Conventional sagittal and axial T2-weighted images are first acquired to plan the two coronal sequences of interest: coronal T2-weighted images (TR=7510 ms, TE=113 ms, voxel size 1.1×0.9, 5 mm thick), and 3D T1-weighted MPRAGE (TR=1600 ms, TE=3.8 ms, TI=1100 ms, voxel size 1.0×1.0, 1.5 mm thick). Coronal imaging is performed with an angulation parallel to the CST observed on the sagittal images. Angulation is further refined by ensuring that the coronal slice intersect the cerebral peduncles and the hyperintense signal of the CST in the posterior limb of the internal capsule and corona radiata on the axial images (Figure 6.3).

Compared Methods

Brain atrophy has been reported in ALS by different research groups [8; 245; 47; 178]. One of the well known methods to measure the brain atrophy is the brain parenchymal fraction (BPF) [167] method. Since this method provides a quantitative measure, it can be compared with the defined texture features.

The method computes the proportion of brain parenchymal volume to the total intracranial volume. However, to have a fair comparison with the texture features the method is modified to be

Table 6.1: Statistical properties (mean±std, and p–value), classification rate, and the AUC of the GLCM features extracted from T1-weighted images. f_4, f_9, and f_{10} represent correlation, contrast, and inverse difference moment normalized, respectively. Sensitivity and specificity is reported for significantly different features.

Slice Location		CST			Occipital Lobe		
GLCM Texture Feature		f_4	f_9	f_{10}	f_4	f_9	f_{10}
$P_{0°,1}$	Patients	$(9.66\pm0.03)\times10^{-1}$	0.65 ± 0.06	$(999.37\pm0.06)\times10^{-3}$	$(9.57\pm0.05)\times10^{-1}$	0.83 ± 0.09	$(999.19\pm0.08)\times10^{-3}$
	Controls	$(9.60\pm0.04)\times10^{-1}$	0.76 ± 0.08	$(999.26\pm0.08)\times10^{-3}$	$(9.55\pm0.04)\times10^{-1}$	0.87 ± 0.09	$(999.15\pm0.08)\times10^{-3}$
	p–value	$< 10^{-3}$	$< 10^{-3}$	$< 10^{-3}$	0.11	0.11	0.11
	Classification Rate	74.82%	74.62%	74.03%	58.58%	58.66%	58.56%
	AUC	0.86	0.86	0.86	0.65	0.65	0.65
	Sensitivity	100.00%	89.47%	89.47%	–	–	–
	Specificity	55.00%	70.00%	70.00%	–	–	–
$P_{45°,1}$	Patients	$(9.43\pm0.05)\times10^{-1}$	1.10 ± 0.10	$(998.93\pm0.09)\times10^{-3}$	$(9.28\pm0.09)\times10^{-1}$	1.39 ± 0.17	$(998.66\pm0.16)\times10^{-3}$
	Controls	$(9.33\pm0.07)\times10^{-1}$	1.28 ± 0.13	$(998.76\pm0.12)\times10^{-3}$	$(9.25\pm0.08)\times10^{-1}$	1.44 ± 0.15	$(998.60\pm0.15)\times10^{-3}$
	p–value	$< 10^{-4}$	$< 10^{-4}$	$< 10^{-4}$	0.47	0.47	0.45
	Classification Rate	76.82%	76.18%	76.00%	47.52%	47.64%	48.23%
	AUC	0.88	0.87	0.87	0.57	0.57	0.57
	Sensitivity	78.95%	78.95%	84.21%	–	–	–
	Specificity	90.00%	85.00%	80.00%	–	–	–
$P_{90°,1}$	Patients	$(9.64\pm0.03)\times10^{-1}$	0.69 ± 0.06	$(999.33\pm0.06)\times10^{-3}$	$(9.59\pm0.05)\times10^{-1}$	0.79 ± 0.10	$(999.23\pm0.10)\times10^{-3}$
	Controls	$(9.59\pm0.04)\times10^{-1}$	0.78 ± 0.08	$(999.24\pm0.08)\times10^{-3}$	$(9.58\pm0.05)\times10^{-1}$	0.81 ± 0.09	$(999.21\pm0.09)\times10^{-3}$
	p–value	$< 10^{-3}$	$< 10^{-3}$	$< 10^{-3}$	0.67	0.59	0.61
	Classification Rate	74.96%	74.35%	74.25%	46.34%	46.53%	46.19%
	AUC	0.83	0.83	0.83	0.54	0.55	0.55
	Sensitivity	94.74%	94.74%	94.74%	–	–	–
	Specificity	65.00%	65.00%	65.00%	–	–	–
$P_{135°,1}$	Patients	$(9.41\pm0.06)\times10^{-1}$	1.13 ± 0.11	$(998.91\pm0.10)\times10^{-3}$	$(9.27\pm0.10)\times10^{-1}$	1.40 ± 0.18	$(998.65\pm0.17)\times10^{-3}$
	Controls	$(9.31\pm0.08)\times10^{-1}$	1.32 ± 0.14	$(998.73\pm0.14)\times10^{-3}$	$(9.24\pm0.09)\times10^{-1}$	1.46 ± 0.17	$(998.59\pm0.16)\times10^{-3}$
	p–value	$< 10^{-3}$	$< 10^{-3}$	$< 10^{-3}$	0.26	0.31	0.30
	Classification Rate	72.63%	72.44%	72.26%	51.93%	51.32%	51.61%
	AUC	0.84	0.84	0.84	0.61	0.60	0.60
	Sensitivity	89.47%	89.47%	100.00%	–	–	–
	Specificity	75.00%	70.00%	60.00%	–	–	–

computed in one slice and the same ROI used for texture analysis.

This modified version is called as the region of interest parenchymal fraction (ROI-PF). To find ROI-PF, first, the brain was automatically segmented into gray matter (GM), white matter (WM), and CSF using SPM8. Then, the parenchymal fraction is computed as $(GM + WM)/(GM + WM + CSF)$. T1-weighted images are used for ROI-PF computation, because of their higher resolution compared to T2-weighted images.

Results of GLCM

The GLCM features extracted from the T1-weighted slice enclosing the CST are statistically different between patients and controls while there is no difference in the occipital lobe slice as shown in Table 6.1.

The direction of the GLCM influences the performance of the features. For instance, the classification performance of $P_{45°,1}$ is higher than that of $P_{0°,1}$, $P_{90°,1}$, and $P_{135°,1}$. However, the performance of the three selected features of the GLCM (f_4, f_9, and f_{10}) are comparable in the same directions. The highest classification and AUC are 76.82% and 0.88, respectively, for $P_{45°,1} : f_4$. Depending on the feature and the direction, the optimal sensitivity ranges from 78.95% to 100% and the optimal specificity from 60% to 90%. The optimal sensitivity and specificity of the best feature, $P_{45°,1} : f_4$, is 78.95% and 90%, respectively. As expected, features are not significantly different in the occipital lobe region and the classification rates are poor.

Similar to the analysis of the T1-weighted images, the GLCM features extracted from the T2-

Table 6.2: Statistical properties (mean±std, and p–value), classification rate, and AUC of the GLCM features extracted from T2-weighted images. f_4, f_9, and f_{10} represent correlation, contrast, and inverse difference moment normalized, respectively. Sensitivity and specificity are reported for significantly different features.

Slice Location		CST			Occipital Lobe		
GLCM Texture Feature		f_4	f_9	f_{10}	f_4	f_9	f_{10}
$P_{0°,1}$	Patients	$(9.18\pm0.11)\times10^{-1}$	1.58 ± 0.21	$(998.48\pm0.19)\times10^{-3}$	$(8.86\pm0.17)\times10^{-1}$	2.20 ± 0.32	$(997.89\pm0.30)\times10^{-3}$
	Controls	$(8.94\pm0.13)\times10^{-1}$	2.03 ± 0.24	$(998.06\pm0.22)\times10^{-3}$	$(8.79\pm0.17)\times10^{-1}$	2.33 ± 0.31	$(997.77\pm0.29)\times10^{-3}$
	p–value	$<10^{-5}$	$<10^{-5}$	$<10^{-5}$	0.26	0.19	0.19
	Classification Rate	82.05%	81.47%	81.83%	52.32%	54.75%	54.34%
	AUC	0.92	0.92	0.92	0.61	0.62	0.62
	Sensitivity	84.21%	78.95%	84.21%	–	–	–
	Specificity	95.00%	95.00%	90.00%	–	–	–
$P_{45°,1}$	Patients	$(8.61\pm0.19)\times10^{-1}$	2.68 ± 0.36	$(997.46\pm0.32)\times10^{-3}$	$(8.12\pm0.33)\times10^{-1}$	3.61 ± 0.61	$(996.58\pm0.56)\times10^{-3}$
	Controls	$(8.22\pm0.23)\times10^{-1}$	3.39 ± 0.41	$(996.83\pm0.36)\times10^{-3}$	$(8.00\pm0.32)\times10^{-1}$	3.82 ± 0.59	$(996.39\pm0.52)\times10^{-3}$
	p–value	$<10^{-4}$	$<10^{-5}$	$<10^{-5}$	0.38	0.43	0.47
	Classification Rate	80.15%	79.17%	78.98%	50.99%	52.07%	51.71%
	AUC	0.91	0.92	0.92	0.58	0.57	0.57
	Sensitivity	89.47%	84.21%	89.47%	–	–	–
	Specificity	90.00%	90.00%	90.00%	–	–	–
$P_{90°,1}$	Patients	$(9.08\pm0.17)\times10^{-1}$	1.79 ± 0.32	$(998.29\pm0.30)\times10^{-3}$	$(8.93\pm0.23)\times10^{-1}$	2.05 ± 0.41	$(998.03\pm0.39)\times10^{-3}$
	Controls	$(8.79\pm0.21)\times10^{-1}$	2.31 ± 0.37	$(997.81\pm0.34)\times10^{-3}$	$(8.85\pm0.23)\times10^{-1}$	2.21 ± 0.41	$(997.89\pm0.38)\times10^{-3}$
	p–value	$<10^{-3}$	$<10^{-3}$	$<10^{-3}$	0.43	0.42	0.40
	Classification Rate	77.05%	77.02%	76.85%	50.74%	50.41%	50.56%
	AUC	0.86	0.86	0.86	0.57	0.58	0.58
	Sensitivity	89.47%	89.47%	89.47%	–	–	–
	Specificity	80.00%	80.00%	80.00%	–	–	–
$P_{135°,1}$	Patients	$(8.52\pm0.25)\times10^{-1}$	2.86 ± 0.48	$(997.29\pm0.43)\times10^{-3}$	$(8.11\pm0.31)\times10^{-1}$	3.64 ± 0.57	$(996.55\pm0.53)\times10^{-3}$
	Controls	$(8.07\pm0.30)\times10^{-1}$	3.69 ± 0.53	$(996.56\pm0.46)\times10^{-3}$	$(8.00\pm0.29)\times10^{-1}$	3.83 ± 0.52	$(998.38\pm0.48)\times10^{-3}$
	p–value	$<10^{-4}$	$<10^{-4}$	$<10^{-4}$	0.37	0.35	0.35
	Classification Rate	77.76%	74.91%	75.05%	51.26%	51.07%	50.55%
	AUC	0.90	0.88	0.88	0.58	0.59	0.59
	Sensitivity	84.21%	84.21%	84.21%	–	–	–
	Specificity	90.00%	90.00%	90.00%	–	–	–

weighted slice enclosing the CST are statistically different between patients and controls and no statistical difference is observed in the occipital lobe slice (Table 6.2).

Similar to the T1-weighted images, the performance of features depends on the direction of GLCM. Here, the features of the GLCM on $P_{0°,1}$ and $P_{45°,1}$ have a higher performance. One can see that in T1-weighted images directions $P_{0°,1}$ and $P_{45°,1}$ also demonstrate higher performance; however, the performance in T1-weighted images is slightly better for direction $P_{45°,1}$. Similarly, by comparing the AUC one can see that both T1-weighted and T2-weighted images demonstrate the lowest performance in direction $P_{90°,1}$. Therefore, both types of images show consistent directionality information.

The highest classification rate of the GLCM features on the T2-weighted images is 82.05% corresponding to $P_{0°,1} : f_4$ higher than the highest classification rate of the GLCM on T1-weighted images. The highest AUC is 0.92 demonstrated by all features of $P_{0°,1}$, and f_9 and f_{10} of $P_{45°,1}$. Similar to T1-weighted images, the performance of the three selected features of the GLCM (f_4, f_9, and f_{10}) are comparable in each direction. Sensitivity and specificity are 84.21% and 95% for $P_{0°,1} : f_4$.

To visualize the power of the texture features, the best features of the GLCM extracted from CST region on T1-weighted and T2-weighted images are depicted in Figure 6.4. These features are computed by $P_{45°,1}$ on the GLCM of T1-weighted images, and $P_{0°,1}$ on the GLCM of T2-weighted images, respectively. The mean and standard deviation of the two groups are also shown

Figure 6.4: The texture feature values for all subjects as well as the mean and the standard deviation of the two groups. The first, second, and third columns represent correlation (f_4), contrast (f_9), and inverse difference moment normalized (f_{10}), respectively. The first row shows the features of the GLCM, $P_{45°,1}$, on the T1-weighted images. The second row represents the features of the GLCM, $P_{0°,1}$, on the T2-weighted images.

for comparison. One can observe that the features extracted from T2-weighted images show a better separation compared to that of T1-weighted images.

Results of GLAM

In order to compute the GLAM features, the shape of the basic neighborhood system should be determined. To find the best performing neighborhood system, all variants of the 3×3 neighborhood systems are examined and the top three neighborhood systems with the highest AUC are chosen. Table 6.3 shows the best basic neighborhood systems and their statistical and classification results on T1-weighted images.

As shown in Table 6.3, there is a statistical difference between the GLAM features of the two groups (p$< 10^{-4}$) in the CST region. The difference is comparable to the statistical difference of the best GLCM on T1-weighted images ($P_{45°,1}$). The classification performance of the GLAM features are also comparable with the best GLCM with a slightly better result (76.92%). The highest AUC is 0.88 for all features of neighborhood structure $N1$ and $N2$, and f_9 and f_{10} in neighborhood structure $N3$. Similar to the GLCM, no significant difference is observed on the features extracted from occipital lobe. By comparing the performance of the best GLAM and the best GLCM, one can see that the GLAM features perform equally or slightly better than those of the GLCM in T1-weighted images.

The best basic neighborhood systems and their statistical and classification results on T2-weighted

75

Table 6.3: Statistical properties (mean±std, and p–value), classification rate, and AUC of the GLAM features extracted from T1-weighted images. Three neighborhood system with the highest AUC are selected. f_4, f_9, and f_{10} represent correlation, contrast, and inverse difference moment normalized, respectively. Sensitivity and specificity are reported for significantly different features.

Slice Location		CST			Occipital Lobe		
GLAM Texture Feature		f_4	f_9	f_{10}	f_4	f_9	f_{10}
N1	Patients	$(9.51\pm0.04)\times10^{-1}$	0.95 ± 0.08	$(999.08\pm0.08)\times10^{-3}$	$(9.38\pm0.07)\times10^{-1}$	1.20 ± 0.14	$(998.84\pm0.13)\times10^{-3}$
	Controls	$(9.42\pm0.06)\times10^{-1}$	1.11 ± 0.11	$(998.93\pm0.10)\times10^{-3}$	$(9.35\pm0.07)\times10^{-1}$	1.25 ± 0.13	$(998.79\pm0.12)\times10^{-3}$
	p–value	$< 10^{-4}$	$< 10^{-4}$	$< 10^{-4}$	0.31	0.38	0.30
	Classification Rate	76.62%	76.69%	76.26%	50.01%	50.36%	49.94%
	AUC	0.88	0.88	0.88	0.58	0.60	0.60
	Sensitivity	78.95%	78.95%	78.95%	–	–	–
	Specificity	90.00%	90.00%	90.00%	–	–	–
N2	Patients	$(9.54\pm0.04)\times10^{-1}$	0.88 ± 0.07	$(999.15\pm0.07)\times10^{-3}$	$(9.42\pm0.07)\times10^{-1}$	1.11 ± 0.12	$(998.92\pm0.12)\times10^{-3}$
	Controls	$(9.47\pm0.05)\times10^{-1}$	1.02 ± 0.10	$(990.01\pm0.10)\times10^{-3}$	$(9.40\pm0.06)\times10^{-1}$	1.16 ± 0.12	$(998.88\pm0.11)\times10^{-3}$
	p–value	$< 10^{-4}$	$< 10^{-4}$	$< 10^{-4}$	0.25	0.27	0.27
	Classification Rate	76.40%	76.92%	76.56%	51.19%	52.24%	51.81%
	AUC	0.88	0.88	0.88	0.60	0.61	0.60
	Sensitivity	84.21%	73.68%	84.21%	–	–	–
	Specificity	85.00%	90.00%	80.00%	–	–	–
N3	Patients	$(9.58\pm0.04)\times10^{-1}$	0.80 ± 0.07	$(999.22\pm0.07)\times10^{-3}$	$(9.47\pm0.06)\times10^{-1}$	1.01 ± 0.11	$(999.02\pm0.11)\times10^{-3}$
	Controls	$(9.51\pm0.05)\times10^{-1}$	0.93 ± 0.09	$(999.10\pm0.09)\times10^{-3}$	$(9.45\pm0.05)\times10^{-1}$	1.06 ± 0.11	$(998.97\pm0.10)\times10^{-3}$
	p–value	$< 10^{-4}$	$< 10^{-4}$	$< 10^{-4}$	0.21	0.26	0.21
	Classification Rate	76.41%	76.57%	75.96%	53.27%	54.32%	53.26%
	AUC	0.87	0.88	0.88	0.62	0.61	0.62
	Sensitivity	84.21%	84.21%	84.21%	–	–	–
	Specificity	85.00%	85.00%	85.00%	–	–	–

Table 6.4: Accuracy, sensitivity, and specificity of the four GLAM features on the T2-weighted images. Four neighborhood system the classification performance of which are the highest are shown. f_4, f_9, and f_{10} represent correlation, contrast, and inverse difference moment normalized, respectively. Sensitivity and specificity are reported for significantly different features.

Slice Location		CST			Occipital Lobe		
GLAM Texture Feature		f_4	f_9	f_{10}	f_4	f_9	f_{10}
N1	Patients	$(8.90\pm0.15)\times10^{-1}$	2.13 ± 0.28	$(997.97\pm0.25)\times10^{-3}$	$(8.49\pm0.25)\times10^{-1}$	2.90 ± 0.46	$(997.24\pm0.42)\times10^{-3}$
	Controls	$(8.58\pm0.18)\times10^{-1}$	2.71 ± 0.31	$(997.45\pm0.28)\times10^{-3}$	$(8.40\pm0.23)\times10^{-1}$	3.07 ± 0.42	$(997.09\pm0.38)\times10^{-3}$
	p–value	$< 10^{-5}$	$< 10^{-5}$	$< 10^{-5}$	0.29	0.33	0.30
	Accuracy	82.15%	81.18%	81.35%	52.15%	52.18%	51.97%
	AUC	0.92	0.93	0.92	0.59	0.60	0.60
	Sensitivity	89.47%	89.47%	89.47%	–	–	–
	Specificity	90.00%	90.00%	90.00%	–	–	–
N2	Patients	$(8.99\pm0.13)\times10^{-1}$	1.95 ± 0.25	$(998.14\pm0.23)\times10^{-3}$	$(8.62\pm0.22)\times10^{-1}$	2.67 ± 0.41	$(997.46\pm0.38)\times10^{-3}$
	Controls	$(8.70\pm0.16)\times10^{-1}$	2.48 ± 0.29	$(997.66\pm0.26)\times10^{-3}$	$(8.53\pm0.21)\times10^{-1}$	2.83 ± 0.37	$(997.32\pm0.34)\times10^{-3}$
	p–value	$< 10^{-5}$	$< 10^{-5}$	$< 10^{-5}$	0.22	0.26	0.25
	Accuracy	80.84%	80.26%	80.75%	52.25%	52.26%	52.15%
	AUC	0.92	0.92	0.92	0.61	0.62	0.61
	Sensitivity	89.47%	89.47%	89.47%	–	–	–
	Specificity	90.00%	90.00%	85.00%	–	–	–
N3	Patients	$(9.01\pm0.15)\times10^{-1}$	1.58 ± 0.21	$(998.48\pm0.19)\times10^{-3}$	$(8.86\pm0.17)\times10^{-1}$	2.20 ± 0.32	$(997.89\pm0.30)\times10^{-3}$
	Controls	$(8.94\pm0.13)\times10^{-1}$	2.03 ± 0.24	$(998.06\pm0.22)\times10^{-3}$	$(8.79\pm0.17)\times10^{-1}$	2.33 ± 0.31	$(997.77\pm0.29)\times10^{-3}$
	p–value	$< 10^{-5}$	$< 10^{-5}$	$< 10^{-5}$	0.19	0.26	0.19
	Accuracy	80.78%	80.22%	79.82%	53.19%	54.48%	54.38%
	AUC	0.92	0.92	0.92	0.61	0.62	0.62
	Sensitivity	84.21%	78.95%	84.21%	–	–	–
	Specificity	95.00%	95.00%	90.00%	–	–	–

images are shown in Table 6.4. Similar to the GLCM features of T2-weighted images, there is a statistical difference between the GLAM features of the ALS patients and that of the control subjects ($p< 10^{-5}$). One of the best neighborhood systems for T2-weighted is $N3$, which includes only one neighborhood pixel. One may note that the GLAM with one neighborhood pixel is equivalent to the GLCM. For instance, in this experiment $N3$ is equivalent to $P_{180^\circ,1}$ (or $P_{0^\circ,1}$) in the GLCM. Comparing the statistical properties and the AUC, one can see that the features of GLCM $P_{180^\circ,1}$ (Table 6.2) are equivalent to the GLAM features computed by $N3$ neighborhood system (Table 6.4). In other words, since the GLAM is a generalization of the GLCM, it automatically computes the
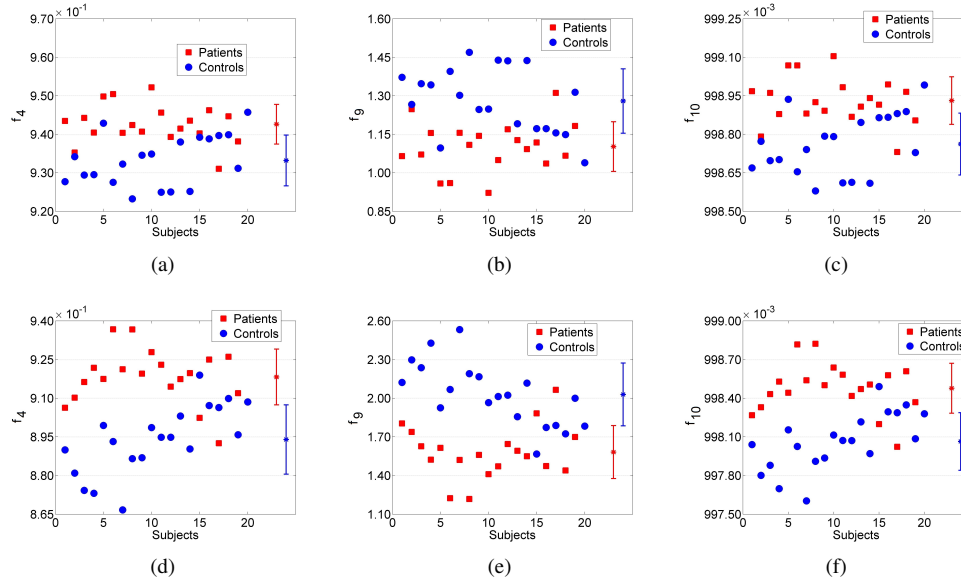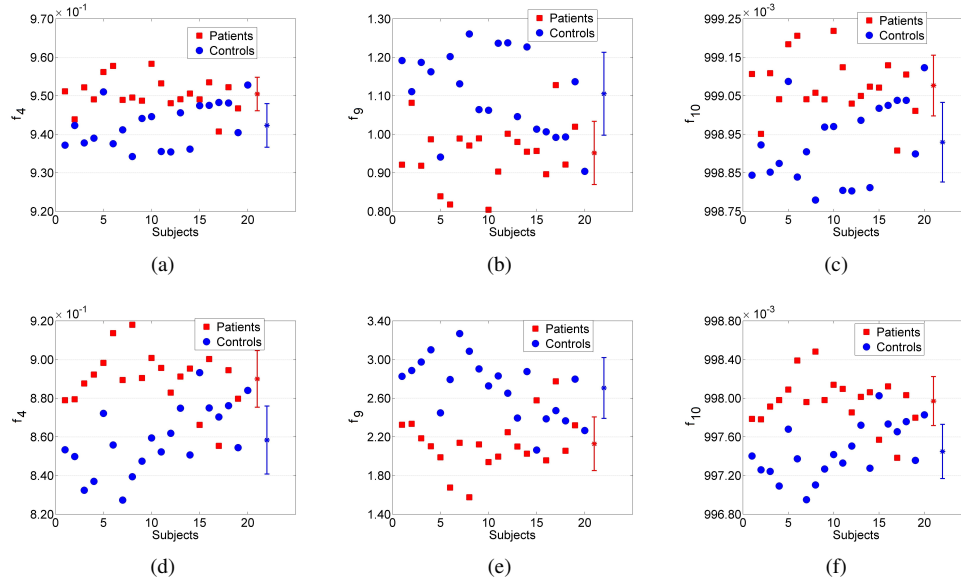
Figure 6.5: The texture feature values for all subjects as well as the mean and the standard deviation of the two groups. The first row depicts the features of the GLAM with $N1$ (Table 6.3), on the T1-weighted images. The second row shows the features of the GLAM with $N2$ (Table 6.4), on the T2-weighted images.

Table 6.5: Statistical analysis and classification results on the ROI-PF measured on the T1-weighted images of ALS patients and control subjects.

Slice Location	CST	Occipital Lobe
Patients	0.79 ± 0.05	0.74 ± 0.08
Controls	0.84 ± 0.04	0.78 ± 0.07
p–value	0.001	0.152
Accuracy	71.16	56.45
AUC	0.80	0.63
Sensitivity	57.89	–
Specificity	95.00	–

GLCM features. The highest classification accuracy is 82.15% corresponding to f_4 of $N1$ neighborhood system. The highest AUC is 0.93 which is slightly higher (0.01) than the highest AUC of GLCM. As expected, there is no statistical difference in the occipital lobe area.

The best features of the GLAM extracted from CST region on T1-weighted and T2-weighted images are depicted in Figure 6.5. These features are computed by $N1$ on the GACM of T1-weighted and T2-weighted images. The mean and standard deviation of the two groups are also shown for comparison. One can observe that the features extracted from T2-weighted images show a better separation compared to that of T1-weighted images.

Results of ROI-PF

The last analysis is the ROI-PF measured on the T1-weighted images of the two groups. As shown in Table 6.5, there is mild atrophy in the CST slice in patients as evident by a 6% reduction in ROI-PF. A reduction in ROI-PF calculated from the occipital lobe is not statistically significant (Table 6.5)
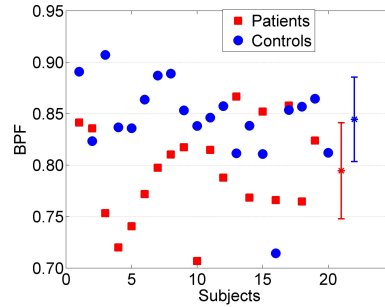
Figure 6.6: The ROI-PF measured on the T1-weighted MR images.

A moderately good separation exist in the ROI-PF between groups on the CST slice (Figure6.6). Increased variability is evident in the ALS group compared to the control group which have a more uniform distribution with the exception of a single outlier (case 16). Notably, this case is not an extreme outlier in the texture analyses.

Group difference in mean ROI-PF, its classification accuracy and the AUC are lower compared to those of the GLCM texture features. Comparing the ROI-PF (Figure 6.6) with the features of the GLCM and the GLAM (Figures 6.4 and 6.5) shows a better separation in texture features between the two groups.

6.2.3 Discussion

So far, the usage of conventional MR images is limited to ruling out diseases mimicking ALS, as they have had poor diagnostic accuracy. In this section the power of 2D texture analysis to differentiate the images of ALS patients versus control subjects is examined. The GLCM and the GLAM texture analysis methods could achieve high classification rates with more than 82% accuracy and an AUC of 0.93. The significance of this work is that it uses conventional T1-weighted and T2-weighted MR images which are routine and widely available acquisition methods.

The potential diagnostic capacity of non-volumetric imaging been alluded to by reports in a few studies of varying sensitivities and specificities. For example, recent meta-analysis on pooled data from 30 different DTI studies [92] reported sensitivity of 0.65, specificity of 0.67, and AUC of 0.76, concluding that the capability of DTI to make a diagnosis of ALS is only modest.

To our best knowledge, the texture analysis capability of the gray level Aura matrix (GLAM) has not been used to study abnormalities in a disease. It can be observed that the GLAM features are superior to that of the GLCM. The reason is that they are the generalization of the GLCM. In other words, the GLAM features include the GLCM features as well (e.g., the basic neighborhood system with one neighbor equivalent to the GLCM). As a result, using the GLAM can provide similar or better performance compared to the GLCM, though the improvement is very slight in our experiments. One may also note that GLAM is computationally more costly than the GLCM, as it needs to consider different neighborhood systems.

78

BPF has previously shown global cerebral atrophy in ALS [245; 177]. Although ROI-PF (the amended BPF to analyze the same ROI used by texture methods) is reduced in the CST slice, it is an inferior discriminator compared to texture features as indicated by the lower classification rate and AUC.

This study has some limitations. Image acquisition required user input to angulate the coronal slices into the plane approximately in parallel to the CST. The imaging pipeline analysis is not completely user-independent as the ROI was manually delineated. The 3D voxel based texture analysis in the next section addresses these issues.

6.3   3D Texture Analysis

In this section our proposed voxel based texture analysis method (Chapter 5) is applied to study ALS. The same database which is used for 2D analysis (Section 6.2.2) is employed here. In addition to the proposed method, the data is analyzed by VBM. The processing procedure is explained in Section 6.3.1

6.3.1   Processing Procedure

The VBM8 toolbox[1] of the SPM8 software[2] has been used to carry out preprocessing. The procedure involves the following steps. First, the brains are extracted from the images, the intensities of the images are corrected (i.e., standardization, or bias correction), and the brains are segmented into GM, WM and CSF volume probability maps. Then, the high-dimensional DARTEL method [20] is performed to register the images to the MNI152 atlas. Finally, the images are smoothed by a Gaussian kernel with a fullwidth half-maximum (FWHM) of 8 mm.

To perform VBM analysis, the smoothed WM and GM images of the patients and controls undergo the voxel-wise two sample t-test provided by the SMP8 software. The familywise error (FWE) is performed on the statistics to correct for multiple comparisons. The significance level is set to $p < 0.05$ after correction for multiple comparisons.

The output of the DARTEL registration step (before smoothing) is used for voxel based texture analysis. Since VGLCM-TOP-3D has a better performance, it is used for texture computation. Eight texture features (f_1 to f_8 in Table 2.1) are computed in the stereotaxic space. Here, $d = 1$, $R = 3$, and 8 gray levels are used for VGLCM-TOP-3D.

Similar to VBM, statistical analysis is performed by SPM8; however, f-test is used for texture analysis. The reason is that the texture features can have higher or lower values in comparison between the patient and healthy groups.

---

[1]http://dbm.neuro.uni-jena.de/vbm/
[2]http://www.fil.ion.ucl.ac.uk/spm/

Figure 6.7: Statistical map of VGLCM-TOP-3D after FWE correction at $p < 0.05$: (A) f_1: auto-correlation, (B) f_6: sum of squares: variance, (C) f_7: sum average, and (D) f_8: sum variance. The reported clusters appear at least on three texture statistical maps.

6.3.2 Evaluation of 3D Methods

In this section, the results of the VGLCM-TOP-3D method and those of the VBM are presented. The outputs are 3D statistical maps showing the differences between the healthy and ALS groups.

Results of Voxel-based Texture Analysis

As mentioned before, eight texture features are computed for analysis. Four features including autocorrelation (f_1), sum of squares variance (f_6), sum average (f_7), and sum variance (f_8) produce statistical maps (corrected by FEW) that are significantly different between the control and ALS patient groups. The other texture features (f_2, f_3, f_4, and f_5) do not provide difference between the two groups. Figure 6.7 shows the statistical map for f_1, f_6, f_7, and f_8 after FWE correction at $p < 0.05$.

Among the features providing statistical significance, sum variance (f_8) provides the smallest p-value. As one can see, the significant regions on the statistical maps of the textures are quite similar. Several regions are reported consistently by at least three out of four texture features including
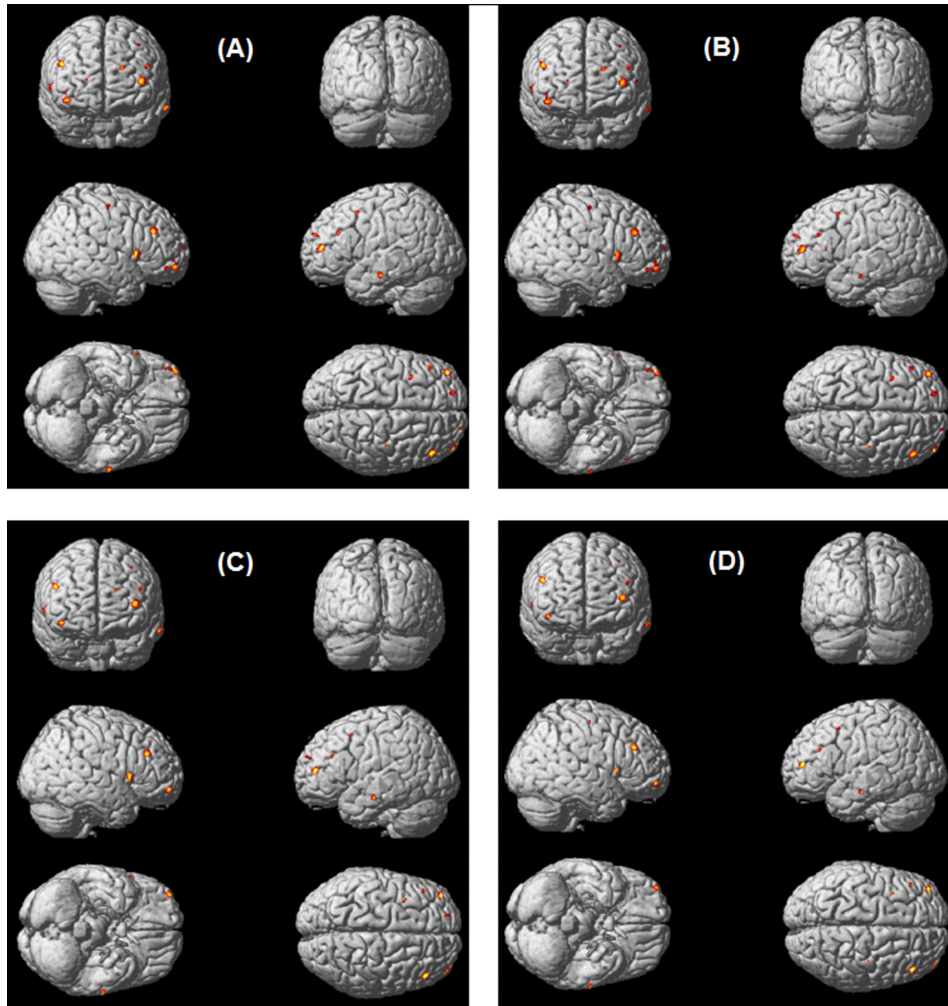
Figure 6.8: Regions with statistical difference rendered on a 3D brain: (A) f_1:autocorrelation, (B) f_6: sum of squares: variance, (C) f_7: sum average, and (D) f_8: sum variance. (FWE correction at $p < 0.05$).

middle frontal gyrus, insula, inferior frontal gyrus, corpus callosum, superior temporal gyrus, and precentral gyrus. Figure 6.8 shows the regions with statistical difference rendered on a 3D brain.

To further explore the regions with statistical difference, the uncorrected p-value is set to 0.00001. Figure 6.9 shows this statistical map. This statistical map represents an extension of what is shown in Figure 6.7. Similarly, the regions with small p-values are quite similar for all the four texture features. However, there are some regions that do not appear at least by three texture features. The 3D rendered images of these regions are shown Figure 6.10.

Results of VBM

The VBM analysis of WM and GM did not show any statistical difference between the ALS patient and the control groups (after applying FWE). The statistical map for the statistics at uncorrected
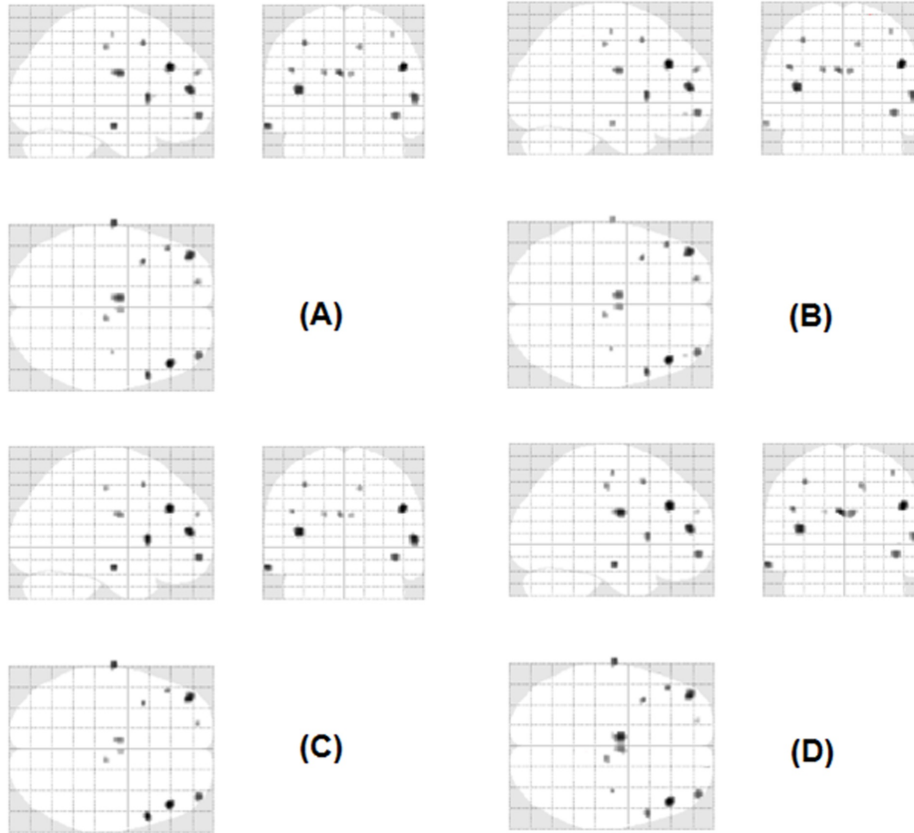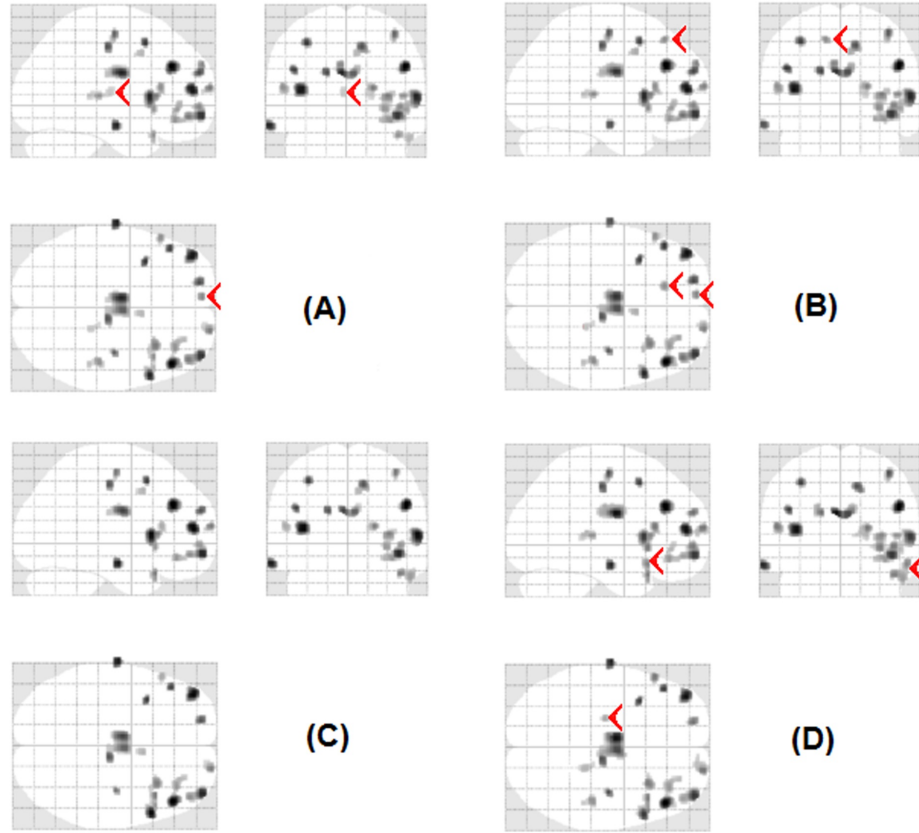
Figure 6.9: Statistical map of VGLCM-TOP-3D at uncorrected $p < 0.00001$: (A) f_1: autocorrelation, (B) f_6: sum of squares: variance, (C) f_7: sum average, and (D) f_8: sum variance. The clusters that do not appear on at least three of the texture features are marked by red arrows.

$p < 0.001$ is show in Figure 6.11.

To better compare the results of VBM and VGLCM-TOP-3D, the important regions of interest with small p-values for each method are shown in Table 6.6. The result of the VGLCM-TOP-3D is presented after FEW correction, and at uncorrected $p = 0.00001$. As one can see, the regions with statistical difference in VGLCM-TOP-3D have a small p-value on VBM statistical map on either WM or GM; however, these regions could not be detected by VBM as statistically different regions (after correction for multiple comparisons).

6.3.3 Discussion

Since this is the first voxel based texture analysis the author could not find any similar method to compare other than VBM. Nonetheless, there are several indications that help us to argue that the results are valid. First, the regions with statistical significance in texture analysis occur in the same regions distinguished by VBM analysis (at uncorrected $p < 0.001$). The smoothing step in VBM which is performed to alleviate misregistration errors can wash out positive results in regions
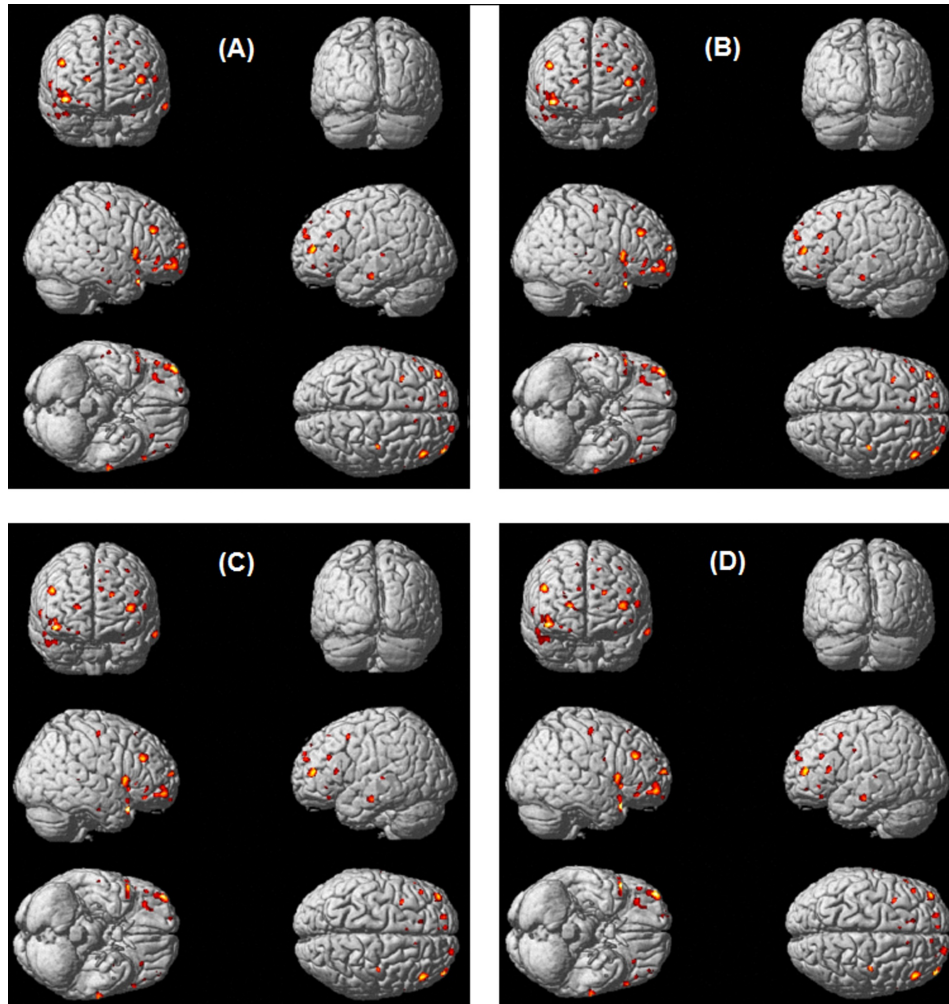
Figure 6.10: Statistical map of VGLCM-TOP-3D at uncorrected $p < 0.00001$ rendered on a 3D brain: (A) f_1: autocorrelation, (B) f_6: sum of squares: variance, (C) f_7: sum average, and (D) f_8: sum variance.

with real difference. In other words, the regions distinguished by small uncorrected p-values in VBM indicate both regions that are different due to pathology and the regions different due to misregistration. For instance, one can see the middle occipital gyrus as a region with statistically significant differences at a small p-value detected by VBM which is unlikely to be affected by ALS disease but could be a result of misregistration errors. On the other hand, there are some regions (e.g., Corpus Callosum, Precentral Gyrus, and regions located in frontal and temporal lobes) that are very likely to be affected in ALS but are not statistically significant due to the smoothing step. Texture analysis does not apply a smoothing step, and this may be the reason why it reports the latter group with statistical significance.

The second reason indicating the validity of the texture analysis is that four features provided quite similar regions. Since the computation of each texture feature is different (Table 2.1), similar
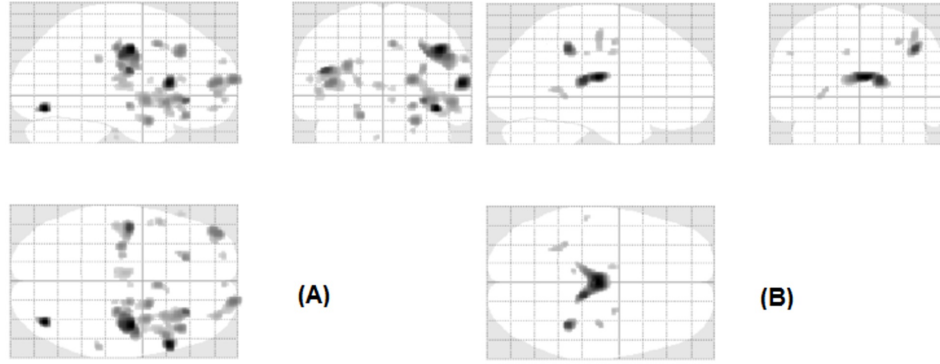
Figure 6.11: VBM analysis on GM (A) and WM (B) comparing patients with ALS to healthy controls (uncorrected at $p < 0.001$). The corrected statistical map (FEW at $p < 0.05$) did not reveal any significant differences.

Table 6.6: Regional differences identified by VGLCM-TOP-3D compared to VBM. The laterality of the findings is indicated by R (Right), L (Left), R/L (Right and Left).

	Analysis Method	VGLCM-TOP-3D								VBM	
	Statistical Significance	Uncorrected $p < 0.00001$				FEW $p < 0.05$				Uncorrected $p < 0.001$	
	Processed Feature / Region	f_1	f_6	f_7	f_8	f_1	f_6	f_7	f_8	GM	WM
1	Middle Frontal Gyrus	R/L	R/L	R/L	R/L	R/L	R/L	R/L	R/L	R/L	
2	Insula	R	R	R	R	R	R		R	R/L	
3	Inferior Frontal Gyrus	R/L	R/L	R/L	R/L	R	R	R	R	R/L	
4	Corpus Callosum	R/L	R/L	R/L	R/L	R/L	R/L	R/L	R/L		R/L
5	Superior Temporal Gyrus	R	R	R	R					R	
6	Middle Temporal Gyrus	L	L	L	L	L	L	L	L		
7	Thalamus	R/L	R		R					R/L	R/L
8	Superior Frontal Gyrus	R/L	R/L	L	L	R/L	L	L	L	R	
9	Precentral Gyrus	R	R	R	R	R	R		R	R	R
10	Cingulate Gyrus	R	R	R	R					R	
11	Middle Occipital Gyrus									R	
12	Parahippocampal Gyrus									R	
13	Inferior Parietal Lobule									R	R

statistical maps possibly indicate differences of local texture changed due to pathological changes of the brain.

Finally, the regions with statistical significance in our method have been repeatedly reported by ALS studies using different methods such as VBM, SBM, and advanced MRI techniques (i.e., DTI, FMRI, and MRS). The regions with statistical significance between healthy subjects and ALS patients include middle frontal gyrus [4; 336; 47], inferior frontal gyrus [8; 339; 47; 4], insula [303; 304; 9; 339], corpus callosum [8; 301; 339], superior temporal gyrus [8; 9; 339; 336], middle temporal gyrus [43; 8; 245; 4], thalamus [301; 339; 47], superior frontal gyrus [47; 4], precentral gyrus [9; 308; 339; 336; 47], and cingulate gyrus [213; 4; 329; 120]. Table 6.7 shows these studies and the methods used by them for analysis.

This study suggests texture as a potential biomarker to quantify cerebral degeneration in ALS.

Table 6.7: Regions with statistical significance (column one) found by the proposed method are also reported by other studies with different imaging methods.

	VBM	DTI	SBM	fMRI	MRS
Middle Frontal Gyrus	[47]			[4; 336]	
Insula	[339]	[304; 303]	[9]		
Inferior Frontal Gyrus	[8; 47; 339]	[8]		[4]	
Corpus Callosum	[177]	[8; 301; 339]			
Superior Temporal Gyrus	[8; 47]	[8; 339]	[9]		
Middle Temporal Gyrus	[245]	[43; 8]		[4]	
Thalamus	[47]	[301; 339]			
Superior Frontal Gyrus	[47]			[4]	
Precentral Gyrus	[47]	[339]	[9]	[336]	[308]
Cingulate Gyrus	[120]	[213]		[4]	[329]

The results of the analysis support the view that ALS is a multi-system disease spread beyond the motor cortex region.

6.4 Summary

In this chapter the capability of texture analysis as a potential biomarker for cerebral degeneration in ALS has been explored. First, two well known 2D methods, the GLCM and GLAM, were applied to conventional T1-weighted and T2-weighted MR images. The statistical properties of the texture features showed a significant difference between patients with ALS and control subjects suggesting that both methods are able to differentiate between the groups. It was observed that the GLAM features slightly outperform the GLCM features. The classification showed high performances with higher accuracy, sensitivity, and specificity for T2-weighted images compared to that for T1-weighted images.

For 3D analysis VGLCM-TOP-3D was applied to T1-weighted MR images to detect regions affected by ALS. The detected regions include middle frontal gyrus, inferior frontal gyrus, insula, corpus callosum, superior temporal gyrus, middle temporal gyrus, thalamus, superior frontal gyrus, precentral gyrus, and cingulate gyrus. These findings are in concordance with other findings in ALS suggesting that ALS is a multi-system disease. It was also observed that VBM is not able to detect any difference after FWE correction. The evaluation results support that the proposed texture analysis method can serve as a tool to detect and monitor ALS disease.

Nevertheless, the methods used in this chapter to analyze cerebral degeneration in ALS are quite old and sensitive to imaging effects such as noise. This further motivates the development of novel methods which are not only more accurate but are also more robust to imaging effects. In the next chapters, an effective and robust approach for texture analysis is introduced.

Chapter 7

Robust 2D Texture Features

7.1   Introduction

Properly chosen texture features should be able to discriminate between patterns that are similar. In addition, texture features should be robust to imaging distortions and be ideally invariant to geometrical transformations. In this chapter, our methods to extract texture features are presented. The proposed methods are not only highly accurate but also robust to imaging effects.

Among different transformation invariance, rotation invariance is more popular. The reason is that the rotation invariant features can be easily extended to become affine invariant [248]. The affine transformation includes transformations such as translation, change of scale, reflection, rotation, and compositions of them. As a result, the features can be used in a wide range of applications. Some examples of advanced applications include sparse texture classification [203] and image matching [248] in which rotation invariant features are employed to obtain affine invariance. In these applications, a set of elliptical regions are found using region detection methods such as Hessian [248], or Harris [246] region detectors. Each elliptical region is normalized to a circle, and rotation invariant features are computed on the normalized circle.

Considering neighbors on a circle (or multiple circles) around a pixel is a popular approach in rotation invariant methods. The values of the circular neighbors are usually encoded in two ways:

1. Applying a threshold (e.g., the center pixel's intensity) similar to the LBP [267] and its variants,

2. Transforming the values into frequency components as used by some texture classification methods [17; 216; 226; 225].

It is demonstrated that the latter approach has several advantages compared to the first one [225]. The frequency components of the circular sampling function are called the Local Frequency Descriptor (LFD) in this thesis. It is shown how the magnitude and the phase of the LFD are used to define robust texture features.

In Section 7.2 the LFD is defined and its advantages are compared to the LBP. The first texture
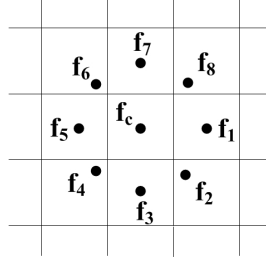
Figure 7.1: A circular sampling with radius of one and sample size of 8.

classification method which is based on the magnitude of LFD is explained in Section 7.3. This method has been presented in [225]. The second proposed method which uses both magnitude and phase of LFD is demonstrated in Section 7.4. The method has been published in [226]. In Section 7.5, it is explained that the LFD can be used to extract image gradient information and the LFD Gradient (LFDG) operator is introduced. This approach has been presented in [228; 227]. The experimental results to evaluate the texture methods and the gradient operator are given in Sections 7.6, and 7.7, respectively. The summary is presented in Section 7.8.

7.2 Local Frequency Descriptor (LFD) in 2D

As mentioned before, sampling on a circle (or multiple circles) around a pixel is a popular approach in many rotation invariant methods. Consider P points with gray values of $f_1, ..., f_P$ on a circle with radius R at center pixel, f_c. The gray level value of a sample, f_i, is determined by interpolation if it is not located at the center of a pixel. Figure 7.1 shows a sampling with radius of one and sample size of 8.

The local circular function at a pixel, $LCF_{P,R} = (f_1, ..., f_P)$, provides useful information. Some methods such as Local Binary Patterns (LBP) and its variants apply a threshold (the gray value of the center pixel, f_c) and binomial factor 2^n to construct the binary patterns from this function:

$$LBP_{P,R} = \sum_{k=1}^{P} s(f_k - f_c).2^k, s(x) = \begin{cases} 1 & x \geq 0 \\ 0 & x < 0 \end{cases}, \qquad (7.1)$$

where s is the sign function.

Similarly, CLBP uses two different thresholds to make two binary patterns from this function using $CLBP\_S$ and $CLBP\_M$ operations. Figure 7.2 shows an example illustrating how $CLBP\_S$ and $CLBP\_M$ generate two different binary patterns from the same function $LCF_{P,R}$.

Although LBP and its variants are very popular they suffer from several drawbacks. One of the drawbacks is the exponential growth of the binary patterns which results in a large feature set (i.e., $2^P - 1$ patterns for a given P). The LBP-based methods are also sensitive to noise, because a small change in the center pixel, f_c, may result in a drastic change of the patterns. Finally, thresholding the $LCF_{P,R}$ function removes some important information. For instance, consider two different circular
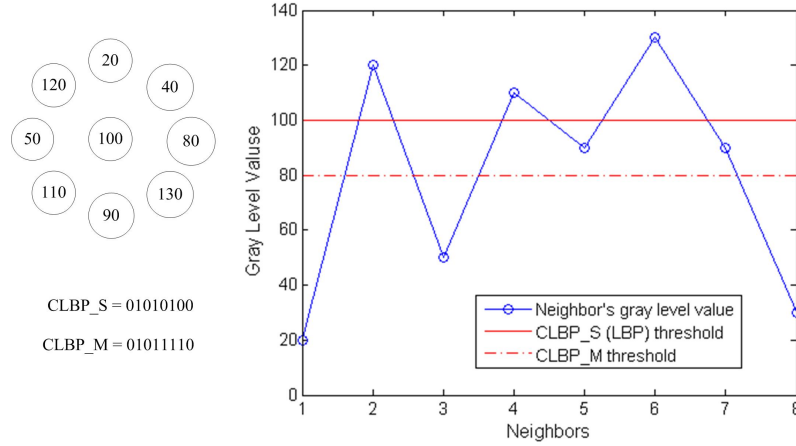
Figure 7.2: Thresholding the $LCF_{P,R}$ function to make binary patterns. Top left, the value of the center pixel and its eight neighbors located on a circle with radius of one. Right, the function and the two thresholds used in $CLBP\_S$ (LBP) and $CLBP\_M$. Bottom left, the two binary patterns generated by $CLBP\_S$ and $CLBP\_M$ [225].

functions, $F1 = \{80, 110, 90, 120, 130, 110, 70, 50\}$ and $F2 = \{50, 130, 75, 150, 110, 130, 80, 90\}$ with $f_c = 100$. Using the center pixel as threshold results in the same LBP code (i.e., 01011100).

The proposed LFD method uses the same circular sampling method. However, to address the mentioned issues of the LBP-based methods, the sampling function, $LCF_{P,R}$, is transformed into the frequency domain using the 1D Discrete Fourier Transform (DFT):

$$LFD(n) = \sum_{k=1}^{P} f_k . e^{\frac{-2\pi i(k-1)(n-1)}{P}}, (n = 1, ..., P),\tag{7.2}$$

where the Local Frequency Descriptor, $LFD(n)$, consists of P complex numbers representing the frequency components of the $LCF_{P,R}$ function. Since the $LCF_{P,R}$ function consists of real numbers, the frequency components are conjugate symmetric about the DC component. That is, the 2nd and the Pth components (similarly the 3rd and the $(P-1)^{th}$, and so on) have the same magnitude but opposite phase.

It is shown later that the low frequency components of LFD comprise the majority of texture signals and by using a few low frequency components of LFD the important features of textures are captured. Hence, a compact feature set can be constructed to address the exponential growth of LBP. In addition, the low frequency components of LFD are not affected by noise and, therefore, the features are robust. Finally, unlike to thresholding, the Fourier transform keeps the important information of textures. For instance, in the $F1$ and $F2$ functions mentioned before, applying the Fourier transform to the two functions results in frequency components FrqComp1=(760.00, $-99.50 - 69.50i$, $50.00 - 50.00i$, $-0.50 - 29.50i$, -20.00, $-0.50 + 29.50i$, $50.00 + 50.00i$, $-99.50 + 69.50i$), and FrqComp2=(815.00, $-102.43 - 37.43i$, $5.00 - 20.00i$, $-17.57 - 47.43i$, -185.00, $-17.57 + 47.43i$, $5.00 + 20.00i$, $-102.43 + 37.43i$), respectively, which are not identical.
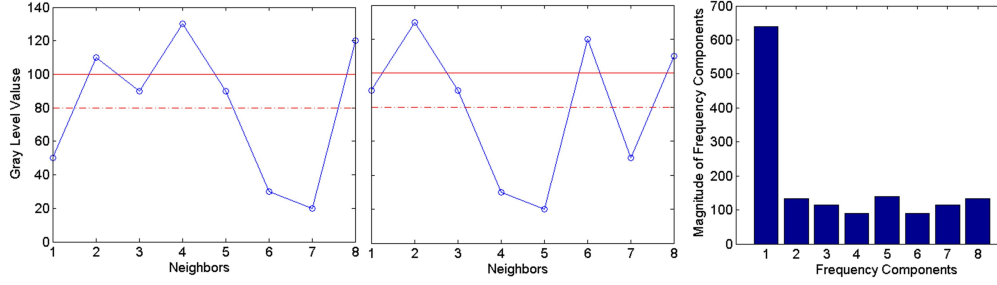
Figure 7.3: Left and middle, the function shown in Figure 7.2 is rotated by $45°$ and $90°$ respectively. Right, the magnitude of the frequency components of the function and its rotated versions [225].

In the next two sections texture feature extraction using the magnitude and phase of LFD is presented. Then, it is demonstrated that the *second* frequency component (or equivalently the Pth component) of LFD is highly affected by the local edge around the pixel and it can be used as an operator to extract image gradient information.

7.3 LFD Magnitude based Features (LFD-MF)

In this section, our first set of texture features, the LFD Magnitude based Feature set (LFD-MF) [225], is introduced. The magnitude of the LFD carries important information which are invariant to rotation and hence, it is useful to construct texture features. Indeed, rotation induces a circular shift on the LCF function, but a circular shift does not change the magnitude of its frequency components. Figure 7.3 shows an example in which the function shown in Figure 7.2 is rotated by $45°$ and $90°$. It can be verified that the magnitude of LFD for all rotated functions remain unchanged.

As mentioned before, applying the Fourier transform on circular samples has been used in research studies [17; 75; 216]. In contrast to these approaches, not all of the frequency components of the Fourier transform are used. It is observed that the low frequency components capture the majority of the energy of the signals in textures. As a result, the method starts with the low frequency components and gradually adds higher frequency components until the best performance is reached. By using low frequency components, the method can effectively suppress the effect of noise which usually appears in high frequencies. The proposed method also applies rotation invariant bandpass filters on the 2D Fourier transform of the LFD to further remove noisy information (which is explained later). Figure 7.4 shows some sample textures and the magnitude of the first three frequency components computed by (P,R)=(8,1).

The local frequencies capture local texture properties. To analyze these properties each frequency channel is considered separately. It is noteworthy that rotation has two consequences. First, the function $LCF_{(P,R)}$ undergoes a circular shift, and second, the location of the function changes (Figure 7.5). As a result, although the magnitude of the LFD does not change by rotation, the rotation of the location should be addressed.
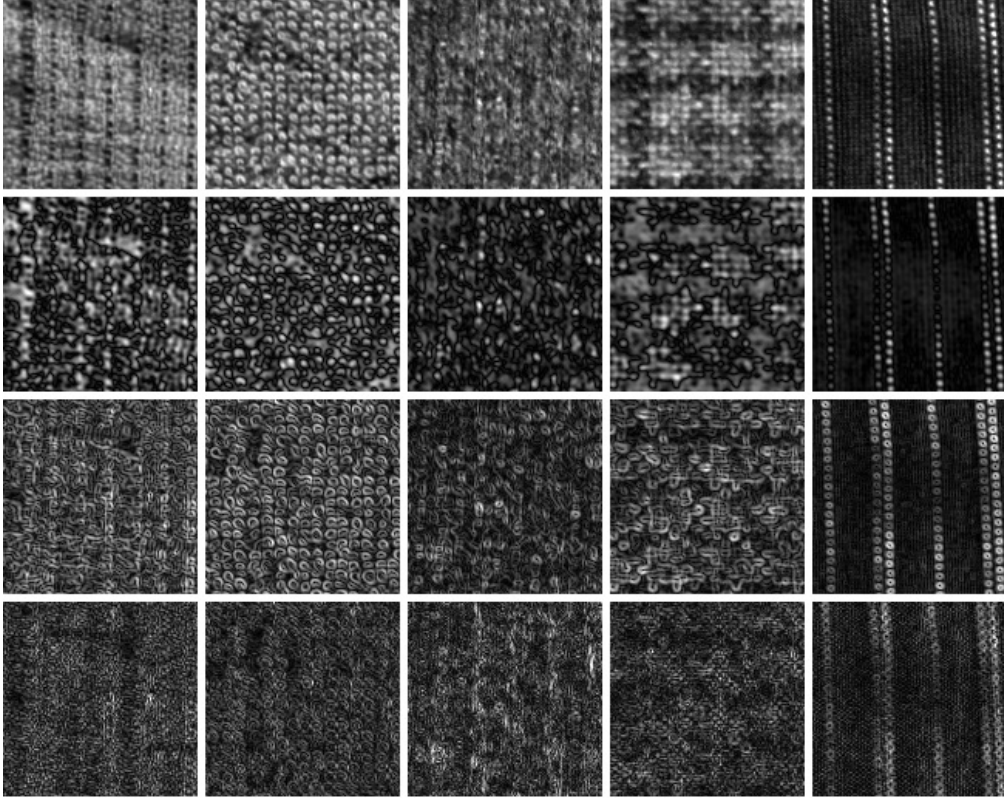
Figure 7.4: Five texture samples and their first three frequency channels. The first row shows five texture samples taken from Outex dataset (see, Section 7.6). The second, third, and fourth rows show the first, second, and third frequency channels of the textures computed by (P,R)=(8,1) [225].
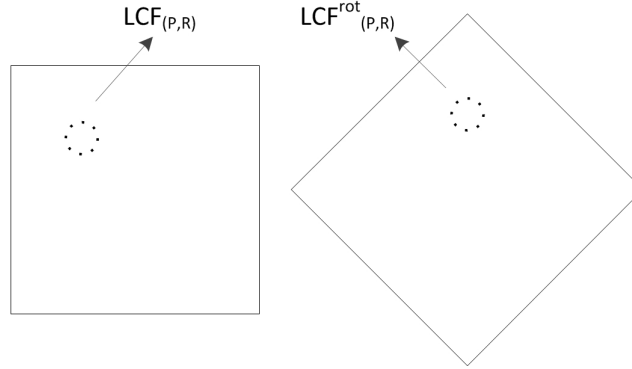
Figure 7.5: A sample $LCF_{(P,R)}$ function when an image is rotated. The rotated version of the function, $LCF_{(P,R)}^{rot}$, is different from $LCF_{(P,R)}$ by a circular shift and its location is rotated [225].

To address the rotation of location and to produce noise robust features, each frequency channel undergoes the 2D DFT and then different filters (circular and directional) are applied to capture textural features. The 2D frequency spectrum of each channel CH_n is computed as:

$$CH_n(k,l) = \sum_{x=0}^{X-1} \sum_{y=0}^{Y-1} |LFD(n)_{(x,y)}|.e^{-2\pi i(\frac{xk}{X} + \frac{yl}{Y})}, \qquad (7.3)$$

90

where X and Y are the number of columns and rows respectively, assuming that the coordinate system ranges from [0,0] to [X-1,Y-1], and $|LFD(n)_{(x,y)}|$ is the magnitude of the nth frequency component of LFD computed at pixel (x,y). It is noteworthy that before applying filters, the spectrum is circularly shifted such that the frequency component (0,0) is translated to the center of the spectrum.

7.3.1 Disk Filters

To define rotation invariant features, disk shape filters are applied to the spectrum of the frequency channels defined in Eq. 7.3. The disk filters are defined as:

$$D_{r_1, r_2}(x, y) = \begin{cases} 1 & \text{if } r_1 \leq \sqrt{x^2 + y^2} \leq r_2 \\ 0 & \text{otherwise,} \end{cases}$$

(7.4)

where r_1 and r_2 are the radii representing the inner and outer boundaries of the disk. The features computed by applying these band-pass filters to the magnitude of spectrum of frequency channels CH_n are called LFD_C (C stands for Circular filter used for computing the features) in this thesis:

$$LFD\_C(r_1, r_2, n) = \frac{\sum\limits_{k=-K/2}^{K/2-1} \sum\limits_{l=-L/2}^{L/2-1} |CH_n(k, l)|.D_{r_1, r_2}(k, l)}{\sum\limits_{k=-K/2}^{K/2-1} \sum\limits_{l=-L/2}^{L/2-1} D_{r_1, r_2}(k, l)},$$

(7.5)

where $|CH_n|$ is the magnitude of the shifted spectrum of the frequency channels computed by Eq. (7.3) and K and L are the number of columns and rows, respectively. The factor in the denominator averages the response of the disk filter and removes the effect of the disk's size.

7.3.2 Directional Filters

Although using disk shape filters makes the features rotation invariant, the directionality information of the spectrum is ignored. In fact, some textures have directionality and capturing that information can lead to better discrimination. Figure 7.6 shows an example in which the texture has directional information appeared in the spectrum of the frequency channels.

To capture the directionality information, directional filters are used. These filters are inspired by the work of Varma and Zisserman [356]. The directional filter-bank are defined by means of Gaussian filters at multiple orientations:

$$G_{\theta, \sigma_1, \sigma_2}(x, y) = \frac{1}{2\pi\sigma_1\sigma_2} e^{-\left(\frac{(x\cos(\theta) - y\sin(\theta))^2}{2\sigma_1^2} + \frac{(x\sin(\theta) + y\cos(\theta))^2}{2\sigma_2^2}\right)}$$

(7.6)

where θ is the angle of the filter, and σ_1 and σ_2 are the parameters controlling the width and length of the filter, respectively. These filters are combined with the disk filters (Eq. 7.4) to create directional bandpass filters. The combination of the disk and Gaussian filters (called DG here) are formally defined as the multiplication of the two filters:

$$DG_{\theta, \sigma_1, \sigma_2, r_1, r_2}(x, y) = D_{r_1, r_2}(x, y) \times G_{\theta, \sigma_1, \sigma_2}(x, y).$$

(7.7)
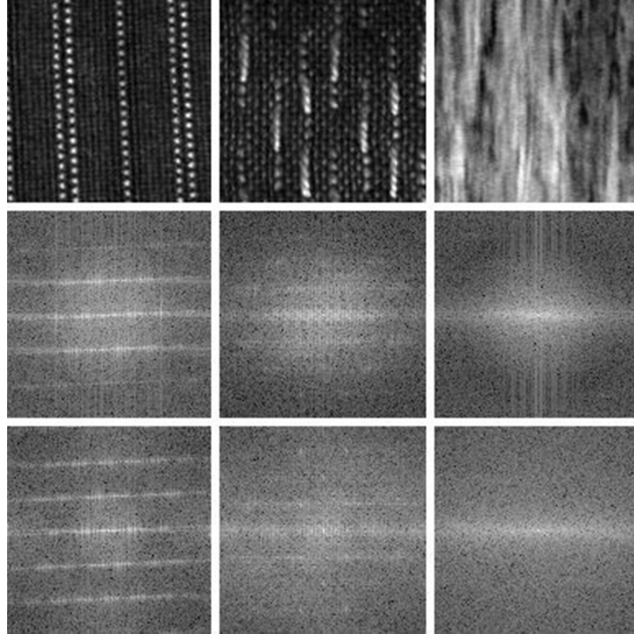
Figure 7.6: Directionality of textures. The first row shows three texture samples taken from Outex dataset. The second and third rows show the logarithm of the magnitude of CH_1 and CH_2 computed by (N,R)=(8,1) [225].
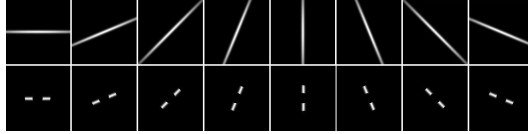
Figure 7.7: Directional filters equally distributed in eight directions. First row, directional Gaussian filters. Second row bandpass directional Gaussian filters [225].

Figure 7.7 shows the directional and directional bandpass Gaussian filters. The first row consists of directional Gaussian filters with $\sigma_1 = 64$ and $\sigma_2 = 2$ equally distributed on eight directions. The second row shows the bandpass version of the same filters.

These directional bandpass filters are applied to the spectrum of frequency channels CH_n. However, to have rotation invariant features, the maximum, the minimum, and the median responses are considered. The idea is similar to the work of Varma and Zisserman [356]; however, in their work only the maximum response is considered. It has been observed that similar to the maximum response, the minimum and median responses carry useful texture information and improve the classification rate. The directional features ($LFD\_D(\theta, \sigma_1, \sigma_2, r_1, r_2)$) produced by directional bandpass Gaussian filters are formally defined as (the subscript variables $r_1, r_2, \theta, \sigma_1$, and σ_2 are dropped from the notation of DG and LFD_D for brevity):

$$LFD\_D_{min} = \min_{\theta \in \Theta} \sum_{k=-K/2}^{K/2-1} \sum_{l=-L/2}^{L/2-1} |CH_n(k,l)|.DG(k,l) \tag{7.8}$$

92
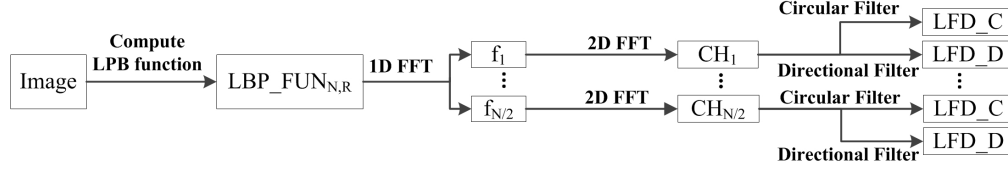
Figure 7.8: The flowchart of the proposed method. The final feature vector consists of LFD_C, and LFD_D [225].

$$LFD\_D_{max} = \max_{\theta \in \Theta} \sum_{k=-K/2}^{K/2-1} \sum_{l=-L/2}^{L/2-1} |CH_n(k,l)|.DG(k,l) \tag{7.9}$$

$$LFD\_D_{med} = \underset{\theta \in \Theta}{\text{median}} \sum_{k=-K/2}^{K/2-1} \sum_{l=-L/2}^{L/2-1} |CH_n(k,l)|.DG(k,l), \tag{7.10}$$

where Θ is the set of directions (e.g., for a set of eight directions $\Theta = \{0, 2\pi/8, ..., 14\pi/8\}$).

The final feature vector consists of the two sets of features: $LFD\_C(r_1, r_2, n)$, and $LFD\_D(r_1, r_2, n)$. Figure 7.8 illustrates the flowchart of the proposed method. The details of the implementation are explained in the next section.

7.3.3 Implementation Details

The implementation is done in Matlab. In the first step, images are normalized to have zero mean and unit variance. The normalization makes the features invariant to linear changes of illumination. In the next step, the local frequency channels are computed using Eqs. 7.2 and 7.3. The number and size of the disk filters depend on the size and content of textures. The datasets that are used in the experiments consist of images of two different sizes: 128×128 and 200×200. In this thesis, the radii used for the disks are chosen empirically as follows: the first disk has an inner radius of 10 and outer radius of 18. The other disk filters are constructed using non-overlapping disks with inner/outer radii starting from 18/21 with an increment of 3. For textures of size 128×128, 10 concentric disks are considered covering an area with inner radius of 10 and outer radius of 45. For images of 200×200 size, 20 concentric disks are used which results in a disk area with inner radius of 10 and outer radius of 75.

After applying the filter disks to the frequency channels, LFD_C is normalized with two different factors:

$$LFD\_C_{norm_1} = \frac{LFD\_C(r_1, r_2, n)}{\sum\limits_{r_1, r_2 \in Rads} LFD\_C(r_1, r_2, n)}, \tag{7.11}$$

$$LFD\_C_{norm_2} = \frac{LFD\_C(r_1, r_2, n)}{\max\limits_{\substack{-\frac{K}{2} \leq k \leq \frac{K}{2} \\ -\frac{L}{2} \leq l \leq \frac{L}{2}}} |CH_n(k,l)|} \tag{7.12}$$

where $Rads$ is the set of inner-outer radii defined for the disk filters. The first normalizing factor, $\sum LFD\_C$, makes the filter responses sum up to one. The term $max|CH_n(k,l)|$ in the second normalizing factor is used to capture the relationship between the average bandpass filtered responses
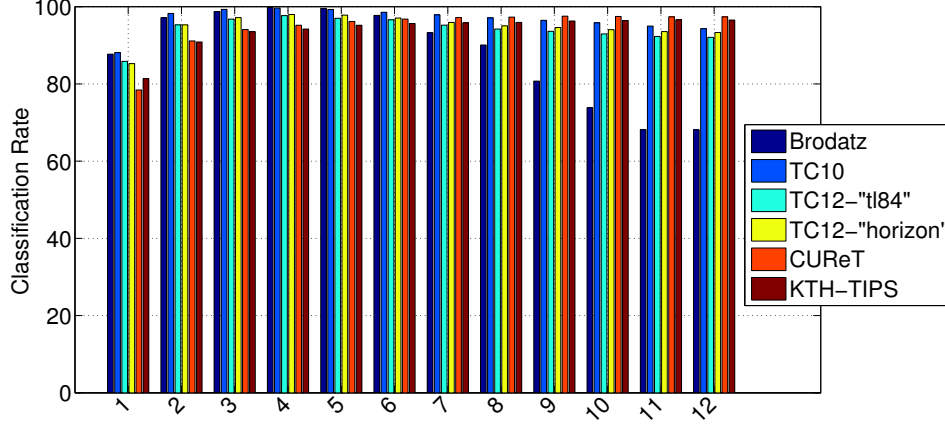
Figure 7.9: The classification rate for the Brodatz, Outex (TC10, TC12-"tl84", and TC12-"horizon"), CUReT, and KTH-TIPS datasets for different number of frequency channels computed by $LFD - MF_{24,3}$.

and the largest response of each channel CH_n. The LFD_D is normalized such that the features add up to one:

$$LFD\_D_{norm\{min,max,med\}} = \frac{LFD\_D_{\{min,max,med\}}(\sigma_1, \sigma_2, r_1, r_2, n)}{\sum\limits_{r_1, r_2 \in Rads} LFD\_D_{\{min,max,med\}}((\sigma_1, \sigma_2, r_1, r_2, n))} \quad (7.13)$$

The final feature vector of the first proposed method, LFD-MF [225], is composed of the normalized features:

- LFD_C_{norm1},

- LFD_C_{norm2},

- $LFD\_D_{norm\{min,max,median\}}$.

The optimum number of channels (n) for LFD_C and LFD_D are found by incrementing the number of channels (starting from one) until the classification accuracy is maximized. Figure 7.9 shows the classification rate for different number of frequency channels used by $LFD - MF_{24,3}$ for the Brodatz [38], Outex [265] (TC10, TC12-"tl84", and TC12-"horizon"), CUReT [71], and KTH-TIPS [96] datasets. The explanation of the datasets are given in Section 7.6.1.

Based on the results shown in Figure 7.9, the number of channels for the Brodatz, Outex, CUReT, and KTH-TIPS is set to 4, 4, 9, and 11, respectively. The size of the final feature vector, LFD-MF, is equal to $(2 \times C + 3) \times N$, where C is the number of disk filters and N the number of frequency channels.

7.4 LFD Magnitude and Phase based Features (LFD-MPF)

This section presents our second set of texture features, the LFD Magnitude and Phase based Feature set (LFD-MPF) [226]. One of our interesting findings is that the major energy of the $LCF_{P,R}$
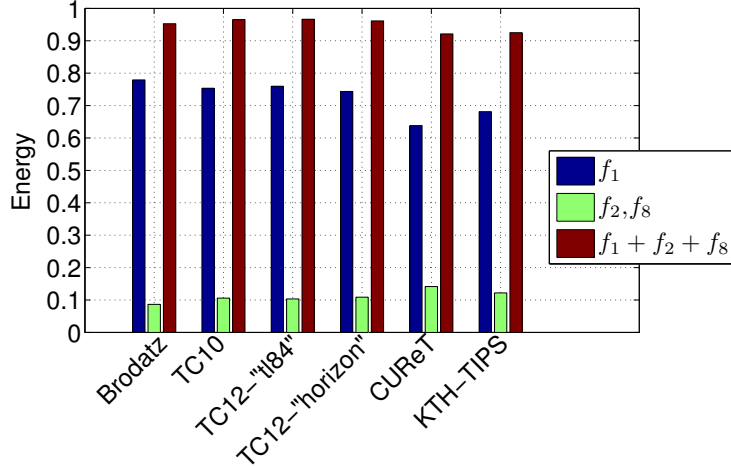
Figure 7.10: The average energy of the low frequency components $LFD(1)$, and $LFD(2)$ (or $LFD(8)$) as well as the aggregated energy of all the three components. A neighborhood setting with $(P, R) = (8, 1)$ is used.

function in textures are captured in the low frequency components of LFD. Figure 7.10 shows the average energy of the low frequency components $LFD(1)$, and $LFD(2)$ for the Brodatz [38], Outex [265], CUReT [71], and KTH-TIPS [96] datasets, using eight neighbors on radius of one. Note that the energy of $LFD(8)$ is equal to that of $LFD(2)$.

As one can observe, the first component, $LFD(1)$, carries the major portion of the energy of $LCF_{P,R}$ function. The second frequency component, $LFD(2)$, (and similarly $LFD(8)$) contributes to about 10% of the energy. The energy captured in the three low frequency components ($LFD(1)$, $LFD(2)$, and $LFD(8)$) consists of more than 90% of the total energy of the signal. Therefore, using these three frequency components can provide enough information for texture discrimination.

Using the low frequency components has two advantages. First, the major energy of the textural signal (which represents texture properties) is carried by the low frequency components. Second, the noise sensitive information which usually appears in high frequencies is avoided. In practice, only $LFD(1)$ and $LFD(2)$ are used, because $LFD(8)$ is the conjugate of $LFD(2)$ and does not give additional information. In our second proposed method both magnitude and phase information of LFD components are used for texture feature construction.

7.4.1 Phase Based Features

The DC frequency component ($LFD(1)$) has no phase information. As a result, the phase based features are extracted from the second frequency component, $LFD(2)$. The issue to be addressed here is how to define rotation invariant features from phase, while the phase of the local frequency components is not rotation invariant.

To have rotation invariant phase-based features, the method uses the phase difference (PHD)

between the second Fourier coefficients of two circular functions located on two different radii:

$$PHD(x,y) = angle\left(LFD(2)^{(P_i,R_i)}_{(x,y)}\right) - angle\left(LFD(2)^{(P_j,R_j)}_{(x,y)}\right),\qquad(7.14)$$

where $angle$ operator gives the phase of a complex number, and $LFD(2)^{(P_i,R_i)}_{(x,y)}$ denotes the second Fourier component of LCF with Radius of R_i and sampling number of P_i at location (x,y). Each circular function carries textural information at a specific scale. When rotation occurs, both functions incur the same amount of circular shift and the phase of $LFD(2)$ of the two functions changes by the same rotation angle. As a result, the phase difference between the $LFD(2)$ components of the two circular functions remains unchanged and this property is used to define rotation invariant features.

So far, the phase difference at each pixel, $PHD(x,y)$, has been defined. The phase difference is an orientational information and has a value in the range of $[0\ 2\pi)$. To construct the final features the Histogram of Local Orientations (HLO) is used. The histogram is defined in a circular area around each pixel, by accumulating the orientational information (here, $PHD(x,y)$) into d orientational bins. Assume that there are d orientational bins centering at ori_i, $(1 \leq i \leq d)$,

$$ori_i = (2\pi/d) \times (i-1). \qquad(7.15)$$

The orientational information, $PHD(x,y)$, is linearly assigned to the closest orientational bins:

$$OriInfBin_i(x,y) = \begin{cases} \frac{2\pi/d - |ori_i - PHD(x,y)|}{2\pi/d} & \text{, if } |ori_i - PHD(x,y)| < 2\pi/d \\ 0 & \text{, otherwise.} \end{cases} \qquad(7.16)$$

The histogram of local orientations $HLO_i(x,y)$ for orientation ori_i is computed on a circular region (C):

$$HLO_i(x,y) = \sum_{(X,Y)\in C} OriInfBin_i(X,Y). \qquad(7.17)$$

The $HLO_i(x,y)$ represents the distribution of the local orientational information (e.g., PHD) around pixel (x,y), discretized into d orientational bins. Figure 7.11 illustrates the steps to construct the HLO. This histogram is comparable to the histogram of orientations in SIFT [224] in a sense that it accumulates the orientations in a region around a keypoint location. However, no weighting is used (e.g., the Gaussian weighting in SIFT) and the orientational information is extracted from the phase of local frequency components instead of gradients.

Now that the histogram of d orientations at each pixel(x,y) is computed, the changes of each histogram bin across the image is used as a texture feature. These changes are found by computing the standard deviation as follows:

$$HLO_{std_i} = \sqrt{\frac{1}{W \times H - 1} \sum_{x=0}^{W-1}\sum_{y=0}^{H-1}(HLO_i(x,y) - \overline{HLO_i})}, \qquad(7.18)$$
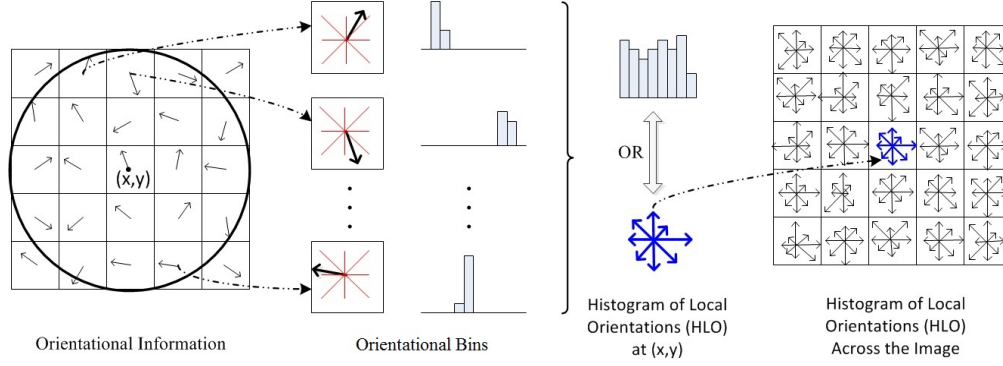
Figure 7.11: The steps for computing the histogram of local orientations for a given pixel(x,y): A circular region is considered, the orientational information is assigned to the two closest directions bilinearly for each point in the region, and finally the bins in the circular region are summed to construct the final histogram [226].

where W and H are the width and height of the image, respectively, and $\overline{HLO_i}$ is the mean value of all $HLO_i(x, y)$:

$$\overline{HLO_i} = \frac{1}{W \times H} \sum_{x=0}^{W-1} \sum_{y=0}^{H-1} HLO_i(x, y). \tag{7.19}$$

To compute the second set of phase-based features, the phase of $LFD(2)$ is used as the orientational information (i.e., $PH(x, y) = angle(LFD(2)_{(x,y)})$). Consequently, $PHD(x, y)$ is replaced by $PH(x, y)$ in Eq. 7.16, resulting in a different set of features after applying Eq. 7.17, and Eq. 7.18. Unlike the histograms of phase difference, the histograms of phase computed by this approach are not rotation invariant. To have rotation invariance, 1D Fourier transform is applied to the standard deviation computed by Eq. 7.18 and the magnitude of the frequency components is used. These features are called the Frequency Magnitude of HLO_{std} or $FMHLO_{std}$ in short form. A rotation causes a circular shift of the output of Eq. 7.18. This circular shift does not change the magnitude of the frequency components of HLO_{std}. This is similar to the magnitude based features of LFD. Since half of the magnitude components are the same, the final feature size is $d/2 + 1$, where d is the number of directions used to compute the HLO.

Our final feature set for the second proposed method, LFD-MPF [226], consists of these sets:

- $LFD\_C_{norm_1}$ (Eq. 7.11): magnitude based features. The difference of this method and the first method is that here only two frequency channels are used ($LFD(1)$ and $LFD(2)$).

- HLO_{std}^{PHD}: the standard deviation of the bins of HLO, where the orientational information is the phase difference of $LFD(2)$ for two given circular functions, $PHD(x, y)$.

- $FMHLO_{std}^{PH}$: the frequency magnitude of the standard deviation of the HLO's bins, where the orientational information is the phase of $LFD(2)$ for a given circular function, $PH(x, y)$.

97

Table 7.1: Circular local function settings used in the experiments.

R	1	2	3	4	5	6	7	8
N	8	16	24	28	32	36	40	44

7.4.2 Implementation Details

The proposed method is implemented in Matlab. In the first step, the images are normalized to have zero mean and unit variance. The normalization step makes the features invariant to linear changes of illumination. The local frequency components are computed using Eq. 7.2 and the low frequency components, $LFD(1)$ and $LFD(2)$, are used. The same setting as our first method was used to compute $LFD\_C_{norm_1}$ features. The HLO (Eq. 7.17) is normalized for both phase and phase difference information such that the HLO histogram at each pixel sums up to one.

To compute the features, eight circular local functions are used. These settings are shown in Table 7.1. The $LFD\_C_{norm_1}$ features are computed using the eight $CLF_{P,R}$ settings shown in Table 7.1 resulting in 160 features (2 channels ($LFD(1)$, and $LFD(2)$) × 10 disk filters × 8 sampling settings). Eight orientations (d=8) are considered for the phase based features and the computation of HLO. To compute the phase difference, two reference phases of the settings with radii of 2 and 3 are used. Then, the difference of the reference phases and the phases of settings with radii of 5, 6, 7, and 8 are found. Following this setting, 64 features are produced from phase difference (2 reference phases × 4 phases × 8 orientations). Finally, the 8 given settings are used to compute the $FMHLO$ which gives 40 features (8 phase settings × 5 features for each setting). The total number of features produced by the mentioned setting is 264.

7.5 Gradient Calculation by LFD

In this section, it is demonstrated that the *second* frequency component (or equivalently the Pth component) of the LFD is highly affected by the local edge around the pixel and can be used to find the magnitude and orientation of local edges. Our motivation is based on the observation that the low frequency components ($LFD(1)$, $LFD(2)$, and $LFD(P)$) comprise more than 90% of the $LCF_{P,R}$ signal in some well known texture datasets (Figure 7.10), and therefore can well represent the texture around a pixel.

7.5.1 Relation of LFD(2) with Edge

To explain the edge detection ability of $LFD(2)$, the characteristics of the $LCF_{P,R}$ function when it is around an edge is described. An edge is defined as the line separating a dark region from a bright region as shown in Figure 7.12(a).

Now, consider the traversal of circular samples shown in Figure 7.12(a). By starting from a dark region (f_1), we cross the edge and go into the bright region (f_i). After traversing the bright
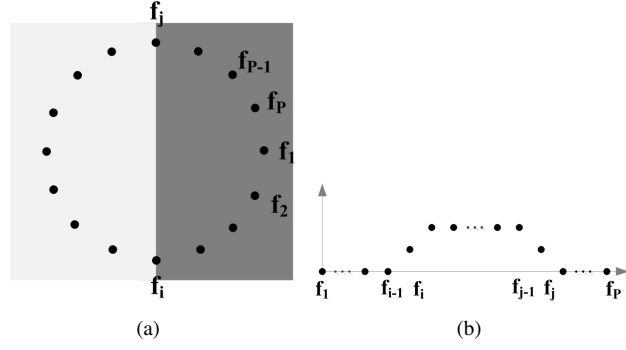
Figure 7.12: Using LFDG operator to compute local edge. a) P sample are located on radius of R around a pixel. b) The function of samples have a rectangular shape [228].
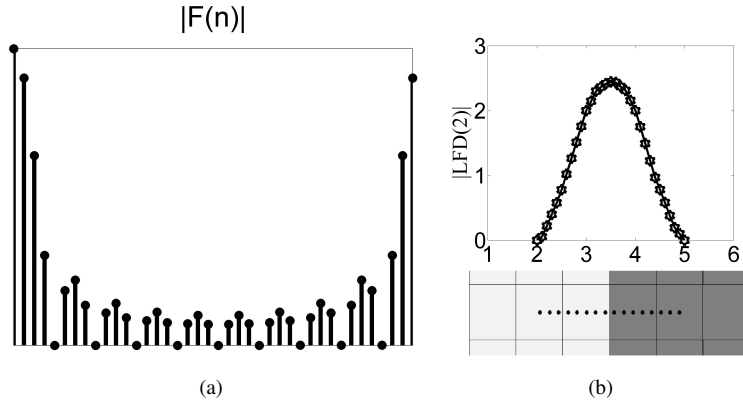
Figure 7.13: a) The DFT of a rectangular shaped function is a sinc. The highest values of the sinc function are at $n = 1$ and $n = \{2, P\}$. b) $|LFD(2)|$ as a function of the distance of the center of the sampling circle from the edge [227].

region and crossing the edge at f_j, we return to the starting point in the dark region. Indeed, by using the circular sampling approach (Figure 7.12(b)), the function of an edge can be characterized as a rectangular shaped $LCF_{P,R}$ function. For simplicity, assume that the rectangular function has a value of one. The DFT of the rectangular shaped function of width M (using Eq. 7.2) is a sinc function of the following form:

$$LFD_{rect} = \frac{sin(\frac{\pi(n-1)M}{P})}{sin(\frac{\pi(n-1)}{P})} \times e^{-\frac{i\pi(n-1)(M-1)}{P}}. \tag{7.20}$$

The magnitude of this sinc function, $|\frac{sin(\pi(n-1)M/P)}{sin(\pi(n-1)/P)}|$, has the highest value at $n = 1$ and then at $n = \{2, P\}$ (Figure 7.13(a)). Therefore, an edge (rectangular shaped $LCF_{P,R}$ function) manifests itself with high values in $LFD(1)$, $LFD(2)$, and $LFD(P)$. This is consistent to the experimental results in Figure 7.10 showing that these low frequency components comprise a large portion of textural signals.

Among these three components, the $LFD(1)$ (DC component) is affected by the average in-

tensity, indicating if a pixel is located in a dark or bright region. Hence, the actual edge information around the pixel is represented by $LFD(2)$ (or $LFD(P)$). Another possible interpretation of $LFD(2)$ is that it approximates a rectangular shaped function better than the other components. To better demonstrate the edge detection ability $|LFD(2)|$ is plotted as a function of the distance of the center of the circle from the edge for the given example shown in Figure 7.13(b). In this example, points are chosen between pixels 2 and 5 with an increment of 0.1 pixels. The magnitude of $LFD(2)$ is shown for each point in Figure 7.13(b). As one can see, $|LFD(2)|$ reaches its maximum value at location 3.5 which is the exact point separating the dark region from the bright region.

7.5.2 LFD Gradient Operator

The Local Frequency Descriptor Gradient ($LFDG$) is formally defined by setting $n = 2$ in the LFD formula (Eq. 7.2):

$$LFDG = \sum_{k=1}^{P} f_k e^{\frac{-2\pi i(k-1)}{P}}. \tag{7.21}$$

The $LFDG$ (i.e., the second component of LFD) is a complex number, and therefore, Eq. 7.21 can be further decomposed into real and imaginary parts:

$$Re(LFDG) = \sum_{k=1}^{P} f_k cos\left(\frac{2\pi(k-1)}{P}\right), \tag{7.22}$$

$$Im(LFDG) = -\sum_{k=1}^{P} f_k sin\left(\frac{2\pi(k-1)}{P}\right). \tag{7.23}$$

The magnitude and phase of the $LFDG$ can be simply computed by using the real and imaginary parts.[1] The magnitude of the $LFDG$ represents the amount of rectangular shaped function (i.e., the strength of an edge), while the phase indicates the starting location of the rectangular shaped function (i.e., the edge orientation).

One may note that the exact value of the phase depends on the neighboring order strategy. The proposed method starts on a horizontal line and traverses the neighbors in the clockwise direction as shown in Figure 7.12(a). Using this protocol will result in the same orientation value computed by the conventional gradient orientation formula.[2]

The rectangular shaped $LCF_{P,R}$ function is analogous to the *uniform* patterns in the LBP method[3] which represent edges of varying positive and negative curvatures [267]. However, the uniform patterns are acquired by applying a threshold which makes the patterns sensitive to noise, while the $LFDG$ is a low frequency component which is less affected by noise. By using different R and P, the edge information at different scales are obtained. Figure 7.14 compares the gradient calculation of the LFDG operator with that of the central difference on a synthetic and a real image.

---

[1]$|LFDG| = \sqrt{Re(LFDG)^2 + Im(LFDG)^2}$, and $\angle LFDG = atan2(Im(LFDG), Re(LFDG))$ where $atan2$ is the operator that computes the arc tangent of the two variables by considering the signs of both arguments.
[2]The conventional gradient orientation is computed by $atan2(\Delta y/\Delta x)$.
[3]Uniform patterns refers the binary patterns in which the transition between 0 and 1 is not greater than 2.
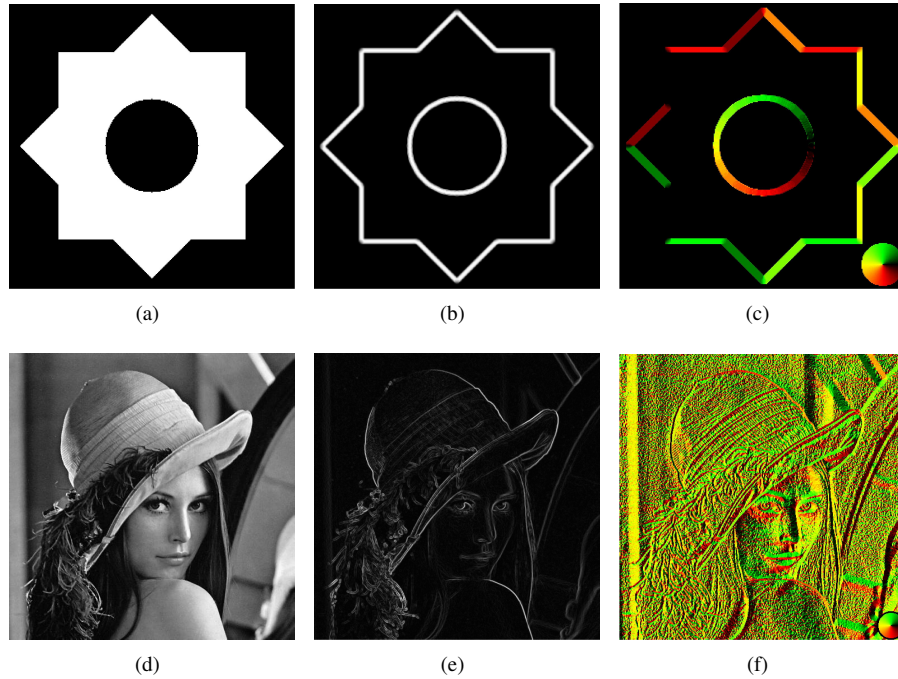
Figure 7.14: Computing gradient on a synthetic (first row) and a real image (second row). The first column is the original image. The 2nd and 3rd columns are the magnitude and orientation of gradient computed by LFDG [227].

READ is computed with setting ($P = 8, R = 1$) and $h = 1$ pixel in the central difference method. To make a fair visual comparison, the magnitude of the gradients are normalized to the range [0 1].

As can be observed, the locations of the maxima of the magnitude of the LFDG precisely corresponds to the location of edges. That is, the magnitude of the LFDG is zero in flat regions, while it is maximized on pixels located on an edge. This can be observed on both straight and curve edges. The phase of the LFDG faithfully represents the orientation of the local edge. One may consider the orientational values around the circle in the synthetic image. The color map in the right bottom of the phase image shows the color associated with a given angle. It starts with black at $0°$ and goes to green at $90°$, yellow at $180°$, and red at $270°$. It can be verified that the colors around the circle in Figure 7.14(c) follow the colors of the color map. In other words, the color around the circle in the phase image is black at $0°$, green at $90°$ and so on. This is because of the sampling protocol used for the order of neighbors. One may note that the orientation value in the flat regions are not the same. This is no surprise because when the magnitude of an edge is zero (i.e., the region is flat), the orientation has no special meaning. This is similar to the gradient information. When the value of the gradient is zero, the orientation of the gradient is meaningless.

Figure 7.15 gives another example of gradient computation on a synthetic image. In this figure, the magnitude and the phase of the $LFDG$ ($P = 8, R = 1$) is compared with the magnitude and orientation of gradients computed by three common approaches: central difference (i.e., $\Delta_h f(x) =$
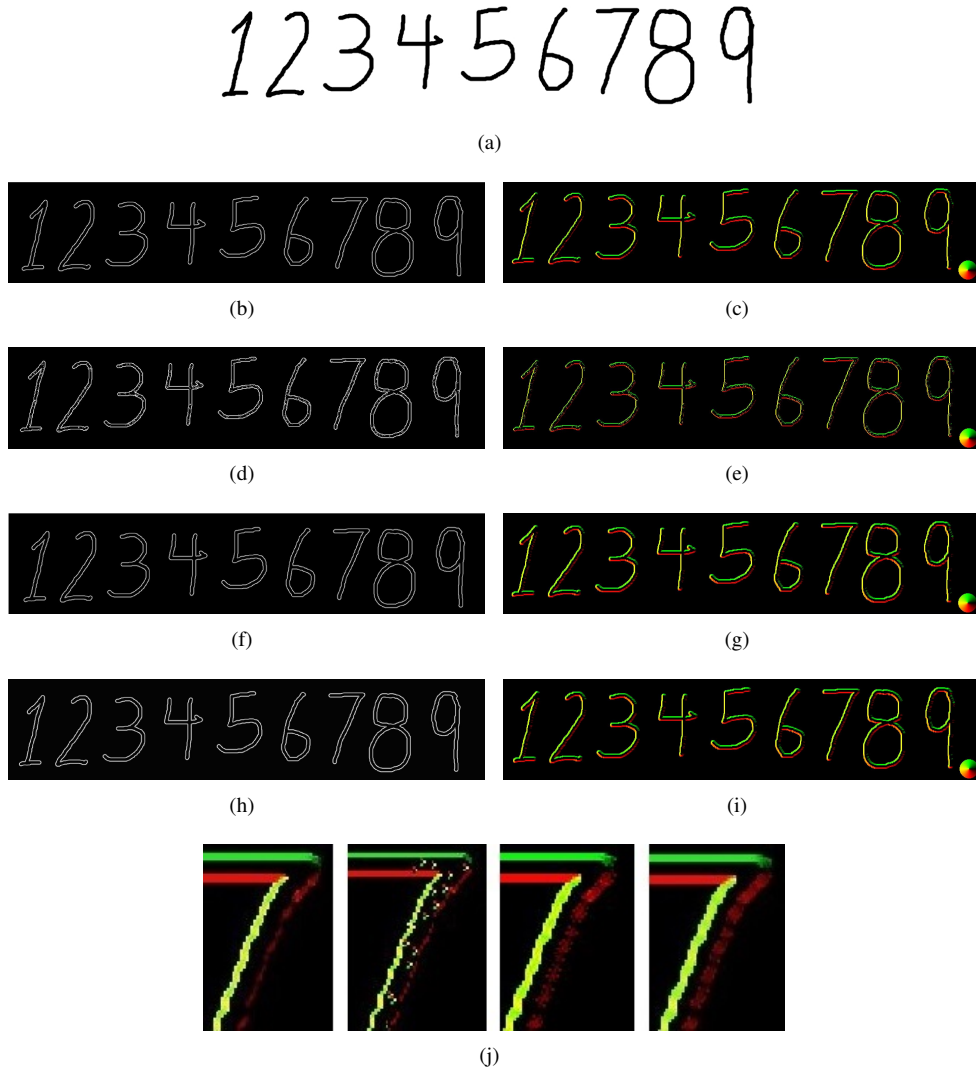
Figure 7.15: Comparing $LFDG$ with other gradient calculators. A sample image is shown in (a). The original size of the sample image is 1152×253 pixels and its format is jpg. The magnitude and orientation of gradients are computed by central difference (b and c), Sobel operator (d and e), first order derivative of Gaussian (f and g), and $LFDG$ (h and i). The upper right part of the number "7" in the orientation maps in its original size is shown in (j) which is computed by central difference, Sobel, derivative of Gaussian, and $LFDG$ from left to right, respectively. The angular color map is shown in the bottom right of the image showing the orientation [228].

$f(x+h/2) - f(x-h/2)$, $h = 2$), the Sobel operator (with size of 3×3), and the first order derivative of Gaussian (i.e., $\Delta f(x) = f(x) * \Delta_G(\sigma)$, where $*$ denotes convolution and $\Delta_G(\sigma) = \frac{-2x}{\sqrt{2\pi\sigma^3}} e^{-\frac{x^2}{2\sigma^2}}$, the normalized derivative of Gaussian, with $\sigma = 0.25$).

Note that the orientational values computed by $LFDG$ is smoother and involves more pixels (see Figure 7.15(j)) compared to other methods. More examples of the $LFDG$ gradient outputs are presented in Appendix B.

The $LFDG$ operator has several advantages that make it favorable for computer vision and

image processing applications [228]. First, it is robust to noise. The reason is that noise appears in the high frequency components. However, the $LFDG$ is based on a low frequency component and hence, is less affected by noise. Section 7.7 presents some experiments to show the robustness of $LFDG$ in the presence of noise.

$LFDG$ can be made invariant to linear changes of illumination. A linear change of illumination changes the magnitude of $LCF_{P,R}$ function linearly. However, it does not change the phase of the $LFDG$ (because the ratio of $Im(LFDG)$ to $Re(LFDG)$ remains the same). If the intensity of an image is normalized before computing the gradients, the magnitude of $LFDG$ remains unchanged. In the proposed methods, the intensities are normalized such that the mean of the intensities is zero and the standard deviation is one.

Finally, $LFDG$ is robust to blurriness. The reason is that the blur effect mainly dampens the high frequency components and the low frequencies (including $LFDG$) are less affected. This property is shown in Section 7.7.

7.5.3   Implementation Details

The proposed LFDG operator for gradient calculation can be efficiently implemented. The idea is to define a kernel to represent Eqs. 7.22, 7.24 and the gradient is computed by convolving the defined kernel with the image. Let us start by the fact that Eqs. 7.22 and 7.23 can be interpreted as the projection of the local samples into the x and y axes or g_x and g_y, respectively ($G = [g_x, g_y]$). Indeed, Eq. 7.23 can be rewritten as:

$$Im(LFDG) = \sum_{k=1}^{P} f_k cos \left(\frac{\pi}{2} + \frac{2\pi(k-1)}{P} \right). \tag{7.24}$$

By comparing this equation with Eq. 7.22 one can see that the two equations differ only by a factor of $\frac{\pi}{2}$ in the cos function. One may also note that the direction of the x axis can be obtained by adding $\frac{\pi}{2}$ to the direction of y axis. Figure 7.16 illustrates the concept using eight samples.

The angle of each sample point with the x and y axes are shown by θ_x and θ_y, respectively. It can be observed that

$$g_x = Re(LFDG) = f_1 cos \left(0 \right) + ... + f_8 cos \left(\frac{14\pi}{8} \right)$$
$$g_y = Im(LFDG) = f_7 cos \left(0 \right) + ... + f_6 cos \left(\frac{14\pi}{8} \right). \tag{7.25}$$

In other words, the gradient along a given axis can be computed by multiplying the intensity value of the samples (f_k) by $cos(\theta)$, where θ is the angle between the sample's location and the axis.

Now, let us construct a kernel which computes the projections of the circular samples onto an axis. For a radius of R, the kernel has a size of $N \times N$ where $N = 2R + 1$. For instance, for $R = 1$, the kernel is 3×3. There are two factors to form the kernel: the value of the samples, f_k, in Eqs. 7.22, 7.24, and the cosine of the angle between each sample and the axis. Since the location of
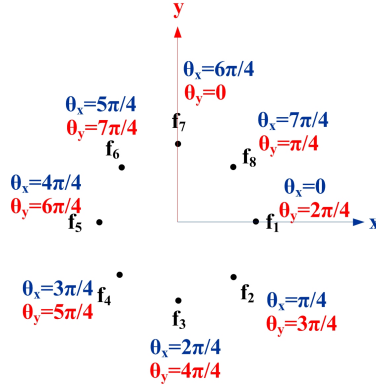
Figure 7.16: LFDG can be interpreted as the projection of the samples' values onto an axis. a) The angle between the samples and the y axis (θ_y) is $\frac{\pi}{2}$ larger than the angle of the samples with the x axis (θ_x) [228].
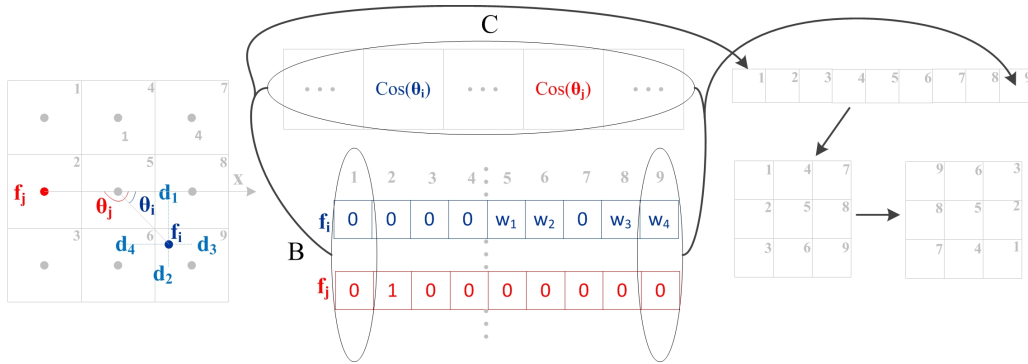
Figure 7.17: Construction of a 3×3 kernel, matrix B represents the bilinear interpolation weights and C the cosine coefficients [228].

the samples are known for a specific R and P, both factors can be found easily. The value of each sample is found using bilinear interpolation from its four nearest neighbors. To compute the value of each sample, f_k, a $P \times N^2$ matrix is considered. The rows of the matrix represent the samples and the columns the weight of each element in the kernel (assume that the elements of are put in a $1 \times N^2$ row vector). If a sample is located on a center of a pixel, no interpolation is needed. In this case, only one element has the value of one and the rest of the elements are zero on that row. For samples that are not located on the pixels' location, bilinear interpolation is used. For these cases, four elements in the corresponding row of the matrix have non zero values. This matrix is called B representing the bilinear weights of the kernel. Figure 7.17 illustrates the construction of a 3×3 kernel.

In this example, f_j is located exactly on pixel 2; hence, the entry $(j, 2)$ in the matrix B is 1 and the rest of the elements on the jth row are zero. On the other hand, f_i is not located on a pixel. Therefore, four elements on the ith row of the B matrix have non-zero values. The values are

0.35	0	-0.35	0.82	0	-0.82
1.29	0	-1.29	2.37	0	-2.37
0.35	0	-0.35	0.82	0	-0.82

Figure 7.18: Two sample kernels for the "x" axis: left $(R = 1, P = 8)$, and right $(R = 1, P = 16)$ [228].

$w_1 = (1-d_1)(1-d_4)$, $w_2 = (1-d_2)(1-d_4)$, $w_3 = (1-d_1)(1-d_3)$, and $w_4 = (1-d_2)(1-d_3)$, where d_i are the distances shown in Figure 7.17.

Now, let us consider a $1 \times P$ row vector called C to represent the cosine weights in Eqs. 7.22, 7.24. Each element of C is the cosine of the angle between sample f_k and the axis. The kernel is defined as $Ker = C \times B$ which is a $1 \times N^2$ row vector. The Ker is reshaped to $N \times N$, and the values of Ker are reflected around the center for the convolution operation. The convolution of Ker with an image is equivalent to the summations in Eqs. 7.22, 7.24.

Figure 7.18 shows two kernels for the "x" axis computed for radius of 1 but with different sample numbers ($P = \{8, 16\}$). It can be observed that both kernels sum to 0, and have the differentiation property (i.e., computing the difference in the direction of the axis) which is common in all gradient calculators. Nonetheless, a different pattern is observed in each kernel.

7.6 Evaluation of Texture Features

In this section, the experimental results for evaluation of the proposed texture features are presented. Four famous datasets are used to compare the proposed methods with the state-of-the-art methods: the Brodatz [38], the Outex [265], the Columbia-Utrecht Reflectance (CUReT) [71], and the KTH-TIPS [96] datasets. The descriptions of the datasets are given in Section 7.6.1. The state-of-the-art methods used for comparison are described in Section 7.6.2.

In the first experiment the classification accuracy of the methods are presented. Then, the robustness of the methods in the presence of different levels of Gaussian noise is shown. For classification, the Nearest Neighbor (NN) classifier and $L1$ distance are used:

$$|f_1 - f_2| = \sum_{n=1}^{N} |(f_1(n) - f_2(n))| \tag{7.26}$$

where f_1 and f_2 are the two given feature vectors, $f_1(n)$ and $f_2(n)$ are the nth feature in the vector, and N is the total number of features. $L1$ distance is chosen because it is less sensitive to outliers compared to $L2$.
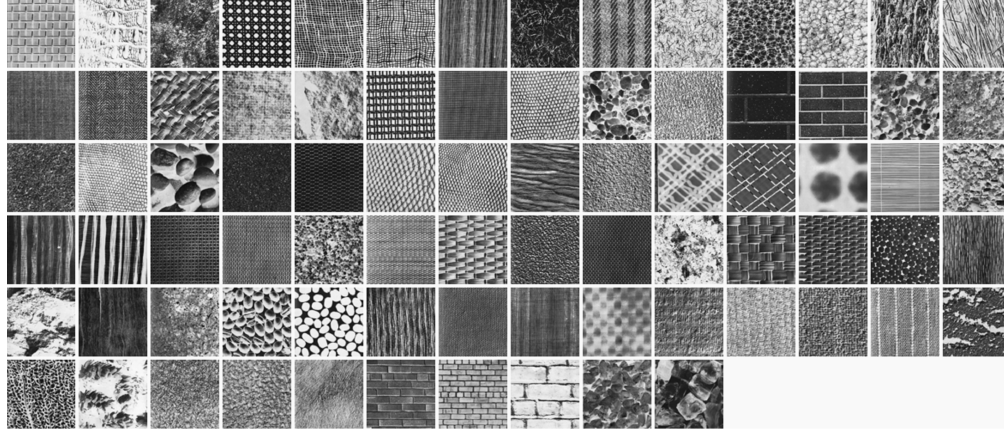
Figure 7.19: The 80 homogeneous texture images of the Brodatz dataset [38].

7.6.1 Datasets

The datasets used for the experiments include the Brodatz [38], the Outex [265], the Columbia-Utrecht Reflectance (CUReT) [71], and the KTH-TIPS [96] datasets.

Brodatz [38] is perhaps the most well-known dataset used by many texture classification methods. This dataset includes texture images with size of 640×640 pixels. To have different images from the same class, the provided texture images are divided into smaller pieces. Since the dataset does not provide any geometric transformation, similar to many rotation invariant methods, the smaller images undergo rotation. Figure 7.19 shows the 80 homogeneous texture images in the Brodatz dataset used for the experiments. Each texture image is divided into four 256×256 subimages, and each subimage is rotated by 10 different angles (i.e., $0°, 15°, 30°, ..., 135°$). Then, the center part of each subimage (with size of 128×128) is taken for the experiments. The first four unrotated images are used for training and the rest (4×9=36) for testing.

Unlike the Brodatz dataset, the Outex and CUReT datasets are designed to evaluate rotation and illumination changes. The Outex dataset includes 24 texture classes shown in Figure 7.20. The images are acquired under nine different rotation angles ($0°, 5°, 10°, 15°, 30°, 45°, 60°, 75°$, and $90°$) and three different illuminations conditions ("horizon", "inca", and "tl84"). For each rotation angle and illumination condition, 20 non-overlapping 128×128 gray-level images are produced. The dataset consists of two test suites: TC10 and TC12.

The TC10 test suite has been designed for rotation invariant analysis. In this test suite, the training set consists of images acquired under illumination condition "inca" and angle $0°$ (i.e., 24×1×1×20=480 samples). The test set includes images produced by the same illumination condition, "inca", but rotated by eight different angles, resulting in 3840 (24×1×8×20) images.

The TC12 test suite has been provided to analyze both rotation and illumination invariance. The training set is the same as the one in TC10. However, the test set consists of two datasets: the first test set includes the images produced under "tl84" illumination condition and the second set consists
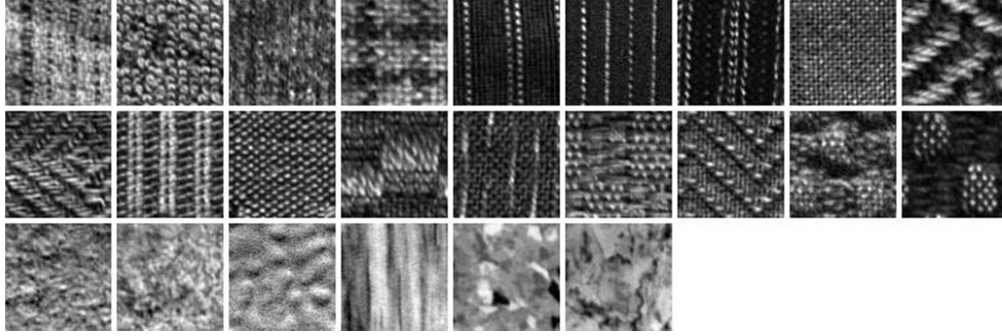
Figure 7.20: The Outex dataset [265] includes 24 different texture classes.

of images acquired under "horizon" illumination condition. Each set includes all rotation resulting in a total of 4320 ($24 \times 1 \times 8 \times 20$) samples.

The CUReT dataset consists of 61 real-world textures acquired under different viewing angles and illumination conditions. Figure 7.21 shows the texture classes in the CUReT dataset. The dataset includes 205 images from 61 texture types. This dataset is very challenging due to the similarity among some of the samples. Following the evaluation method of the previous works [356; 123], 92 images that are large enough to be cropped to an area of 200×200 pixels are selected. The selected images are converted to gray-level before analysis.

To assess the accuracy of the proposed method, the 92 images in each class are selected alternatively for training and for testing. As a result, each training and testing set includes 46 images. Similar to [123] the first 23 samples in each class are used for learning texton dictionary in the VZ_MR8 and VZ_Joint methods and for computing the cutting value of the VAR operation.

The KTH-TIPS dataset tries to add more *real-world* effects to the textures by using different samples of the same material as well as adding scale variations. It consists of 10 CUReT texture classes acquired at different illumination conditions and scales. Figure 7.22 shows the texture classes in the KTH-TIPS dataset. The images in each class are selected alternatively for training and testing sets.

7.6.2 Compared Methods

The proposed methods are compared to some well-known rotation invariant texture classification methods. In general the LBP-based methods outperform the frequency based methods for rotation invariant texture classes. As a result, in addition to some frequency-based methods, the state-of-the-art LBP-based methods are considered for comparison due to their high performance. The original LBP, LBP/VAR, $LBPV$, and $CLBP$ are the LBP-based methods compared in this section. The MR8 method [356] and image patch exemplars [357] proposed by Varma and Zisserman are also among the compared methods. The first approach applies eight different spatial filters (i.e., two anisotropic filters at six orientations and three scales, plus two rotationally symmetric filters) to the textures while the second uses the original texture patches. In addition to the ACGMRF [75] and 1D

Figure 7.21: The CUReT dataset [71] includes 61 different texture classes.
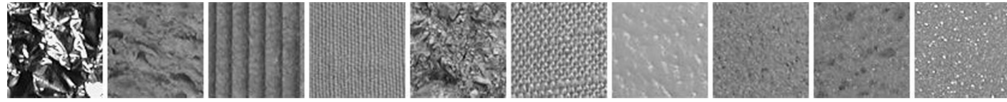
Figure 7.22: The KTH-TIPS dataset [96] includes 10 different texture classes.

DFT of Circular Neighborhood (DFT_CN) [17], two well-known frequency based methods namely the Gabor_Wavelet [238], and the Circular_Gabor filter [125] are also compared.

The proposed methods include $LFD-MPF$, and two versions of $LFD-MF$: $LFD-MF_{24,3}$ which uses features extracted on 24 samples located on radius of three, and $LFD - MF_{24,3} + MF_{32,4}$ which is the multi-resolution extension of LFD. This is similar to the strategy used by some LBP-based method [267; 123; 124] to improve accuracy. To do multi-resolution analysis, the features extracted from two settings (R,N)=(3,24), (4,32), are simply combined using the same number of channels used by $LFD - MF_{24,3}$.

7.6.3 Classification Results

Table 7.2 shows the classification accuracy of the methods on the datasets. As one can see our proposed methods provide the highest classification accuracy for the given datasets. In Brodatz, $LFD - MPF$ provides the perfect classification rate of 100% followed by $LFD - MF_{24,3} + MF_{32,4}$ and $LFD - MF_{24,3}$. The next best methods for this dataset are $CLBP\_S/M/C$ and

Table 7.2: Classification rate on the Brodatz, Outex, CUReT, and KTH-TIPS datasets for different state-of-the-art methods, and the proposed methods.

Method	Brodatz	TC10	TC12 "tl84"	TC12 "horizon"	CUReT	KTH-TIPS
DFT_CN	97.92	88.98	33.36	43.38	74.91	68.64
$ACGMRF$	26.11	61.67	54.77	58.38	86.89	87.27
$Gabor\_Wavelet$	30.87	53.57	57.82	57.89	96.33	92.27
$Circular\_Gabor$	69.24	77.11	77.41	78.61	47.83	60.45
VZ_MR8	94.86	93.59	92.55	92.99	97.51	94.55
VZ_Joint	96.88	92.00	91.41	91.82	97.15	85.45
$LBP_{24,3}^{riu2}$	88.47	95.07	85.04	80.78	87.53	89.09
$LBP_{24,3}^{riu2}/VAR_{24,3}$	95.97	98.15	87.13	87.08	92.23	88.64
$LBPV_{24,3}^{u2}GM_{PD2}$	92.33	97.55	94.23	94.18	93.87	91.81
$CLBP\_S_{24,3}^{riu2}/M_{N,R}^{riu2}$	99.06	99.32	93.58	93.35	93.83	95.91
$CLBP\_S_{24,3}^{riu2}/M_{N,R}^{riu2}/C$	99.31	98.93	95.32	94.53	96.12	95.45
$LFD-MF_{24,3}$	99.79	**99.64**	97.69	97.99	97.65	97.27
$LFD-MF_{24,3}+MF_{32,4}$	99.69	99.40	97.62	98.29	**98.08**	**97.73**
$LFD-MPF$	**100.00**	99.38	**98.77**	**98.66**	97.90	**97.73**

$CLBP\_S/M$ with 99.31% and 99.06% classification accuracies, respectively. DFT_CN, texton-based methods (VZ_Joint and VZ_MR8) and LBP-based methods performs quite well for this dataset. On the other side, $ACGMRF$, $Gabor\_Wavelet$, and $Circular\_Gabor$ perform poorly for this dataset.

The proposed methods outperform other methods in all test suites of the Outex dataset. In TC10 $LFD-MF_{24,3}$ has the highest performance followed by $LFD-MF_{24,3}+MF_{32,4}$ and $LFD-MPF$. In this test suite, LBP based methods are the best methods after LFD based methods. Texton based methods and DFT_CN stand in the middle of ranking and the $Circular\_Gabor$, $ACGMRF$, and $Gabor\_Wavelet$ have the lowest performances. The illumination changes of the TC12 test suites make LBP and LBP/VAR lose much of their performances (more than 10%). The performance drop in DFT_CN is also remarkable (i.e., more than 45% and 55% in TC12-"horizon" and TC12-"tl84", respectively). The other methods do not lose much of their performances in illumination change conditions. Among LFD based methods, $LFD-MPF$ provides the highest classification accuracy in TC12-"horizon" and TC12-"tl84" test suites.

By looking at the CUReT results in Table 7.2, it can be observed that the proposed method outperforms the other methods on this dataset too. Unlike the Outex dataset, the texton-based methods provide higher accuracy than those of the other LBP-based methods. Here, VZ_MR8 is slightly better than VZ_Joint. After texton-based methods, the next top methods are the $Gabor\_Wavelet$ and the LBP based methods. $ACGMRF$, DFT_CN, and $Circular\_Gabor$ provide the lowest performances in the CUReT dataset. In this dataset, $LFD-MF_{24,3}+MF_{32,4}$ provides the highest
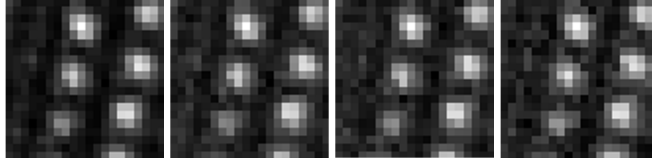
Figure 7.23: A sample texture image undergoing different noise levels. From left to right: the original texture image, the noisy image with SNR=5, 4, and 3 [226].

classification accuracy followed by $LFD - MPF$ and $LFD - MF_{24,3}$.

The last dataset is KTH-TIPS. Similar to the previous datasets, the LFD based methods have the highest classification accuracy. The next top methods are $CLBP\_S/M$, $CLBP\_S/M/C$, and VZ_MR8. The other LBP based methods, $Gabor\_Wavelet$, $ACGMRF$, and VZ_Joint stand in the middle of ranking. DFT_CN and $Circular\_Gabor$ have the lowest performance on this dataset. Among LFD based methods $LFD - MPF$ and $LFD - MF_{24,3} + MF_{32,4}$ are equally the best methods followed by $LFD - MF_{24,3}$.

7.6.4 Noise Robustness

Robustness to noise is one of the most important factors to assess texture methods. To measure the robustness of the proposed method the three test suites of the Outex dataset are used. The reason that the Outex dataset is chosen is because the impact of illumination changes and of rotation can be separately studied on the robustness of the compared methods against noise. In addition to LFD based methods, four top methods in the Outex dataset are chosen for noise robustness comparison. In each experiment, random Gaussian noise with a specific Signal to Noise Ratio (SNR) is added. In particular, the robustness of the methods with high levels of noise is studied. Figure 7.23 shows a sample image with SNR={5, 4, 3}. To reduce the variability of randomness, each experiment is repeated fifty times. The first noise experiment is conducted on the TC10 test suite. The average and standard deviation of the classification rate for different SNRs on the Outex test suites are reported in Table 7.3.

As one can see, the proposed LFD based method outperforms other methods in all levels of noise for the TC10 datasets, particularly in high levels of noise. The most noise sensitive method is $CLBP\_S/M$. The compared methods keep their performance for SNR≤10; however, their performance drops suddenly when the SNR is decreased to 5. This drop ranges from about 7% for the $LBPV$ to more than 26% for the $CLBP\_S/M$. All the methods except the proposed methods perform very poorly in extremely noisy conditions (SNR={4, 3}). While $LFD - MPF$ and $LFD - MF$ lose less than 3% and 4% of their performances for SNR=3, the second best method's performance ($LBPV$) drops by about 30%. The loss is more than 62% for $CLBP\_S/M$.

The next experiment is conducted on the TC12 test suites. Similar to the TC10 test suite, LFD based methods outperform the other methods on both TC12-"tl84" and TC12-"horizon" test suites

Table 7.3: Classification rate on the Outex test suites with different signal to noise ratio.

		SNR=10	SNR=5	SNR=4	SNR=3
TC10	$LBP_{24,3}^{riu2}/VAR_{24,3}$	96.02±0.11	73.88±0.17	60.64±0.25	43.07±0.23
	$CLBP\_S_{24,3}^{riu2}/M_{N,R}^{riu2}$	98.28±0.10	72.87±0.24	53.31±0.21	36.72±0.19
	$CLBP\_S_{24,3}^{riu2}/M_{N,R}^{riu2}/C$	98.53±0.09	82.66±0.20	61.74±0.20	40.40±0.16
	$LBPV_{24,3}^{u2}GM_{PD2}$	96.74±0.13	90.36±0.21	85.07±0.22	67.28±0.24
	$LFD-MF_{24,3}$	**99.61±0.05**	**99.24±0.11**	98.63±0.12	95.73±0.13
	$LFD-MPF$	99.33±0.03	99.10±0.05	**98.65±0.08**	**96.68±0.13**
TC12-"tl84"	$LBP_{24,3}^{riu2}/VAR_{24,3}$	87.95±0.16	64.91±0.18	55.53±0.17	42.34±0.18
	$CLBP\_S_{24,3}^{riu2}/M_{N,R}^{riu2}$	90.63±0.14	60.51±0.20	45.70±0.17	33.92±0.14
	$CLBP\_S_{24,3}^{riu2}/M_{N,R}^{riu2}/C$	94.22±0.11	72.85±0.19	52.72±0.21	37.00±0.13
	$LBPV_{24,3}^{u2}GM_{PD2}$	92.26±0.21	84.50±0.24	77.43±0.23	61.25±0.31
	$LFD-MF_{24,3}$	97.52±0.06	96.91±0.06	96.13±0.27	92.23±0.22
	$LFD-MPF$	**98.63±0.04**	**97.57±0.10**	**96.42±0.11**	**92.98±0.13**
TC12-"horizon"	$LBP_{24,3}^{riu2}/VAR_{24,3}$	82.64±0.16	60.58±0.15	51.87±0.18	39.93±0.24
	$CLBP\_S_{24,3}^{riu2}/M_{N,R}^{riu2}$	90.19±0.14	58.45±0.20	41.95±0.18	31.31±0.13
	$CLBP\_S_{24,3}^{riu2}/M_{N,R}^{riu2}/C$	92.20±0.11	67.87±0.19	52.44±0.22	35.88±0.13
	$LBPV_{24,3}^{u2}GM_{PD2}$	90.73±0.17	81.61±0.20	75.28±0.22	59.20±0.25
	$LFD-MF_{24,3}$	97.67±0.05	96.38±0.10	94.88±0.12	89.98±0.27
	$LFD-MPF$	**98.32±0.06**	**97.40±0.07**	**96.14 ±0.11**	**92.32±0.12**

and in all levels of noise. The LFD-based methods also keep their high performances even in extremely noisy conditions. For instance, at SNR=3 the accuracy of the $LFD-MPF$ is about 93% for TC12-"tl84" and more than 92% for TC12-"horizon". At this level of noise, $LFD-MF$ has the classific accuracy of about 92% and 90% for TC12-"tl84" and TC12-"horizon", respectively. However, the accuracy of the second top method ($LBPV$) is less than 62% and 60% for the TC12-"tl84" and TC12-"horizon" test suites, respectively. As one can see, the most noise sensitive method is the $CLBP\_S/M$ for the TC-12 test suites.

A common observation in all Outex test suites is that the $CLBP\_S/M/C$ is more accurate than $LBPV$ in low and moderate levels of noise; however, $LBPV$ outperforms the $CLBP\_S/M/C$ in higher levels of noise (SNR≤5).

One can observe that all methods are more sensitive to noise when the illumination condition is different for the training and the test sets. There is no exception to our methods. In general, $LFD-MPF$ shows more robustness to noise in comparison to $LFD-MF$. For instance at noise level of SNR=3, the performance of $LFD-MPF$ drops about 2.7%, 5.8%, and 6.3% on TC10, TC12-"tl84", and TC12-"horizon" test suites, respectively. This drop is about 3.9%, 5.5% and 8% in these test suites. Hence, $LFD-MPF$ is not only robust to noise in rotation condition, it is quite robust in more complicated conditions when the illumination changes as well.

Table 7.4: Number of features used by each method

Method	Brodatz	Outex	CUReT	KTH-TIPS
DFT_CN	16	16	16	16
$ACGMRF$	36	36	36	36
$Gabor\_Wavelet$	48	48	48	48
$Circular\_Gabor$	4	4	4	4
VZ_MR8	960	960	2440	2440
VZ_Joint	960	960	2440	2440
$LBP_{24,3}^{riu2}$	26	26	26	26
$LBP_{24,3}^{riu2}/VAR_{24,3}$	416	416	416	416
$LBPV_{24,3}^{u2}GM_{PD2}$	1071	1071	1071	1071
$CLBP\_S_{24,3}^{riu2}/M_{N,R}^{riu2}$	676	676	676	676
$CLBP\_S_{24,3}^{riu2}/M_{N,R}^{riu2}/C$	1352	1352	1352	1352
$LFD-MF_{24,3}$	92	92	387	473
$LFD-MF_{24,3}+MF_{32,4}$	184	184	774	964
$LFD-MPF$	264	264	264	264

Table 7.5: Average computation time per image (in seconds) in each dataset.

Method	Brodatz	Outex	CUReT	KTH-TIPS
$LFD-MF_{24,3}$	0.09	0.09	0.26	0.25
$LFD-MF_{24,3}+MF_{32,4}$	0.19	0.19	0.56	0.54
$LFD-MPF$	0.27	0.27	0.78	0.75

7.6.5 Feature Size Comparison

The number of features are usually noted for comparison of methods. Table 7.4 shows the number of features used by each method for the datasets used in our experiments. Some methods have quite a small number of features including $Circular\_Gabor$, $LBP_{24,3}^{riu2}$, DFT_CN, $ACGMRF$, and $Gabor\_Wavelet$. On the other hand, some methods have a large feature size including VZ_MR8 and VZ_Joint, $LBPV$, $CLBP\_S/M$, and $CLBP\_S/M/C$. The LFD based methods have medium feature size. While the size of $LFD-MF$ features varies depending on the number of channels, $LFD-MPF$ has a constant number of features.

7.6.6 Computation Time

The proposed methods are implemented by Matlab. Table 7.5 shows the average computation time per image in each dataset. The runtime is measured on a PC with an Intel quad core 2.60 GHz i7 CPU with 16GB RAM running Windows 7. It can be observed that the LFD based features can be computed in a reasonable time.

7.7 Evaluation of Gradient Operator

In this section, the robustness of our proposed gradient operator, LFDG, is evaluated in different imaging effects and artifacts including Gaussian noise, Salt & Pepper noise, Gaussian blur, and motion blur. LFDG is compared with the central difference, the first order derivative of Gaussian (i.e., $\Delta f(x) = f(x) * \Delta_G(\sigma)$, where $*$ is convolution and $\Delta_G(\sigma) = \frac{-2x}{\sqrt{2\pi}\sigma^3} e^{-\frac{x^2}{2\sigma^2}}$), and Sobel operator. Central difference is an old operator which is still used by many methods. First order derivative of Gaussian is used in the Canny edge detector (a popular edge detector) and Sobel is a known gradient operator. For the experiments the Flower, Foliage, Fruit, Winter, and Man Made datasets from the McGill color image collections[4] are used. This collection includes 821 color images which are converted to the gray scale format. For the noise experiments, two types of noise are added: Gaussian noise with a specific standard deviation ($\sigma = 1, 1.5, ..., 3$) and the Salt & Pepper noise with different noise densities ($density = 0.05, 0.10, ..., 0.35$). For the blur effect experiment, the images are smoothed with a Gaussian kernel (i.e., $K(x,y) = e^{-\frac{x^2+y^2}{2\sigma^2}}$) with a window size of $W \times W$ ($W = (1.5 \times \sigma + .5) \times 2 + 1$). The experiment is performed for $\sigma = 1, 1.5, ..., 3$. Finally, the motion blur effect is generated by Matlab using distances of 4 to 36 pixels with a step size of 4 pixels. To make the result of the methods comparable, the gradient vector at pixels ($G_i = [g_x, g_y]^T$) is normalized in each image I:

$$G_i = \frac{G_i}{\sum_{\forall G_i \in I} |G_i|}. \tag{7.27}$$

Then the normalized error is measured:

$$Err = \frac{1}{N} \sum_{i=1}^{N} \frac{|G_i^{cor} - G_i^{orig}|}{|G_i^{orig}|}, \tag{7.28}$$

where G_i^{cor} and G_i^{orig} are the gradient vectors in the corrupted and the original image, and N the number of pixels in the image. To avoid instability due to small values in the denominator, the vectors with small magnitudes ($|G_i^{orig}| < 10^{-6}$) are excluded. Figure 7.24 compares the normalized error of the different methods.

As can be observed, in the noise conditions (both Gaussian and Salt & Pepper) the proposed LFDG operator and the first order derivative of Gaussian are equally the most robust methods. In blur conditions (Motion and Gaussian) the LFDG operator outperforms the other methods. The central difference is the most sensitive method in all experiments.

7.8 Summary

In this chapter the proposed 2D methods were presented. First, the local frequency descriptor (LFD) was introduced as the frequency components of circular samples around each pixel. Then it is explained how the magnitude and the phase of the LFD can be used to construct robust texture

---

[4]http://tabby.vision.mcgill.ca/html/welcome.html
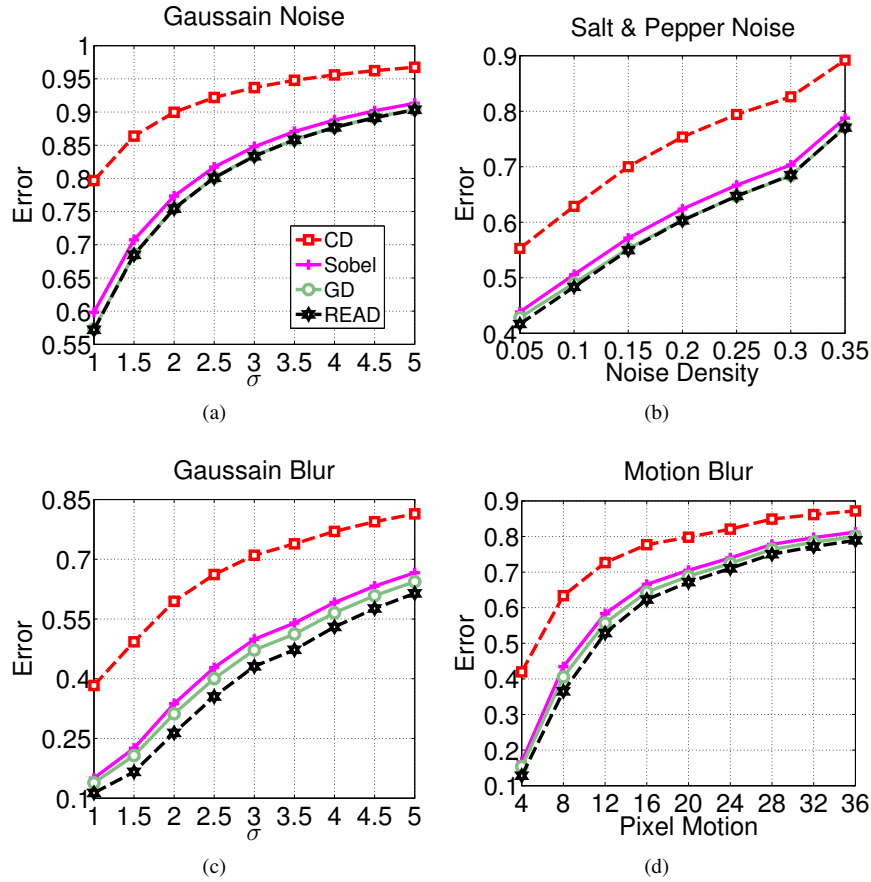
Figure 7.24: The robustness of Central Difference (CD), Gaussian Derivative (GD), Sobel, and LFDG for different imaging effects.

features. Four well-known datasets were used for the evaluation of methods including Brodatz, Outex, CUReT, and KTH-TIPS. The experimental results on these datasets demonstrate the superior performace of the proposed LFD based methods. The LFD based methods also show robustness to Gaussian noise particularly in high levels of noise (SNR of 5, 4, and 3) in our experiments.

Also, it is explained that there is a close relationship between local edges and the second frequency component of LFD. Then a robust local gradient calculator, LFDG, is presented. An efficient kernel based implementation for LFDG is suggested which makes the usage of LFDG efficient in practical applications. The experimental results show that LFDG provides comparable robustness to Gaussian Derivative operator in noise conditions. As well, LFDG show more robustness to blur effects compared to central difference, Gaussian derivative, and Sobel operators.

Chapter 8

Image Matching

8.1 Introduction

In this chapter a robust and accurate region descriptor based on information extracted from our gradient operator $LFDG$ is presented. Local feature detection and description are among the most important tasks in computer vision. The extracted descriptors are used in a variety of applications such as object recognition and image matching, motion tracking, facial expression recognition, and human action recognition.

The whole process can be divided into two major tasks: region detection, and region description. The goal of the first task is to detect regions that are invariant to a class of transformations such as rotation, change of scale, and change of viewpoint. These regions are usually defined by an ellipse to account for affine geometric transformations. The detected regions are then described by a feature vector. An ideal region descriptor should not only be invariant to geometric transformations but also be robust to imaging effects such as blurriness, noise, distortions, and illumination changes [248].

This chapter focuses on the second task, region description. Local gradients are commonly used by the state-of-the-art methods. Although local gradient information is very powerful, it is susceptible to imaging effects such as noise, illumination changes, and blurriness. As discussed before, the gradient information computed by $LFDG$ is robust to imaging effects which makes it suitable for region description.

In addition to using robust gradient information, a novel method for determining support regions around the elliptical regions detected by affine detectors is presented. First, it is shown that in theory the support regions can be scaled (with different scaling factors along the eigenvectors of the elliptical affine region) and rotated. Then, through experiments it is demonstrated that this method of support region definition can improve the results compared to the simple method of isotropic scaling of the original elliptical regions which is suggested in [86].

The advantages of the new descriptor are first explored in common geometric transformations, and then in more challenging imaging effects such as motion blur, non-uniform illumination changes with moving shadows, and images with different levels and types of noise. Although they are very

important, these challenging effects are less noted in the evaluation of the previous descriptors. The descriptor proposed in this chapter is called Robust Edge Aware Descriptor (READ) and has been published in [227].

8.2 Related Works

There are two main steps in finding corresponding points in two images. In the first step, interest points (regions) are found in the images. Ideal points should be highly discriminative and robustly detectable under different imaging conditions and geometric transformations. Some examples of detection methods include Difference of Gaussian (DoG) [224], Harris-Affine [246], and Hessian-Affine [248]. A review and comparison of region detection methods can be found in [248; 350].

Many detectors provide circular or elliptical regions with different sizes around the detected points for point description. The size of the detected region is determined by the detected scale of the region. By transforming the detected regions (elliptical and circular) to a circular region of a fixed radius, the regions are normalized into a canonical form. As a result, an affine transformation is reduced to a rotation, and an affine invariance on the original image can be obtained by rotation invariance on the canonical region [248]. Hence, region descriptors usually define rotation invariant features to provide descriptors that are invariant to local affine geometric transformations.

One of the most popular descriptors is the Scale Invariant Feature Transform (SIFT) [224]. The main information used in SIFT is the magnitude and orientation of local gradients accumulated in subregions. SIFT is later extended to the Gradient Location and Orientation Histogram (GLOH) method [247]. Mikolajczyk and Schmid [247] demonstrate that SIFT and GLOH outperform other descriptors such as those that use shape context, steerable filters, spin images, differential invariants, complex filters, and moment invariants. Some other descriptors include the Center-Symmetric Local Binary Pattern (CS-LBP) [137], the shape of MSER [93], the Local Intensity Order Pattern (LIOP) [365], and KAZE [14].

DAISY is a successful method recently proposed by Tola et al. [341]. Similar to SIFT, DAISY uses the magnitude and orientation of local gradients; however, the weighted sum of gradient orientation is replaced by the convolution of the gradient in specific directions with several Gaussian filters. Recently, it has been shown that the intensity ordinal information is more useful than the fixed location bins used by many descriptors such as SIFT and DAISY. The idea has been used by several descriptors such as LIOP [365], MROGH, and MRRID [85; 86].

A new promising approach is in developing *binary* descriptors such as BRIEF [42], Brisk [209], ORB [299], Freak [12], and BinBoost [343] for real-time applications. A comparative evaluation of these descriptors is presented in [138]. The recent paper by Miksik and Mikolajczyk [249] also compares some of these methods in the accuracy and speed trade-offs suggesting that binary descriptors provide comparable precision/recall results with SIFT and outperform in speed. On the other hand, LIOP, MRRID, MROGH are slower but outperform SIFT and other binary descriptors.

Figure 8.1: An example of two corresponding points detected by the Hessian-Affine detector.

8.3 Robust Edge Aware Descriptor

In this section the procedures to construct the new descriptor are presented. As mentioned before, region detectors usually provide circular or elliptical regions with different sizes around the detected points for point description. Figure 8.1 shows an example of two corresponding points detected by the Hessian-Affine detector.

Using vector notation, a point X_L in an ellipse satisfies $X_L^T M_L X_L = 0$ in the homogeneous representation, where M_L is a symmetric matrix. The ellipse is transformed into its canonical form (i.e., circle) easily by $X_{Lc} = M_L^{1/2} X_L$. As shown by Mikolajczyk and Schmid [246], when two elliptical regions $X_L^T M_L X_L = 0$ and $X_R^T M_R X_R = 0$ are corresponding, their canonical regions, $X_{Lc} = M_L^{1/2} X_L$ and $X_{Rc} = M_R^{1/2} X_R$, are related by a rotation:

$$X_{Rc} = R(\alpha) X_{Lc}$$
$$\Rightarrow X_R = M_R^{-1/2} R(\alpha) M_L^{1/2} X_L. \tag{8.1}$$

Figure 8.2 illustrates the canonical circular form of the detected elliptical regions shown in Figure 8.1.

The intensity information in the canonical regions is used by region descriptors to construct a feature vector. Many successful descriptors such as SIFT, GLOH, DAISY, and MROGH define the histogram of orientations. Similarly our descriptor is defined using the histogram of orientations; however, instead of gradients the LFDG is used to find the orientation and magnitude of the underlying structure around a pixel.

One may note that although the magnitude of LFDG is rotation invariant, the phase of LFDG changes by rotation. Assume that the phase of LFDG at an arbitrary point x is α. When a rotation by $\theta°$ occurs, the phase will change to $\alpha' = \alpha + \theta$. To achieve rotation invariance, the phase of LFDG (i.e., α, α') is decomposed into two components: a constant part related to the underlying structure (β) and a variable part related to the the location of the point (γ, γ') as shown in Figure 8.3.
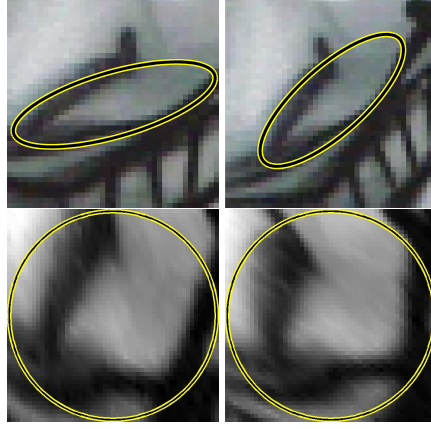
Figure 8.2: First row, the elliptical shape regions shown in Figure 8.1. Second row, the canonical form of the elliptical regions.
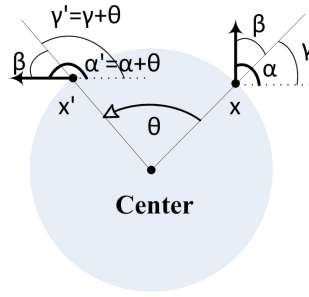
Figure 8.3: Rotation invariant phase information [227].

This approach is similar to the local rotation invariant coordinate system used by some descriptors such as MROGH [85], RIFT [203], and RIFF [332]. Instead of considering a new coordinate system, this can be easily done in LFDG by just subtracting the angle of the location of the point from the phase of LFDG computed in the regular coordinate system (i.e., $\beta = \gamma - \alpha = \gamma' - \alpha'$) which makes the computation fast.

By considering d orientational bins centering at ori_i, $(1 \leq i \leq d)$, the phase of LFDG is linearly assigned to the two closest orientational bins:

$$ori_i = (2\pi/d) \times (i-1). \tag{8.2}$$

$$Bin_i(x,y) = \begin{cases} \frac{(2\pi/d) - |ori_i - \angle LFDG(x,y)|}{(2\pi/d)} & \text{, if } |ori_i - \angle LFDG(x,y)| < 2\pi/d \\ 0 & \text{, otherwise.} \end{cases} \tag{8.3}$$

The intensity ordinal information is used to form subregions. First, the pixels are sorted in a non-descending order of their intensity values, $X_1, ..., X_n$. Then, the ordered pixels, X_i, are divided into k partitions,

$$Pr(p) = \{X_i | X_{\lceil n(p-1)/k+1 \rceil} \leq X_i < X_{\lceil np/k \rceil}\}, \tag{8.4}$$

118

where $\lceil \rceil$ denotes the ceiling operator. The orientational histograms in each partition, $Pr(p)$, is accumulated and weighted with the average magnitude of the LFDG in that partition,

$$Hist(p, i) = \sum_{\forall (x,y) \in Pr(p)} Bin_i(x, y).\mu_{LFDG}(p), \tag{8.5}$$

where $Bin_i(x, y)$ is computed by Eq. 8.3 and $\mu_{LFDG}(p)$ by

$$\mu_{LFDG}(p) = \frac{1}{|Pr(p)|} \sum_{\forall (x,y) \in Pr(p)} |LFDG(x, y)|, \tag{8.6}$$

where $|Pr(p)|$ denotes the number of pixels in partition p. The final descriptor is a $d \times k$ feature vector constructed by concatenating the orientational histograms in all subregions.

Some descriptors (e.g., MROGH, MRRID) use support regions defined as the scaled version of the original detected region to improve their performance. Here, a novel and more flexible support region definition is presented. It is suggested that the support region is obtained by rotating and scaling with different scaling factors along the eigenvectors of the elliptical affine region (anisotropic scaling). While below shows the necessary steps of the proofs, Appendix D provides more details.

As mentioned before, when two elliptical regions $X_L^T M_L X_L = 0$ and $X_R^T M_R X_R = 0$ are corresponding, their canonical regions, $X_{Lc} = M_L^{1/2} X_L$ and $X_{Rc} = M_R^{1/2} X_R$, are related by a rotation (Eq. 8.1).

Since M_L (and similarly M_R) is a symmetric matrix, it can be decomposed as $M_L = \Sigma_L \Lambda_L \Sigma_L^T$, where Σ_L is the orthogonal eigenvector matrix, and Λ_L the diagonal eigenvalue matrix. The transformation H is defined for the scale matrix $S = \begin{bmatrix} s_1 & 0 \\ 0 & s_2 \end{bmatrix}$:

$$H = \Sigma_L S^{-1} \Sigma_L^T, \tag{8.7}$$

Lemma 1. Transformation H maps $X_L^T M_L X_L = 0$ into a new ellipse, the eigenvectors of which are the same as that of the old ellipse but the eigenvalues are scaled by the $(s_1)^2$ and $(s_2)^2$ factors.

Proof. If the ellipse $X_L^T M_L X_L = 0$ undergoes the H transformation, the new ellipse is defined as $X_L^{\prime T} M_L^{\prime} X_L^{\prime} = 0$, where $X_L^{\prime} = H X_L$ and $M_L^{\prime} = H^{-T} M_L H^{-1}$. Substituting $M_L = \Sigma_L \Lambda_L \Sigma_L^T$ in the $M_L^{\prime}$ equation results in:

$$M_L^{\prime} = (\Sigma_L S^{-1} \Sigma_L^T)^{-T} \Sigma_L \Lambda_L \Sigma_L^T (\Sigma_L S^{-1} \Sigma_L^T)^{-1} \tag{8.8}$$

After a few steps of reduction this equation results in $M_L^{\prime} = \Sigma_L S \Lambda_L S^T \Sigma_L^T$. Denoting the new eigenvalue matrix, $\Lambda_L^{\prime} = S \Lambda_L S^T$, then $M_L^{\prime} = \Sigma_L \Lambda_L^{\prime} \Sigma_L^T$ which is claimed in Lemma 1. $\square$

Before presenting the theorem the following equations are required. Assume that S and D are diagonal and Q is orthogonal, then it is easy to show (see Appendix D for details):

$$(QDQ^T)^{1/2} = QD^{1/2}Q^T = QD^{1/2}Q^{-1}, \text{ and} \tag{8.9}$$

$$(QSDS^T Q^T)^{1/2} = QD^{1/2}S^T Q^T = QD^{1/2}SQ^T. \tag{8.10}$$

119

Theorem 1. Assume that the original ellipses defined by M_L and M_R undergo the H_L and H_R transformations, $X'_L = R\Sigma_L S^{-1}\Sigma_L^T X_L$, and $X'_R = R\Sigma_R S^{-1}\Sigma_R^T X_R$, where R is an arbitrary rotation matrix. The canonical regions of X'_L and X'_R are related by a rotation.

Proof. It is enough to show that Eq. 8.1 holds for X'_L and X'_R with the new elliptical regions defined by M'_L and M'_R. Let us start by multiplying Eq. 8.1 with H_R

$$
\begin{aligned}
H_R X_R &= H_R M_R^{-1/2} R(\alpha) M_L^{1/2} X_L \\
&= H_R M_R^{-1/2} R(\alpha) M_L^{1/2} H_L^{-1} H_L X_L \\
&= (R\Sigma_R S^{-1}\Sigma_R^T)(\Sigma_R \Lambda_R^{-1/2}\Sigma_R^T) R(\alpha)(\Sigma_L \Lambda_L^{1/2}\Sigma_L^T)(\Sigma_L^{-T} S\Sigma_L^{-1} R^{-1}) H_L X_L \\
&= (R\Sigma_R S^{-1}\Lambda_R^{-1/2}\Sigma_R^T R^{-1}) R R(\alpha) R^{-1}(R\Sigma_L \Lambda_L^{1/2} S\Sigma_L^{-1} R^{-1}) H_L X_L \\
&= (H_R^{-T} M_R H_R^{-1})^{-1/2} R R(\alpha) R^{-1}(H_L^{-T} M_L H_L^{-1})^{1/2} H_L X_L.
\end{aligned}
$$

$$
\Rightarrow X'_R = M_R'^{-1/2} R(\gamma) M_L'^{1/2} X'_L. \tag{8.11}
$$

$\square$

Figure 8.4 illustrates the concept. The original regions detected by an affine detector (yellow) are related by rotation. The red regions are anisotropically scaled and rotated version of the original regions detected by an affine detector (yellow). It can be observed that the red regions are related by rotation as well. This idea can be considered as a generalized form of support regions suggested in MROGH in which R in the H transformation is an identity matrix and $s_1 = s_2$ in the S matrix. Nonetheless, this generalized form gives more flexibility to choose the support regions.

8.4   Experimental Results

In this section, the experimental results for evaluation of the proposed READ descriptor are presented. First, it is shown how the parameters are tuned. Then the results for different datasets are shown.

8.4.1   Tuning Parameters

First, an experiment is performed to find the best tuning parameters for the gradient scale, rotation, and scaling factors of the supporting regions. A total of 50 image pairs with different transformations (mainly rotation and zoom) are used [1]. Six regions are considered (Figure 8.5).

All regions undergo isotropic scaling (IS) by a factor of 1.5 from the previous region, regions 1–3 undergo anisotropic scaling (AS) in the direction of eigenvectors of the elliptic region, regions 1 and 4 and regions 3 and 6 are rotated by $\theta°$ and $-\theta°$. The best gradient scale is searched for $R = 1, 2, 3, 4, 5$ with corresponding $P = 6, 8, 10, 12, 14$. The best s_1 and s_2 are searched in the range $[0.7, 1.3]$ in steps of 0.05, and the best rotation angle from the range $[0, 25]°$ with a step of

---

[1]Images downloaded from http://lear.inrialpes.fr/people/mikolajczyk/
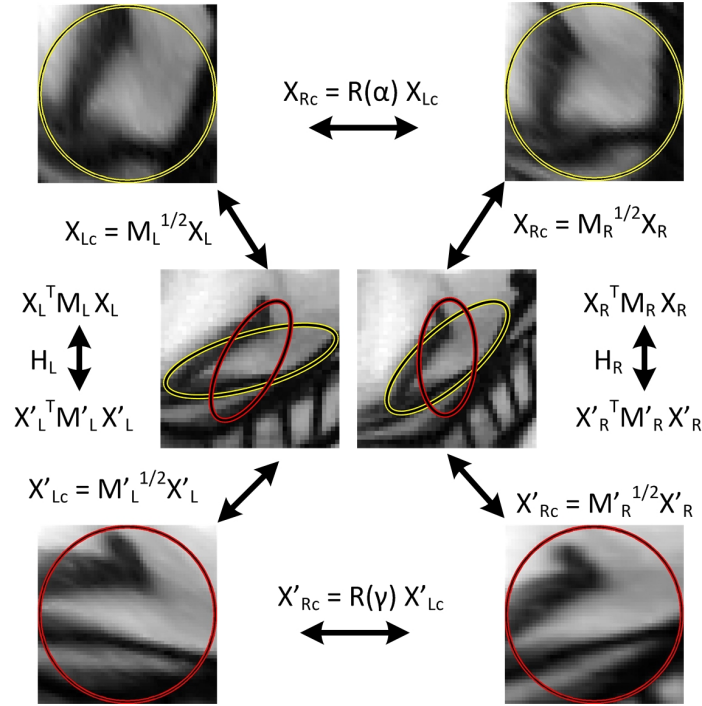
Figure 8.4: Using new support regions (red) as anisotropically scaled and rotated version of the original regions detected by an affine detector (yellow). The new red regions are related by rotation [227].
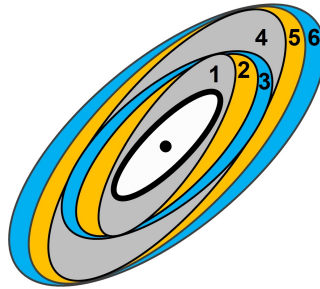
Figure 8.5: Using six support regions which are the anisotropically scaled and rotated versions of the original region [227].

$5°$, respectively. One may note that other configurations are also possible, and similar to DAISY the best parameters can be learned systematically [369]. Nonetheless, this specific configuration is sufficient to show the capability of the new descriptor. The best configuration is found to be $R = 4$, $P = 12$, $s_1 = 0.75$, $s_2 = 1.25$, and $\theta = 20°$. Figure 8.6 compares the configuration with only isotropic scaling (IS), and its combinations with anisotropic scaling (AS) and rotation (R). As one can see, the suggested strategy to define support region improves the performance of the descriptor.
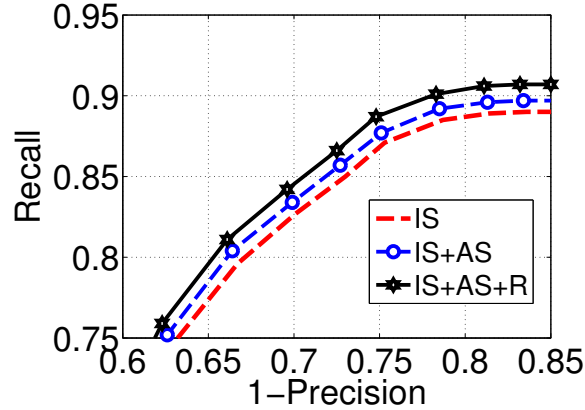
Figure 8.6: Comparing different support region strategies: IS, and its combination with AS, and R [227].

8.4.2 Oxford dataset

To evaluate the performance of the proposed descriptor, the evaluation protocol described by Miko-lajczyk and Schmid [247] is employed which uses the standard Oxford dataset[2]. The dataset includes image sets to evaluate different geometric transformations and imaging effects. The first image in each set is considered as a reference image and the other images are acquired under the designated change. A match is considered correct if the overlap error in the image area covered by two corresponding regions is less than 50% of the union of the regions and the recall/1-precision is reported.

The proposed method is compared to SIFT (as the baseline), DAISY, and LIOP and MROGH which have the highest performance according to the recent descriptor comparison study by Miksik and Mikolajczyk [249]. Figures 8.7 and 8.8 shows the performance of the descriptors.

Two versions of our method are shown: 1) using only isotropic scaling for support regions ($READ^-$), and 2) adding anisotropic scaling and rotation to the previous version ($READ$). As one can see, the proposed method outperforms the other methods in all cases including illumination change (leuven), rotation and zoom (bark, boat), blur effect (trees, bikes), and view point change (wall, graf). An interesting case is the "1-5" pair in the graf dataset in which adding anisotropic scaling and rotation degrades the performance. This case shows that the performance of rotated and anisotropically scaled support regions relies on the accuracy of the affine region detector. The regions detected by the Hessian-affine detector is not very precise on the graf dataset due to the textureless nature of the scene. Therefore, due to a large view-point change, a small inaccuracy produces a large error when rotation and anisotropic scaling are used to define the support regions. Without using rotation or scaling ($READ^-$), however, a much better result for this special case is obtained. Nevertheless, if the viewpoint change is smaller (e.g., less than $40°$ as shown in "1-4" pair in graf) or if the scene has some texture to help better detection (e.g., the wall), anisotropic scaling and rotation improve the result as shown in the other cases.

---

[2]Available at http://www.robots.ox.ac.uk/ vgg/research/affine/
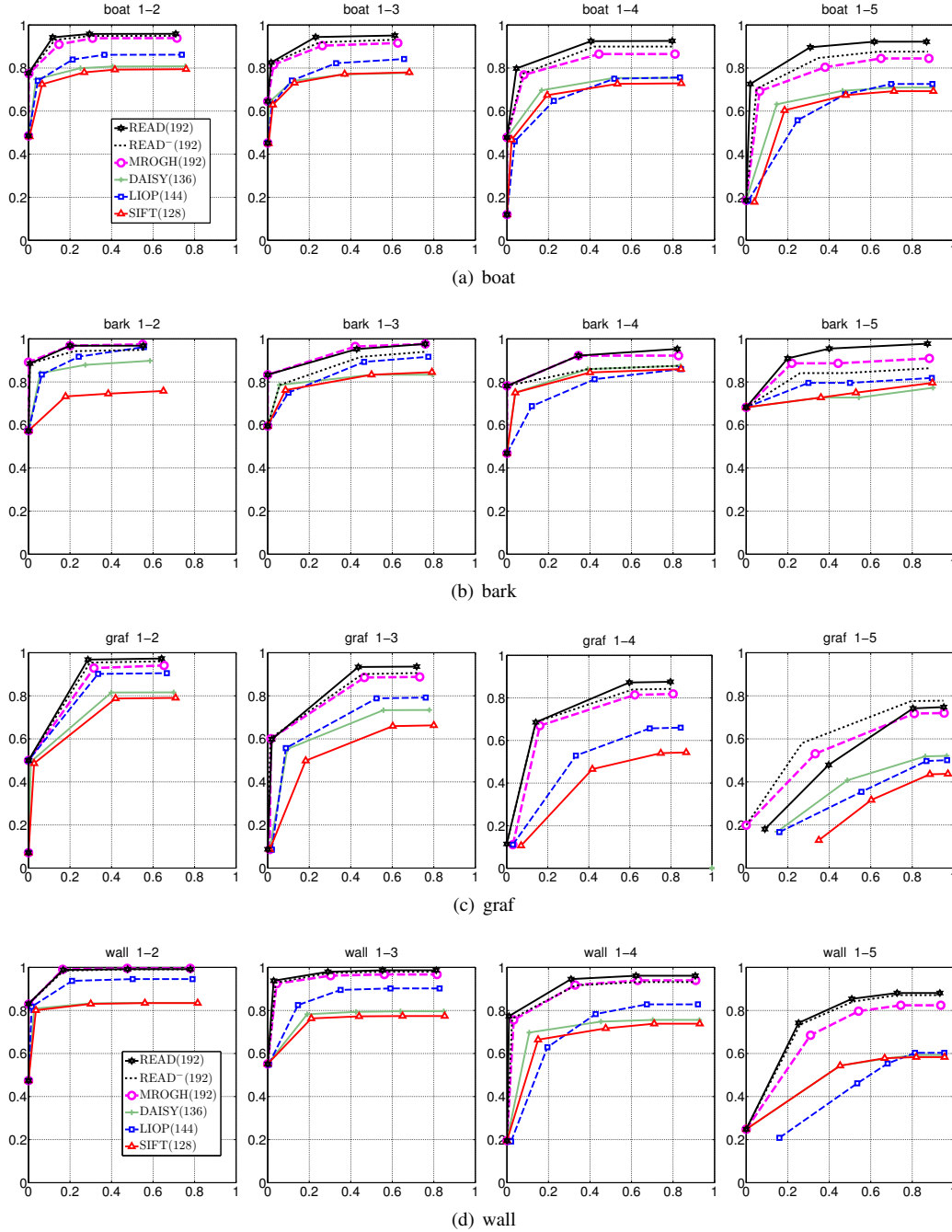
Figure 8.7: Performance of the descriptors on the Oxford dataset: boat (zoom and rotation), bark (zoom and rotation), graf (viewpoint change), and wall (viewpoint change). The $READ^-$ is our descriptor with no anisotropic scaling or rotation of support regions. The y axis is recall and the x axis is 1-precision.

With the exception of "1-5" pair in leuven, the MROGH is the second best method. In general, all the examined descriptors perform better than SIFT. The average runtime to compute the descriptors on a PC with an Intel quad core 2.60 GHz CPU with 16GB RAM running Windows 7 Professional is 2.4 ms for READ, 3.1 ms for MROGH, 2.1 ms for LIOP, 1.9 ms for DAISY, and 1.0 ms for SIFT.

(a) leuven
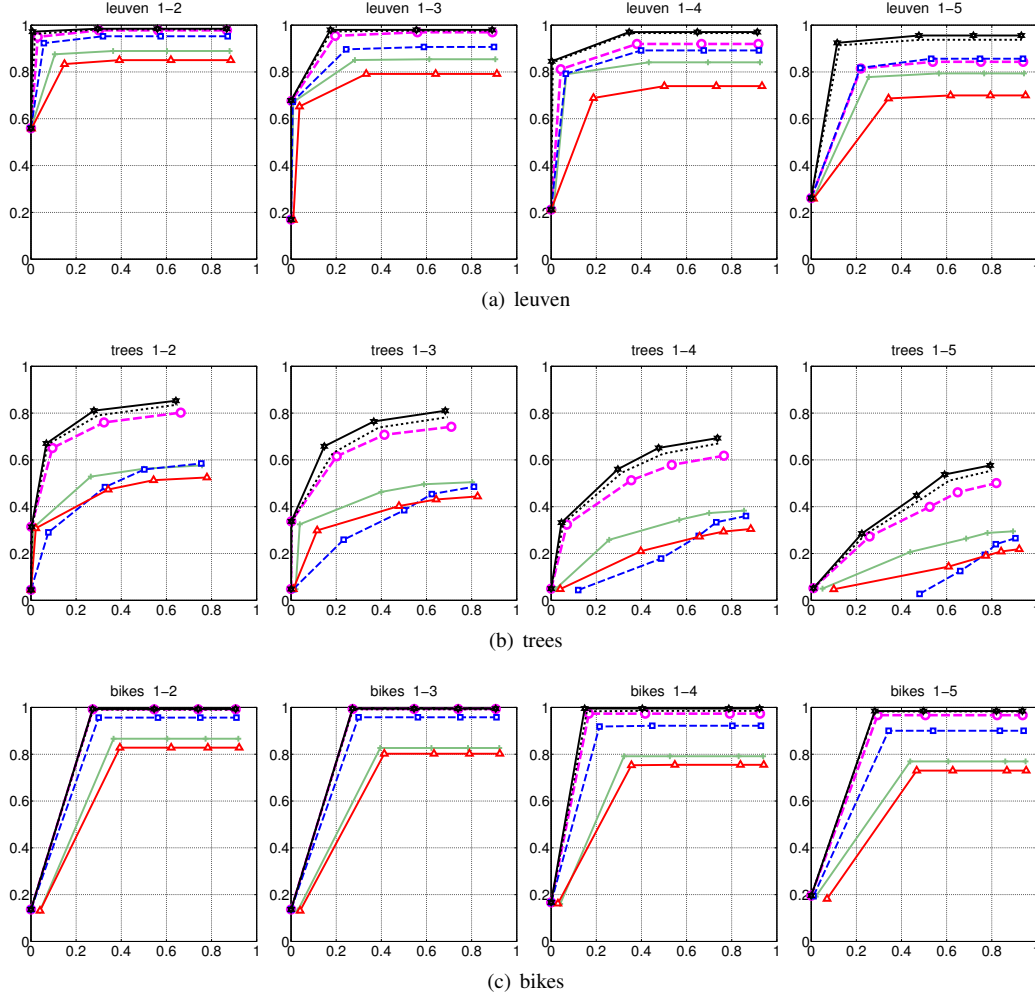
(b) trees

(c) bikes

Figure 8.8: Performance of the descriptors on the Oxford dataset: leuven (illumination change), trees (blur), and bikes (blur). The $READ^-$ is our descriptor with no anisotropic scaling or rotation of support regions. The y axis is recall and the x axis is 1-precision.

Therefore, our method not only outperforms MROGH but also is quite faster.

8.4.3 Noise

To evaluate the performance of the descriptors in the presence of noise, the "1-5" image pairs of the Oxford dataset and two types of noise (i.e., Gaussian and the salt & pepper, SP) are considered. The Gaussian noise with different Signal to Noise Ratio (SNR), and SP noise with different noise density are added to the "5" image while the reference image "1" is unchanged. The area under the curve (AUC) is used for the recall/1-precision graphs for the original (AUC^{orig}) and the noisy (AUC^{noise}) conditions. The AUC drop ratio ($(AUC^{orig} - AUC^{noise})/AUC^{orig}$) is shown in Figure 8.9. As one can see, the READ method is the most robust one in all levels of both types of noise. In some levels of noise $READ^-$ is slightly more robust than READ. After READ, the next robust methods are MROGH, and DAISY. SIFT and LIOP are the most sensitive methods in the

124
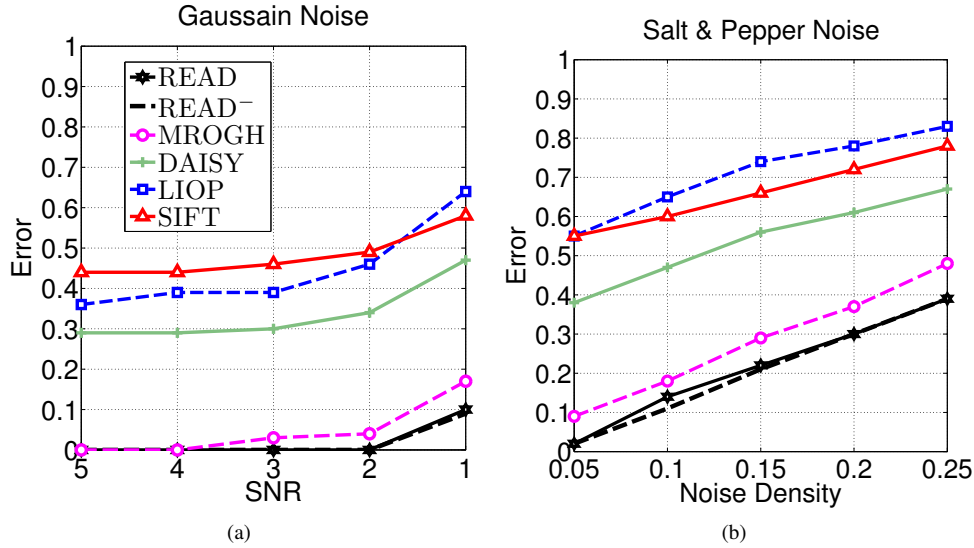
Figure 8.9: The AUC drop ratio in different levels of noise for a) Gaussian noise, b) salt & pepper noise [227].

Gaussian and SP noise, respectively.

8.4.4 Motion Blur

Motion blur is one of the common and challenging problems in many computer vision applications. In spite of its importance, and to the best knowledge of the author, the effect of motion blur on the performance of descriptors have not been explored. To do so, the motion blur effect function in MATLAB is applied to our images. This includes motion blur effect with distances of 4 to 16 pixels with a step size of 4 pixels. The images are shown in Figure 8.10. The performance of the descriptors for this dataset is shown in Figure 8.11. One can see that the READ descriptor notably outperforms the other methods.

8.4.5 Non-uniform Illumination

Non-uniform illumination and shadows are among the most challenging effects. To evaluate the performance of the descriptors the "1-2" and "1-3" image pairs from the nuts dataset[3] shown in Figure 8.12 are used.

The performance of the descriptors in the nuts dataset is shown in Figure 8.13. It can be observed that the READ descriptor remarkably outperforms the other methods.

8.5 Summary

In this chapter a novel region descriptor called READ has been described. The main goal for this descriptor is robustness to imaging effects. In addition to using gradient information computed by

---

[3] Accessible at http://lear.inrialpes.fr/people/mikolajczyk/Database/

(a)

(b)

(c)

(d)

(e)

Figure 8.10: Images used for the motion blur experiments. a) The original image, b) motion offset of 4 pixels, c) 8 pixels, d) 12 pixels, and e) 16 pixels.
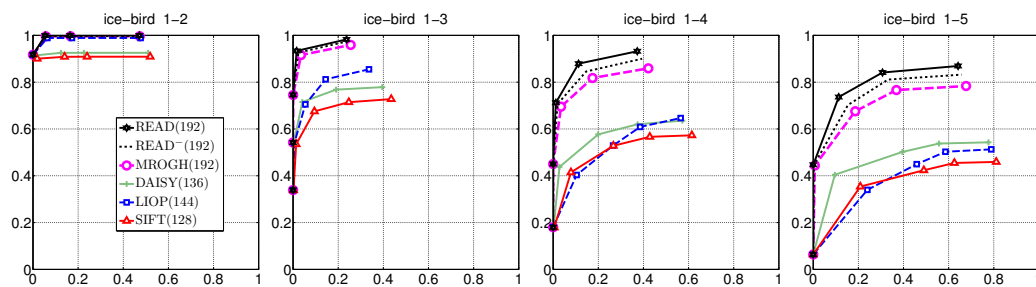
Figure 8.11: Performance of the descriptors on the additional ice-bird dataset (motion blur).

(a)

(b)   (c)

Figure 8.12: Images used for the non-uniform illumination change experiments: a) reference image (nuts1), b) nuts2, and c) nuts3.
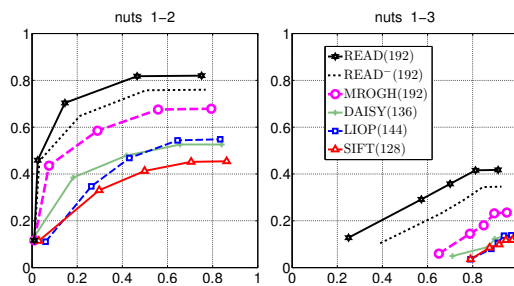
Figure 8.13: Performance of the descriptors on the additional nuts dataset (non-uniform illumination changes).

LFDG, a novel method to define support regions has been described. The experimental results show that the READ descriptor outperforms the state-of-the-art descriptors such as SIFT, LIOP, DAISY, and MROGH in ordinary geometric transformations and common imaging effects. Additional ex-

periments on noise, motion blur, and non-uniform illumination change further demonstrated the robustness and superior performance of the proposed method.

Chapter 9

Robust 3D Texture Features

9.1 Introduction

Texture analysis of 3D data can be broadly divided into two categories: spacetime texture and volumetric texture. Spacetime texture considers phenomena evolving in time such as fire flames, waterfalls, or even a group of runners on a street. The 3D data includes a sequence of 2D images, each of which is acquired at a different time, and the data is defined as (x, y, t) where x and y denote space and t represents time.

The second group, volumetric texture, is about the data acquired from a 3D volume. The data is represented by (x, y, z), where x, y, and z denote space. Examples include medical images acquired by different modalities such as magnetic resonance imaging (MRI), computed tomography (CT), and ultrasound (US). There are a few methods to analyze 3D volumetric data. The developed methods are usually extensions of current popular 2D methods. Nonetheless, the need for analysis of volumetric data, particularly in the domain of medical image analysis, encourages developing new texture methods that are able to analyze volumetric data in a robust and accurate manner.

In this chapter a novel 3D method to analyze volumetric data is presented. In this method first the LFDG is extended to compute local gradient in 3D space. The construction of texture features is based on 3D and 2D gradient information at each voxel. By using LFDG in 2D the gradient information is extracted on the XYZ orthogonal planes at each voxel. This information is used to form a local coordinate system. The local coordinate system and the local 3D gradient computed by the proposed 3D LFDG are then used to define volumetric texture features. This method have been published in [228].

In Section 9.2, the extension of LFDG into 3D Gradient operator is explained. The construction of texture features is demonstrated in Section 9.3. The evaluation of the method is presented in Section 9.4. Finally, the summary of this chapter is given in Section 9.5
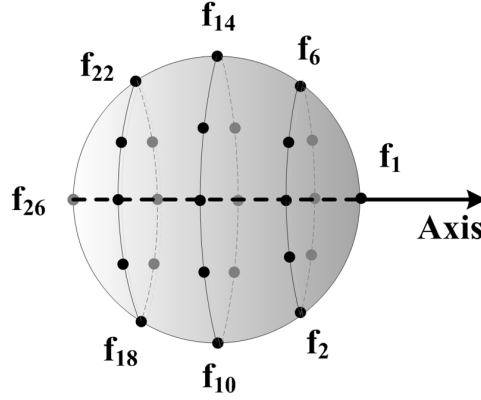
Figure 9.1: Extension of LFDG to 3D by sampling on a sphere using $N = 4$ and $M = 8$ setting [228].

9.2 3D Gradient Estimation

In Section 7.5.3, it is explained that the 2D LFDG can be interpreted as the projection of the local samples into the x and y axes. As a result, the gradient for a given axis can be computed by multiplying the intensity value of the samples by the cosine of the angle between the sample's location and the axis. Using this intuition, the $LFDG$ can be easily extended to 3D:

$$LFDG_a = \sum_{k=1}^{P} f_k cos(\theta_a),\tag{9.1}$$

where θ_a is the angle between an arbitrary axis (a) and the kth sample and the samples are located on a sphere of radius R. To define the location of samples the range $[-1\ 1]$ on axis a is divided into N intervals. At each interval, M samples are used on the sphere. By considering 2 samples on the poles (i.e., parallel, and anti parallel to the axis), $(N - 1)M + 2$ samples on the sphere are used (Figure 9.1).

An example of gradient computation for a 3D MRI brain image is shown in Figure 9.2. In this example, the gradients are computed for the x, y, and z axes ($R = 2$, $N = 16$, $M = 4$). The brain is shown in 3 views: axial, coronal, and sagittal, and the coordinate system is shown for each view.

It is noteworthy that the pattern of distribution of samples on the sphere and the number of patterns will produce different gradient estimation. Also, using a non-symmetric shape (e.g., elliptic in 3D or oval in 2D) is possible. All these settings give further flexibility to generate different estimations of gradients.

Similar to the 2D LFDG, the 3D LFDG can be implemented by an efficient kernel computation. For a radius of R, the kernel has a size of $N \times N \times N$ in 3D where $N = 2R + 1$. For instance, for $R = 1$, the kernel is $3 \times 3 \times 3$. Here, the value of each sample is found using trilinear interpolation from its eight nearest neighbors. A matrix T is defined to incorporate the estimation of each sample f_k (the matrix called B in the 2D LFDG to represent Bilinear interpolation). T is a $P \times N^3$ matrix
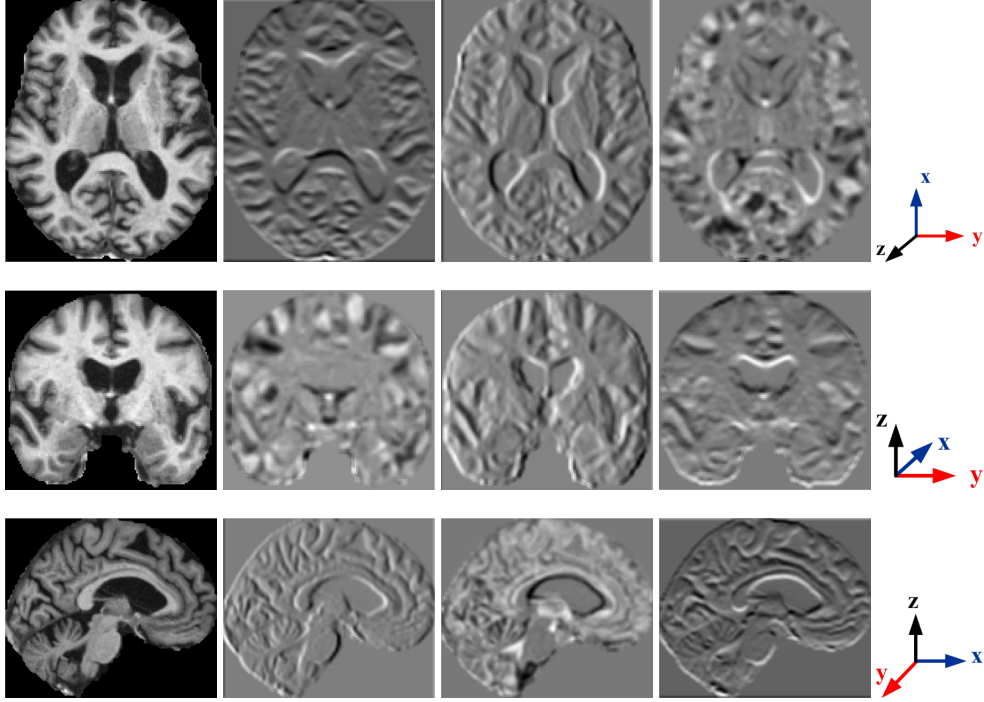
Figure 9.2: 3D $LFDG$ on a sample MRI brain image. The rows show Axial, Coronal, and Sagittal views. The first column is the original image, the next 3 columns are the g_x, g_y, and g_z, and the last column is the coordinate system for each view [228].

where the rows of the matrix represent the samples and the columns the weight of each element in the kernel. If a sample is located in the center of a voxel, in the corresponding row only one element has the value of one and the rest of the elements are zero. Otherwise, eight elements in the corresponding row of the T matrix have non zero values representing the weights of the nearest voxels to the location of that sample.

Similar to the 2D LFDG, a $1 \times P$ row vector called C is considered to represent the cosine weights in Eq 9.1. Each element of C is the cosine of the angle between the sample f_k and the axis. The kernel is defined as $Ker = C \times T$ which is a $1 \times N^3$ row vector. The Ker is reshaped to $N \times N \times N$, and the values of Ker are reflected around the center for the convolution operation.

9.3   3D Texture Features

In this section, the construction of the 3D texture features is explained. In the first step, the gradient information is extracted on the XYZ orthogonal planes at each voxel using the 2D LFDG. This information is used to form a local coordinate system. In the second step, the 3D gradient information is extracted by the 3D LFDG and is quantized using the local coordinate system. Finally, the features are constructed by pooling the quantized gradients into histogram bins using their intensity values. These steps are explained in the next subsections.
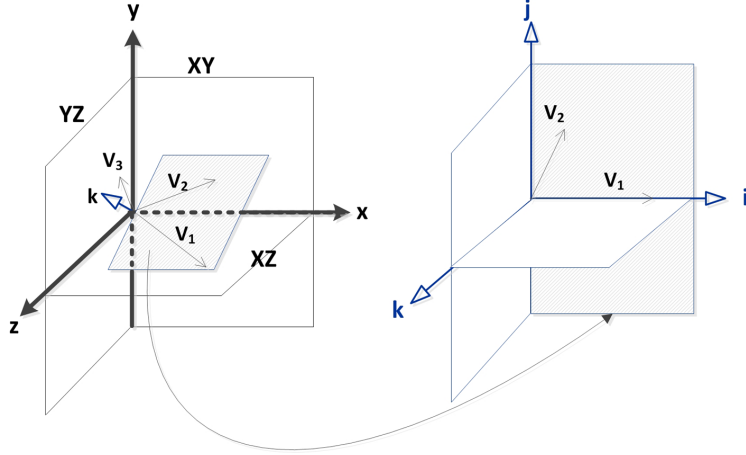
Figure 9.3: Construction of the local coordinate system. On the left, the original coordinate system is shown. In this example, $\vec{V_1} = \vec{V}_{XZ}$ and $\vec{V_2} = \vec{V}_{XY}$. The plane through $\vec{V_1}$ and $\vec{V_2}$ with normal vector $\vec{k}$ is shown. On the right, the new local coordinate system is shown [228].

9.3.1 Local Coordinate System

To compute 3D texture features, first a local coordinate system is defined at each voxel. The 2D $LFDG$ operator is used to form the local coordinate system. To do so, the 2D $LFDG$ is applied to the XY, XZ, and YZ planes to give local gradients on each plane. The 2D local gradient vectors are called $\vec{V}_{XY}$, $\vec{V}_{XZ}$, and $\vec{V}_{YZ}$. The $\vec{V}_{XY}$, $\vec{V}_{XZ}$, and $\vec{V}_{YZ}$ vectors are sorted based on their magnitude. Assume that $\vec{V_1}$, $\vec{V_2}$, and $\vec{V_3}$ are the sorted version of $\vec{V}_{XY}$, $\vec{V}_{XZ}$, and $\vec{V}_{YZ}$:

$$|\vec{V_1}| \geq |\vec{V_2}| \geq |\vec{V_3}|, \tag{9.2}$$

where $|\ |$ denotes the $L2$ norm operator. To avoid confusion with the original axes $\vec{x} = [1, 0, 0]^T$, $\vec{y} = [0, 1, 0]^T$, and $\vec{z} = [0, 0, 1]^T$, assume that the local coordinate system is represented by $\vec{i} = [x_i, y_i, z_i]^T$, $\vec{j} = [x_j, y_j, z_j]^T$, and $\vec{k} = [x_k, y_k, z_k]^T$ (using the right-hand rule), respectively. To define the local coordinate system $\vec{V_1}$ and $\vec{V_2}$ are considered. The local coordinate system is constructed such that the $\vec{i}$ and $\vec{j}$ axis are located on the plane passing from $\vec{V_1}$ and $\vec{V_2}$. To do so, $\vec{i}$ is set in the direction of $\vec{V_1}$. Then $\vec{k}$ is set as:

$$\vec{k} = \frac{\vec{V_1} \times \vec{V_2}}{|\vec{V_1} \times \vec{V_2}|}. \tag{9.3}$$

Using this strategy, $\vec{k}$ is perpendicular to the plane passing through $\vec{V_1}$ and $\vec{V_2}$. Therefore, $\vec{i}$ and $\vec{j}$ are located on the same plane passing through $\vec{V_1}$ and $\vec{V_2}$. Figure 9.3 illustrates the construction of the local coordinate system.

The local 3D gradient $\vec{V}(v_x, v_y, v_z)$ is computed along the x, y, and z axes using Eq. 9.1. The direction of the gradient vectors are computed by normalizing the local gradients:

$$\vec{V}^{norm} = \frac{\vec{V}}{|\vec{V}|}. \tag{9.4}$$
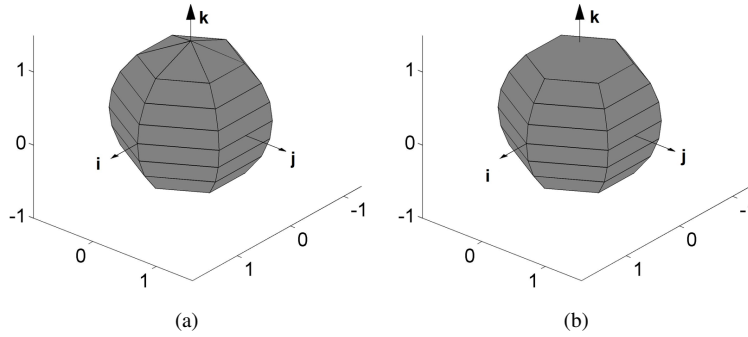
Figure 9.4: Tessellation of a unit circle for $N = 8$ and $M = 6$. a) The original tessellation (histogram bins), b) The triangle bins around the pole are merged to form one bin [228].

The normalization step makes the vector a point on the surface of a unit sphere.

9.3.2 Orientation Quantization

In the next step, the direction of local gradients are quantized into 3D histogram bins using their local coordinate system. In order to quantize the vectors, the idea presented in [192] is used with some modifications. In this approach, a unit sphere is parameterized by the elevation $(-1 \leq z \leq 1)$ and azimuth $(0 \leq \phi < 2\pi)$. In order to have regions with equal area on the sphere, the elevation $(-1 \leq z \leq 1)$ is divided into N equal distances and the azimuth into M equal intervals. This tessellation results in $2M$ spherical triangles at the poles and $(N - 2)M$ spherical quadrangles on the rest of the sphere each of which has the same solid angle of $4\pi/(NM)$. In this thesis the triangles around the poles are merged which results in $(N - 2)M + 2$ regions. Figure 9.4 illustrates a quantization for $N = 8$ and $M = 6$.

The regions around the two poles are merged to avoid instabilities occurring when a vector is close to a pole. In such cases a small difference (e.g., noise) can change the vector's designated bin.

9.3.3 3D Texture Features

Since a local coordinate system is used, it is needed to find an efficient way to assign vectors to the bins. One may note that Eq. 9.4 gives the local gradients in the original coordinate system. Therefore, the vectors $\vec{i}$, $\vec{j}$, and $\vec{k}$ are used to find the corresponding bin for each vector $\vec{V}^{norm}$. The elevation (e) and azimuth (a) indices are computed for this purpose. The elevation of $\vec{V}^{norm}$ is found by projecting $\vec{V}^{norm}$ on the $\vec{k}$ axis:

$$\vec{E} = (\vec{V}^{norm} \cdot \vec{k})\vec{k}, \tag{9.5}$$

where operator $\cdot$ is the dot product of the two vectors. The elevation index is then computed by:

$$e = \left\lfloor \frac{\left(Sign(|\vec{E}|)|\vec{E}| + 1\right)}{2}(N - \epsilon) \right\rfloor, \tag{9.6}$$

where $\lfloor \ \rfloor$ denotes the floor operator, ϵ a small positive number (i.e., 10^{-10}), and $Sign(|\vec{E}|)$ the sign operator:

$$Sign(|\vec{E}|) = \begin{cases} -1 & \text{, if } \vec{V}^{norm} \cdot \vec{k} < 0 \\ 0 & \text{, if } \vec{V}^{norm} \cdot \vec{k} = 0 \\ +1 & \text{, if } \vec{V}^{norm} \cdot \vec{k} > 0. \end{cases} \tag{9.7}$$

The range of the elevation index using Eq. 9.6 is $[0 \ N - 1]$. To compute azimuth first the projection of $\vec{V}^{norm}$ onto the ij plane is found. This can be done by subtracting $\vec{E}$ from $\vec{V}^{norm}$:

$$\vec{V}_{ij} = \vec{V}^{norm} - \vec{E}. \tag{9.8}$$

The angle between $\vec{V}_{ij}$ and $\vec{i}$ can be found by:

$$\phi = acos\left(\frac{\vec{V}_{ij}}{|\vec{V}_{ij}|} \cdot \vec{i}\right), \tag{9.9}$$

where $acos$ denotes arc cosine. One may note that this equation does not differentiate between the vectors that have an angle of ϕ in the clockwise direction and those in the counter-clockwise direction on the ij plane. To correct this, the cross product of $\vec{V}_{ij}$ and $\vec{i}$ is used:

$$\vec{C} = \vec{i} \times \vec{V}_{ij}. \tag{9.10}$$

If $\vec{C}$ is in the direction of $\vec{k}$ (i.e., their dot product is greater than zero) then ϕ is a positive angle. Otherwise ϕ is replaced by $2\pi - \phi$:

$$\phi = \begin{cases} \phi & \text{, if } \vec{C} \bullet \vec{k} \geq 0 \\ 2\pi - \phi & \text{, otherwise.} \end{cases} \tag{9.11}$$

The angle ϕ is in the range $[0 \ 2\pi)$. The azimuth index is now defined as:

$$a = \left\lfloor \frac{\phi M}{2\pi} \right\rfloor, \tag{9.12}$$

where a is in the range $[0 \ M - 1]$. The bin index is a number in the range $[1 \ (N - 2)M + 2]$ computed based on the elevation and azimuth indices:

$$index(\vec{V}^{norm}) = \begin{cases} 1 & \text{, if } e = 0 \\ (N - 2)M + 2 & \text{, if } e = N - 1 \\ (e - 1)M + a + 2 & \text{, otherwise.} \end{cases} \tag{9.13}$$

To construct the final texture features the intensity ordering approach [86] is used. Assume that a voxel with index n is represented by a quadruple $VOX_{(n)} = (I_{(n)}, \vec{V}_{(n)}, \vec{V}_{1(n)}, \vec{V}_{2(n)})$, where $I_{(n)}$ is the intensity of the voxel, $\vec{V}_{(n)}$ the 3D gradient, $\vec{V}_{1(n)}$, and $\vec{V}_{2(n)}$, the two larger gradients computed by the 2D $LFDG$ (i.e., sorted "in-plane" gradients using Eq. 9.2). The voxels are sorted

in ascending order of their intensity values, $VOX_{(1)}, ..., VOX_{(N)}$, where N is the total number of voxels in the volume and $I_{(1)} \leq I_{(2)} \leq ... \leq I_{(N)}$. The ordered voxels are divided into K partitions,

$$Pr(k) = \left\{ VOX_{(n)} | I_{\left(\lceil \frac{N(k-1)}{K} + 1 \rceil\right)} \leq I_{(n)} < I_{\left(\lceil \frac{N.k}{K} \rceil\right)} \right\}, \tag{9.14}$$

where $\lceil \rceil$ denotes the ceiling operator. In each partition, $Pr(k)$, the orientation histograms are computed separately:

$$H(k, i) = \frac{1}{|Pr(k)|} \sum_{\forall VOX_{(n)} \in Pr(k)} Bin(\vec{V}_{(n)}, i).\mu(k) \tag{9.15}$$

where i is the index of the bins ($i = \{1, ..., (N-2)M + 2\}$), $|Pr(k)|$ the cardinality of partition k,

$$Bin(\vec{V}_{(n)}, i) = \begin{cases} 1, & \text{if } index \left(\frac{\vec{V}_{(n)}}{|\vec{V}_{(n)}|} \right) = i \\ 0, & \text{otherwise,} \end{cases} \tag{9.16}$$

and $\mu(k)$ the ratio of the magnitude of the larger "in-plane" gradients in partition k with respect to the whole volume

$$\mu(k) = \frac{\sum_{\forall VOX_{(n)} \in Pr(k)} |\vec{V1}_{(n)}||\vec{V2}_{(n)}|}{\sum_{\forall VOX_{(n)}} |\vec{V1}_{(n)}||\vec{V2}_{(n)}|}. \tag{9.17}$$

The final feature vector is a $(N-2)M + 2 \times K$ feature vector constructed by concatenating the orientation histograms in all subregions:

$$LFD - 3D = \{H(1, 1), H(1, 2), ..., H(K, (N-2)M + 2)\}. \tag{9.18}$$

9.4 Evaluation

In this section the evaluation of the proposed method is explained. First, the description of the datasets is given. After describing how the parameters are tuned, the classification results and robustness evaluations are presented. Finally, the run time of the methods is compared.

9.4.1 Datasets

In contrast to the 2D texture classification problem for which there are several standard evaluation datasets, there is no standard 3D texture dataset for evaluation. As a result, it is common that each method uses its own synthetic or realistic data which makes the comparison between methods hard. To address this issue, four datasets (one synthetic and three realistic) that are publicly available are used. The synthetic dataset [271][1] is composed of 15 texture classes. Each class has ten $64 \times 64 \times 64$ samples generated by Fourier texture synthesis [210].

The realistic datasets are MRI images of the brain. In the first realistic dataset texture features are evaluated for distinguishing between young versus old brains. It is well known that the brain structure changes by aging [91], and therefore, it is useful if texture features can detect the changes.

---

[1] http://www.rfai.li.univ-tours.fr/fr/ressources/
3Dsynthetic_images_database.html

Table 9.1: Specifications of 3D datasets.

Dataset	Class No.	Images in Class	Type
Fourier	15	10	Synthetic
Aging	2	20	MRI
ISBR	3	18	MRI
Brain Tumor	2	10	MRI

Twenty images of young brains (average age of 18.6) and 20 old brains (average age of 86.8) from the OASIS brain database [2] are picked. In each group half of the images belong to females and half to males. The images are T1-weighted, with size of $176 \times 208 \times 176$ and voxel size of $1 \times 1 \times 1 \ mm^3$. All images are preprocessed to remove the skull, to register to the Talairach atlas [334], and to correct the intensity values (normalized).

The second realistic dataset aims to evaluate the capability of texture features for tissue classification problem. To do this, the segmentation dataset of ISBR [294][3] is used. This dataset includes 18 T1-weighted brain MRIs (4 females and 14 males) in which the gray matter (GM), white matter (WM) and cerebrospinal fluid (CSF) are segmented. The images are $256 \times 128 \times 256$ with voxel size of $0.94 \times 0.94 \times 1.5 \ mm^3$.

The third realistic dataset helps to evaluate the performance of the texture features to classify tumour versus normal tissues in the brain. The pre-operative MRI (group 2) images from the BITE (Brain Images of Tumors for Evaluation) dataset [243][4] are used. This brain tumour dataset consists of 14 images of T1-weighted MRI with gadolinium. These images have been registered to a common coordinate space. The images are $394 \times 466 \times 378$ with voxel size of $0.5 \times 0.5 \times 0.5 \ mm^3$. The masks of the tumors are provided. To do the experiments the locations of the tumors are used to define the non-tumour regions at the same location but on the opposite hemispheres. By this approach, for each tumour region there is a corresponding non-tumour region. For simplicity the brains that have only one tumour region are considered. Therefore, only 10 brains could be used. Table 9.1 shows the specifications of the datasets.

9.4.2 Tuning Parameters

Three main parameters are used to compute the texture features. The first parameter is the scale at which the 2D LFDG is computed. This information is used to construct the local coordinate system. The radius of the 2D LFDG scale, R_c, is determined by the user. The number of samples, P_c, is determined automatically from the size of the radius, $P_c = 4 + 4R_c$[5]. The second parameter is the scale at which the 3D LFDG is computed. This is used for computing the 3D gradient information which is later quantized into orientational bins. Similarly, the radius, R_g, is defined by user. The

---

[2]http://www.oasis-brains.org/
[3]http://www.nitrc.org/projects/ibsr
[4]http://www.bic.mni.mcgill.ca/Services/ServicesBITE
[5]This is similar to the strategy of LBP-based methods in which the radius is set by the user and the number of samples is determined by the given radius.

Table 9.2: The parameter values used for each dataset.

Dataset	R_g	P_g	R_c	P_c	K
Fourier	3	16	2	66	1
Aging	1	8	2	66	6
ISBR	3	16	2	66	2
Brain Tumor	3	16	1	34	3

	Rc		
94.05	97.95	97.47	97.25
96.48	97.15	98.59	97.33
96.59	98.97	98.93	98.11
98.69	96.53	95.55	96.56

Fourier (K=1)

	Rc		
99.50	100	100	100
99.70	100	100	100
99.20	99.50	99.70	97.30
96.50	96.70	94.60	94.20

Aging (K=6)

	Rc		
83.11	94.15	98.22	96.96
97.56	98.00	97.63	96.52
99.04	99.74	96.37	97.48
99.41	99.19	97.70	96.22

ISBR (K=2)

	Rc		
83.80	83.00	83.00	82.60
83.60	84.20	84.60	82.40
87.00	86.40	84.80	86.20
86.00	86.40	86.00	86.40

Brain Tumor (K=3)
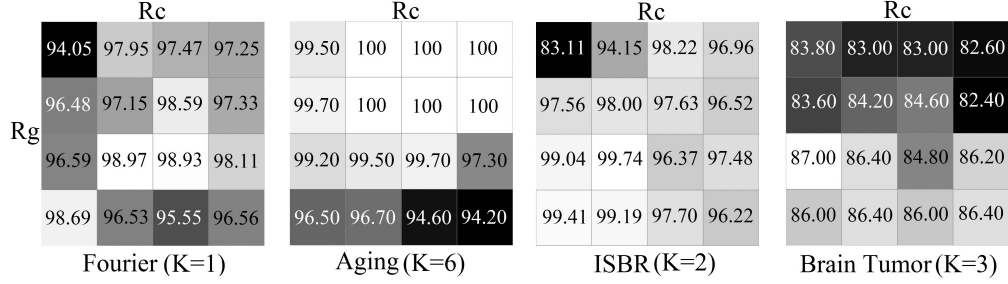
(a)
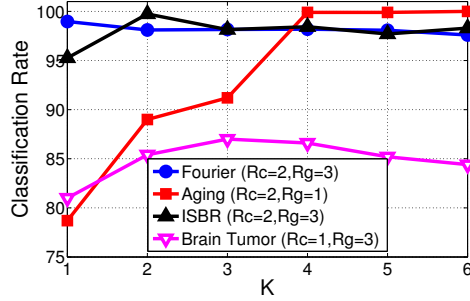
(b)

Figure 9.5: Parameters tuning step. a) the classification rate for the bast K for datasets. The entry (i, j) in each 4×4 matrix shows the classification accuracy for $R_c = i$ and $R_g = j$. b) the classification rate for different values of K and best R_g and R_c.

number of samples, P_c, is set to $P_g = 2+32 R_g$ for the 3D LFDG. The third parameter is the number of partitions, K. To learn these parameters, half of the data in each dataset is used. The radii of the scales (R_c and R_g) are searched from $1, 2, 3, 4$, and the best K is found from $1, 2, ..., 6$. Table 9.2 shows the best parameters used for texture computation. Figure 9.5(a) shows the classification rate for the best K for each dataset (e.g., $K = 2$ for ISBR). The entry (i,j) on each 4×4 matrix shows the classification accuracy for $R_c = i$ and $R_g = j$. For example, the classification rate for the ISBR with $R_g = 3, R_c = 2$ is 99.74%. The higher classifcation rates are shown with a brighter color. In Figure 9.5(b) the classification rate for different values of K and the best R_g and R_c are shown.

As one can see, the classification rate is affected by parameters changes. However, in most of cases (specially R_c and R_g) the effect is quite small. In the Aging dataset there are several parameters that result in 100% accuracy. In these cases any of the values could be selected. The value of K=1 in the Fourier dataset indicates that partitioning (increasing K) does not improve the

Table 9.3: The classification accuracy (mean±std) of different methods for the datasets. Methods which significantly outperform are shown in bold.

Methods	Datasets			
	Fourier	Aging	ISBR	Brain Tumor
3D GLCM	(77.95±3.74)%	(94.10±5.18)%	(98.30±3.10)%	(70.00±10.10)%
3D LBP	(86.13±3.45)%	(72.00±8.64)%	(93.63±3.18)%	**(82.40±11.70)%**
SOP	(92.91±2.81)%	(97.60±2.91)%	(94.52±4.11)%	(61.60±12.18)%
LFD-3D	**(98.64±1.09)%**	**(100.00±0.00)%**	**(100.00±0.00)%**	**(84.20±9.71)%**

results in this dataset.

No specific pattern is observed for choosing the number of partitions (K); however, it seems that choosing a larger number ($K \geq 4$) is a good option in a majority of cases. One may note that increasing K has remarkably improved the performance in the Aging dataset. The best values for R_c and R_g change from database to database, but there are some combinations which provide high classification rates for all datasets (e.g., $R_c = 2$, $R_g = 3$).

9.4.3 Texture Classification

The proposed $LFD-3D$ method is compared with three well-known texture classification methods: 3D GLCM [191], 3D LBP [270], and multiresolution Second Orientation Pyramid (SOP) [15; 289]. The author has implemented the first two methods since their codes are not publicly available and uses the implementation provided the authors of the SOP method[6]. The recommended parameters provided by the authors of these methods are applied. For GLCM the parameters have been set to 8 bins for intensity, 6 bins for gradient magnitude, 6 bins for gradient angle, and distance of 4. For LBP, the parameters are: 2 for radius, 10 for number of samples, and 12 for number of uniform patterns. For SOP the level of the pyramid is set to 4. For classification, the Nearest Neighbor (NN) classifier, and $L1$ distance are used.

Half of the data are randomly selected for training and the rest are used for testing. To reduce the variability of randomness, the classification is repeated 50 times. The classification accuracy of the methods (mean±standard deviation) are shown in Table 9.3 and the best methods that are statistically better than the others are shown in bold for each dataset.

As one can see, the proposed method provides the highest classification accuracy in all four datasets. In the Tumor dataset 3D LBP is equally as good as the proposed method. While 3D GLCM is the second best method for the ISBR, it is the third best method in the Aging, and Tumor datasets, and the worst method in the Fourier dataset. SOP is the second best method for the Fourier and Aging datasets, third best method for ISBR, and the worst method for the Tumor dataset. Finally, 3D LBP is one of the best methods in the Tumor dataset and is the third best method in the Fourier dataset,

---

[6]http://www.dcs.warwick.ac.uk/~creyes/m-vts/
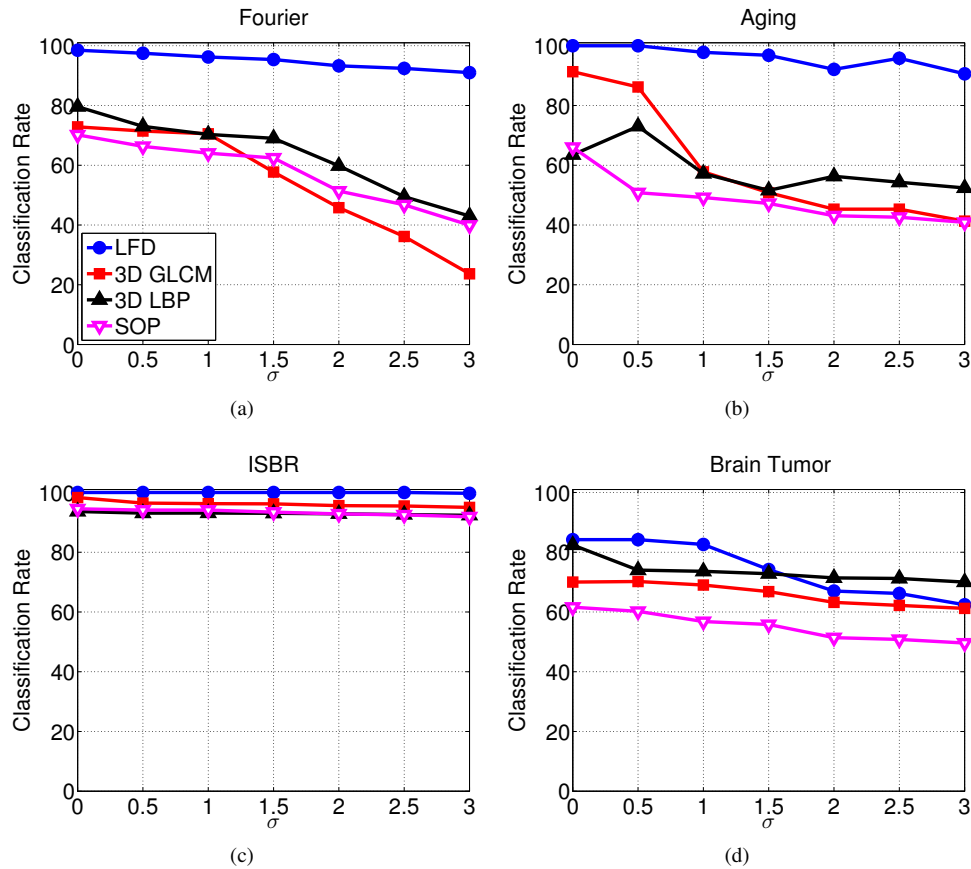
Figure 9.6: Classification rate of the methods in the presence of different levels of noise in the four datasets: a) Fourier, b) Aging, c) ISBR, and d) Brain Tumor.

but has the lowest performance in the Aging and ISBR datasets. Overall, the proposed method consistently outperforms the other methods. However, the performance of the other methods highly depends on the dataset.

9.4.4 Robustness

To examine the robustness of the methods, noise and blur effects are added to the 3D images. In the first experiment, a random Gaussian noise with a specific standard deviation ($\sigma = 1, 1.5, ..., 3$) is added and the experiment is repeated 50 times. Figure 9.6 plots the average classification rate. The image with $\sigma = 0$ represents the original classification where there is no noise.

It can be observed that the LFD-3D method has the highest classification rate at all levels of noise in the Fourier, Aging, and ISBR datasets. The only exception is the Brain Tumor dataset in which LFD-3D is the best method for low levels of noise, while for $\sigma \geq 2$ 3D LBP is the best method. The most noise sensitive method in the Fourier and Aging datasets is the 3D GLCM which looses its performance more than other methods. All methods have a good performance in the ISBR
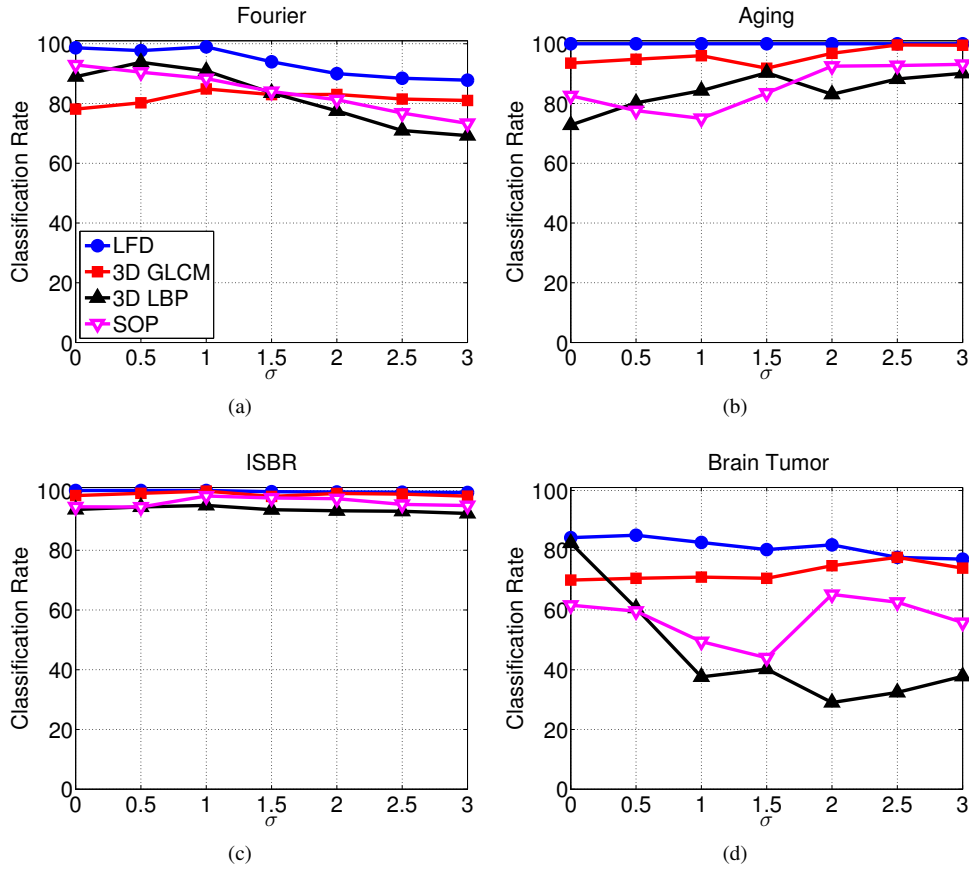
Figure 9.7: Classification rate of the methods in the presence of different levels of blur effect in the four datasets: a) Fourier, b) Aging, c) ISBR, and d) Brain Tumor.

dataset. A possible reason is that that the texture of the white matter, gray matter, and CSF are quite different and the noise does not change their separability very much. The ranking of the methods remains the same in the Fourier, and ISBR; however, in the Aging and Brain Tumor datasets 3D LBP improves its ranking.

In the next experiment the 3D images are blurred with a 3D Gaussian kernel with different band-widths ($\sigma = 1, 1.5, ..., 3$). Figure 9.7 shows the performance of the methods. The first difference between the noise and the blur effect is that the blur effect can improve the results in some cases. This is no surprise as many applications in computer vision and image processing apply Gaussian smoothing in the preprocessing step. This phenomenon is more obvious for the 3D GLCM. For instance, in the Fourier dataset, 3D GLCM is fourth in ranking when there is no blur effect; however, after applying Gaussian blur its performance improves and the method becomes the second best method at $\sigma \geq 2$. Similarly, in the Brain Tumor dataset, 3D GLCM becomes the second best method at $\sigma \geq 0.5$. The most sensitive method to the blur effect is 3D LBP the performance of which decreases in the Fourier, ISBR, and Brain Tumor dataset. The drop is quite significant in

Table 9.4: The average run time in seconds of different methods for each image in different datasets.

Methods	Datasets			
	Fourier	Aging	ISBR	Brain Tumor
3D GLCM	18.78	317.21	590.59	93.92
3D LBP	1.84	137.14	46.98	7.63
SOP	2.41	59.70	104.41	21.00
LFD-3D	**0.91**	**9.51**	**22.91**	**3.79**

the Brain Tumor dataset. The 3D LBP method has a different behavior in the Aging dataset and its performance increases by applying the Gaussian blur kernel. The performance of SOP increases in the Aging, ISBR, and Brain Tumor datasets; however, its performance decreases in the Fourier dataset after the blur effect. The performance of LFD-3D in the Aging, ISBR, and Brain Tumor datasets does not change noticeably, while its performance decreases slightly at $\sigma \geq 1.5$ in the Fourier dataset. Nonetheless, the LFD-3D has the best performance in all levels of blur effect for all four datasets.

As one can observe, in general noise and blur effects have two different impacts. Increasing the amount of noise usually degrades the performance of the methods. However, the blur effect sometimes improves the performance. The reason is that the blur effect removes the noise and smooths the images which alleviates the effect of noise. This is particularly observable in the realistic datasets (which have inherent noise) that the performance of some methods is improved. Nevertheless, because of the robustness of 2D and 3D gradient operators, the proposed method keeps its rank (as the best method) in majority of cases for both effects.

9.4.5 Run Time

One important factor in practical usage is the run time of a method particularly in 3D data which usually requires a high amount of processing. The efficient kernel based implementation of the proposed method for gradient calculation makes it useful for practical usages. Table 9.4 shows the run time of the methods. All methods have been efficiently implemented in Matlab (using vectorization for speed). The programs run on a PC with an Intel quad core CPU with 16GB RAM running Windows 7 Professional.

It can be observed that LFD-3D is the fastest method in all datasets. The next method is 3D LBP in the Fourier, ISBR, and Brian Tumor. However, it has a slower runtime in the Aging dataset which consists of large images. The slowest method is 3D GLCM since it needs to compute the cooccurrence matrix for all directions with distances of 1 to 4. The proposed method is more than two times faster than 3D LBP in small datasets, and more than 6 times faster than SOP (the second fastest method) in the Aging dataset. Indeed, for the Aging dataset, LFD-3D can be computed in

about 10 seconds, while it takes about 1 minute for SOP, more than 2 minutes for 3D LBP, and more than 5 minutes for 3D GLCM.

9.5   Summary

In this chapter, a robust method for 3D texture classification has been presented. First, the LFDG gradient operator was extended to 3D. The texture features are based on the proposed local gradients computed "in plane" (by 2D LFDG) and "in volume" (by 3D LFDG). The 2D local gradients are used to define a local coordinate system at each voxel. Using the two larger gradients make the local coordinate system robust. The direction of the 3D local gradient vectors are quantized in 3D orientational bins defined using a local coordinate system. The local gradient computation is efficiently implemented by 2D and 3D kernels. The experimental results on synthetic and realistic image datasets demonstrate the accuracy, robustness, and speed of the proposed method compared to that of the state-of-the-art volumetric texture classification methods. The proposed 3D gradient operator can be used in general applications where a robust 3D gradient computation is needed.

Chapter 10

Summary and Conclusions

Developing novel and robust texture analysis methods is important for many applications. One of the main applications is in medical image analysis. Although texture analysis has been successfully used in many medical imaging applications, its usage is challenging in some specific diseases. To motivate the usage of texture analysis in more challenging medical applications, for the first time this thesis has explored the power of texture features to study ALS (Chapter 6). The challenge in ALS is that the pathological changes in the brain are not visible in MR images. The analysis shows that texture features can distinguish between healthy subjects and patients with ALS. Also, the proposed voxel based method is able to find regions with statistical difference. These regions have been reported by other ALS studies.

This thesis presents novel voxel based texture analysis methods for the brain image analysis (Chapter 5). While the current texture analysis applications in medical imaging need *a priori* hypotheses for defining the region of interests, the provided hypothesis free method detects significant statistical difference automatically. The Statistical MAp fRom Texture (SMART) Toolbox has been developed for public usage (Appendix A) which is a toolbox for SPM8 software.

This thesis also addresses the robustness issues by proposing the LFD which is first inspired by the LBP. Based on the LFD, several methods have been established including two 2D and one 3D texture classification methods (Chapters 7 and 9). It is shown that the proposed methods are not only more accurate than the state-of-the-art methods but are also more robust to imaging effects such as noise, blurriness, and illumination changes. These advantages led to defining novel gradient operators for 2D and 3D data. It is also shown that the application of the proposed LFD features is not limited to texture classification. The robust edge aware descriptor (READ) has been developed which outperforms the state-of-the-art region descriptors for image matching (Chapter 8).

The list of the contributions of this thesis is:

1. Study ALS using 2D texture analysis: This is the first research work to apply texture analysis to study ALS [229]. Two well-established 2D methods (e.g., GLAM and GLCM) are applied to study ALS. The results justify using texture analysis to study ALS.

2. A study of ALS using the voxel based texture analysis method: this study found several regions affected by ALS and supports the view that ALS is a multisystem disease.

3. A new voxel based texture analysis framework: novel methods for texture analysis are presented for hypothesis free brain analysis.

4. A Computer Aided Diagnosis (CAD) tool for texture analysis of the brain: a CAD tool called SMART is developed as a toolbox for SPM8 software to help doctors making diagnosis and monitoring the progression of diseases by means of texture analysis.

5. Texture classification methods for 2D images: two methods are proposed based on LFD [225; 226]. the first method uses only the magnitude information of LFD, while the second method employs both magnitude and phase information.

6. A new robust gradient operator for 2D images: it is shown that the phase and the magnitude of the second frequency component of LFD can well represent local gradient orientation and magnitude [228]. Therefore, a gradient operator has been defined. The method is implemented by kernels and, hence, it is fast for common computer vision and image processing applications.

7. Texture classification method for 3D images: a novel 3D volumetric texture classification method is proposed which is based on the local gradients computed "in plane" (2D) and "in volume" (3D) using the LFD gradient operators [228].

8. A robust gradient operator for 3D images: the 2D gradient operator is extended to 3D [228]. Similar to 2D operator, the 3D operator is implemented by kernels.

9. A new image matching method: a novel region descriptor, READ, is developed for image matching [227]. By extending the LFD method to image matching application, the discriminative power of the proposed method is further demonstrated.

10.1 Future Works

There are several works that can be done to extend work done in this thesis. Regarding data analysis, T1 and T2 weighted MR images have been used in 2D ALS analysis. In 3D voxel based analysis T1 weighted images are used. Analysis can be performed in other imaging types such as DTI images (e.g., FA map). Also, using larger and more datasets may help to see if the patterns of degeneration are the same in this disease. Longitudinal analysis can be done as well.

The robust LFD-based methods proposed in this thesis are ROI based. The next interesting work is to extend the idea to voxel based analysis and to apply it to ALS as well as other brain related diseases. In addition, the CAD tool can be extended to include more texture analysis methods. At

the moment, the toolbox includes VGLCM-3D, VGLCM-TOP-3D, and 3D GLCM ROI analysis methods, but other analysis methods will enrich the toolbox.

The proposed LFD-based methods could be further improved. The $LFD-MF$ method needs to choose the right number of channels for analysis. To include discriminative channels to the feature vector, the channels are added from lower frequency to higher frequency one by one. Although this strategy does not guarantee the best result, it has provided the highest accuracy compared to the state-of-the-art methods. As a future work, the number of channels can be automatically selected based on the frequency channel properties.

In $LFD-MF$ and $LFD-MPF$ the number and size of disk filters and the area of frequency that the filters cover should be set by the user. There is a trade-off between the filtering area and the robustness of method against noise. In conditions with high levels of noise, one may remove the higher frequency components; however, in a normal condition the high frequencies may provide useful information about the textures. Empirically 10 and 20 disks are chosen for the 128×128 and 200×200 images, respectively. Determining the disk filter settings based on the noise information is an interesting research topic.

The 2D texture features and the proposed gradient operators can be used in several applications. Robustness to noise, blur effect, and illumination changes makes the features favorable for different computer vision and image processing applications. This thesis has extended the application of the methods to image matching. Some other applications are:

- Segmentation: the texture features can be used to distinguish between different regions. The features can be accompanied by intensity and/or color information. The noise robustness makes the features more interesting for medical image segmentation where the noise is unavoidable.

- Registration: the texture features can be used for registration. The first approach is to find landmarks using detectors such as SIFT and descriptors such as READ. Then by matching the landmarks the transformation between the images could be found. The second approach is to use texture information in addition to intensity information in the optimization-based registrations.

- Search engines: the texture features can well represent the characteristics of images. As a result, they can provide a concise representation of images favorable for search engines.

- Texture synthesis: the features can be extended for texture synthesis which has many applications including computer games and cartoon productions.

- Underwater imaging: the underwater images usually have poor quality. The proposed texture features are robust to imaging effects and therefore are suitable for this type of images.

The 3D texture features have been examined on MRI data. However, due to its accuracy and robustness the method can be used for analysis of other types of medical images. As future works one can explore the capabilities of the proposed feature in other image types. The proposed 3D LFD method is not developed as a part of the CAD tool. A future work is to add this method to the SMART toolbox.

Finally, the READ descriptor can be extended for object recognitions especially when illumination changes drastically and non-uniformly. A possible approach is to use bag of words using the features as the words.

Bibliography

[1] Neuron definition in wikipedia. http://en.wikipedia.org/wiki/Neuron, 2014.

[2] Oxford medicine online. http://oxfordmedicine.com, 2014.

[3] Primary motor cortex definition in wikipedia. http://http://en.wikipedia.org/wiki/Primary_motor_cortex, 2014.

[4] S. Abrahams, L.H. Goldstein, A. Simmons, M. Brammer, S.C.R. Williams, V. Giampietro, and P.N. Leigh. Word retrieval in Amyotrophic Lateral Sclerosis: a functional magnetic resonance imaging study. *Brain*, 127(7):1507–1517, 2004.

[5] F. Agosta, A. Chio, M. Cosottini, N. De Stefano, A. Falini, M. Mascalchi, M.A. Rocca, V. Silani, G. Tedeschi, and M. Filippi. The present and the future of neuroimaging in Amyotrophic Lateral Sclerosis. *American Journal of Neuroradiology*, 31(10):1769–1777, 2010.

[6] F. Agosta, M.L. Gorno-Tempini, E. Pagani, S. Sala, D. Caputo, M. Perini, I. Bartolomei, M.E. Fruguglietti, and M. Filippi. Longitudinal assessment of grey matter contraction in Amyotrophic Lateral Sclerosis: A tensor based morphometry study. *Amyotrophic Lateral Sclerosis*, 10(3):168–174, 2009.

[7] F. Agosta, E. Pagani, M. Petrolini, D. Caputo, M. Perini, A. Prelle, F. Salvi, and M. Filippi. Assessment of white matter tract damage in patients withAmyotrophic Lateral Sclerosis: a diffusion tensor MR imaging tractography study. *American Journal of Neuroradiology*, 31(8):1457–1461, 2010.

[8] F. Agosta, E. Pagani, M.A. Rocca, D. Caputo, M. Perini, F. Salvi, A. Prelle, and M. Filippi. Voxel-based morphometry study of brain volumetry and diffusivity in Amyotrophic Lateral Sclerosis patients with mild disability. *Human Brain Mapping*, 28(12):1430–1438, 2007.

[9] F. Agosta, P. Valsasina, N. Riva, M. Copetti, M.J. Messina, A. Prelle, G. Comi, and M. Filippi. The cortical signature ofAmyotrophic Lateral Sclerosis. *PLOS ONE*, 7(8):e42816, 2012.

[10] A. Ahmed, P. Gibbs, M. Pickles, and L. Turnbull. Texture analysis in assessment and prediction of chemotherapy response in breast cancer. *Journal of Magnetic Resonance Imaging*, 38(1):89–101, 2012.

[11] T. Ahonen, A. Hadid, and M. Pietikäinen. Face description with local binary patterns: Application to face recognition. *IEEE Transactions on Pattern Analysis and Machine Intelligence*, 28(12):2037–2041, 2006.

[12] A. Alahi, R. Ortiz, and P. Vandergheynst. Freak: Fast retina keypoint. In *IEEE Conference on Computer Vision and Pattern Recognition , CVPR*, pages 510–517, 2012.

[13] N.K. Alapati and A.C. Sanderson. Texture classification using multi-resolution rotation-invariant operators. *Intelligent Robotics and Computer Vision*, 579:27–38, 1985.

[14] P.F. Alcantarilla, A. Bartoli, and A.J. Davison. Kaze features. *European Conference on Computer Vision, ECCV*, pages 214–227, 2012.

[15] C.C.R. Aldasoro and A. Bhalerao. Volumetric texture segmentation by discriminant feature selection and multiresolution classification. *IEEE Transactions on Medical Imaging*, 26(1):1–14, 2007.

[16] S.B. Antel, D.L. Collins, N. Bernasconi, F. Andermann, R. Shinghal, R.E. Kearney, D.L. Arnold, and A. Bernasconi. Automated detection of focal cortical dysplasia lesions using computational models of their MRI characteristics and texture analysis. *NeuroImage*, 19(4):1748–1759, 2003.

[17] H. Arof and F. Deravi. Circular neighbourhood and 1-d dft features for texture classification and segmentation. *IEE Proceedings on Vision, Image and Signal Processing*, 145(3):167–172, 1998.

[18] S. Arya, S. Khan D. Kumar, M. Dutta, and P. Lehana. Image enhancement technique on ultrasound images using aura transformation. *International Journal in Foundations of Computer Science and Technology*, 2(3):1–10, 2012.

[19] A. Asano, M. Miyagawa, and M. Fujio. Texture modelling by optimal gray scale structuring elements using morphological pattern spectrum. In *15th International Conference on Pattern Recognition*, volume 3, pages 475–478, 2000.

[20] J. Ashburner. A fast diffeomorphic image registration algorithm. *NeuroImage*, 38(1):95–113, 2007.

[21] J. Ashburner and K.J. Friston. Voxel-based morphometry – the methods. *NeuroImage*, 11(6):805–821, 2000.

[22] J. Ashburner and K.J. Friston. Unified segmentation. *NeuroImage*, 26(3):839–851, 2005.

[23] J. Ashburner, K.J. Friston, and W. Penny. *Human Brain Function*. Academic Press, 2004.

[24] J. Ashburner, C. Good, and K.J. Friston. Tensor based morphometry. *NeuroImage*, 11(5):S465, 2000.

[25] Y. Assaf and O Pasternak. Diffusion tensor imaging DTI-based white matter mapping in brain research: a review. *Journal of Molecular Neuroscience*, 34(1):51–61, 2008.

[26] G. Ayala and J. Domingo. Spatial size distributions: applications to shape and texture analysis. *IEEE Transactions on Pattern Analysis and Machine Intelligence*, 23(12):1430–1442, 2001.

[27] R. Azencott, Jia-Ping Wang, and L. Younes. Texture classification using windowed fourier filters. *IEEE Transactions on Pattern Analysis and Machine Intelligence*, 19(2):148–153, 1997.

[28] M.A. Balafar, A.R. Ramli, and S. Mashohor. A new method for MR grayscale inhomogeneity correction. *Artificial Intelligence Review*, 34(2):195–204, 2010.

[29] V. Barra. Expanding the local binary pattern to multispectral images using total orderings. *Computer Vision, Imaging and Computer Graphics. Theory and Applications*, pages 67–80, 2011.

[30] S. Batman and E.R. Dougherty. Size distributions for multivariate morphological granulometries: texture classification and statistical properties. *Optical Engineering*, 36(5):1518–1529, 1997.

[31] F. Benhammadi, M.N. Amirouche, H. Hentous, K. Bey Beghdad, and M. Aissani. Fingerprint matching from minutiae texture maps. *Pattern Recognition*, 40(1):189–197, 2007.

[32] G. Bensimon, L. Lacomblez, and V. Meininger. A controlled trial of riluzole in Amyotrophic Lateral Sclerosis. *New England Journal of Medicine*, 330(9):585–591, 1994.

[33] A. Bernasconi, S.B. Antel, D.L. Collins, N. Bernasconi, A. Olivier, F. Dubeau, G.B. Pike, F. Andermann, and D.L. Arnold. Texture analysis and morphological processing of magnetic resonance imaging assist detection of focal cortical dysplasia in extra-temporal partial epilepsy. *Annals of Neurology*, 49(6):770–775, 2001.

[34] D. Le Bihan, J.F. Mangin, C. Poupon, C.A. Clark, S. Pappata, N. Molko, and H. Chabriat. Diffusion tensor imaging: concepts and applications. *Journal of Magnetic Resonance Imaging*, 13(4):534–546, 2001.

[35] L. Bonilha, E. Kobayashi, G. Castellano, G. Coelho, E. Tinois, F. Cendes, and L.M. Li. Texture analysis of hippocampal sclerosis. *Epilepsia*, 44(12):1546–1550, 2003.

[36] A.C. Bovik, M. Clark, and W.S. Geisler. Multichannel texture analysis using localized spatial filters. *IEEE Transactions on Pattern Analysis and Machine Intelligence*, 12(1):55–73, 1990.

[37] B.H. Brinkmann, A. Manduca, and R.A. Robb. Optimized homomorphic unsharp masking for MR grayscale inhomogeneity correction. *IEEE Transactions on Medical Imaging*, 17(2):161–171, 1998.

[38] P. Brodatz. *Textures: A Photographic Album for Artists and Designers*. Dover Publications, 1966.

[39] B.R. Brooks, R.G. Miller, M. Swash, and T. L. Munsat. El escorial revisited: Revised criteria for the diagnosis of Amyotrophic Lateral Sclerosis. *Amyotrophic Lateral Sclerosis*, 1(5):293–299, 2000.

[40] R. Brown, M. Zlatescu, A. Sijben, G. Roldan, J. Easaw, P. Forsyth, I. Parney, R. Sevick, E. Yan, D. Demetrick, D. Schiff, G. Cairncross, and R. Mitchell. The use of magnetic resonance imaging to noninvasively detect genetic signatures in oligodendroglioma. *Clinical Cancer Research*, 14(8):2357–2362, 2008.

[41] P.D. Bruen, W.J. McGeown, M.F. Shanks, and A. Venneri. Neuroanatomical correlates of neuropsychiatric symptoms in Alzheimer's disease. *Brain*, 131(9):2455–2463, 2008.

[42] M. Calonder, V. Lepetit, C. Strecha, and P. Fua. Brief: Binary robust independent elementary features. In *European Conference on Computer Vision, ECCV*, pages 778–792. Springer, 2010.

[43] E. Canu, F. Agosta, N. Riva, S. Sala, A. Prelle, D. Caputo, M. Perini, G. Comi, and M. Filippi. The topography of brain microstructural damage in Amyotrophic Lateral Sclerosis assessed using diffusion tensor MR imaging. *American Journal of Neuroradiology*, 32(7):1307–1314, 2011.

[44] V. Caselles, B. Coll, and J.M. Morel. Topographic maps and local contrast changes in natural images. *International Journal of Computer Vision*, 33(1):5–27, 1999.

[45] T.M. Chaim, F.L.S. Duran, R.R. Uchida, C.A.M. Périco, C.C. de Castro, and G.F. Busatto. Volumetric reduction of the corpus callosum in Alzheimer's disease in vivo as assessed with voxel-based morphometry. *Psychiatry Research: Neuroimaging*, 154(1):59–68, 2007.

[46] V.V. Chamundeeswari, D. Singh, and K. Singh. An analysis of texture measures in pca-based unsupervised classification of SAR images. *IEEE Geoscience and Remote Sensing Letters*, 6(2):214–218, 2009.

[47] J.L. Chang, C. Lomen-Hoerth, J. Murphy, R.G. Henry, J.H. Kramer, B.L. Miller, and M.L. Gorno-Tempini. A voxel-based morphometry study of patterns of brain atrophy in ALS and ALS/FTLD. *Neurology*, 65(1):75–80, 2005.

[48] T. Chang. Texture analysis of digitized fingerprints for singularity detection. In *Fifth International Conference on Pattern Recognition*, pages 478–480, 1980.

[49] T. Chang and C.J. Kuo. Texture analysis and classification with tree-structured wavelet transform. *IEEE Transactions on Image Processing*, 2(4):429–441, 1993.

[50] D. Chen, L. Li, D. Yoon, J.H. Lee, and Z. Liang. Renormalization method for inhomogeneity correction of MR images. In *SPIE Medical Imaging*, pages 939–942, 2001.

[51] Z. Chen and L. Ma. Grey matter volume changes over the whole brain in Amyotrophic Lateral Sclerosis: A voxel-wise meta-analysis of voxel based morphometry studies. *Amyotrophic Lateral Sclerosis*, 11(6):549–554, 2010.

[52] G. Cheung, M.J. Gawel, P.W. Cooper, R.I. Farb, L.C. Ang, and M.J. Gawal. Amyotrophic lateral sclerosis: correlation of clinical and MR imaging findings. *Radiology*, 194(1):263–270, 1995.

[53] S. Chikkerur, A.N. Cartwright, and V. Govindaraju. Fingerprint enhancement using STFT analysis. *Pattern Recognition*, 40(1):198–211, 2007.

[54] S. Chikkerur, S. Pankanti, A. Jea, N. Ratha, and R. Bolle. Fingerprint representation using localized texture features. In *Eighteenth International Conference on Pattern Recognition*, volume 4, pages 521–524, 2006.

[55] A. Chincarini, P. Bosco, P. Calvini, G. Gemme, M. Esposito, C. Olivieri, L. Rei, S. Squarcia, G. Rodriguez, R. Bellotti, P. Cerellog, I. De Mitrii, A. Reticoj, and F. Nobilid. Local MRI analysis approach in the diagnosis of early and prodromal Alzheimer's disease. *NeuroImage*, 58(2):469–480, 2011.

[56] X. Chu and K. Chan. Rotation and scale invariant texture analysis with tunable gabor filter banks. In *Advances in Image and Video Technology*, volume 5414, pages 83–93, 2009.

[57] S. Chuang, J. Li, X. Sun, A. Vadlamudi, B. Sun, L. Cazares, J. Nyalwidhe, D. Troyer, J. Semmes, and F.D. McKenzie. Prostate cancer region prediction by fusing results from maldi spectra–processing and texture analysis. *Simulation*, 88(10):1247–1259, 2012.

[58] M. Cirillo, F. Esposito, G. Tedeschi, G. Caiazzo, A. Sagnelli, G. Piccirillo, R. Conforti, F. Tortora, M.R. Monsurrò, S. Cirillo, and F. Trojsia. Widespread microstructural white matter involvement in Amyotrophic Lateral Sclerosis: a whole-brain DTI study. *American Journal of Neuroradiology*, 33(6):1102–1108, 2012.

[59] F. S. Cohen, Z. Fan, and M. A. Patel. Classification of rotated and scaled textured images using gaussian markov random field models. *IEEE Transactions on Pattern Analysis and Machine Intelligence*, 13(2):192–202, 1991.

[60] M.S. Cohen, R.M. DuBois, and M.M. Zeineh. Rapid and effective correction of RF inhomogeneity for high field magnetic resonance imaging. *Human Brain Mapping*, 10(4):204–211, 2000.

[61] C. Cortes and V. Vapnik. Support-vector networks. *Machine Learning*, 20:273–297, 1995.

[62] M. Cosottini, I. Pesaresi, S. Piazza, S. Diciotti, P. Cecchi, S. Fabbri, C. Carlesi, M. Mascalchi, and G. Siciliano. Structural and functional evaluation of cortical motor areas in Amyotrophic Lateral Sclerosis. *Experimental Neurology*, 234(1):169–180, 2011.

[63] P. Coupé, P. Hellier, S. Prima, C. Kervrann, and C. Barillot. 3D wavelet subbands mixing for image denoising. *Journal of Biomedical Imaging*, 2008(3):1–11, 2008.

[64] P. Coupé, J.V. Manjon, M. Robles, and D.L. Collins. Adaptive multiresolution non-local means filter for three-dimensional magnetic resonance image denoising. *IET Image Processing*, 6(5):558–568, 2012.

[65] P. Coupé, P. Yger, S. Prima, P. Hellier, C. Kervrann, and C. Barillot. An optimized blockwise nonlocal means denoising filter for 3-d magnetic resonance images. *IEEE Transactions on Medical Imaging*, 27(4):425–441, 2008.

[66] G.R. Cross and A.K. Jain. Markov random field texture models. *IEEE Transactions on Pattern Analysis and Machine Intelligence*, (1):25–39, 1983.

[67] O.G. Cula and K.J. Dana. 3D texture recognition using bidirectional feature histograms. *International Journal of Computer Vision*, 59(1):33–60, 2004.

[68] V.A. Cwik, C.C. Hanstock, P.S. Allen, and W.R.W. Martin. Estimation of brainstem neuronal loss in Amyotrophic Lateral Sclerosis with in vivo proton magnetic resonance spectroscopy. *Neurology*, 50(1):72–77, 1998.

[69] A.M. Dale, B. Fischl, and M.I. Sereno. Cortical surface-based analysis: I. Segmentation and surface reconstruction. *NeuroImage*, 9(2):179–194, 1999.

[70] J.S. Damoiseaux, K.E. Prater, B.L. Miller, and M.D. Greicius. Functional connectivity tracks clinical deterioration in Alzheimer's disease. *Neurobiology of Aging*, 33(4):828–e19, 2012.

[71] K.J. Dana, B. van Ginneken, S.K. Nayar, and J.J. Koenderink. Reflectance and texture of real-world surfaces. *ACM Transactions on Graphics*, 18(1):1–34, January 1999.

[72] J. Dauguet, J.F. Mangin, T. Delzescaux, and V. Frouin. Robust inter-slice intensity normalization using histogram scale-space analysis. *Medical Image Computing and Computer-Assisted Intervention*, pages 242–249, 2004.

[73] M.S. de Oliveira, M.L. Balthazar, A. D'Abreu, C.L. Yasuda, B.P. Damasceno, F. Cendes, and G. Castellano. MR imaging texture analysis of the corpus callosum and thalamus in amnestic mild cognitive impairment and mild Alzheimer disease. *American Journal of Neuroradiology*, 32(1):60–66, 2011.

[74] R.J. Dekker. Texture analysis and classification of ERS SAR images for map updating of urban areas in the netherlands. *IEEE Transactions on Geoscience and Remote Sensing*, 41(9):1950–1958, 2003.

[75] H. Deng and DA. Clausi. Gaussian mrf rotation-invariant features for image classification. *IEEE Transactions on Pattern Analysis and Machine Intelligence*, 26(7):951–955, 2004.

[76] H. Derin and W.S. Cole. Segmentation of textured images using gibbs random fields. *Computer Vision, Graphics, and Image Processing*, 35(1):72–98, 1986.

[77] K.G. Derpanis and R.P. Wildes. Dynamic texture recognition based on distributions of space-time oriented structure. In *IEEE Conference on Computer Vision and Pattern Recognition*, pages 191–198, 2010.

[78] G. Douaud, N. Filippini, S. Knight, K. Talbot, and M.R. Turner. Integration of structural and functional magnetic resonance imaging in Amyotrophic Lateral Sclerosis. *Brain*, 134(12):3470–3479, 2011.

[79] S. Drabycz, G. Roldán, P. de Robles, D. Adler, J.B. McIntyre, A.M. Magliocco, J.G. Cairncross, and J.R. Mitchell. An analysis of image texture, tumor location, and MGMT promoter methylation in glioblastoma using magnetic resonance imaging. *NeuroImage*, 2010.

[80] D.Salas-Gonzalez, J.M. Górriz, J. Ramírez, M. López, I.A. Illan, F. Segovia, C.G. Puntonet, and M. Gómez-Río. Analysis of SPECT brain images for the diagnosis of Alzheimer's disease using moments and support vector machines. *Neuroscience Letters*, 461(1):60–64, 2009.

[81] S. Dubois, R. Péteri, and M. Ménard. A comparison of wavelet based spatio-temporal decomposition methods for dynamic texture recognition. *Pattern Recognition and Image Analysis*, pages 314–321, 2009.

[82] A. Einstein. *Investigations on the Theory of the Brownian Movement*. Dover publications, 1956.

[83] I. M. Elfadel and R. W. Picard. Gibbs random fields, cooccurrences, and texture modeling. *IEEE Transactions on Pattern Analysis and Machine Intelligence*, 16(1):24–37, 1994.

[84] T. Esch, A. Schenk, M. Thiel, T. Ullmann, M. Schmidt, and S. Dech. Land cover classification based on single-polarized VHR SAR images using texture information derived via speckle analysis. In *IEEE International Geoscience and Remote Sensing Symposium*, pages 1875–1878, 2010.

[85] B. Fan, F. Wu, and Z Hu. Aggregating gradient distributions into intensity orders: A novel local image descriptor. In *IEEE Conference on Computer Vision and Pattern Recognition , CVPR*, pages 2377–2384, 2011.

[86] B. Fan, F. Wu, and Z. Hu. Rotationally invariant descriptors using intensity order pooling. *IEEE Transactions on Pattern Analysis and Machine Intelligence*, 34(10):2031–2045, 2012.

[87] P. Filipczuk, T. Fevens, A. Krzyżak, and A. Obuchowicz. Glcm and glrlm based texture features for computer-aided breast cancer diagnosis. *Journal of Medical Informatics*, 19:109–115, 2012.

[88] N. Filippini, G. Douaud, C.E. Mackay, S. Knight, K. Talbot, and M.R. Turner. Corpus callosum involvement is a consistent feature ofAmyotrophic Lateral Sclerosis. *Neurology*, 75(18):1645–1652, 2010.

[89] B. Fischl and A.M. Dale. Measuring the thickness of the human cerebral cortex from magnetic resonance images. *Proceedings of the National Academy of Sciences*, 97(20):11050–11055, 2000.

[90] B. Fischl, M.I. Sereno, and A.M. Dale. Cortical surface-based analysis II: Inflation flattening and a surface-based coordinate system. *NeuroImage*, 9(2):195–207, 1999.

[91] A.M. Fjell and K.B. Walhovd. Structural brain changes in aging: courses, causes and cognitive consequences. *Reviews in the Neurosciences*, 21(3):187–222, 2010.

[92] B.R. Foerster, B.A. Dwamena, M. Petrou, R.C. Carlos, B.C. Callaghan, and M.G. Pomper. Diagnostic accuracy using diffusion tensor imaging in the diagnosis of ALS: a meta-analysis. *Academic Radiology*, 19(9):1075–1086, 2012.

[93] P.E. Forssen and D.G Lowe. Shape descriptors for maximally stable extremal regions. In *International Conference on Computer Vision, ICCV*, pages 1–8, 2007.

[94] P.A. Freeborough and N.C. Fox. Mr image texture analysis applied to the diagnosis and tracking of Alzheimer's disease. *IEEE Transactions on Medical Imaging*, 17(3):475–478, 1998.

[95] K.J. Friston, K.J. Worsley, R.S.J. Frackowiak, J.C. Mazziotta, and A.C. Evans. Assessing the significance of focal activations using their spatial extent. *Human Brain Mapping*, 1(3):210–220, 1994.

[96] M. Fritz, E. Hayman, B. Caputo, and J.-O. Eklundh. On the significance of real-world conditions for material classification. In *European Conference on Computer Vision 2004(ECCV)*, pages 253–266, 2004.

[97] F. Galasso and J. Lasenby. Shape from texture of developable surfaces via fourier analysis. *Advances in Visual Computing*, pages 702–713, 2007.

[98] F. Galasso and J. Lasenby. Fourier analysis and gabor filtering for texture analysis and local reconstruction of general shapes. In *IEEE Conference on Computer Vision and Pattern Recognition*, pages 2342–2349, 2009.

[99] M.M. Galloway. Texture analysis using gray level run lengths. *Computer Graphics and Image Processing*, 4(2):172–179, 1975.

[100] B. Ganeshan, S. Abaleke, R.C.D. Young, C.R. Chatwin, and K.A. Miles. Texture analysis of non-small cell lung cancer on unenhanced computed tomography: initial evidence for a relationship with tumour glucose metabolism and stage. *Cancer Imaging*, 10(1):137, 2010.

[101] B. Ganeshan, K.A. Miles, R.C.D. Young, and C.R. Chatwin. Hepatic enhancement in colorectal cancer: texture analysis correlates with hepatic hemodynamics and patient survival. *Academic Radiology*, 14(12):1520–1530, 2007.

[102] B. Ganeshan, E. Panayiotou, K. Burnand, S. Dizdarevic, and K. Miles. Tumour heterogeneity in non-small cell lung carcinoma assessed by CT texture analysis: a potential marker of survival. *European radiology*, pages 1–7, 2012.

[103] Y. Ge, J.K. Udupa, L.G. Nyul, L. Wei, and R.I. Grossman. Numerical tissue characterization in ms via standardization of the MR image intensity scale. *Journal of Magnetic Resonance Imaging*, 12(5):715–721, 2000.

[104] M. Geilhufe, D.B. Percival, and H.L. Stern. Two-dimensional wavelet variance estimation with application to sea ice SAR images. *Computers & Geosciences*, 39(5):569–574, 2012.

[105] S. Geman and D. Geman. Stochastic relaxation, gibbs distributions, and the bayesian restoration of images. *IEEE Transactions on Pattern Analysis and Machine Intelligence*, (6):721–741, 1984.

[106] C.R. Genovese, N.A. Lazar, and T. Nichols. Thresholding of statistical maps in functional neuroimaging using the false discovery rate. *NeuroImage*, 15(4):870–878, 2002.

[107] P. Georgiadis, D. Cavouras, I. Kalatzis, A. Daskalakis, G.C. Kagadis, K. Sifaki, M. Malamas, G. Nikiforidis, and E. Solomou. Improving brain tumor characterization on MRI by probabilistic neural networks and non-linear transformation of textural features. *Computer methods and programs in biomedicine*, 89(1):24–32, 2008.

[108] M. Ghazel, A. Traboulsee, and R.K. Ward. Optimal filter design for multiple sclerosis lesions segmentation from regions of interest in brain MRI. In *IEEE International Symposium on Signal Processing and Information Technology*, pages 1–5, 2006.

[109] M. Ghazel, A. Traboulsee, and R.K. Ward. Semi-automated segmentation of multiple sclerosis lesions in brain MRI using texture analysis. In *IEEE International Symposium on Signal Processing and Information Technology*, pages 6–10, 2006.

[110] T. Gili, M. Cercignani, L. Serra, R. Perri, F. Giove, B. Maraviglia, C. Caltagirone, and M. Bozzali. Regional brain atrophy and functional disconnection across Alzheimer's disease evolution. *Journal of Neurology, Neurosurgery & Psychiatry*, 82(1):58–66, 2011.

[111] L. Glodzik, L Mosconi, W. Tsui, S. De Santi, R. Zinkowski, E. Pirraglia, K.E. Rich, P. McHugh, Y. Li, S. Williams, F. Alia, H. Zetterberge, K. Blennowe, P. Mehtaf, and M.J. de Leona. Alzheimer's disease markers, hypertension, and gray matter damage in normal elderly. *Neurobiology of Aging*, 33(7):1215–1227, 2012.

[112] R.C. Gonzalez and R.E. Woods. Digital image processing, 2002.

[113] D.S. Goodin, H.A. Rowley, and R.K. Olney. Magnetic resonance imaging in Amyotrophic Lateral Sclerosis. *Annals of Neurology*, 23(4):418–420, 2004.

[114] R.K. Goyal, W.L. Goh, D.P. Mital, and K.L Chan. A translation rotation and scale invariant texture analysis technique based on structural properties. In *Proceedings of the Third International Conference on Automation Technology*, 1994.

[115] R.K. Goyal, W.L. Goh, D.P. Mital, and K.L Chan. Scale and rotation invariant texture analysis based on structural property. In *Proceedings of the 21st International Conference on Industrial Electronics, Control, and Instrumentation*, volume 2, pages 1290–1294, 1995.

[116] D.J. Graber, W.F. Hickey, and B.T. Harris. Progressive changes in microglia and macrophages in spinal cord and peripheral nerve in the transgenic rat model of Amyotrophic Lateral Sclerosis. *Journal of neuroinflammation*, 7(1):8, 2010.

[117] C. Grana, D. Borghesani, and R. Cucchiara. Automatic segmentation of digitalized historical manuscripts. *Multimedia Tools and Applications*, 55(3):483–506, 2011.

[118] O. Gredal, S. Rosenbaum, S. Topp, M. Karlsborg, P. Strange, and L. Werdelin. Quantification of brain metabolites in Amyotrophic Lateral Sclerosis by localized proton magnetic resonance spectroscopy. *Neurology*, 48(4):878–881, 1997.

[119] J. Grosskreutz, J. Kaufmann, J. Frädrich, R. Dengler, H.J. Heinze, and T. Peschel. Widespread sensorimotor and frontal cortical atrophy in Amyotrophic Lateral Sclerosis. *BMC Neurology*, 6(1):1–10, 2006.

[120] J. Grosskreutz, T. Peschel, A. Unrath, R. Dengler, A.C. Ludolph, and J. Kassubek. Whole brain-based computerized neuroimaging in ALS and other motor neuron disorders. *Amyotrophic Lateral Sclerosis*, 9(4):238–248, 2008.

[121] Q. Guo, J. Shao, and V. Ruiz. Characterization and classification of tumor lesions using computerized fractal-based texture analysis and support vector machines in digital mammograms. *International Journal of Computer Assisted Radiology and Surgery*, 4:11–25, 2009.

[122] Y. Guo, G. Zhao, M. Pietikäinen, and Z. Xu. Descriptor learning based on fisher separation criterion for texture classification. In *Asian conference on Computer Vision, ACCV*, pages 185–198, 2011.

[123] Z. Guo, L. Zhang, and D. Zhang. A completed modeling of local binary pattern operator for texture classification. *IEEE Transactions on Image Processing*, 19(6):1657–1663, 2010.

[124] Z. Guo, L. Zhang, and D. Zhang. Rotation invariant texture classification using lbp variance (lbpv) with global matching. *Pattern Recognition*, 43(3):706–719, 3 2010.

[125] G.M. Haley and B.S. Manjunath. Rotation-invariant texture classification using a complete space-frequency model. *IEEE Transactions on Image Processing*, 8(2):255–269, 1999.

[126] H.M. Hamdan and L.M. Larson. Texture classification through level lines. In *International Conference on Image Processing*, volume 3, pages 937–940, 2002.

[127] C. Han, T.S. Hatsukami, and C. Yuan. A multi-scale method for automatic correction of intensity non-uniformity in MR images. *Journal of Magnetic Resonance Imaging*, 13(3):428–436, 2001.

[128] C. Han, E. Risser, R. Ramamoorthi, and E. Grinspun. Multiscale texture synthesis. In *ACM Transactions on Graphics*, volume 27, page 51, 2008.

[129] E. Haneda and C.A. Bouman. Text segmentation for MRC document compression. *IEEE Transactions on Image Processing*, 20(6):1611–1626, 2011.

[130] S.M. Hanif and L. Prevost. Text detection in natural scene images using spatial histograms. In *Second Workshop on Camera Based Document Analysis and Recognition*, pages 122–129, 2007.

[131] R.M. Haralick, K. Shanmugam, and I.H. Dinstein. Textural features for image classification. *IEEE Transactions on Systems, Man and Cybernetics*, 3(6):610–621, 1973.

[132] L.C. Harrison, M. Raunio, K.K. Holli, T. Luukkaala, S. Savio, I. Elovaara, S. Soimakallio, H.J. Eskola, and P. Dastidar. MRI texture analysis in multiple sclerosis: toward a clinical analysis protocol. *Academic Radiology*, 17(6):696, 2010.

[133] R. Hartley and A. Zisserman. *Multiple view geometry in computer vision*. Cambridge Univ Press, second edition, 2000.

[134] M.J. Hecht, F. Fellner, C. Fellner, M.J. Hilz, D. Heuss, and B. Neundörfer. MRI-FLAIR images of the head show corticospinal tract alterations in ALS patients more frequently than T2-, T1-and proton-density-weighted images. *Journal of the Neurological Sciences*, 186(1):37–44, 2001.

[135] M.J. Hecht, F. Fellner, C. Fellner, M.J. Hilz, B. Neundörfer, and D. Heuss. Hyperintense and hypointense MRI signals of the precentral gyrus and corticospinal tract in ALS: a follow-up examination including FLAIR images. *Journal of the Neurological Sciences*, 199(1):59–65, 2002.

[136] M. Heikkila and M. Pietikäinen. A texture-based method for modeling the background and detecting moving objects. *IEEE Transactions on Pattern Analysis and Machine Intelligence*, 28(4):657–662, 2006.

[137] M. Heikkila, M. Pietikäinen, and C. Schmid. Description of interest regions with local binary patterns. *Pattern Recognition*, 42(3):425–436, 3 2009.

[138] J. Heinly, E. Dunn, and J.M. Frahm. Comparative evaluation of binary features. In *European Conference on Computer Vision, ECCV*, pages 759–773. 2012.

[139] S. Herlidou-Meme, J.M. Constans, B. Carsin, D. Olivie, P.A. Eliat, L. Nadal-Desbarats, C. Gondry, E. Le Rumeur, I. Idy-Peretti, and J.D. de Certaines. MRI texture analysis on texture test objects, normal brain and intracranial tumors. *Magnetic Resonance Imaging*, 21(9):989–993, 2003.

[140] K. Holli, A.L. Lääperi, L. Harrison, T. Luukkaala, T. Toivonen, P. Ryymin, P. Dastidar, S. Soimakallio, and H. Eskola. Characterization of breast cancer types by texture analysis of magnetic resonance images. *Academic Radiology*, 17(2):135, 2010.

[141] J. Huang, J. Tian, X. Tang, and J. Liua. Fully automatic and segmentation-robust classification of breast tumors based on local texture analysis of ultrasound images. *Pattern Recognition*, 43(1):280–298, 2010.

[142] J. Huang, D. Yang, and C. Gong. Inspection of pcb line defects based on directionality measurements. *Circuit World*, 38(3):130–141, 2012.

[143] X. Huang, S.Z. Li, and Y. Wang. Shape localization based on statistical method using extended local binary pattern. In *Third International Conference on Image and Graphics 2004*, pages 184–187, 2004.

[144] K.M. Iftekharuddin, S. Ahmed, and J. Hossen. Multiresolution texture models for brain tumor segmentation in MRI. In *Annual International Conference of the IEEE in Engineering in Medicine and Biology Society*, pages 6985–6988, 2011.

[145] K.M. Iftekharuddin, M.A. Islam, J. Shaik, C. Parra, and R. Ogg. Automatic brain tumor detection in MRI: methodology and statistical validation. In *Proc. of SPIE Medical Imaging*, volume 5747, pages 2012–2022, 2005.

[146] K.M. Iftekharuddin, W. Jia, and R. Marsh. Fractal analysis of tumor in brain MR images. *Machine Vision and Applications*, 13(5):352–362, 2003.

[147] K.M. Iftekharuddin, J. Zheng, M.A. Islam, R.J. Ogg, and F. Lanningham. Brain tumor detection in MRI: technique and statistical validation. In *Fortieth Asilomar Conference on Signals, Systems and Computers*, pages 1983–1987, 2006.

[148] M. Irish, O. Piguet, J.R. Hodges, and M. Hornberger. Common and unique gray matter correlates of episodic memory dysfunction in frontotemporal dementia and Alzheimer's disease. *Human Brain Mapping*, 35(4):1422–1435, 2014.

[149] Y. Iwahori, D. Kumar, T. Nakagawa, and M.K. Bhuyan. Improved defect classification of printed circuit board using SVM. *Intelligent Decision Technologies*, pages 355–363, 2012.

[150] N.K. Iwata, S. Aoki, S. Okabe, N. Arai, Y. Terao, S. Kwak, O. Abe, I. Kanazawa, S. Tsuji, and Y. Ugawa. Evaluation of corticospinal tracts in ALS with diffusion tensor MRI and brainstem stimulation. *Neurology*, 70(7):528–532, 2008.

[151] K.J. Friston J. Ashburner. Voxel-based morphometry-the methods. *NeuroImage*, 11(6):805–821, 2000.

[152] K. Jafari-Khouzani, K. Elisevich, S. Patel, B. Smith, and H. Soltanian-Zadeh. Flair signal and texture analysis for lateralizing mesial temporal lobe epilepsy. *NeuroImage*, 49(2):1559–1571, 2010.

[153] K. Jafari-Khouzani, M.R. Siadat, H. Soltanian-Zadeh, and K.L. Elisevich. Texture analysis of hippocampus for epilepsy. In *Proceedings of SPIE Medical Imaging*, volume 5031, pages 279–288, 2003.

[154] K. Jafari-Khouzani and H. Soltanian-Zadeh. Rotation-invariant multiresolution texture analysis using radon and wavelet transforms. *IEEE Transactions on Image Processing*, 14(6):783–795, 2005.

[155] K. Jafari-Khouzani, H. Soltanian-Zadeh, and K. Elisevich. Hippocampus volume and texture analysis for temporal lobe epilepsy. In *IEEE International Conference on Electro/information Technology*, pages 394–397, 2006.

[156] K. Jafari-Khouzani, H. Soltanian-Zadeh, K. Elisevich, and S. Patel. Comparison of 2D and 3D wavelet features for tle lateralization. In *SPIE Medical Imaging*, pages 593–601, 2004.

[157] F. Jager and J. Hornegger. Nonrigid registration of joint histograms for intensity standardization in magnetic resonance imaging. *IEEE Transactions on Medical Imaging*, 28(1):137–150, 2009.

[158] S. Jain, M. Papadakis, S. Upadhyay, and R. Azencott. Rigid-motion-invariant classification of 3-D textures. *IEEE Transactions on Image Processing*, 21(5):2449–2463, 2012.

[159] J.C.T.Wong, L. Concha, C. Beaulieu, W. Johnston, P.S. Allen, and S. Kalra. Spatial profiling of the corticospinal tract in Amyotrophic Lateral Sclerosis using diffusion tensor imaging. *Journal of Neuroimaging*, 17(3):234–240, 2007.

[160] H. Ji, X. Yang, H. Ling, and Y. Xu. Wavelet domain multifractal analysis for static and dynamic texture classification. *IEEE Transactions on Image Processing*, 22(1):286 –299, 2013.

[161] Q. Ji, J. Engel, and E. Craine. Texture analysis for classification of cervix lesions. *IEEE Transactions on Medical Imaging*, 19(11):1144–1149, 2000.

[162] M. Jiang, J.E. Schuster, R. Fu, T. Siddique, and C.J. Heckman. Progressive changes in synaptic inputs to motoneurons in adult sacral spinal cord of a mouse model ofAmyotrophic Lateral Sclerosis. *The Journal of Neuroscience*, 29(48):15031–15038, 2009.

[163] J.K.Sing, D.K. Basu, M. Nasipuri, C. Biswas, and P.K. Saha. Gaussian surface ensemble-based intensity inhomogeneity correction in MR images. In *International Conference on Recent Trends in Information Systems*, pages 275–280, 2011.

[164] I. Jolliffe. *Principal component analysis*. Wiley Online Library, 2005.

[165] M.S. Joshi, P.P. Bartakke, and M.S. Sutaone. Texture representation using autoregressive models. In *International Conference on Advances in Computational Tools for Engineering Applications*, pages 386–390, 2009.

[166] T.J. Kwiatkowski Jr., D.A. Bosco, A.L. Leclerc, E. Tamrazian, C.R. Vanderburg, C. Russ, A. Davis, J. Gilchrist, E.J. Kasarskis, T. Munsat, P. Valdmanis, G.A. Rouleau, B.A. Hosler, P. Cortelli, P.J. de Jong, Y. Yoshinaga, J.L. Haines, M.A. Pericak-Vance, J. Yan, N. Ticozzi, T. Siddique, D. McKenna-Yasek, P.C. Sapp, H.R. Horvitz, J.E. Landers, and R.H. Brown. Mutations in the FUS/TLS gene on chromosome 16 cause familialAmyotrophic Lateral Sclerosis. *Science*, 323(5918):1205–1208, 2009.

[167] F.D. Juengling and J. Kassubek. Standardized calculation of brain parenchymal fraction: an approach to objective assessment of cerebral atrophy. *American Journal of Neuroradiology*, 24(7):1492–1493, 2003.

[168] B. Julesz. Experiments in the visual perception of texture. *Scientific American*, 232:34–43, 1975.

[169] B. Julesz and T. Caelli. On the limits of fourier decompositions in visual texture perception. *Perception*, 8(1):69–73, 1979.

[170] T. Kaeriyama, N. Kodama, T. Shimada, and I. Fukumoto. Application of run length matrix to magnetic resonance imaging diagnosis of Alzheimer-type dementia. *Nihon Hoshasen Gijutsu Gakkai Zasshi*, 58(11):1502, 2002.

[171] S. Kalra, N.R. Cashman, Z. Caramanos, A. Genge, and D.L. Arnold. Gabapentin therapy forAmyotrophic Lateral Sclerosis: lack of improvement in neuronal integrity shown by MR spectroscopy. *American Journal of Neuroradiology*, 24(3):476–480, 2003.

[172] S. Kalra, C.C. Hanstock, W.R. Martin, P.S. Allen, and W.S. Johnston. Detection of cerebral degeneration in Amyotrophic Lateral Sclerosis using high-field magnetic resonance spectroscopy. *Archives of Neurology*, 63(8):1144, 2006.

[173] S. Kalra, P. Tai, A. Genge, and D.L. Arnold. Rapid improvement in cortical neuronal integrity in Amyotrophic Lateral Sclerosis detected by proton magnetic resonance spectroscopic imaging. *Journal of Neurology*, 253(8):1060–1063, 2006.

[174] L.M. Kaplan. Extended fractal analysis for texture classification and segmentation. *IEEE Transactions on Image Processing*, 8(11):1572–1585, 1999.

[175] A. Kassner and R.E. Thornhill. Texture analysis: A review of neurologic MR imaging applications. *American Journal of Neuroradiology*, 31:809–816, 2010.

[176] J. Kassubek, V. Bretschneider, and A.D. Sperfeld. Corticospinal tract MRI hyperintensity in x-linked charcot-marie-tooth disease. *Journal of Clinical Neuroscience*, 12(5):588–589, 2005.

[177] J. Kassubek, A. Unrath, H.J. Huppertz, , D. Lulé, T. Ethofer, A.D. Sperfeld, and A.C. Ludolph. Global brain atrophy and corticospinal tract alterations in ALS, as investigated by voxel-based morphometry of 3-D MRI. *Amyotrophic Lateral Sclerosis*, 6(4):213–220, 2005.

[178] J. Kassubek, A. Unrath, H.J. Huppertz, D. Lulé, T. Ethofer, A.D. Sperfeld, and A.C. Ludolph. Global brain atrophy and corticospinal tract alterations in ALS, as investigated by voxel-based morphometry of 3-D MRI. *Amyotrophic Lateral Sclerosis*, 6(4):213–220, 2005.

[179] A. Kharrat, N. Benamrane, M. Ben Messaoud, and M. Abid. Detection of brain tumor in medical images. In *Third International Conference on Signals, Circuits and Systems*, pages 1–6, 2009.

[180] M. Khatun, A. Gray, and S. Marshall. Morphological granulometry for predicting evolution time of evolving grey-scale texture images. In *19th European Signal Processing Conference*, volume 19, pages 759–763, 2011.

[181] H. Kim, T. Mansi, N. Bernasconi, and A. Bernasconi. Robust surface-based multi-template automated algorithm to segment healthy and pathological hippocampi. *Medical Image Computing and Computer-Assisted Intervention*, pages 445–453, 2011.

[182] H. Kim, T. Mansi, N. Bernasconi, and A. Bernasconi. Surface-based multi-template automated hippocampal segmentation: Application to temporal lobe epilepsy. *Medical Image Analysis*, 16(7):1445–1455, 2012.

[183] J.S. Kim and K.S. Hong. Color–texture segmentation using unsupervised graph cuts. *Pattern Recognition*, 42(5):735–750, 2009.

[184] M. Kim, G. Wu, W. Li, L. Wang, Y.D. Son, Z.H. Cho, and D Shen. Segmenting hippocampus from 7.0 tesla mr images by combining multiple atlases and auto-context models. *Machine Learning in Medical Imaging*, pages 100–108, 2011.

[185] A. Klein, J. Andersson, B.A. Ardekani, J. Ashburner, B. Avants, M.C Chiang, G.E. Christensen, D.L. Collins, J. Gee, P. Hellier, J.H. Songh, M. Jenkinsonb, C. Lepagei, D. Rueckertm, P. Thompsong, T. Vercauterenn, R.P. Woodso, J.J Manna, and R.V. Parsey. Evaluation of 14 nonlinear deformation algorithms applied to human brain MRI registration. *NeuroImage*, 46(3):786–802, 2009.

[186] N. Kodama and Y. Kawase. Computerized method for classification between dementia with lewy bodies and Alzheimers disease by use of texture analysis on brain MRI. In *World Congress on Medical Physics and Biomedical Engineering*, pages 319–321. Springer, 2009.

[187] S. Koelstra, M. Pantic, and I. Patras. A dynamic texture-based approach to recognition of facial actions and their temporal models. *IEEE Transactions on Pattern Analysis and Machine Intelligence*, 32(11):1940–1954, 2010.

[188] C. Konrad, H. Henningsen, J. Bremer, B. Mock, M. Deppe, C. Buchinger, P. Turski, S. Knecht, and B. Brooks. Pattern of cortical reorganization in Amyotrophic Lateral Sclerosis: a functional magnetic resonance imaging study. *Experimental Brain Research*, 143(1):51–56, 2002.

[189] C. Konrad, A. Jansen, H. Henningsen, J. Sommer, P.A. Turski, B.P. Brooks, and S. Knecht. Subcortical reorganization in Amyotrophic Lateral Sclerosis. *Experimental Brain Research*, 172(3):361–369, 2006.

[190] J. Kopf, C.W. Fu, D. Cohen-Or, O. Deussen, D. Lischinski, and T.T. Wong. Solid texture synthesis from 2d exemplars. *ACM Transactions on Graphics*, 26(3):2, 2007.

[191] V.A. Kovalev, F. Kruggel, H.J. Gertz, and D.Y. Von Cramon. Three-dimensional texture analysis of MRI brain datasets. *IEEE Transactions on Medical Imaging*, 20(5):424–433, 2001.

[192] V.A. Kovalev, M. Petrou, and Y.S. Bondar. Texture anisotropy in 3-D images. *IEEE Transactions on Image Processing*, 8(3):346–360, 1999.

[193] K. Krissian and S. Aja-Fernández. Noise-driven anisotropic diffusion filtering of MRI. *IEEE Transactions on Image Processing*, 18(10):2265–2274, 2009.

[194] W.H. Kruskal and W.A. Wallis. Use of ranks in one-criterion variance analysis. *Journal of the American statistical Association*, 47(260):583–621, 1952.

[195] A. Kumar. Computer-vision-based fabric defect detection: a survey. *IEEE Transactions on Industrial Electronics*, 55(1):348–363, 2008.

[196] A. Kurani, D.H. Xu, J.D. Furst, and D.S. Raicu. Co-occurrence matrices for volumetric data. In *The Seventh IASTED International Conference on Computer Graphics and Imaging*, pages 426–443, 2004.

[197] F. Kurth and E. Lüders. Vbm8 toolbox manual. URL: `http://dbm.neuro.uni-jena.de/vbm8/VBM8-Manual.pdf`, Accessed in September, 2014.

[198] E.C. Kyriacou, C. Pattichis, M. Pattichis, C. Loizou, C. Christodoulou, S.K. Kakkos, and A. Nicolaides. A review of noninvasive ultrasound image processing methods in the analysis of carotid plaque morphology for the assessment of stroke risk. *IEEE Transactions on Information Technology in Biomedicine*, 14(4):1027–1038, 2010.

[199] L. Lacomblez, G. Bensimon, V. Meininger, P.N. Leigh, and P. Guillet. Dose-ranging study of riluzole in Amyotrophic Lateral Sclerosis. *The Lancet*, 347(9013):1425–1431, 1996.

[200] A. Laddi, S. Sharma, A. Kumar, and P. Kapur. Classification of tea grains based upon image texture feature analysis under different illumination conditions. *Journal of Food Engineering*, 115(2):226–231, 2012.

[201] S.H. Lai and M. Fang. A new variational shape-from-orientation approach to correcting intensity inhomogeneities in magnetic resonance images. *Medical Image Analysis*, 3(4):409–424, 1999.

[202] H. Lategahn, S. Gross, T. Stehle, and T. Aach. Texture classification by modeling joint distributions of local patterns with gaussian mixtures. *IEEE Transactions on Image Processing*, 19(6):1548–1557, 2010.

[203] S. Lazebnik, C. Schmid, and J. Ponce. A sparse texture representation using local affine regions. *IEEE Transactions on Pattern Analysis and Machine Intelligence*, 27(8):1265–1278, 2005.

[204] J.D. Lee, H.R. Su, P.E. Cheng, M. Liou, J. Aston, A.C. Tsai, and C.Y. Chen. MR image segmentation using a power transformation approach. *IEEE Transactions on Medical Imaging*, 28(6):894–905, 2009.

[205] K. Van Leemput, F. Maes, D. Vandermeulen, and P. Suetens. Automated model-based bias field correction of MR images of the brain. *IEEE Transactions on Medical Imaging*, 18(10):885–896, 1999.

[206] P. Lehana, S. Devi, S. Singh, P. Abrol, S. Khan, and S. Arya. Investigations of the MRI images using aura transformation. *Signal and Image Processing: An International Journal*, 3(1):95–104, 2012.

[207] R.A. Lerski, K. Straughan, L.R. Schad, D. Boyce, S. Blüml, and I. Zuna. MR image texture analysis–An approach to tissue characterization. *Magnetic Resonance Imaging*, 11(6):873–887, 1993.

[208] T. Leung and J. Malik. Representing and recognizing the visual appearance of materials using three-dimensional textons. *International Journal of Computer Vision*, 43(1):29–44, 2001.

[209] S. Leutenegger, M. Chli, and R.Y. Siegwart. Brisk: Binary robust invariant scalable keypoints. In *International Conference on Computer Vision, ICCV*, pages 2548–2555, 2011.

[210] J.P. Lewis. Texture synthesis for digital painting. In *ACM SIGGRAPH Computer Graphics*, volume 18, pages 245–252, 1984.

[211] H. Li, M. Giger, O. Olopade, and L. Lan. Validation of mammographic texture analysis for assessment of breast cancer risk. *Digital Mammography*, pages 267–271, 2010.

[212] J. Li, Q. Du, and C. Sun. An improved box-counting method for image fractal dimension estimation. *Pattern Recognition*, 42(11):2460–2469, 2009.

[213] J.P. Li, P.L. Pan, W. Song, R. Huang, K. Chen, and H.F. Shang. A meta-analysis of diffusion tensor imaging studies in Amyotrophic Lateral Sclerosis. *Neurobiology of Aging*, 33(8):1833–1838, 2012.

[214] W.C. Li and D.M. Tsai. Wavelet-based defect detection in solar wafer images with inhomogeneous texture. *Pattern Recognition*, 45(2):742–756, 2012.

[215] X. Li, H. Xia, Z. Zhou, and L. Tong. 3d texture analysis of hippocampus based on mr images in patients with Alzheimer disease and mild cognitive impairment. In *Third International Conference on Biomedical Engineering and Informatics*, volume 1, pages 1–4, 2010.

[216] S. Liao and A. Chung. A new subspace learning method in fourier domain for texture classification. In *17th IEEE International Conference on Image Processing 2010(ICIP)*, pages 4589 –4592, 2010.

[217] S. Liao, M. W. K. Law, and A. C. S. Chung. Dominant local binary patterns for texture classification. *IEEE Transactions on Image Processing*, 18(5):1107–1118, 2009.

[218] B. Likar, M.A. Viergever, and F. Pernus. Retrospective correction of MR intensity inhomogeneity by information minimization. *IEEE Transactions on Medical Imaging*, 20(12):1398–1410, 2001.

[219] F.H. Lin, Y.J. Chen, J.W. Belliveau, and L.L. Wald. A wavelet-based approximation of surface coil sensitivity profiles for correction of image intensity inhomogeneity and parallel imaging reconstruction. *Human Brain Mapping*, 19(2):96–111, 2003.

[220] Y. Liu and S.N. Srihari. Document image binarization based on texture features. *IEEE Transactions on Pattern Analysis and Machine Intelligence*, 19(5):540–544, 1997.

[221] A. Lobay and D.A. Forsyth. Shape from texture without boundaries. *International Journal of Computer Vision*, 67(1):71–91, 2006.

[222] C.P. Loizou, V. Murray, M.S. Pattichis, M. Pantziaris, and C.S. Pattichis. Multiscale amplitude-modulation frequency-modulation (am-fm) texture analysis of ultrasound images of the intima and media layers of the carotid artery. *IEEE Transactions on Information Technology in Biomedicine*, 15(2):178–188, 2011.

[223] C. Lomen-Hoerth, T. Anderson, and B. Miller. The overlap ofAmyotrophic Lateral Sclerosis and frontotemporal dementia. *Neurology*, 59(7):1077–1079, 2002.

[224] D.G. Lowe. Distinctive image features from scale-invariant keypoints. *International Journal of Computer Vision*, 60:91–110, 2004.

[225] R. Maani, S. Kalra, and Y. H. Yang. Noise robust rotation invariant features for texture classification. *Pattern Recognition*, 46(8):2103–2116, 2013.

[226] R. Maani, S. Kalra, and Y. H. Yang. Rotation invariant local frequency descriptors for texture classification. *IEEE Transactions on Image Processing*, 22(6):2409–2419, 2013.

[227] R. Maani, S. Kalra, and Y. H. Yang. Robust edge aware descriptor for image matching. In *Asian conference on Computer Vision, ACCV*. 2014. To appear.

[228] R. Maani, S. Kalra, and Y.H. Yang. Robust volumetric texture classification of magnetic resonance images of the brain using local frequency descriptor. *IEEE Transactions on Image Processing*, 23(10):4625–4636, 2014.

[229] R. Maani, Y. H. Yang, and S. Kalra. Texture analysis of the brain in Amyotrophic Lateral Sclerosis, 2013. Poster presented at 19th Annual Meeting of the Organization for Human Brain Mapping (OHBM), June 16–20, Seattle, USA.

[230] I.R.A. Mackenzie, R. Rademakers, and M. Neumann. TDP-43 and FUS in Amyotrophic Lateral Sclerosis and frontotemporal dementia. *The Lancet Neurology*, 9(10):995–1007, 2010.

[231] A. Madabhushi, M. Feldman, D. Metaxas, D. Chute, and J. Tomaszewski. A novel stochastic combination of 3D texture features for automated segmentation of prostatic adenocarcinoma from high resolution MRI. *Medical Image Computing and Computer-Assisted Intervention*, pages 581–591, 2003.

[232] A. Madabhushi and J.K. Udupa. New methods of MR image intensity standardization via generalized scale. *Medical physics*, 33:3426, 2006.

[233] A. Mahmoud, S. Elbialy, B. Pradhan, and M. Buchroithner. Field-based landcover classification using TerraSAR-X texture analysis. *Advances in Space Research*, 48(5):799–805, 2011.

[234] P. Maillard. Comparing texture analysis methods through classification. *Photogrammetric Engineering and Remote Sensing*, 69(4):357–368, 2003.

[235] S.G. Mallat. A theory for multiresolution signal decomposition: the wavelet representation. *IEEE Transactions on Pattern Analysis and Machine Intelligence*, 11(7):674–693, 1989.

[236] J.V. Manjón, P. Coupé, A. Buades, D. Louis Collins, and M. Robles. New methods for MRI denoising based on sparseness and self-similarity. *Medical Image Analysis*, 16(1):18–27, 2012.

[237] J.V. Manjón, P. Coupé, L. Martí-Bonmatí, D.L. Collins, and M. Robles. Adaptive non-local means denoising of mr images with spatially varying noise levels. *Journal of Magnetic Resonance Imaging*, 31(1):192–203, 2010.

[238] B.S. Manjunath and W.Y. Ma. Texture features for browsing and retrieval of image data. *IEEE Transactions on Pattern Analysis and Machine Intelligence*, 18(9):837–842, 1996.

[239] J. Mao and A.K. Jain. Texture classification and segmentation using multiresolution simultaneous autoregressive models. *Pattern Recognition*, 25(2):173–188, 2 1992.

[240] D.S. Marcus, T.H. Wang, J. Parker, J.G. Csernansky, J.C. Morris, and R.L. Buckner. Open access series of imaging studies (oasis): cross-sectional MRI data in young, middle aged, nondemented, and demented older adults. *Journal of cognitive neuroscience*, 19(9):1498–1507, 2007.

[241] J.M. Mathias, P.S. Tofts, and N.A. Losseff. Texture analysis of spinal cord pathology in multiple sclerosis. *Magnetic Resonance in Medicine*, 42(5):929–935, 1999.

[242] M.E. Mayerhoefer, P. Szomolanyi, D. Jirak, A. Materka, and S. Trattnig. Effects of MRI acquisition parameter variations and protocol heterogeneity on the results of texture analysis and pattern discrimination: An application-oriented study. *Medical physics*, 36:1236, 2009.

[243] L. Mercier, R.F. Del Maestro, K. Petrecca, D. Araujo, C. Haegelen, and D.L. Collins. Online database of clinical MR and ultrasound images of brain tumors. *Medical Physics*, 39:3253, 2012.

[244] C.R. Meyer, P.H. Bland, and J. Pipe. Retrospective correction of intensity inhomogeneities in MRI. *IEEE Transactions on Medical Imaging*, 14(1):36–41, 1995.

[245] D.M. Mezzapesa, A. Ceccarelli, F. Dicuonzo, A. Carella, M.F. De Caro, M. Lopez, V. Samarelli, P. Livrea, and I.L. Simone. Whole-brain and regional brain atrophy in Amyotrophic Lateral Sclerosis. *American Journal of Neuroradiology*, 28(2):255–259, 2007.

[246] K. Mikolajczyk and C. Schmid. Scale & affine invariant interest point detectors. *International Journal of Computer Vision*, 60:63–86, 2004.

[247] K. Mikolajczyk and C. Schmid. A performance evaluation of local descriptors. *IEEE Transactions on Pattern Analysis and Machine Intelligence*, 27(10):1615 –1630, 2005.

[248] K. Mikolajczyk, T. Tuytelaars, C. Schmid, A. Zisserman, J. Matas, F. Schaffalitzky, T. Kadir, and L. Van Gool. A comparison of affine region detectors. *International Journal of Computer Vision*, 65:43–72, 2005.

[249] O. Miksik and K. Mikolajczyk. Evaluation of local detectors and descriptors for fast feature matching. In *International Conference on Pattern Recognition, ICPR*, pages 2681–2684, 2012.

[250] K.A. Miles, B. Ganeshan, M.R. Griffiths, R.C.D. Young, and C.R. Chatwin. Colorectal cancer: Texture analysis of portal phase hepatic CT images as a potential marker of survival1. *Radiology*, 250(2):444–452, 2009.

[251] R.G. Miller, J.D. Mitchell, M. Lyon, and D.H. Moore. Riluzole forAmyotrophic Lateral Sclerosis (als)/motor neuron disease (mnd). *The Cochrane Library*, 1(CD001447), 2004.

[252] S. Mirowitz, K. Sartor, M. Gado, and R. Torack. Focal signal-intensity variations in the posterior internal capsule: normal MR findings and distinction from pathologic findings. *Radiology*, 172(2):535–539, 1989.

[253] B. Mohammadi, K. Kollewe, A. Samii, K. Krampfl, R. Dengler, and T.F. Münte. Changes of resting state brain networks in Amyotrophic Lateral Sclerosis. *Experimental Neurology*, 217(1):147, 2009.

[254] P. Monasse and F. Guichard. Fast computation of a contrast-invariant image representation. *IEEE Transactions on Image Processing*, 9(5):860–872, 2000.

[255] Y.S. Moon, J.S. Chen, K.C. Chan, K. So, and K.C. Woo. Wavelet based fingerprint liveness detection. *Electronics Letters*, 41(20):1112–1113, 2005.

[256] V. Murino, C. Ottonello, and S. Pagnan. Noisy texture classification: A higher-order statistics approach. *Pattern Recognition*, 31(4):383–393, 4 1998.

[257] G. Naghdy, M. Ros, C. Todd, and E. Norahmawati. Cervical cancer classification using gabor filters. In *First IEEE International Conference on Healthcare Informatics, Imaging and Systems Biology*, pages 48–52, 2011.

[258] G. Nair, J.D. Carew, S. Usher, D. Lu, X.P. Hu, and M. Benatar. Diffusion tensor imaging reveals regional differences in the cervical spinal cord in Amyotrophic Lateral Sclerosis. *NeuroImage*, 53(2):576–583, 2010.

[259] L. Nanni and A. Lumini. Local binary patterns for a hybrid fingerprint matcher. *Pattern recognition*, 41(11):3461–3466, 2008.

[260] P.J. Nestor, T.D. Fryer, P. Smielewski, and J.R. Hodges. Limbic hypometabolism in Alzheimer's disease and mild cognitive impairment. *Annals of Neurology*, 54(3):343–351, 2003.

[261] H.Y.T. Ngan, G.K.H. Pang, and N.H.C. Yung. Automated fabric defect detectiona review. *Image and Vision Computing*, 29(7):442–458, 2011.

[262] R.D. Nowak. Wavelet-based rician noise removal for magnetic resonance imaging. *IEEE Transactions on Image Processing*, 8(10):1408–1419, 1999.

[263] G. Nyul and J.K. Udupa. On standardizing the MR image intensity scale. *Magnetic Resonance in Medicine*, 42(6):1072–1081, 1999.

[264] L.G. Nyul, J.K. Udupa, and X. Zhang. New variants of a method of MRI scale standardization. *IEEE Transactions on Medical Imaging*, 19(2):143–150, 2000.

[265] T. Ojala, T. Mäenpää, M. Pietikäinen, J. Viertola, J. Kyllonen, and S. Huovinen. Outex - new framework for empirical evaluation of texture analysis algorithms. In *International Conference on Pattern Recognition, ICPR*, volume 1, pages 701–706 vol.1, 2002.

[266] T. Ojala and M. Pietikäinen. Texture classification. *CVonline: The Evolving, Distributed, Non-Proprietary, On-Line Compendium of Computer Vision*, 2001.

[267] T. Ojala, M. Pietikäinen, and T. Mäenpää. Multiresolution gray-scale and rotation invariant texture classification with local binary patterns. *IEEE Transactions on Pattern Analysis and Machine Intelligence*, 24(7):971–987, 2002.

[268] V. Ojansivu and J. Heikkilä. Blur insensitive texture classification using local phase quantization. *Image and Signal Processing*, pages 236–243, 2008.

[269] R. Paget and I.D. Longstaff. Texture synthesis via a noncausal nonparametric multiscale markov random field. *IEEE Transactions on Image Processing*, 7(6):925–931, 1998.

[270] L. Paulhac, P. Makris, and J.Y. Ramel. Comparison between 2D and 3D local binary pattern methods for characterisation of three-dimensional textures. *Image Analysis and Recognition*, pages 670–679, 2008.

[271] L. Paulhac, P. Makris, J.Y. Ramel, et al. A solid texture database for segmentation and classification experiments. In *International Conference on Computer Vision Theory and Applications*, pages 135–141, 2009.

[272] G. Peyre. Texture synthesis with grouplets. *IEEE Transactions on Pattern Analysis and Machine Intelligence*, 32(4):733–746, 2010.

[273] Y.S. Piao, K. Wakabayashi, A. Kakita, M. Yamada, S. Hayashi, T. Morita, F. Ikuta, K. Oyanagi, and H. Takahashi. Neuropathology with clinical correlations of sporadicAmyotrophic Lateral Sclerosis: 102 autopsy cases examined between 1962 and 2000. *Brain Pathology*, 13(1):10–22, 2003.

[274] R. W. Picard and I. Elfadel. Structure of aura and co–occurrence matrices for the gibbs texture model. *Journal of Mathematical Imaging and Vision*, 2(1):5–25, 1992.

[275] R. W. Picard and I. Elfadel. Gibbs random fields, co-occurrences, and texture modeling. *IEEE Transactions on Pattern Analysis and Machine Intelligence*, 16(1):24–37, 1994.

[276] E.P. Pioro, J.P. Antel, N.R. Cashman, and D.L. Arnold. Detection of cortical neuron loss in motor neuron disease by proton magnetic resonance spectroscopic imaging in vivo. *Neurology*, 44(10):1933–1933, 1994.

[277] E.P. Pioro, A.W. Majors, H. Mitsumoto, D.R. Nelson, and T.C. Ng. 1h-mrs evidence of neurodegeneration and excess glutamate glutamine in ALS medulla. *Neurology*, 53(1):71–71, 1999.

[278] C. Pohl, W. Block, J. Karitzky, F. Traber, S. Schmidt, C. Grothe, R. Lamerichs, H. Schild, and T. Klockgether. Proton magnetic resonance spectroscopy of the motor cortex in 70 patients withAmyotrophic Lateral Sclerosis. *Archives of Neurology*, 58(5):729, 2001.

[279] J. Prudlo, C. Bißbort, A. Glass, A. Grossmann, K. Hauenstein, R. Benecke, and S.J. Teipel. White matter pathology in ALS and lower motor neuron ALS variants: a diffusion tensor imaging study using tract-based spatial statistics. *Journal of Neurology*, 259:1848–1859, 2012.

[280] F.R. Punzalan, T. Sato, T. Okada, S. Kuhara, K. Togashi, and K. Minato. Joint histogram-based intensity standardization of diffusion-weighted MRI images. In *World Congress on Medical Physics and Biomedical Engineering*, pages 1067–1070, 2010.

[281] T. Pyra, B. Hui, C. Hanstock, L. Concha, J.C.T. Wong, C. Beaulieu, W. Johnston, and S. Kalra. Combined structural and neurochemical evaluation of the corticospinal tract in Amyotrophic Lateral Sclerosis. *Amyotrophic Lateral Sclerosis*, 11(1-2):157–165, 2010.

[282] X. Qin and Y.H. Yang. Similarity measure and learning with gray level aura matrices (GLAM) for texture image retrieval. In *IEEE Conference on Computer Vision and Pattern Recognition, CVPR*, volume 1, pages 326–333, 2004.

[283] X. Qin and Y.H. Yang. Basic gray level aura matrices: theory and its application to texture synthesis. In *IEEE International Conference on Computer Vision, ICCV*, volume 1, pages 128–135, 2005.

[284] X. Qin and Y.H. Yang. Aura 3D textures. *IEEE Transactions on Visualization and Computer Graphics*, 13(2):379–389, 2007.

[285] G.D. Rabinovici, W.W. Seeley, E.J. Kim, M.L. Gorno-Tempini, K. Rascovsky, T.A. Pagliaro, S.C. Allison, C. Halabi, J.H. Kramer, J.K. Johnson, M.W. Weiner, M.S. Forman, J.Q. Tro-janowski, S.J. DeArmond, B.L. Miller, and H.J. Rosen. Distinct MRI atrophy patterns in autopsy-proven Alzheimer's disease and frontotemporal lobar degeneration. *American Journal of Alzheimer's Disease and Other Dementias*, 22(6):474–488, 2008.

[286] M.H. Rahman, M. Pickering, and D. Kundu. Efficient rotation invariant gabor descriptors for texture classification. In *International Conference on Informatics, Electronics & Vision*, pages 661–666, 2012.

[287] E. Rahtu, J. Heikkilä, V. Ojansivu, and T. Ahonen. Local phase quantization for blur-insensitive image analysis. *Image and Vision Computing*, 2012.

[288] E. Ranguelova and A. Quinn. Analysis and synthesis of three-dimensional Gaussian Markov Random fields. In *International Conference on Image Processing*, volume 3, pages 430–434, 1999.

[289] C. Reyes-Aldasoro and A. Bhalerao. Volumetric texture description and discriminant feature selection for MRI. In *Information Processing in Medical Imaging*, pages 282–293, 2003.

[290] G.M. Ringholz, S.H. Appel, M. Bradshaw, N.A. Cooke, and D.M. Mosnik. Prevalence and patterns of cognitive impairment in sporadic ALS. *Neurology*, 65(4):586–590, 2005.

[291] M.G. Roberts, E.M.B. Pacheco, R. Mohankumar, T.F. Cootes, and J.E. Adams. Detection of vertebral fractures in dxa vfa images using statistical models of appearance and a semi-automatic segmentation. *Osteoporosis International*, 21(12):2037–2046, 2010.

[292] N. Robitaille, A. Mouiha, B. Crépeault, F. Valdivia, and S. Duchesne. Tissue-based MRI intensity standardization: application to multicentric datasets. *Journal of Biomedical Imaging*, 2012:4, 2012.

[293] L. Roccatagliata, L. Bonzano, G. Mancardi, C. Canepa, and C. Caponnetto. Detection of motor cortex thinning and corticospinal tract involvement by quantitative MRI in Amyotrophic Lateral Sclerosis. *Amyotrophic Lateral Sclerosis*, 10(1):47–52, 2009.

[294] T. Rohlfing. Image similarity and tissue overlaps as surrogates for image registration accuracy: widely used but unreliable. *IEEE Transactions on Medical Imaging*, 31(2):153–163, 2012.

[295] S.E. Rose, L. Andrew, and J.B. Chalk. Gray and white matter changes in Alzheimer's disease: a diffusion tensor imaging study. *Journal of Magnetic Resonance Imaging*, 27(1):20–26, 2008.

[296] J.D. Rothstein. Current hypotheses for the underlying biology of Amyotrophic Lateral Sclerosis. *Annals of Neurology*, 65(S1):S3–S9, 2009.

[297] M. Rovaris, C. Confavreux, R. Furlan, L. Kappos, G. Comi, and M. Filippi. Secondary progressive multiple sclerosis: current knowledge and future challenges. *Lancet Neurology*, 5(4):343–354, 2006.

[298] S. Roy, A. Carass, P.L. Bazin, and J.L. Prince. Intensity inhomogeneity correction of magnetic resonance images using patches. In *SPIE Medical Imaging*, pages 79621F–79621F, 2011.

[299] E. Rublee, V. Rabaud, K. Konolige, and G. Bradski. Orb: an efficient alternative to sift or surf. In *International Conference on Computer Vision, ICCV*, pages 2564–2571, 2011.

[300] G.A. Ruz, P.A. Estévez, and P.A. Ramirez. Automated visual inspection system for wood defect classification using computational intelligence techniques. *International Journal of Systems Science*, 40(2):163–172, 2009.

[301] M. Sach, G. Winkler, V. Glauche, J. Liepert, B. Heimbach, M.A. Koch, C. Büchel, and C. Weiller. Diffusion tensor MRI of early upper motor neuron involvement in Amyotrophic Lateral Sclerosis. *Brain*, 127(2):340–350, 2004.

[302] J. Saeedi, R. Safabakhsh, and S. Mozaffari. Document image segmentation using fuzzy classifier and the dual-tree DWT. In *International Computer Conference*, pages 385–391, 2009.

[303] C.A. Sage, W. Van Hecke, R. Peeters, J. Sijbers, W. Robberecht, P. Parizel, G. Marchal, A. Leemans, and S. Sunaert. Quantitative diffusion tensor imaging in Amyotrophic Lateral Sclerosis: revisited. *Human Brain Mapping*, 30(11):3657–3675, 2009.

[304] C.A. Sage, R.R. Peeters, A. Görner, W. Robberecht, and S. Sunaert. Quantitative diffusion tensor imaging in Amyotrophic Lateral Sclerosis. *NeuroImage*, 34(2):486–499, 2007.

[305] P. Salembier, A. Oliveras, and L Garrido. Antiextensive connected operators for image and sequence processing. *IEEE Transactions on Image Processing*, 7(4):555 –570, apr 1998.

[306] P. Salembier and J. Serra. Flat zones filtering, connected operators, and filters by reconstruction. *IEEE Transactions on Image Processing*, 4(8):1153–1160, 1995.

[307] T. Sankar, N. Bernasconi, H. Kim, and A. Bernasconi. Temporal lobe epilepsy: Differential pattern of damage in temporopolar cortex and white matter. *Human Brain Mapping*, 29(8):931–944, 2008.

[308] P. Sarchielli, G.P. Pelliccioli, R. Tarducci, P. Chiarini, O. Presciutti, G. Gobbi, and V. Gallai. Magnetic resonance imaging and 1 h-magnetic resonance spectroscopy in Amyotrophic Lateral Sclerosis. *Neuroradiology*, 43(3):189–197, 2001.

[309] N. Sarkar and B.B. Chaudhuri. An efficient differential box-counting approach to compute fractal dimension of image. *IEEE Transactions on Systems, Man and Cybernetics*, 24(1):115–120, 1994.

[310] J.I. Satoh, H. Tokumoto, K. Kurohara, M. Yukitake, M. Matsui, Y. Kuroda, T. Yamamoto, H. Furuya, N. Shinnoh, T. Kobayashi, Y. Kukita, and K. Hayashi. Adult-onset Krabbe disease with homozygous T1853C mutation in the galactocerebrosidase gene. *Neurology*, 49(5):1392–1399, 1997.

[311] S.J. Savio, L.C.V. Harrison, T. Luukkaala, T. Heinonen, P. Dastidar, S. Soimakallio, and H.J. Eskola. Effect of slice thickness on brain magnetic resonance image texture analysis. *Biomedical Engineering Online*, 9(1):60, 2010.

[312] A. Sayeed, M. Petrou, N. Spyrou, A. Kadyrov, and T. Spinks. Diagnostic features of Alzheimer's disease extracted from pet sinograms. *Physics in Medicine and Biology*, 47(1):137, 2001.

[313] L.R. Schad, S. Blüml, and I. Zuna. MR tissue characterization of intracranial tumors by means of texture analysis. *Magnetic Resonance Imaging*, 11(6):889–896, 1993.

[314] M.A. Schoenfeld, C. Tempelmann, C. Gaul, G.R. Kühnel, E. Düzel, J.M. Hopf, H. Feistner, S. Zierz, H.J. Heinze, and S. Vielhaber. Functional motor compensation in Amyotrophic Lateral Sclerosis. *Journal of Neurology*, 252(8):944–952, 2005.

[315] J. Senda, S. Kato, T. Kaga, M. Ito, N. Atsuta, T. Nakamura, H. Watanabe, F. Tanaka, S. Naganawa, and G. Sobue. Progressive and widespread brain damage in ALS: MRI voxel-based morphometry and diffusion tensor imaging study. *Amyotrophic Lateral Sclerosis*, 12(1):59–69, 2011.

[316] Z. Shahvaran, K. Kazemi, M.S. Helfroush, N. Jafarian, and N. Noorizadeh. Variational level set combined with markov random field modeling for simultaneous intensity non-uniformity correction and segmentation of MR images. *Journal of Neuroscience Methods*, 2012.

[317] A. Shiino, T. Watanabe, K. Maeda, E. Kotani, I. Akiguchi, and M. Matsuda. Four subgroups of Alzheimer's disease based on patterns of atrophy using VBM and a unique pattern for early onset disease. *NeuroImage*, 33(1):17–26, 2006.

[318] J. Shin, S.Y. Lee, S.J. Kim, S.H. Kim, S.J. Cho, and Y.B. Kim. Voxel-based analysis of Alzheimer's disease pet imaging using a triplet of radiotracers: Pib, fddnp, and fdg. *NeuroImage*, 52(2):488–496, 2010.

[319] P. Shivakumara, T.Q. Phan, and C.L. Tan. New fourier-statistical features in rgb space for video text detection. *IEEE Transactions on Circuits and Systems for Video Technology*, 20(11):1520–1532, 2010.

[320] D.G. Sim, H.K. Kim, and R.H. Park. Invariant texture retrieval using modified zernike moments. *Image and Vision Computing*, 22(4):331–342, 4/1 2004.

[321] J.K. Sing, K. Khan, D.K. Basu, M. Nasipuri, and P.K. Saha. Polynomial surface fitting based method for retrospective correction of intensity inhomogeneity in MR images. In *International Conference on Communications and Signal Processin*, pages 405–409, 2011.

[322] C.B. Singh, R. Choudhary, D.S. Jayas, and J. Paliwal. Wavelet analysis of signals in agriculture and food quality inspection. *Food and Bioprocess Technology*, 3(1):2–12, 2010.

[323] J.G. Sled, A.P. Zijdenbos, and A.C. Evans. A nonparametric method for automatic correction of intensity nonuniformity in MRI data. *IEEE Transactions on Medical Imaging*, 17(1):87–97, 1998.

[324] J. Śmietański and R. Tadeusiewicz. Discriminatory power of co-occurrence features in perfusion CT prostate images. *Machine Graphics & Vision International Journal*, 19(2):185–199, 2010.

[325] S. Song, Z. Zhan, Z. Long, J. Zhang, and L. Yao. Comparative study of svm methods combined with voxel selection for object category classification on fMRI data. *PLOS ONE*, 6(2):e17191, 2011.

[326] B.R. Stanton, V.C. Williams, P.N. Leigh, S.C.R. Williams, Blain, J.M. Jarosz, and A. Simmons. Altered cortical activation during a motor task in ALS. *Journal of Neurology*, 254(9):1260–1267, 2007.

[327] R.G. Stockwell, L. Mansinha, and R.P. Lowe. Localization of the complex spectrum: The s transform. *IEEE Transactions on Signal Processing*, 44(4):998–1001, 1996.

[328] M. Styner, C. Brechbuhler, G. Szckely, and G. Gerig. Parametric estimate of intensity inhomogeneities applied to MRI. *IEEE Transactions on Medical Imaging*, 19(3):153–165, 2000.

[329] N. Sudharshan, C. Hanstock, B. Hui, T. Pyra, W. Johnston, and S. Kalra. Degeneration of the mid-cingulate cortex in Amyotrophic Lateral Sclerosis detected in vivo with MR spectroscopy. *American Journal of Neuroradiology*, 32(2):403–407, 2011.

[330] J. Suhy, R.G. Miller, R. Rule, N. Schuff, J. Licht, V. Dronsky, D. Gelinas, A.A. Maudsley, and M.W. Weiner. Early detection and longitudinal changes in Amyotrophic Lateral Sclerosis by 1H MRSI. *Neurology*, 58(5):773–779, 2002.

[331] P.M. Szczypiński, M. Strzelecki, A. Materka, and A. Klepaczko. Mazdaa software package for image texture analysis. *Computer Methods and Programs in Biomedicine*, 94(1):66–76, 2009.

[332] G. Takacs, V. Chandrasekhar, S.S. Tsai, D. Chen, R. Grzeszczuk, and B. Girod. Fast computation of rotation-invariant image features by an approximate radial gradient transform. *IEEE Transactions on Image Processing*, 22(8):2970–2982, 2013.

[333] V. Takala, T. Ahonen, and M. Pietikäinen. Block-based methods for image retrieval using local binary patterns. In *Image Analysis*, pages 882–891. Springer, 2005.

[334] J. Talairach and P. Tournoux. Co-planar stereotaxic atlas of the human brain. 3-dimensional proportional system: an approach to cerebral imaging. 1988.

[335] X. Tang. Texture information in run-length matrices. *IEEE Transactions on Image Processing*, 7(11):1602–1609, 1998.

[336] C. Tempelmann, C. Gaul, G.R. Kühnel, E. Düzel, J.M. Hopf, H. Feistner, S. Zierz, H.J. Heinze, and S. Vielhaber. Functional motor compensation in Amyotrophic Lateral Sclerosis. *Journal of Neurology*, 252(8):944–952, 2005.

[337] C. Teriitehau, C. Adamsbaum, V. Merzoug, G. Kalifa, A. Tourbah, and P. Aubourg. Subtle brain abnormalities in adrenomyeloneuropathy. *Journal de Radiologie*, 88(7-8):957–961, 2007.

[338] P. Theocharakis, D. Glotsos, I. Kalatzis, S. Kostopoulos, P. Georgiadis, K. Sifaki, K. Tsakouridou, M. Malamas, G. Delibasis, D. Cavouras, and G. Nikiforidisa. Pattern recognition system for the discrimination of multiple sclerosis from cerebral microangiopathy lesions based on texture analysis of magnetic resonance images. *Magnetic Resonance Imaging*, 27(3):417–422, 2009.

[339] L. Thivard, P.F. Pradat, S. Lehéricy, L. Lacomblez, D. Dormont, J. Chiras, H. Benali, and V. Meininger. Diffusion tensor imaging and voxel based morphometry study in Amyotrophic Lateral Sclerosis: relationships with motor disability. *Journal of Neurology, Neurosurgery & Psychiatry*, 78(8):889–892, 2007.

[340] P.A. Thomann, T. Wüstenberg, J. Pantel, M. Essig, and J. Schröder. Structural changes of the corpus callosum in mild cognitive impairment and Alzheimers disease. *Dementia and geriatric cognitive disorders*, 21(4):215–220, 2006.

[341] E. Tola, V. Lepetit, and P Fua. Daisy: An efficient dense descriptor applied to wide-baseline stereo. *IEEE Transactions on Pattern Analysis and Machine Intelligence*, 32(5):815–830, 2010.

[342] D.J. Tozer, G. Marongiu, J.K. Swanton, A.J. Thompson, and D.H. Miller. Texture analysis of magnetization transfer maps from patients with clinically isolated syndrome and multiple sclerosis. *Journal of Magnetic Resonance Imaging*, 30(3):506–513, 2009.

[343] T. Trzcinski, M. Christoudias, P. Fua, and V. Lepetit. Boosting binary keypoint descriptors. In *IEEE Conference on Computer Vision and Pattern Recognition , CVPR*, pages 2874–2881, 2013.

[344] D.M. Tsai and J.Y. Luo. Mean shift-based defect detection in multicrystalline solar wafer surfaces. *IEEE Transactions on Industrial Informatics*, 7(1):125–135, 2011.

[345] M. K. Tsatsanis and G. B. Giannakis. Object and texture classification using higher order statistics. *IEEE Transactions on Pattern Analysis and Machine Intelligence*, 14(7):733–750, 1992.

[346] S. Tsermentseli, F. Dell'Acqua, S. Landau, S.C.R. Williams, D.K. Jones, P.N. Leigh, M. Catani, and L.H. Goldstein. P20 frontal white matter connections and cognitive change in Amyotrophic Lateral Sclerosis: a DTI-tractography study. *Journal of Neurology, Neurosurgery & Psychiatry*, 83(10):e1, 2012.

[347] M. Tsujimoto, J. Senda, T. Ishihara, Y. Niimi, Y. Kawai, N. Atsuta, H. Watanabe, F. Tanaka, S. Naganawa, and G. Sobue. Behavioral changes in early ALS correlate with voxel-based morphometry and diffusion tensor imaging. *Journal of the Neurological Sciences*, 307(1–2):34 – 40, 2011.

[348] M.R. Turner, J. Grosskreutz, J. Kassubek, S. Abrahams, F. Agosta, M. Benatar, M. Filippi, L.H. Goldstein, M. van den Heuvel, S. Kalra, D. Lulé, and B. Mohammadi. Towards a neuroimaging biomarker forAmyotrophic Lateral Sclerosis. *Lancet Neurology*, 10(5):400, 2011.

[349] M.R. Turner, M.J. Parton, C.E. Shaw, P.N. Leigh, and A. Al-Chalabi. Prolonged survival in motor neuron disease: a descriptive study of the king's database 1990–2002. *Journal of Neurology, Neurosurgery & Psychiatry*, 74(7):995–997, 2003.

[350] T. Tuytelaars and K Mikolajczyk. Local invariant feature detectors: a survey. *Foundations and Trends in Computer Graphics and Vision*, 3(3):177–280, 2008.

[351] S. Upadhyay, S. Jain, M. Papadakis, and R. Azencott. 3D-rigid motion invariant discrimination and classification of 3D-textures. In *Society of Photo-Optical Instrumentation Engineers (SPIE) Conference Series*, volume 8138, page 77, 2011.

[352] E.R. Urbach, J.B.T.M. Roerdink, and M.H.F. Wilkinson. Connected shape-size pattern spectra for rotation and scale-invariant classification of gray-scale images. *IEEE Transactions on Pattern Analysis and Machine Intelligence*, 29(2):272–285, 2007.

[353] U. Usman, C. Choi, R. Camicioli, P. Seres, M. Lynch, R. Sekhon, W. Johnston, and S. Kalra. Mesial prefrontal cortex degeneration in Amyotrophic Lateral Sclerosis: A high-field proton MR spectroscopy study. *American Journal of Neuroradiology*, 32(9):1677–1680, 2011.

[354] T. Van Langenhove, J. van der Zee, and C. Van Broeckhoven. The molecular basis of the frontotemporal lobar degeneration-amyotrophic lateral sclerosis spectrum. *Annals of Medicine*, 44(8):817–828, 2012.

[355] C. Vance, B. Rogelj, T. Hortobágyi, Kurt J. De Vos, A.L. Nishimura, J. Sreedharan, X. Hu, B. Smith, D. Ruddy, P. Wright, J. Ganesalingam, K.L. Williams, V. Tripathi, S. Al-Saraj, A. Al-Chalabi, P.N. Leigh, I.P. Blair, G. Nicholson, J. de Belleroche, J.M. Gallo, C.C. Miller, and C.E. Shaw. Mutations in FUS, an RNA processing protein, cause familial Amyotrophic Lateral Sclerosis type 6. *Science*, 323(5918):1208–1211, 2009.

[356] M. Varma and A. Zisserman. A statistical approach to texture classification from single images. *International Journal of Computer Vision*, 62(1):61–81, 2005.

[357] M. Varma and A. Zisserman. A statistical approach to material classification using image patch exemplars. *IEEE Transactions on Pattern Analysis and Machine Intelligence*, 31(11):2032–2047, 2009.

[358] E. Verstraete, M.P. van den Heuvel, J.H. Veldink, N. Blanken, R.C. Mandl, H.E.H. Pol, and L.H. van den Berg. Motor network degeneration in Amyotrophic Lateral Sclerosis: a structural and functional connectivity study. *PLOS ONE*, 5(10):e13664, 2010.

[359] E. Verstraete, J.H. Veldink, J. Hendrikse, H.J. Schelhaas, M.P. van den Heuvel, and L.H. van den Berg. Structural MRI reveals cortical thinning in Amyotrophic Lateral Sclerosis. *Journal of Neurology, Neurosurgery & Psychiatry*, 83(4):383–388, 2012.

[360] E.A. Vokurka, N.A. Thacker, and A. Jackson. A fast model independent method for automatic correction of intensity nonuniformity in MRI data. *Journal of Magnetic Resonance Imaging*, 10(4):550–562, 1999.

[361] S.B. Vos, D.K. Jones, M.A. Viergever, and A. Leemans. Partial volume effect as a hidden covariate in DTI analyses. *NeuroImage*, 55(4):1566–1576, 2011.

[362] L. Wang and G. Healey. Using zernike moments for the illumination and geometry invariant classification of multispectral texture. *IEEE Transactions on Image Processing*, 7(2):196–203, 1998.

[363] S. Wang, H. Poptani, J.H. Woo, L.M. Desiderio, L.B. Elman, L.F. McCluskey, J. Krejza, and E.R. Melhem. Amyotrophic lateral sclerosis: Diffusion-Tensor and chemical shift MR imaging at 3.0 t1. *Radiology*, 239(3):831–838, 2006.

[364] X. Wang, H. Yang, L. Tong, and W. Liu. MR image texture analysis of the corpus callosum in different gender patients with Alzheimer's disease. In *Third International Conference on Intelligent Control and Information Processing*, pages 290–292, 2012.

[365] Z. Wang, B. Fan, and F. Wu. Local intensity order pattern for feature description. In *International Conference on Computer Vision, ICCV*, pages 603–610, 2011.

[366] M. Waragai. MRI and clinical features in Amyotrophic Lateral Sclerosis. *Neuroradiology*, 39(12):847–851, 1997.

[367] J.L. Whitwell, S.A. Przybelski, S.D. Weigand, D.S. Knopman, B.F. Boeve, R.C. Petersen, and C.R. Jack. 3D maps from multiple MRI illustrate changing atrophy patterns as subjects progress from mild cognitive impairment to Alzheimer's disease. *Brain*, 130(7):1777–1786, 2007.

[368] J.L. Whitwell, S.D. Weigand, M.M. Shiung, B.F. Boeve, T.J. Ferman, G.E. Smith, D.S. Knopman, R.C. Petersen, E.E. Benarroch, K.A. Josephs, and R.J. Clifford. Focal atrophy in dementia with lewy bodies on MRI: a distinct pattern from Alzheimer's disease. *Brain*, 130(3):708–719, 2007.

[369] S. Winder, G. Hua, and M. Brown. Picking the best daisy. In *IEEE Conference on Computer Vision and Pattern Recognition , CVPR*, pages 178–185, 2009.

[370] B. Wohlberg and G. De Jager. A review of the fractal image coding literature. *IEEE Transactions on Image Processing*, 8(12):1716–1729, 1999.

[371] S.C. Woolley and J.S. Katz. Cognitive and behavioral impairment in Amyotrophic Lateral Sclerosis. *Physical Medicine and Rehabilitation Clinics of North America*, 19(3):607–617, 2008.

[372] G.S. Xia, J. Delon, and Y. Gousseau. Shape-based invariant texture indexing. *International Journal of Computer Vision*, 88(3):382–403, 2010.

[373] H. Xia, L. Tong, X. Zhou, J. Zhang, Z. Zhou, and W. Liu. Texture analysis and volumetry of hippocampus and medial temporal lobe in patients with Alzheimer's disease. In *International Conference on Biomedical Engineering and Biotechnology (iCBEB)*, pages 905–908, may 2012.

[374] Y. Xia, D. Feng, and R. Zhao. Morphology-based multifractal estimation for texture segmentation. *IEEE Transactions on Image Processing*, 15(3):614–623, 2006.

[375] X. Xie. A review of recent advances in surface defect detection using texture analysis techniques. *Electronic Letters on Computer Vision and Image Analysis*, 7(3):1–22, 2008.

[376] D.H. Xu, A. Kurani, J.D. Furst, and D.S. Raicu. Run-length encoding for volumetric texture. In *The 4th IASTED International Conference on Visualization, Imaging, and Image Processing*, pages 6–8, 2004.

[377] P. Xu, H. Yao, R. J, X. Sun, and X. Liu. A robust texture descriptor using multifractal analysis with gabor filter. In *Proceedings of the Second International Conference on Internet Multimedia Computing and Service*, pages 147–150, 2010.

[378] Q. Xu, J. Zheng, Y.C. Cheng, and Q.Y. Ji. Application of texture analysis to identification of oil spills in SAR images. *Journal of Hohai University: Natural Sciences*, 39(5):569–574, 2011.

[379] Y. Xu, H. Ji, and C. Fermüller. A projective invariant for textures. In *IEEE Conference on Computer Vision and Pattern Recognition, CVPR*, volume 2, pages 1932–1939, 2006.

[380] Y. Xu, H. Ji, and C. Fermüller. Viewpoint invariant texture description using fractal analysis. *International Journal of Computer Vision*, 83(1):85–100, 2009.

[381] Y. Xu, Y. Quan, H. Ling, and H. Ji. Dynamic texture classification using dynamic fractal analysis. In *IEEE International Conference on Computer Vision, ICCV*, pages 1219–1226, 2011.

[382] Y. Xu, X. Yang, H. Ling, and H. Ji. A new texture descriptor using multifractal analysis in multi-orientation wavelet pyramid. In *IEEE Conference on Computer Vision and Pattern Recognition, CVPR*, pages 161–168, 2010.

[383] Y. Xu and X. Zhang. Gabor filterbank and its application in the fingerprint texture analysis. In *Sixth International Conference on Parallel and Distributed Computing, Applications and Technologies*, pages 829–831, 2005.

[384] X. Xuan and Q. Liao. Statistical structure analysis in MRI brain tumor segmentation. In *Fourth International Conference on Image and Graphics*, pages 421–426, 2007.

[385] T. Das L. Bai K. Robson D. Auer Y. Liu, M. Muftah. Classification of MR tumor images based on gabor wavelet analysis. *Journal of Medical and Biological Engineering*, 32:22–28, 2012.

[386] X. Yan, M.X. Zhou, L. Xu, W. Liu, and G. Yang. Noise removal of MRI data with edge enhancing. In *Fifth International Conference on Bioinformatics and Biomedical Engineering*, pages 1–4, 2011.

[387] X.F. Yang, D. Schuster, V. Master, P. Nieh, A. Fenster, and B. Fei. Automatic 3D segmentation of ultrasound images using atlas registration and statistical texture prior. In *Proceedings of SPIE*, volume 7964, page 796432, 2011.

[388] M. Yazdchi, M. Yazdi, and A.G. Mahyari. Steel surface defect detection using texture segmentation based on multifractal dimension. In *International Conference on Digital Image Processing*, pages 346–350, 2009.

[389] Q. Ye, J. Jiao, J. Huang, and H. Yu. Text detection and restoration in natural scene images. *Journal of Visual Communication and Image Representation*, 18(6):504–513, 2007.

[390] L. Yeffet and L Wolf. Local trinary patterns for human action recognition. In *IEEE 12th International Conference on Computer Vision*, pages 492–497. IEEE, 2009.

[391] C. Yi and Y. Tian. Text detection in natural scene images by stroke gabor words. In *International Conference on Document Analysis and Recognition*, pages 177–181, 2011.

[392] S. Yousefi and N. Kehtarnavaz. A new stochastic image model based on markov random fields and its application to texture modeling. In *IEEE International Conference on Acoustics, Speech and Signal Processing 2011 (ICASSP)*, pages 1285–1288, 2011.

[393] O. Yu, Y. Mauss, I.J. Namer, and J. Chambron. Existence of contralateral abnormalities revealed by texture analysis in unilateral intractable hippocampal epilepsy. *Magnetic Resonance Imaging*, 19(10):1305–1310, 2001.

[394] O. Yu, Y. Mauss, G. Zollner, I.J. Namer, and J. Chambron. Distinct patterns of active and non-active plaques using texture analysis on brain nmr images in multiple sclerosis patients: preliminary results. *Magnetic Resonance Imaging*, 17(9):1261–1267, 1999.

[395] S.N. Yu, J.H. Jang, and C.S. Han. Auto inspection system using a mobile robot for detecting concrete cracks in a tunnel. *Automation in Construction*, 16(3):255–261, 2007.

[396] E.I. Zacharaki, S. Wang, S. Chawla, D. Soo Yoo, R. Wolf, E.R. Melhem, and C. Davatzikos. Classification of brain tumor type and grade using MRI texture and shape in a machine learning scheme. *Magnetic Resonance in Medicine*, 62(6):1609–1618, 2009.

[397] C. Zhang, S.E. Franklin, and M.A. Wulder. Geostatistical and texture analysis of airborne-acquired images used in forest classification. *International Journal of Remote Sensing*, 25(4):859–865, 2004.

[398] J. Zhang, J. Liang, and H. Zhao. Local energy pattern for texture classification using self-adaptive quantization thresholds. *IEEE Transactions on Image Processing*, 22(1):31–42, 2012.

[399] J. Zhang and T. Tan. Affine invariant texture analysis based on structural properties. In *Asian Conference on Computer Vision, ACCV*, pages 216–221, 2002.

[400] J. Zhang and T. Tan. Brief review of invariant texture analysis methods. *Pattern Recognition*, 35(3):735–747, 2002.

[401] J. Zhang, L. Tong, L. Wang, and N. Li. Texture analysis of multiple sclerosis: a comparative study. *Magnetic Resonance Imaging*, 26(8):1160–1166, 2008.

[402] J. Zhang, L. Wang, and L Tong. Feature reduction and texture classification in MRI-Texture analysis of multiple sclerosis. In *IEEE/ICME International Conference on Complex Medical Engineering*, pages 752–757, 2007.

[403] J. Zhang, C. Yu, G. Jiang, W. Liu, and L. Tong. 3D texture analysis on MRI images of Alzheimer's disease. *Brain imaging and behavior*, pages 1–9, 2011.

[404] S. Zhang, H. Yao, and S. Liu. Dynamic background modeling and subtraction using spatio-temporal local binary patterns. In *IEEE International Conference on Image Processing*, pages 1556–1559, 2008.

[405] Y. Zhang, N. Schuff, S.C. Woolley, G.C. Chiang, L. Boreta, J. Laxamana, J.S. Katz, and M.W. Weiner. Progression of white matter degeneration in Amyotrophic Lateral Sclerosis: a diffusion tensor imaging study. *Amyotrophic Lateral Sclerosis*, 12(6):421–429, 2011.

[406] Y. Zhang, A. Traboulsee, Y. Zhao, L.M. Metz, and D.K. Li. Texture analysis differentiates persistent and transient T1 black holes at acute onset in multiple sclerosis: A preliminary study. *Multiple Sclerosis Journal*, 17(5):532–540, 2011.

[407] Y. Zhang, H. Zhu, J.R. Mitchell, F. Costello, and L.M. Metz. T2 MRI texture analysis is a sensitive measure of tissue injury and recovery resulting from acute inflammatory lesions in multiple sclerosis. *NeuroImage*, 47(1):107, 2009.

[408] G. Zhao and M. Pietikainen. Dynamic texture recognition using local binary patterns with an application to facial expressions. *IEEE Transactions on Pattern Analysis and Machine Intelligence*, 29(6):915–928, 2007.

[409] M. Zhao, S. Li, and J. Kwok. Text detection in images using sparse representation with discriminative dictionaries. *Image and Vision Computing*, 28(12):1590–1599, 2010.

[410] Y. Zheng, C. Shen, R. Hartley, and X. Huang. Pyramid center-symmetric local binary/trinary patterns for effective pedestrian detection. In *Asian conference on Computer vision, ACCV*, volume 6495, pages 281–292, 2011.

[411] J. Zhou and L. Ma. Research on on-line grading system for pearl defect based on machine vision. In *Photonics Asia 2007*, page 68332E, 2007.

[412] L.Q. Zhou, Y.M. Zhu, C. Bergot, A.M. Laval-Jeantet, V. Bousson, J.D. Laredo, and M. Laval-Jeantet. A method of radio-frequency inhomogeneity correction for brain tissue segmentation in MRI. *Computerized Medical Imaging and Graphics*, 25(5):379–389, 2001.

[413] A.P. Zijdenbos, B.M. Dawant, and R.A. Margolin. Inter-and intra-slice intensity correction in MR images. In *Information Processing in Medical Imaging*, volume 14, pages 349–350.

[414] J.M. Zook and K.M. Iftekharuddin. Statistical analysis of fractal-based brain tumor detection algorithms. *Magnetic Resonance Imaging*, 23(5):671–678, 2005.

[415] J.H. Yong Z.Z. Wang. Texture analysis and classification with linear regression model based on wavelet transform. *IEEE Transactions on Image Processing*, 17(8):1421 –1430, 2008.

Appendix A

Statistical MAp fRom Texture (SMART) Toolbox

A.1   Introduction

In this appendix, the toolbox developed for 3D voxel based texture analysis is described. This toolbox is provided for SPM8[1] software using the Matlab[2] programming language and is called Statistical MAp fRom Texture (SMART).

To the best knowledge of the author, there are few publically available texture analysis toolboxes for brain image analysis. The most well-known software product is MAZDA [331]. MAZDA provides only ROI analysis. Also, it is not incorporated into commonly used brain analysis tools such as SPM or FSL and therefore is not easy to use for brain analysis. The SMART toolbox addresses these issues and not only provides the voxel-based and ROI analyses but also is incorporated into the SPM software which makes the texture analysis of the brain easy for research studies.

As described in Section 5.2 the processing pipeline includes, pre-processing, texture feature computation, and voxel-based statistical analysis. Several brain analysis tools including SPM8 and FSL[3] provide the first and last parts in the processing pipeline. In this section the description of performing these steps using SPM8 is given.

A.2   Preprocessing

The preprocessing step includes intensity bias correction and brain spatial normalization (i.e., registering to atlas). The VBM8 toolbox (http://dbm.neuro.uni-jena.de/vbm/) is used to perform preprocessing. It is an extension of the unified segmentation model [22] using the high-dimensional DARTEL procedure [20] to normalize images to the MNI152 atlas.

The *Estimate and Write* module in VBM8 toolbox provides functionality to correct the intensity bias and to normalize (register) T1 weighted images to the MNI152 atlas. The default parameters

---

[1] http://www.fil.ion.ucl.ac.uk/spm/
[2] http://www.mathworks.com
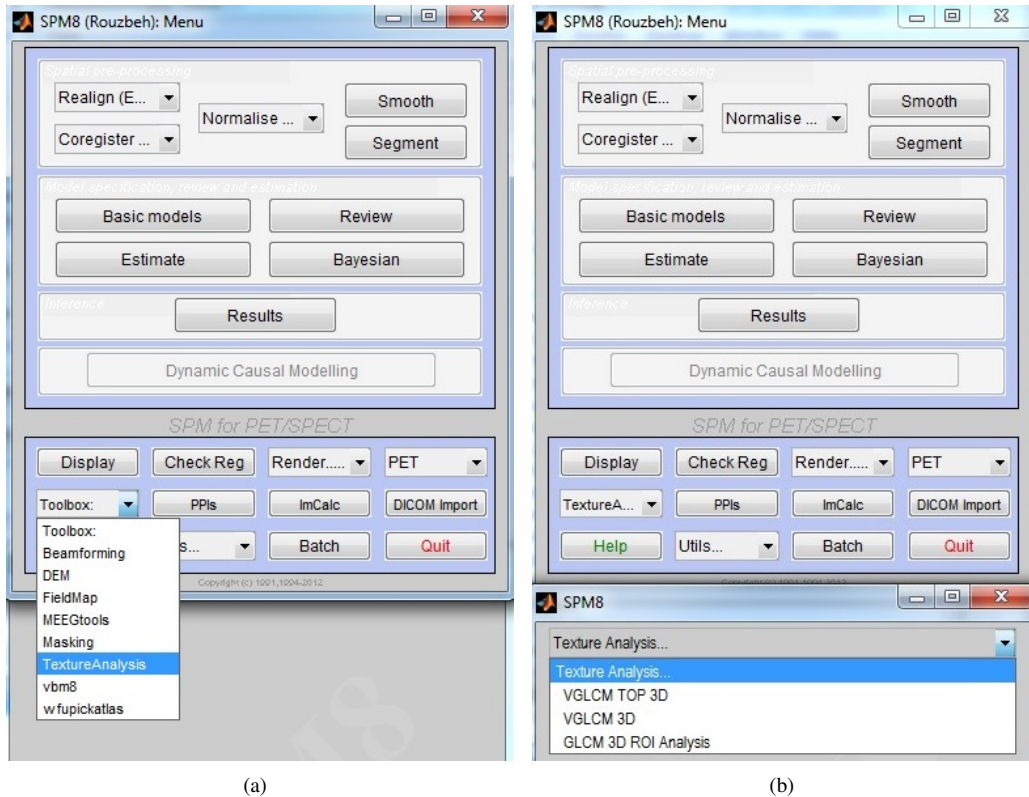[3] http://www.fmrib.ox.ac.uk/fsl/

Figure A.1: The SMART toolbox, a) selecting the toolbox from SPM, and b) the three types of texture analysis available in the toolbox.

are usually good for preprocessing step. The explanation of the parameters can be found in [197]. The outputs of this step are identified by the prefix *wmr*, which stands for warped (w), bias corrected (m), and realigned (r).

A.3   Texture Analysis

In order to install the SMART toolbox the provided zip file should be uncompressed and copied into the toolbox folder in the SPM8. After installation, the texture analysis toolbox appears in the SPM toolbox section (Figure A.1(a)). Three types of texture analysis are available in the toolbox: VGLCM-TOP-3D, VGLCM-3D, and GLCM 3D ROI analysis (Figure A.1(b)).

The first two methods are the voxel based texture analysis methods explained in Sections 5.2.2 and 5.2.3. Once the user selects the VGLCM-TOP-3D or VGLCM-3D analysis, a form similar to the form shown in Figure A.2 is displayed. In this form the values of the parameters of the method can be adjusted. The parameters include:

1. **Volumes**: In this part the user should choose the location of the input images. These images are the outputs of the preprocessing step (identified by the prefix *wmr*).
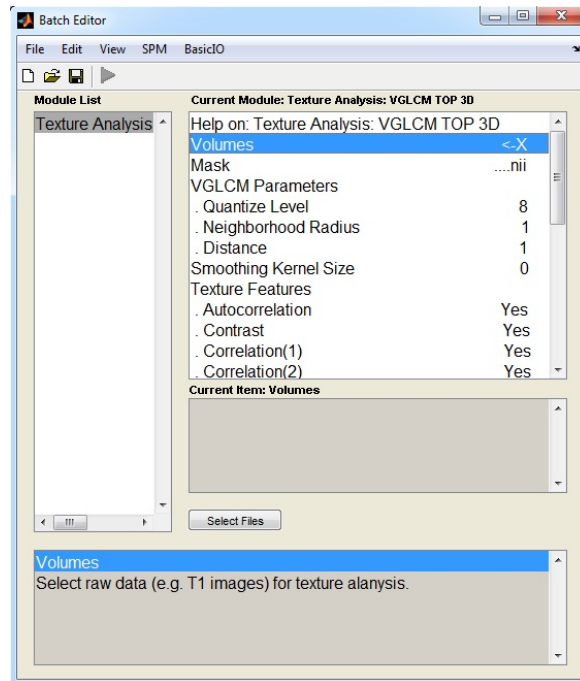
171

Figure A.2: The parameters shown for the VGLCM-TOP-3D and VGLCM-3D methods.

2. **Mask**: The user should specify the location of the mask. The mask should be inclusive (i.e., the voxels that are marked by 1 are processed and those marked by 0 are ignored) and should have the same size as the input images. The mask could be provided for analysis of the whole brain or just a part of the brain (e.g., thalamus, white matter, etc.).

3. **VGLCM Parameters**: The parameters include the quantization level, the radius of neighborhood, and the distance explained in Sections 5.2.2 and 5.2.3.

4. **Smoothing Kernel Size**: The output images could undergo the Gaussian smoothing if the data is quite noisy. If the user chooses the kernel size of zero no smoothing is applied.

5. **Texture Features**: The texture features to be computed are selected in this section.

The outputs of the VGLCM-TOP-3D and VGLCM-3D methods are saved with the postfix of *TextureFuture_D_N_Q_S* denoting the name of the texture features and the values of the parameters (distance, neighborhood radius, quantization level, and smoothing kernel size). The runtime for computing all texture features for an MR image with size of $94 \times 188 \times 100$ voxels using 8 quantization levels, neighborhood radius of 1, and distance of 1 is about 27 minutes for VGLCM-TOP-3D and 166 minutes for VGLCM-3D on a PC with an Intel quad core 2.60 GHz CPU with 16GB RAM running Windows 7 Professional.

The third analysis option in Figure A.1(b) provides the conventional ROI analysis which computes a texture feature for a given region of interest. There are two approaches to using ROI analysis. In the first approach images are not registered into an atlas. For this approach the user should provide
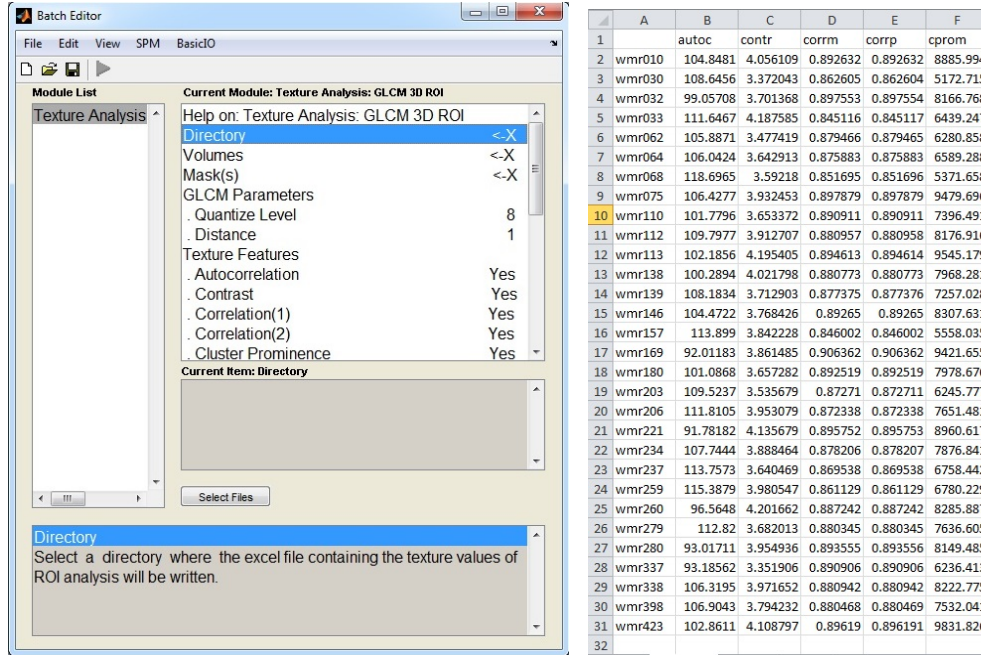
Figure A.3: ROI Analysis. a) Parameters form. b) Sample results in an excel file.

a mask for each image separately to specify the region of interest on that image. In the second approach all the images are registered into an atlas. Hence, the users need to provide only one mask to mark the region of interest. Figure A.3(a) shows the form to define the parameters for ROI analysis. The parameters include:

1. **Directory**: The output directory is specified in this part. The output is an *excel* file with the name format of *ROI_D ROI_Q* denoting the distance and the quantization level used for ROI analysis. In this excel file the value of the texture features are reported (Figure A.3(b)).

2. **Volumes**: The 3D MRI images are selected in this part.

3. **Mask(s)**: The mask(s) should be inclusive (i.e., the voxels that are marked by 1 are processed and those marked by 0 are ignored) and should have the same size as the input images. If the images are registered to an atlas, one mask is enough; otherwise, a separate mask should be provided for each image. In this case the order of the mask files should be the same as the order of the image volumes listed above in the item 2.

4. **GLCM Parameters**: The parameters include the quantization level and the distance explained in Section 5.2.2.

5. **Texture Features**: The texture features to be computed are selected in this part.

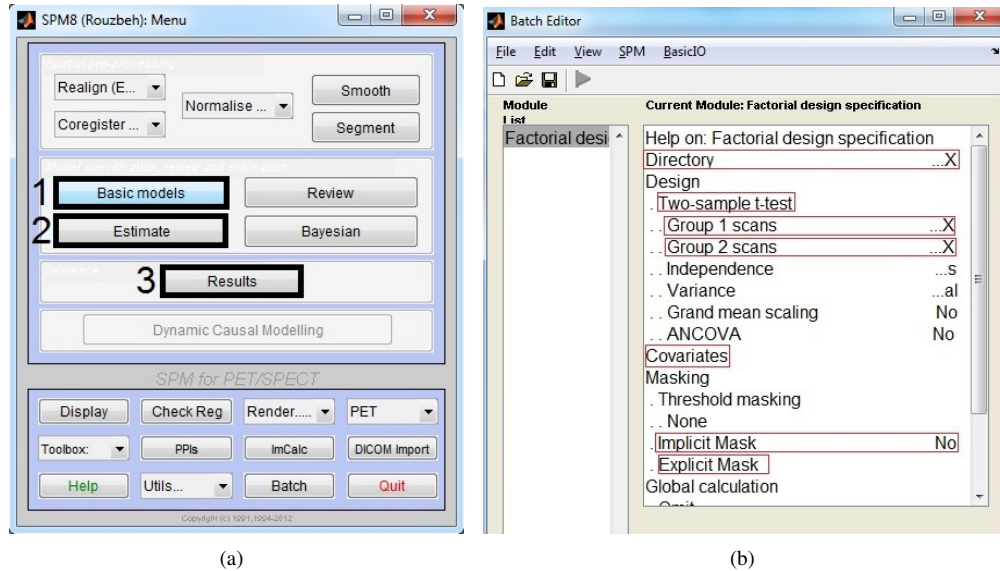Figure A.4: a) Performing voxel based statistical analysis includes 3 steps: 1) constructing the model (Basic Models), 2) estimation of the model (Estimate), and 3) displaying the results (Results). b) Defining the statistical model (*Basic models* module).

A.4 Statistical Analysis

The first two types of texture analyses, VGLCM-TOP-3D and VGLCM-3D, need a further step. In this last step the texture features undergo voxel by voxel statistical analysis. Here, it is explained how to perform the voxel based two-sample t-test analysis in SPM8 to distinguish differences between a group of patients and healthy subjects. Performing voxel based statistical analysis includes 3 steps: constructing the model, estimation of the model, and displaying the results (Figure A.4(a)).

First, it is required to specify the statistical model. In the main menu of SPM8 the *Basic models* module is chosen. In the model specification, these parameters are determined:

1. **Directory**: The output directory is specified as to where the analysis results are stored.

2. **Design**: *Two-sample t-test* is chosen. Then, the texture features computed by VGLCM-TOP-3D or VGLCM-3D methods are selected. All the texture images that belong to patients are put in one group (e.g., Group 1 scans) and all the texture images that belong to healthy subjects are put in the other group (e.g., Group 2 scans).

3. **Covariates**: If the user wants to count the covariates (e.g., age and gender), they should be specified in this part.

4. **Masking**: The *Implicit Mask* should be set to **No** and the same mask used for texture computation (item 2 in VGLCM-TOP-3D and VGLCM-3D parameters form) should be selected as the *Explicit Mask*.
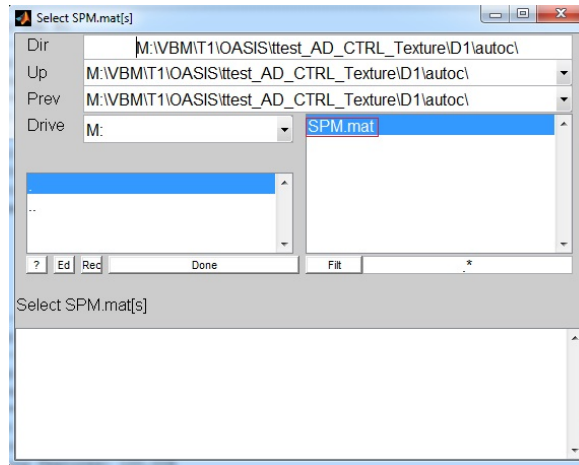
174

Figure A.5: To estimate the model the user should select the SPM.mat file in the directory where the statistical model is constructed.

These parameters are shown by red boxes in Figure A.4(b). The default values for the other parameters are used. For more details please see the manual of SPM8. Now, the user may run this module to create the statistical model. Once the model is generated, the *Estimate* module from the SPM8 main menu is selected (Figure A.4(a)). In this module the SPM.mat file in the directory where the statistical model is constructed (Figure A.5) is chosen.

After the estimation of the model, the results can be observed by selecting the *Results* module from the SPM8 main menu (Figure A.4(a)). After selecting *Results*, similar to the previous step it is needed to specify the SPM.mat file in the directory where the statistical model is located. Once the SPM.mat file is selected the contrast is specified. A contrast is used to compare different conditions in the study. Here there are two conditions: patient, and healthy.

There are two contrast types: T-contrast and F-contrast. T-contrast examines only a single constraint on the model. For instance, it can be examined if the texture value of healthy subjects is higher than the texture value of patients. An F-contrast can be thought of an *OR* statement containing several T-contrasts. If any of the T-contrasts is true, then the F-contrast is true.

Since the difference of textures are found and the difference can appear as either higher or lower values in patients compared to healthy subjects, it is required to define the F-contrast as follows:

$$\begin{bmatrix} 0.5 & -0.5 \\ -0.5 & 0.5 \end{bmatrix} \tag{A.1}$$

Each row in the above matrix is a T-contrast. The first row tests that the value of texture is higher in the first group while the second row examines that the value of the texture is lower in the first group. If there are some covariates, then for each covariate a column of zeros should be added to mask the effect of the covariate. For instance, if age and gender are entered as covariates, then the F-contrast is defined as:

$$\begin{bmatrix} 0.5 & -0.5 & 0 & 0 \\ -0.5 & 0.5 & 0 & 0 \end{bmatrix} \tag{A.2}$$

175
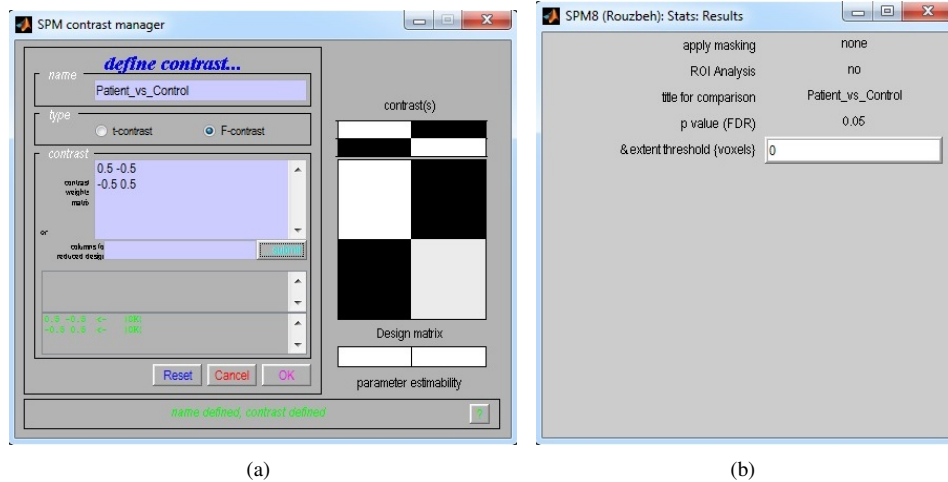
Figure A.6: a) Defining contrast. b) Setting parameters to display

Figure A.6(a) illustrates the form used to define contrast. Once the contrast is defined, the following parameters are specified to display the result (Figure A.6(b)):

1. **Applying Mask**: No.

2. **ROI Analysis**: No.

3. **Title for comparison**: The title of the form displaying the result is entered into this box.

4. **p value**: The method of correction for multiple comparison should be selected (FDR or FWE). Also need to set the p values for level of significance (often 0.05 or 0.01).

5. **Extent threshold**{**voxels**}: The clusters (i.e., adjacent voxels which are statistically different between the two groups) smaller than this value are ignored.

The final display looks like Figure A.7 showing the regions statistically different between the patient and control groups.

A.5 Summary

In this appendix the SMART toolbox has been presented. This toolbox has been developed for SPM8 software and provides three types of texture analysis: VGLCM-TOP-3D, VGLCM-3D and the conventional 3D ROI GLCM. The outputs of the two methods are the statistical maps representing the differences between groups. This toolbox can help doctors to have a new analysis tool to study brain related diseases.
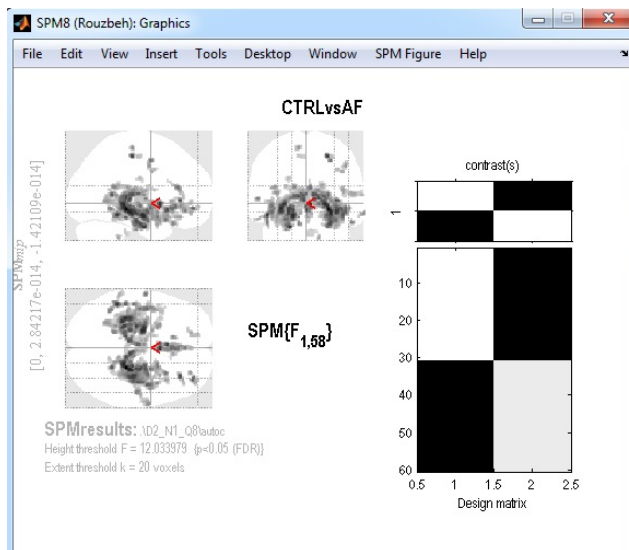
Figure A.7: Displaying the regions statistically different between the patient and control groups.

Appendix B

Gradient Computation with LFDG

In this appendix the $LFDG$ gradient outputs for more images are shown. These images are obtained from the Kodak dataset[1].

(a)

(b)

(c)

(d)

(e)
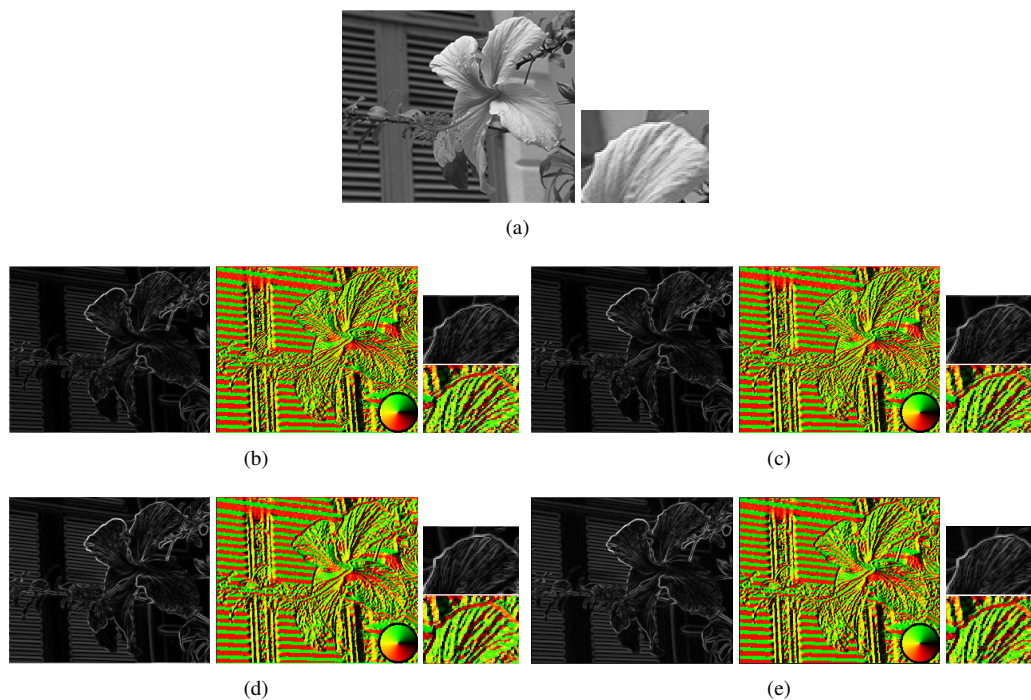
Figure B.1: Edge characterization on a realistic image from the Kodak dataset. a) original image, b) central difference, c) derivative of Gaussian, d) Sobel, e) $LFDG$. The last column is an enlarged version of a part of image. The gradient orientation is smoother in $LFDG$.

---

[1] http://r0k.us/graphics/kodak/kodim08.html
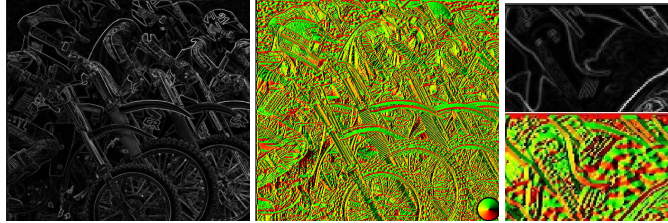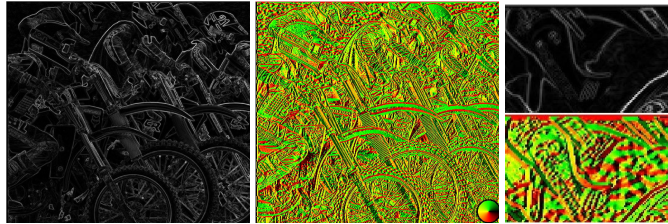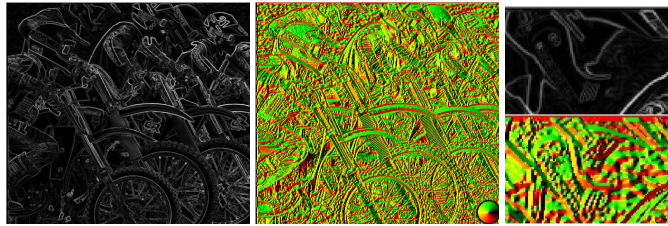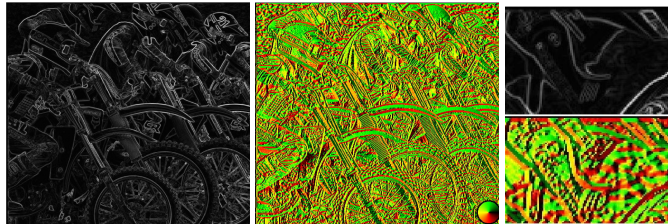
Figure B.2: Edge characterization on a realistic image from the Kodak dataset. a) original image, b) central difference, c) derivative of Gaussian, d) Sobel, e) $LFDG$. The last column is an enlarged version of a part of image. The writing on the helmet has faint edges that are more evident in the magnitude of $LFDG$.
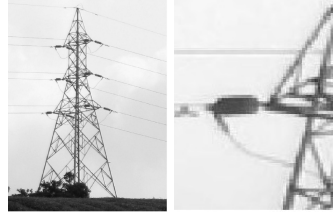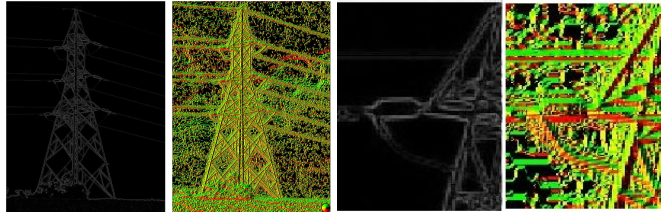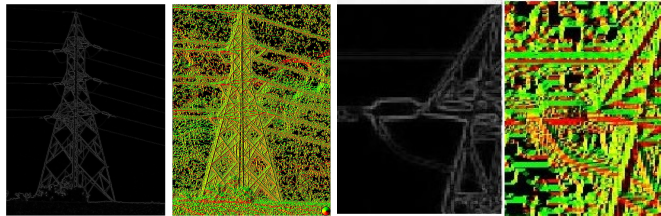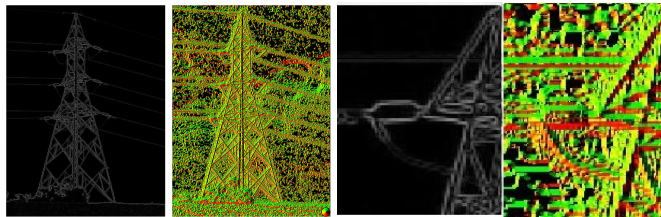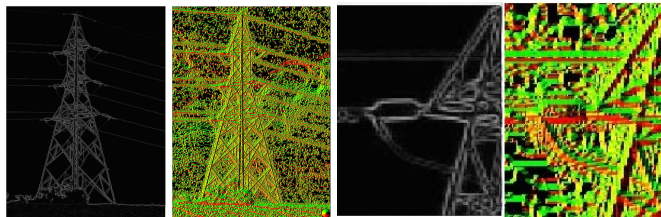
Figure B.3: Edge characterization on a realistic image from the Kodak dataset. a) original image, b) central difference, c) derivative of Gaussian, d) Sobel, e) $LFDG$. The last two columns are the enlarged version. The faint wire edges are more evident in the magnitude of $LFDG$.

Appendix C

Additional Results of Voxel-based Texture Analysis

In this appendix, the performance of the texture features obtained by voxel-based methods, VGLCM-3D, and VGLCM-TOP-3D are presented. The performance metrics include detection rate, union overlap, false negative error, and false positive error. These measurements are reported for each of the eight lesion types and for texture features f_1, f_2, f_3, f_4, f_5, f_7, and f_8 in Table 2.1.

Table C.1: The performance of f_1 (Autocorrelation) computed for the 8 artificial effect types. For each artificial effect type 60 artificial lesions are generated. The statistical significance of quantization level is denoted by †. That is, if a quantization level significantly improves a measurement (its result is significantly better), it is denoted by †. The statistical significance of method (VGLCM-TOP-3D vs VGLCM-3D) is denoted by *. That is, if a method has a significantly better performance in a specific measurement, that measurement is denoted by * for the better method. The significance is set to ($p < 0.05$).

		Q=8			Q=16			
	Type	Detect	UO	FN Error	FP Error	Detect	UO	FN Error	FP Error
VGLCM-TOP-3D	I	98%	0.67±0.26	0.20±0.29	0.14±0.17	98%	0.63±0.23	0.17±0.26	0.21±0.20
	II	92%	0.53±0.28	0.42±0.31	0.06±0.11	95%	0.64±0.27	0.24±0.31	0.13±0.18
	III	100%	0.51±0.17	0.01±0.03	0.48±0.19	100%	0.48±0.18	0.01±0.04	0.51±0.20
	IV	100%	0.58±0.16	0.01±0.03	0.42±0.18	100%	0.62±0.18	0.02±0.03	0.37±0.19
	V	100%	0.71±0.16	0.12±0.19	0.18±0.15	100%	0.66±0.15	0.10±0.18	0.26±0.16
	VI	100%	0.74±0.19	0.17±0.21	0.10±0.12	100%	0.72±0.17	0.11±0.19	0.18±0.15
	VII	100%	0.53±0.16	0.00±0.01	0.47±0.17	100%	0.50±0.17	0.00±0.01	0.50±0.18
	VIII	100%	0.65±0.15	0.00±0.01	0.35±0.16	100%	0.68±0.16	0.01±0.01	0.32±0.17
	ALL	99%	0.61±0.20*	0.11±0.19*	0.28±0.20*†	99%	0.61±0.21*	0.08±0.19*†	0.31±0.22*
VGLCM-3D	I	98%	0.60±0.25	0.23±0.29	0.18±0.20	98%	0.55±0.24	0.21±0.29	0.26±0.22
	II	90%	0.42±0.27	0.53±0.31	0.06±0.12	93%	0.56±0.26	0.30±0.32	0.15±0.19
	III	100%	0.43±0.16	0.02±0.05	0.56±0.19	100%	0.40±0.16	0.02±0.06	0.58±0.19
	IV	100%	0.51±0.17	0.03±0.08	0.47±0.20	100%	0.57±0.20	0.04±0.08	0.40±0.23
	V	100%	0.61±0.15	0.15±0.22	0.27±0.17	100%	0.55±0.13	0.13±0.21	0.35±0.18
	VI	100%	0.66±0.18	0.22±0.23	0.14±0.14	100%	0.63±0.17	0.15±0.21	0.24±0.17
	VII	100%	0.45±0.12	0.01±0.02	0.55±0.13	100%	0.43±0.13	0.01±0.03	0.56±0.14
	VIII	100%	0.56±0.14	0.01±0.03	0.44±0.16	100%	0.59±0.15	0.02±0.03	0.40±0.17
	ALL	98%	0.52±0.21	0.16±0.26	0.33±0.25†	99%	0.53±0.20	0.11±0.22†	0.37±0.23

Table C.2: The performance of f_2 (Homogeneity) computed for the 8 artificial effect types. For each artificial effect type 60 artificial lesions are generated. The statistical significance of quantization level is denoted by $\dagger$. That is, if a quantization level significantly improves a measurement (its result is significantly better), it is denoted by $\dagger$. The statistical significance of method (VGLCM-TOP-3D vs VGLCM-3D) is denoted by $*$. That is, if a method has a significantly better performance in a specific measurement, that measurement is denoted by $*$ for the better method. The significance is set to ($p < 0.05$).

		Q=8				Q=16			
	Type	Detect	UO	FN Error	FP Error	Detect	UO	FN Error	FP Error
VGLCM-TOP-3D	I	100%	0.44±0.19	0.29±0.29	0.39±0.22	100%	0.44±0.15	0.21±0.25	0.43±0.22
	II	88%	0.45±0.27	0.42±0.36	0.20±0.23	90%	0.41±0.23	0.31±0.38	0.33±0.25
	III	100%	0.34±0.09	0.03±0.11	0.66±0.09	100%	0.36±0.12	0.05±0.13	0.63±0.14
	IV	100%	0.34±0.10	0.06±0.18	0.64±0.10	100%	0.41±0.12	0.15±0.24	0.49±0.19
	V	100%	0.39±0.12	0.40±0.23	0.39±0.20	100%	0.41±0.10	0.28±0.24	0.43±0.20
	VI	100%	0.44±0.17	0.30±0.31	0.36±0.17	100%	0.40±0.15	0.31±0.30	0.41±0.19
	VII	100%	0.37±0.07	0.07±0.12	0.61±0.07	100%	0.39±0.09	0.09±0.15	0.59±0.10
	VIII	100%	0.36±0.07	0.09±0.17	0.62±0.06	100%	0.36±0.10	0.30±0.25	0.54±0.13
	ALL	98%	0.39±0.16*	0.21±0.28	0.48±0.23*	99%	0.39±0.14*	0.21±0.27	0.48±0.20*
VGLCM-3D	I	97%	0.39±0.13	0.28±0.28	0.45±0.20	97%	0.39±0.14	0.22±0.27	0.49±0.24
	II	87%	0.37±0.23	0.45±0.37	0.27±0.26	90%	0.31±0.16	0.33±0.40	0.41±0.28
	III	100%	0.30±0.06	0.02±0.05	0.70±0.06	100%	0.31±0.08	0.02±0.06	0.68±0.09
	IV	98%	0.29±0.08	0.07±0.20	0.67±0.13	98%	0.34±0.11	0.11±0.25	0.59±0.17
	V	100%	0.35±0.10	0.37±0.24	0.50±0.15	100%	0.38±0.08	0.26±0.23	0.52±0.13
	VI	96%	0.39±0.12	0.26±0.31	0.46±0.17	98%	0.37±0.11	0.25±0.30	0.50±0.15
	VII	100%	0.32±0.05	0.04±0.11	0.67±0.05	100%	0.33±0.05	0.05±0.10	0.66±0.05
	VIII	100%	0.32±0.06	0.06±0.15	0.67±0.07	100%	0.31±0.09	0.22±0.26	0.63±0.09
	ALL	97%	0.34±0.13	0.20±0.29	0.54±0.21	98%	0.34±0.11	0.18±0.28	0.56±0.19

Table C.3: The performance of f_3 (Energy) computed for the 8 artificial effect types. For each artificial effect type 60 artificial lesions are generated. The statistical significance of quantization level is denoted by $\dagger$. That is, if a quantization level significantly improves a measurement (its result is significantly better), it is denoted by $\dagger$. The statistical significance of method (VGLCM-TOP-3D vs VGLCM-3D) is denoted by $*$. That is, if a method has a significantly better performance in a specific measurement, that measurement is denoted by $*$ for the better method. The significance is set to ($p < 0.05$).

		Q=8				Q=16			
	Type	Detect	UO	FN Error	FP Error	Detect	UO	FN Error	FP Error
VGLCM-TOP-3D	I	100%	0.43±0.15	0.32±0.27	0.38±0.20	100%	0.44±0.15	0.30±0.31	0.34±0.20
	II	83%	0.36±0.25	0.52±0.35	0.23±0.24	87%	0.36±0.23	0.41±0.41	0.29±0.21
	III	100%	0.43±0.11	0.07±0.12	0.55±0.12	100%	0.48±0.15	0.17±0.26	0.42±0.16
	IV	100%	0.42±0.10	0.08±0.16	0.55±0.13	93%	0.35±0.17	0.43±0.34	0.39±0.18
	V	100%	0.37±0.11	0.44±0.22	0.40±0.18	100%	0.42±0.15	0.35±0.31	0.35±0.16
	VI	100%	0.41±0.17	0.35±0.32	0.39±0.14	98%	0.36±0.18	0.45±0.34	0.38±0.17
	VII	100%	0.44±0.08	0.12±0.12	0.52±0.09	100%	0.48±0.13	0.20±0.25	0.42±0.14
	VIII	100%	0.41±0.09	0.15±0.16	0.55±0.10	98%	0.35±0.15	0.48±0.27	0.40±0.18
	ALL	98%	0.41±0.15*	0.26±0.28†	0.44±0.19*	97%	0.41±0.18*	0.35±0.33	0.37±0.18*†
VGLCM-3D	I	100%	0.34±0.12	0.40±0.29	0.43±0.22	97%	0.35±0.13	0.35±0.34	0.41±0.25
	II	88%	0.29±0.20	0.57±0.33	0.35±0.25	92%	0.28±0.16	0.40±0.41	0.39±0.27
	III	100%	0.34±0.07	0.12±0.14	0.63±0.09	100%	0.37±0.09	0.17±0.24	0.57±0.13
	IV	100%	0.32±0.08	0.13±0.20	0.64±0.11	96%	0.27±0.11	0.38±0.33	0.61±0.17
	V	100%	0.32±0.08	0.45±0.21	0.50±0.15	100%	0.36±0.09	0.34±0.28	0.46±0.15
	VI	100%	0.34±0.12	0.35±0.33	0.49±0.16	96%	0.30±0.11	0.40±0.32	0.53±0.17
	VII	100%	0.36±0.05	0.14±0.13	0.61±0.05	100%	0.38±0.07	0.18±0.22	0.56±0.08
	VIII	100%	0.33±0.07	0.15±0.18	0.63±0.08	100%	0.28±0.10	0.41±0.26	0.61±0.13
	ALL	98%	0.33±0.11	0.29±0.29	0.53±0.19	98%	0.32±0.12	0.33±0.32	0.52±0.20

Table C.4: The performance of f_4 (Correlation) computed for the 8 artificial effect types. For each artificial effect type 60 artificial lesions are generated. The statistical significance of quantization level is denoted by $\dagger$. That is, if a quantization level significantly improves a measurement (its result is significantly better), it is denoted by $\dagger$. The statistical significance of method (VGLCM-TOP-3D vs VGLCM-3D) is denoted by $*$. That is, if a method has a significantly better performance in a specific measurement, that measurement is denoted by $*$ for the better method. The significance is set to ($p < 0.05$).

	Type	Q=8				Q=16			
		Detect	UO	FN Error	FP Error	Detect	UO	FN Error	FP Error
VGLCM-TOP-3D	I	95%	0.22±0.11	0.70±0.17	0.37±0.28	98%	0.29±0.15	0.59±0.20	0.39±0.26
	II	73%	0.12±0.11	0.85±0.14	0.25±0.26	93%	0.20±0.13	0.73±0.20	0.39±0.28
	III	100%	0.27±0.12	0.51±0.16	0.56±0.26	100%	0.30±0.14	0.42±0.20	0.59±0.23
	IV	100%	0.27±0.09	0.51±0.18	0.55±0.22	98%	0.30±0.15	0.49±0.23	0.53±0.24
	V	96%	0.20±0.11	0.71±0.18	0.47±0.22	100%	0.23±0.13	0.65±0.20	0.48±0.22
	VI	95%	0.19±0.11	0.76±0.15	0.35±0.21	98%	0.26±0.11	0.64±0.19	0.40±0.21
	VII	100%	0.24±0.07	0.52±0.19	0.59±0.20	100%	0.27±0.09	0.47±0.18	0.60±0.19
	VIII	100%	0.27±0.08	0.49±0.19	0.57±0.14	100%	0.31±0.09	0.49±0.16	0.50±0.18
	ALL	95%	0.22±0.11*	0.63±0.21	0.46±0.26*	98%	0.26±0.13*†	0.56±0.22†	0.48±0.24*
VGLCM-3D	I	98%	0.21±0.09	0.65±0.20	0.49±0.25	100%	0.27±0.13	0.48±0.25	0.59±0.21
	II	82%	0.12±0.09	0.84±0.12	0.37±0.32	97%	0.22±0.12	0.63±0.21	0.54±0.22
	III	100%	0.23±0.11	0.41±0.17	0.72±0.14	100%	0.20±0.08	0.30±0.22	0.78±0.09
	IV	100%	0.23±0.09	0.49±0.21	0.65±0.18	100%	0.25±0.10	0.39±0.23	0.66±0.18
	V	98%	0.20±0.10	0.65±0.21	0.59±0.17	100%	0.23±0.08	0.54±0.22	0.63±0.13
	VI	100%	0.18±0.09	0.74±0.15	0.49±0.22	98%	0.26±0.09	0.55±0.18	0.54±0.16
	VII	100%	0.23±0.05	0.40±0.17	0.70±0.10	100%	0.23±0.06	0.27±0.14	0.75±0.08
	VIII	100%	0.26±0.08	0.45±0.19	0.64±0.11	100%	0.29±0.09	0.35±0.16	0.63±0.15
	ALL	97%	0.20±0.10	0.59±0.24*	0.58±0.23†	99%	0.24±0.10†	0.44±0.24*†	0.64±0.18

Table C.5: The performance of f_5 (Dissimilarity) computed for the 8 artificial effect types. For each artificial effect type 60 artificial lesions are generated. The statistical significance of quantization level is denoted by $\dagger$. That is, if a quantization level significantly improves a measurement (its result is significantly better), it is denoted by $\dagger$. The statistical significance of method (VGLCM-TOP-3D vs VGLCM-3D) is denoted by $*$. That is, if a method has a significantly better performance in a specific measurement, that measurement is denoted by $*$ for the better method. The significance is set to ($p < 0.05$).

	Type	Q=8				Q=16			
		Detect	UO	FN Error	FP Error	Detect	UO	FN Error	FP Error
VGLCM-TOP-3D	I	97%	0.37±0.20	0.40±0.30	0.48±0.24	98%	0.36±0.17	0.28±0.30	0.53±0.22
	II	85%	0.38±0.27	0.52±0.35	0.24±0.27	92%	0.38±0.23	0.35±0.38	0.40±0.26
	III	98%	0.26±0.10	0.17±0.28	0.73±0.09	100%	0.24±0.08	0.10±0.23	0.75±0.07
	IV	96%	0.26±0.11	0.20±0.32	0.72±0.09	100%	0.31±0.12	0.15±0.29	0.66±0.12
	V	100%	0.33±0.13	0.53±0.20	0.43±0.20	100%	0.36±0.13	0.35±0.25	0.50±0.20
	VI	100%	0.39±0.18	0.40±0.31	0.41±0.18	100%	0.38±0.17	0.31±0.31	0.49±0.16
	VII	100%	0.31±0.09	0.18±0.25	0.67±0.07	100%	0.29±0.08	0.11±0.21	0.70±0.07
	VIII	100%	0.30±0.09	0.20±0.27	0.68±0.06	100%	0.32±0.10	0.21±0.25	0.64±0.09
	ALL	97%	0.33±0.17*	0.33±0.32	0.54±0.24*†	99%	0.33±0.15*	0.24±0.30	0.58±0.20*
VGLCM-3D	I	97%	0.34±0.14	0.36±0.29	0.50±0.20	95%	0.32±0.13	0.27±0.30	0.57±0.20
	II	85%	0.34±0.23	0.48±0.38	0.28±0.27	90%	0.32±0.18	0.35±0.38	0.47±0.26
	III	100%	0.23±0.06	0.09±0.20	0.77±0.06	100%	0.21±0.06	0.06±0.17	0.79±0.06
	IV	98%	0.25±0.09	0.13±0.27	0.71±0.13	100%	0.28±0.10	0.11±0.25	0.69±0.13
	V	100%	0.30±0.10	0.47±0.23	0.55±0.14	100%	0.31±0.10	0.34±0.26	0.59±0.12
	VI	96%	0.37±0.13	0.32±0.30	0.48±0.16	98%	0.36±0.13	0.25±0.31	0.54±0.14
	VII	100%	0.26±0.06	0.12±0.22	0.73±0.05	100%	0.25±0.06	0.07±0.18	0.75±0.06
	VIII	100%	0.27±0.07	0.13±0.24	0.71±0.06	100%	0.30±0.09	0.12±0.25	0.67±0.07
	ALL	97%	0.30±0.13	0.27±0.31*	0.59±0.22†	98%	0.30±0.12	0.20±0.29†	0.63±0.18

Table C.6: The performance of f_7 (Sum average) computed for the 8 artificial effect types. For each artificial effect type 60 artificial lesions are generated. The statistical significance of quantization level is denoted by †. That is, if a quantization level significantly improves a measurement (its result is significantly better), it is denoted by †. The statistical significance of method (VGLCM-TOP-3D vs VGLCM-3D) is denoted by *. That is, if a method has a significantly better performance in a specific measurement, that measurement is denoted by * for the better method. The significance is set to ($p < 0.05$).

	Type	Q=8				Q=16			
		Detect	UO	FN Error	FP Error	Detect	UO	FN Error	FP Error
VGLCM-TOP-3D	I	98%	0.67±0.26	0.22±0.29	0.13±0.16	98%	0.61±0.23	0.19±0.28	0.22±0.19
	II	90%	0.52±0.28	0.45±0.31	0.05±0.10	95%	0.62±0.27	0.27±0.31	0.12±0.17
	III	100%	0.51±0.17	0.01±0.03	0.49±0.18	100%	0.48±0.18	0.01±0.02	0.51±0.19
	IV	100%	0.60±0.17	0.01±0.03	0.39±0.19	100%	0.64±0.19	0.03±0.05	0.34±0.21
	V	100%	0.70±0.17	0.12±0.20	0.19±0.15	100%	0.65±0.15	0.11±0.19	0.26±0.16
	VI	100%	0.73±0.19	0.19±0.22	0.09±0.11	100%	0.72±0.17	0.13±0.20	0.16±0.14
	VII	100%	0.53±0.16	0.00±0.01	0.47±0.16	100%	0.50±0.17	0.00±0.01	0.50±0.17
	VIII	100%	0.67±0.16	0.01±0.01	0.32±0.16	100%	0.71±0.17	0.01±0.02	0.28±0.18
	ALL	98%	0.62±0.22*	0.13±0.24*	0.26±0.22*†	99%	0.62±0.21*	0.10±0.20*†	0.30±0.22*
VGLCM-3D	I	95%	0.58±0.25	0.26±0.30	0.18±0.20	97%	0.54±0.23	0.23±0.30	0.26±0.22
	II	88%	0.41±0.26	0.55±0.31	0.06±0.12	93%	0.53±0.25	0.34±0.32	0.15±0.19
	III	100%	0.42±0.16	0.02±0.06	0.56±0.18	100%	0.41±0.16	0.02±0.06	0.58±0.18
	IV	100%	0.53±0.17	0.04±0.09	0.44±0.21	100%	0.58±0.19	0.06±0.10	0.38±0.23
	V	100%	0.60±0.15	0.16±0.22	0.27±0.17	100%	0.54±0.14	0.15±0.22	0.35±0.18
	VI	100%	0.64±0.19	0.24±0.24	0.14±0.14	100%	0.63±0.17	0.17±0.22	0.22±0.17
	VII	100%	0.45±0.12	0.01±0.03	0.54±0.13	100%	0.44±0.13	0.01±0.03	0.56±0.13
	VIII	100%	0.58±0.15	0.02±0.04	0.41±0.16	100%	0.61±0.16	0.03±0.04	0.37±0.18
	ALL	98%	0.53±0.20	0.17±0.26	0.32±0.24†	99%	0.53±0.20	0.13±0.23†	0.36±0.24

Table C.7: The performance of f_8 (Sum entropy) computed for the 8 artificial effect types. For each artificial effect type 60 artificial lesions are generated. The statistical significance of quantization level is denoted by †. That is, if a quantization level significantly improves a measurement (its result is significantly better), it is denoted by †. The statistical significance of method (VGLCM-TOP-3D vs VGLCM-3D) is denoted by *. That is, if a method has a significantly better performance in a specific measurement, that measurement is denoted by * for the better method. The significance is set to ($p < 0.05$).

	Type	Q=8				Q=16			
		Detect	UO	FN Error	FP Error	Detect	UO	FN Error	FP Error
VGLCM-TOP-3D	I	100%	0.34±0.14	0.46±0.23	0.48±0.20	100%	0.36±0.10	0.36±0.25	0.48±0.19
	II	93%	0.31±0.18	0.54±0.31	0.37±0.22	100%	0.32±0.15	0.42±0.35	0.42±0.23
	III	100%	0.32±0.09	0.20±0.24	0.66±0.08	100%	0.34±0.09	0.15±0.20	0.63±0.09
	IV	100%	0.28±0.09	0.21±0.26	0.69±0.08	100%	0.31±0.08	0.30±0.24	0.61±0.13
	V	100%	0.32±0.10	0.53±0.17	0.45±0.16	100%	0.37±0.11	0.37±0.23	0.46±0.17
	VI	100%	0.34±0.13	0.41±0.29	0.50±0.13	100%	0.33±0.10	0.40±0.27	0.51±0.13
	VII	100%	0.35±0.09	0.22±0.20	0.61±0.07	100%	0.37±0.08	0.17±0.20	0.60±0.07
	VIII	100%	0.31±0.08	0.23±0.23	0.65±0.06	100%	0.30±0.07	0.38±0.21	0.60±0.11
	ALL	99%	0.32±0.12*	0.35±0.28	0.55±0.18*	100%	0.34±0.10*†	0.32±0.27	0.54±0.17*
VGLCM-3D	I	100%	0.30±0.10	0.46±0.25	0.53±0.15	100%	0.30±0.08	0.36±0.27	0.56±0.15
	II	93%	0.26±0.14	0.48±0.35	0.52±0.21	100%	0.24±0.08	0.39±0.35	0.59±0.20
	III	100%	0.27±0.04	0.17±0.16	0.71±0.05	100%	0.27±0.05	0.14±0.15	0.72±0.06
	IV	100%	0.24±0.05	0.14±0.19	0.74±0.07	100%	0.25±0.05	0.22±0.22	0.73±0.07
	V	100%	0.30±0.07	0.48±0.18	0.55±0.10	100%	0.32±0.07	0.36±0.23	0.57±0.10
	VI	100%	0.29±0.09	0.34±0.30	0.61±0.09	100%	0.28±0.07	0.34±0.27	0.63±0.09
	VII	100%	0.30±0.05	0.17±0.15	0.67±0.05	100%	0.30±0.05	0.15±0.13	0.68±0.06
	VIII	100%	0.26±0.06	0.16±0.20	0.72±0.08	100%	0.26±0.05	0.27±0.17	0.70±0.08
	ALL	99%	0.28±0.09	0.31±0.28*	0.63±0.14	100%	0.28±0.07	0.28±0.25*	0.65±0.13

Appendix D

Proofs in Details

In this section a more detailed version of the proof is presented which is not given in the paper due to the space limit. Before we start, let's establish the required equations and facts.

Using vector notation, a point X_L in an ellipse satisfies $X_L^T M_L X_L = 0$ in the homogeneous representation, where M_L is a symmetric matrix. Consider two elliptical regions $X_L^T M_L X_L = 0$ and $X_R^T M_R X_R = 0$ with canonical regions, X_{Lc} and X_{Rc}:

$$X_{Lc} = M_L^{1/2} X_L \tag{D.1}$$

$$X_{Rc} = M_R^{1/2} X_R \tag{D.2}$$

As shown by Mikolajczyk and Schmid [246], if the two elliptical regions are corresponding, their canonical regions are related by a rotation:

$$X_{Rc} = R(\alpha) X_{Lc}$$

Substituting Eq. (D.1),(D.2) $\Rightarrow$

$$M_R^{1/2} X_R = R(\alpha) M_L^{1/2} X_L$$
$$X_R = M_R^{-1/2} R(\alpha) M_L^{1/2} X_L \tag{D.3}$$

Since M_L and M_R are symmetric matrices, they can be decomposed to the following forms:

$$M_L = \Sigma_L \Lambda_L \Sigma_L^T, \tag{D.4}$$

$$M_R = \Sigma_R \Lambda_R \Sigma_R^T, \tag{D.5}$$

where Σ_L and Σ_R are eigenvector matrices (i.e., orthogonal), and Λ_L and Λ_R the eigenvalue matrices (i.e., diagonal). We define the transformation H:

$$H = \Sigma_L S^{-1} \Sigma_L^T, \tag{D.6}$$

where Σ_L represents the eigenvector matrix of M_L, and

$$S = \begin{bmatrix} s_1 & 0 \\ 0 & s_2 \end{bmatrix}. \tag{D.7}$$

185

Lemma A. When D is diagonal and Q is orthogonal, then:

$$(QDQ^T)^{1/2} = QD^{1/2}Q^T = QD^{1/2}Q^{-1}.$$

Proof. Since D is a diagonal matrix, $D = D^{1/2}D^{1/2}$:

$$D = \begin{bmatrix} d_1 & 0 \\ 0 & d_2 \end{bmatrix}$$
$$= \begin{bmatrix} \sqrt{d_1} & 0 \\ 0 & \sqrt{d_2} \end{bmatrix} \begin{bmatrix} \sqrt{d_1} & 0 \\ 0 & \sqrt{d_2} \end{bmatrix}$$

Moreover, Q is orthogonal ($Q^T = Q^{-1}$) and therefore $Q^T Q = Q^{-1}Q$ is the identity matrix.

$$\begin{aligned}
(QDQ^T)^{1/2} =& (QD^{1/2}D^{1/2}Q^T)^{1/2} \\
& \text{Adding } Q^T Q \Rightarrow \\
=& (QD^{1/2}Q^T QD^{1/2}Q^T)^{1/2} \\
=& ((QD^{1/2}Q^T)(QD^{1/2}Q^T))^{1/2} \\
=& ((QD^{1/2}Q^T)(QD^{1/2}Q^T)^T)^{1/2} \\
=& ((QD^{1/2}Q^T)^2)^{1/2} \\
=& QD^{1/2}Q^T \\
=& QD^{1/2}Q^{-1}
\end{aligned}$$

$\square$

Lemma B. When S and D are diagonal and Q is orthogonal, then:

$$(QSDS^T Q^T)^{1/2} = QD^{1/2}S^T Q^T = QD^{1/2}SQ^T.$$

Proof. The proof is similar to that of Lemma A. We just need to consider that the multiplication of *diagonal matrices* has the commutative property (i.e., $SD = DS$).

$$\begin{aligned}
(QSDS^T Q^T)^{1/2} =& (QSDSQ^T)^{1/2} \\
=& (QSD^{1/2}D^{1/2}SQ^T)^{1/2} \\
& \text{Adding } Q^T Q \Rightarrow \\
=& (QSD^{1/2}Q^T QD^{1/2}SQ^T)^{1/2} \\
=& ((QSD^{1/2}Q^T)(QD^{1/2}SQ^T))^{1/2} \\
=& ((QSD^{1/2}Q^T)(QSD^{1/2}Q^T)^T)^{1/2} \\
=& ((QSD^{1/2}Q^T)^2)^{1/2} \\
=& QSD^{1/2}Q^T \\
& \text{commutativity of } D^{1/2}S \Rightarrow \\
=& QD^{1/2}SQ^T \\
=& QD^{1/2}S^T Q^T.
\end{aligned}$$

$\square$

D.1 Lemma 1 Detailed Proof

Lemma 1. Transformation H maps $X_L^T M_L X_L = 0$ into a new ellipse, the eigenvectors of which are the same as the old ellipse but the eigenvalues are scaled by the $(s_1)^2$ and $(s_2)^2$ factors.

Proof. If the ellipse $X_L^T M_L X_L = 0$ undergoes the H transformation, the new ellipse is defined as

$$X_L'^T M_L' X_L' = 0, \tag{D.8}$$

where X_L' and M_L' are

$$X_L' = H X_L, \text{ and} \tag{D.9}$$

$$M_L' = H^{-T} M_L H^{-1}, \tag{D.10}$$

respectively (refer to [133] for more information). We substitute M_L (Eq. D.4), and H (Eq. D.6) in Eq. (D.10):

$$
\begin{aligned}
M_L' &= (\Sigma_L S^{-1} \Sigma_L^T)^{-T} \Sigma_L \Lambda_L \Sigma_L^T (\Sigma_L S^{-1} \Sigma_L^T)^{-1} \\
&= (\Sigma_L^{-T} S \Sigma_L^{-1}) \Sigma_L \Lambda_L \Sigma_L^T (\Sigma_L^{-T} S \Sigma_L^{-1}) \\
&= \Sigma_L^{-T} S (\Sigma_L^{-1} \Sigma_L) \Lambda_L (\Sigma_L^T \Sigma_L^{-T}) S \Sigma_L^{-1} \\
&= \Sigma_L^{-T} S \Lambda_L S \Sigma_L^{-1}.
\end{aligned} \tag{D.11}
$$

Σ_L is orthogonal and S is diagonal; therefore,

$$\Sigma_L^{-1} = \Sigma_L^T \tag{D.12}$$

$$S = S^T. \tag{D.13}$$

As a result, Eq. D.11 can be written as

$$
\begin{aligned}
M_L' &= (\Sigma_L^{-1})^T S \Lambda_L S^T \Sigma_L^{-1} \\
&= (\Sigma_L^T)^T S \Lambda_L S^T \Sigma_L^T \\
&= \Sigma_L S \Lambda_L S^T \Sigma_L^T.
\end{aligned} \tag{D.14}
$$

Hence, the eigenvectors of the transformed ellipse are the same as one before transformation and the eigenvalues are scaled by s_1^2, and s_2^2, respectively, which are claimed in Lemma 1. $\square$

D.2 Theorem 1 Detailed Proof

Theorem 1. Assume that the original ellipses defined by M_L and M_R undergo the H_L and H_R transformations:

$$H_L = R \Sigma_L S^{-1} \Sigma_L^T, \tag{D.15}$$

$$H_R = R\Sigma_R S^{-1}\Sigma_R^T, \tag{D.16}$$

where R is an arbitrary rotation matrix. Then, the ellipses are:

$$X_L'^T M_L' X_L' = 0, \tag{D.17}$$

$$X_R'^T M_R' X_R' = 0, \tag{D.18}$$

where X_L', X_R', M_L', and M_R' are

$$X_L' = H_L X_L, \text{and} \tag{D.19}$$

$$M_L' = H_L^{-T} M_L H_L^{-1}, \tag{D.20}$$

$$X_R' = H_R X_R, \text{and} \tag{D.21}$$

$$M_R' = H_R^{-T} M_R H_R^{-1}, \tag{D.22}$$

respectively. The canonical regions of X_L' and X_R' (i.e., X_{Lc}' and X_{Rc}') are related by a rotation.

Proof. We need to show that Eq. D.3 holds for X_L' and X_R' under the new elliptical regions defined by M_L' and M_R'. To perform the proof, we may recall that R, Σ_L, and Σ_R are orthogonal and S, Λ_L, and Λ_R are diagonal matrices. We also use Lemma C, presented after this theorem, to shorten

the proof. We start by multiplying Eq. D.3 with H_R

$$H_R X_R = H_R M_R^{-1/2} R(\alpha) M_L^{1/2} X_L$$

Adding $H_L^{-1} H_L \Rightarrow$

$$= H_R M_R^{-1/2} R(\alpha) M_L^{1/2} H_L^{-1} H_L X_L$$

Substituting $M_L, M_R, H_L,$ and $H_R,$ using Eqs. (D.4),(D.5),(D.15),(D.16) $\Rightarrow$

$$= (R \Sigma_R S^{-1} \Sigma_R^T)(\Sigma_R \Lambda_R \Sigma_R^T)^{-1/2} R(\alpha)(\Sigma_L \Lambda_L \Sigma_L^T)^{1/2}(\Sigma_L^{-T} S \Sigma_L^{-1} R^{-1}) H_L X_L$$

Lemma A $\Rightarrow$

$$= (R \Sigma_R S^{-1} \Sigma_R^T)(\Sigma_R \Lambda_R^{-1/2} \Sigma_R^T) R(\alpha)(\Sigma_L \Lambda_L^{1/2} \Sigma_L^T)(\Sigma_L^{-T} S \Sigma_L^{-1} R^{-1}) H_L X_L$$

$$= R \Sigma_R S^{-1} (\Sigma_R^T \Sigma_R) \Lambda_R^{-1/2} \Sigma_R^T R(\alpha) \Sigma_L \Lambda_L^{1/2} (\Sigma_L^T \Sigma_L^{-T}) S \Sigma_L^{-1} R^{-1} H_L X_L$$

$$= R \Sigma_R S^{-1} \Lambda_R^{-1/2} \Sigma_R^T R(\alpha) \Sigma_L \Lambda_L^{1/2} S \Sigma_L^{-1} R^{-1} H_L X_L$$

Adding $R^{-1} R \Rightarrow$

$$= R \Sigma_R S^{-1} \Lambda_R^{-1/2} \Sigma_R^T (R^{-1} R) R(\alpha)(R^{-1} R) \Sigma_L \Lambda_L^{1/2} S \Sigma_L^{-1} R^{-1} H_L X_L$$

$$= (R \Sigma_R S^{-1} \Lambda_R^{-1/2} \Sigma_R^T R^{-1}) R R(\alpha) R^{-1} (R \Sigma_L \Lambda_L^{1/2} S \Sigma_L^{-1} R^{-1}) H_L X_L$$

Lemma C (see below) $\Rightarrow$

$$= (H_R^{-T} M_R H_R^{-1})^{-1/2} R R(\alpha) R^{-1} (H_L^{-T} M_L H_L^{-1})^{1/2} H_L X_L$$

R and $R(\alpha)$ are both rotation matrices, therefore, substitute $R R(\alpha) R^{-1}$ with $R(\gamma) \Rightarrow$

$$= (H_R^{-T} M_R H_R^{-1})^{-1/2} R(\gamma)(H_L^{-T} M_L H_L^{-1})^{1/2} H_L X_L$$

Substituting $X_R', M_R', M_L',$ and $X_L',$ using Eqs. (D.21),(D.22),(D.20),(D.19) $\Rightarrow$

$$X_R' = M_R'^{-1/2} R(\gamma) M_L'^{1/2} X_L'.$$

$$\tag{D.23}$$

$\square$

Lemma C. The followings hold in the proof of Theorem 1:

$$R \Sigma_R S^{-1} \Lambda_R^{-1/2} \Sigma_R^T R^{-1} = (H_R^{-T} M_R H_R^{-1})^{-1/2}, \tag{D.24}$$

$$R \Sigma_L \Lambda_L^{1/2} S \Sigma_L^{-1} R^{-1} = (H_L^{-T} M_L H_L^{-1})^{1/2}. \tag{D.25}$$

Proof. We give the proof for Eq. (D.25). Eq. (D.24) can be proven using similar steps with an aditional power of -1. We start from the right hand side of Eq. (D.25) and show that it is equal to

the left hand side. First, let's find H_L^{-1} and H_L^{-T}.

$$H_L^{-1} = (R\Sigma_L S^{-1}\Sigma_L^T)^{-1}$$
$$= \Sigma_L^{-T} S \Sigma_L^{-1} R^{-1}$$

Eq. (D.12) $\Rightarrow$

$$= (\Sigma_L^T)^T S \Sigma_L^T R^{-1}$$
$$= \Sigma_L S \Sigma_L^T R^{-1}$$
$$= \Sigma_L S \Sigma_L^T R^T \tag{D.26}$$

$$H_L^{-T} = (H_L^{-1})^T$$

Substituting H_L^{-1} using Eq. (D.26) $\Rightarrow$

$$= (\Sigma_L S \Sigma_L^T R^T)^T$$
$$= R \Sigma_L S^T \Sigma_L^T$$

Eq. (D.13) $\Rightarrow$

$$= R \Sigma_L S \Sigma_L^T \tag{D.27}$$

Now, we begin from the right hand side of Eq. (D.25) and substitute H_L^{-T}, H_L^{-1}, and M_L using Eqs. (D.27),(D.26),(D.4), respectively:

$$(H_L^{-T} M_L H_L^{-1})^{1/2} = [(R\Sigma_L S \Sigma_L^T)(\Sigma_L \Lambda_L \Sigma_L^T)(\Sigma_L S \Sigma_L^T R^T)]^{1/2}$$
$$= [(R\Sigma_L S)(\Sigma_L^T \Sigma_L)\Lambda_L(\Sigma_L^T \Sigma_L)S \Sigma_L^T R^T)]^{1/2}$$
$$= (R\Sigma_L S \Lambda_L S \Sigma_L^T R^T)^{1/2}$$

Eq. (D.13): $S = S^T \Rightarrow$

$$= (R\Sigma_L S \Lambda_L S^T \Sigma_L^T R^T)^{1/2}$$

$R\Sigma_L$ is orthogonal, (R and Σ_L are both orthogonal), therefore, Lemma B $\Rightarrow$

$$= R\Sigma_L \Lambda_L^{1/2} S \Sigma_L^T R^T$$
$$= R\Sigma_L \Lambda_L^{1/2} S \Sigma_L^{-1} R^{-1}. \tag{D.28}$$

$\square$